Title
Accounting for Viscous Effects in Nonlinear Analyses of Strain Softening Clays

Author
Oathes, Tyler J

Publication Date
2022

Peer reviewed|Thesis/dissertation

Accounting for Viscous Effects in Nonlinear Analyses of Strain Softening Clays

By

TYLER J. OATHES
DISSERTATION

Submitted in partial satisfaction of the requirements for the degree of

DOCTOR OF PHILOSOPHY

in

Civil and Environmental Engineering

in the

OFFICE OF GRADUATE STUDIES

of the

UNIVERSITY OF CALIFORNIA

DAVIS

Approved:

Ross W. Boulanger, Chair

Jason T. DeJong

Katerina Ziotopoulou

Committee in Charge

2022

Contents

List of Figures

List of Tables

Abstract

Accounting for Viscous Effects in Nonlinear Analyses of Strain Softening Clays

The results of static and dynamic nonlinear analyses of earthen structures are dependent on the implemented numerical methods including the constitutive models, the solution scheme, and the modeling software. Recent significant static failures (e.g., Feijão Dam 1) and past dynamic failures (e.g., 4th Ave. landslide in Anchorage, Alaska) have occurred due to yielding of the plastic soils. These failures were influenced by the strain-softening tendencies of the plastic soils, which highlights the need for continued development of numerical tools to model plastic soils in nonlinear analyses. This dissertation presents the development of a new constitutive model, a relationship that connects element level viscous behavior to field scale analyses, and system level analyses with new solution schemes that incorporate viscous effects and strain- softening in nonlinear analyses.

First, a viscoplastic constitutive model for representing plastic silts and clays in geotechnical static slope stability applications is presented. The PM4SiltR model builds on the stress ratio-controlled, critical state-based, bounding surface plasticity model PM4Silt and is coded as a dynamic link library for use in the finite difference program FLAC 8.1. PM4SiltR incorporates strain rate-dependent shear strength, stress relaxation, and creep using a consistency approach combined with an internal strain rate and auto-decay process. Six parameters are introduced to control the viscous response of PM4SiltR while the parameters controlling the nonviscous portion of the response are the same as for PM4Silt. Single element simulations are presented to illustrate the influence

of viscoplasticity on the constitutive response in direct simple shear loading and undrained creep. Single element responses are shown to be consistent with observed experimental results. Simulations of a hypothetical tailings dam of upstream construction are performed to illustrate use of PM4SiltR at the field scale. Results of field scale simulations show PM4SiltR can model undrained creep and progressive failure leading to delayed slope instability after relatively minor changes in loading conditions at.

A numerical study is then presented that shows the effect that viscoplasticity can have on the localization process in sensitive, saturated clays and plastic silts. Numerical simulations of laboratory specimens of sensitive, viscoplastic soil subjected to monotonic, undrained, direct simple shear loading were performed using the PM4SiltR constitutive model. Parametric analyses evaluated the effects of soil sensitivity, post-peak strain-softening rate, and strain rate-dependency, as well as specimen size, mesh discretization, and loading rate. The numerical results showed that the global strain at which a localization forms primarily depends on the strain rate-dependency of the soil's shearing resistance relative to its rate of post-peak strain-softening. A regression model is subsequently presented that relates the global strain at the onset of localization to the soil's strain rate-dependency and post-peak strain-softening rate. The results indicate that the inclusion of reasonable levels of viscoplasticity significantly increases the strain that can develop before a localization develops in clays and plastic silts with modest strain-softening rates. The consistency of the numerical results with available laboratory observations is discussed. Implications for practice and future research needs are discussed.

Next, two-dimensional viscoplastic nonlinear analyses of the 2019 Feijão Dam 1 failure in Brazil are performed using the finite difference program FLAC 8.1 with the user-defined constitutive models PM4SiltR and PM4Sand. A brief history of Feijão Dam 1, its failure, and the conflicting findings from two previous independent failure investigations are summarized. The present study uses the site characterization from those prior studies to develop the dam cross section, define material index properties, and establish groundwater conditions, but uses alternative techniques for characterizing undrained shear strengths. Simulations show that the dam was marginally stable against long-term consolidated, undrained conditions and that modest loading changes were sufficient to trigger failure with deformation patterns consistent with the observed failure. Simulations further show that collapse could have been triggered by a modest wetting event causing an increase in water content and loss of suction above the phreatic surface, by ongoing drilling activities causing a localized loss of shear strength in the tailings, or a combination of both mechanisms. Sensitivity of the results to choices in the calibration process and the numerical solution scheme are discussed. The implications of these results on the interpretation of the Feijão Dam 1 failure and long-term slope stability assessment procedures in practice are discussed.

Finally, two investigations look at the influence of sensitivity and strain-softening on the seismic deformations of a set-back levee. First, nonlinear dynamic analyses are used to investigate how seismic deformations of a 6-m tall levee founded on a deposit of normally consolidated clay may vary with the sensitivity of the clay. The analysis results showed that strain-softening and associated strength loss in the clay layer increased with increasing clay sensitivity, but it did not result in increased levee deformations for the

conditions examined. Instead, the results showed that increasing clay sensitivity slightly reduced the levee deformations, which was attributed to the strength loss in the clay also causing a reduction in the accelerations that developed in the levee. Second, the results of nonlinear dynamic analyses (NDAs) of an idealized levee founded on a sensitive clay are compared with simplified procedures that combine limit equilibrium (LE) and Newmark sliding block methods. The tendency for simplified procedures to underestimate or overestimate seismic deformations compared with NDA results is shown to depend on the specific conditions (e.g., soil sensitivity and brittleness, ground motion intensity, margin of safety against instability) and how potential strength loss is accounted for in the simplified methods. Limitations of these findings for practice are discussed.

Overall, the outcomes from this dissertation contribute to an increased understanding on how to account for viscous effects and strain-softening in static and dynamic nonlinear analyses.

Acknowledgements

My time at the University of California, Davis would not have been possible without the guidance, mentorship, and friendship of many people. While I cannot acknowledge them all, I wish to recognize a few of them here:

First, I am thankful for my advisor, Professor Ross Boulanger, for his guidance first as a master's student and then as a doctoral student. Working with him continually challenged me to learn new ideas, reassess my prior conceptions, and to constantly ask the next question. His interest in all aspects of geotechnical engineering enabled me to be exposed to numerous topics both related and unrelated to my research. I am grateful for his willingness to always have discussions on any topic, whether it is soil or IPAs.

I am extremely grateful to Professor Katerina Ziotopoulou and Professor Jason DeJong for serving on my dissertation committee. Their guidance, mentorship, and friendship greatly enhanced not only my research but also my experience as a graduate student. Additionally, I am thankful to Katerina for her many discussions and comments during my job search and for helping me to understand the importance of only trying to control what I can control. I am very thankful to Jason for his guidance during the many terms that I taught with him.

I would also like to thank Professor Colleen Bronner for her mentorship on teaching which dramatically improved my teaching ability and approach. I also am deeply appreciative of her willingness to have the many conversations on numerous subjects that we had over my time in Davis.

I am thankful for my partner, Rebeca, for helping guide me through the ups and downs of a Ph.D. I am extremely grateful for her advice and support as well as her ability to challenge me to constantly improve and think in new ways which has proven to be invaluable not only in research but also in life.

The friendships I developed with Professor Trevor Carey, Ms. Maya El Kortbawi, and Mr. Kyle O'Hara are invaluable. Their advice, conversation, and energy throughout the years helped ensure the meandering path of research remained enjoyable and productive. I would like to especially thank Trevor for his assistance during my job search. Additionally, I am thankful for the other friends that I have made on this journey. Specifically, I would like to thank Mr. Brian Sawyer, Mr. Nick Stone, and Mr. James Heins for their friendship and conversation.

I would like to thank my family for their support throughout this process. They were always extremely supportive of my choices, even if they did not fully understand what I was doing at most points of my time in Davis.

Lastly, I would like to thank the California Department of Water Resources for helping to fund my dissertation.

Chapter 1: Introduction

1.1 Background

Nonlinear analyses are often used to assess the static and dynamic performance of earthen structures. The applicability of the results depends on the ability of the numerical tools (constitutive models, modeling software, and solution schemes) to accurately simulate the soil behavior and failure mechanisms that will govern the structures performance in the field. Recent significant static failures (e.g., Feijão Dam 1) and past dynamic failures (i.e., 4th Ave. landslide) have been attributed to strength loss in plastic fine grained soils. These failures highlight the need to develop numerical tools that better account for strength loss and viscous effects in plastic soils (e.g., clays, silts clays, or clayey silts) in static and dynamic nonlinear analyses.

Experimental testing on plastic silts and clays has shown that plastic soil behavior depends on the applied loading rate or loading duration, which can be referred to as viscous behavior or viscous tendencies. The peak strength of plastic soils increases approximately 10% per log cycle of loading rate (Kulhawy and Mayne, 1990). The magnitude of the strength increase depends on soil properties including the plasticity, loading history, and rate of loading. The fundamental mechanism has been postulated to be either a suppression of shear induced pore pressure, a change in the failure envelope, or a combination of the two (Sheahan et al. 1996, Lefebvre and LeBouef 1987, and Sorenson et al. 2006). DeGroot (2004) indicated that the shear strength rate dependency may decrease at slower applied strain rates and increase at faster applied strain rates. In addition, plastic soils subjected to sustained shear stresses accumulate shear strain in

time, a process known as creep, with deformations increasing with higher sustained stress levels. At high stress levels, deformations tend to increase rapidly leading to failure known as creep rupture. Plastic soils subjected to a fixed displacement (the corollary boundary condition to creep) have been shown to shed shear stress in time which is known as stress relaxation.

Sheehan (1995) discussed the existence of a static yield surface that separates viscous and inviscid behavior. This stems from experimental results which indicate that there may be a strain rate or stress level below which the behavior becomes inviscid for the suite of viscous behaviors discussed above. The results suggest that the strain rate dependence of the peak strength decreases at lower strain rates and that a stress level exists below which creep rupture or stress relaxation do not occur. A static yield surface can be used in combination with a viscous yield surface that evolves with the applied strain rate; this enables the peak strength to vary with the applied strain rate. As the strain rate slows or ceases, the viscous yield surface shrinks towards the static yield surface which may induce creep or stress relaxation (depending on the applied boundary conditions). This reduces the stress ratio to remain consistent with the shrinking yield surface while also decreasing the peak strength that can be mobilized.

Strength characterization is critical when performing nonlinear analyses. For plastic soils in seismic analyses (undrained conditions assumed), characterization of undrained strength depends on the applied loading rate and likely is larger than imposed in traditional laboratory or field-testing programs, due to the rapid loading rate during an earthquake. One common method for characterizing the undrained strength of plastic soils during earthquake loading is to assume that the increased strength due to the

increased strain rate (viscous effects) is offset by the strength loss due to cyclic degradation. This assumption often characterizes strengths using standard laboratory or field testing and applying these strengths in analysis and design. However, this is an approximation and may not fully account for other aspects of clay behavior that can contribute to additional strength loss, such as strain-softening and cementation. This method also does not account for the potential delay in the onset of localization and associated large strength loss that is attributed to viscous regularization (Needleman 1988). Often this delay is accounted for by incorporating a length scale (i.e., Kiernan and Montgomery 2018) wherein it is assumed a localization develops at a specified shear strain. This requires a numerical modeler to make assumptions on the shear strain at which to incorporate the length scale, the magnitude of a localization thickness, and the rate of strength loss after the length scale is incorporated.

When assessing static slope stability, often the potential for undrained creep to occur in plastic soils over the life of a structure, which can reduce the shear strength and decrease the overall slope stability, is not considered. Creep can result in slope instability depending on the magnitude and rate of strength loss and the initial level of stability against undrained loading as seen in the Feijão Dam 1 failure. Both major investigations (Robertson et al. 2019 and Arroyo and Gens 2021) into this failure required the development of novel numerical models and solution schemes to account for the viscous tendencies for the nonlinear analyses performed. This highlights the need for the development of numerical tools that can model viscous tendencies in strain-softening plastic soils in an easy to follow, replicable manner.

1.2 Dissertation Scope

The research presented in this dissertation focuses on developing tools and methodologies to account for viscous tendencies and strain-softening in static and dynamic nonlinear analyses of plastic silts and clays. The outcomes from this research include: 1) the development of a new constitutive model (PM4SiltR) that directly simulates viscous effects in plastic soils for slope stability applications, 2) a regression that relates strain-softening and viscous strength gain to the onset of localization and associated large strength loss, 3) validation of PM4SiltR and a new solution scheme at the field scale in a static slope stability application, and 4) an increased understanding of how to predict seismic deformations of earthen structures overlying sensitive clays.

This dissertation is divided into seven chapters. The scope of each chapter is discussed below. The chapters consist of journal submissions under review for publication (Chapters 2-4) or published peer-reviewed conference papers (Chapters 5-6) which are presented as published or submitted with minor modifications made to avoid redundancy and for consistency in format. Supplemental information is provided in the appendices.

Chapter 1: Outlines the background, motivation, and scope of the dissertation.

Chapter 2: This chapter presents the development of a new viscoplastic constitutive model (PM4SiltR) for modeling slope stability in plastic soils. The constitutive model development, element level constitutive response, and validation at the system level is presented. The content of this chapter has been submitted to the ASCE Journal of Geotechnical and Geoenvironmental Engineering for publication as “A viscoplastic constitutive model for plastic silts and

clays for static slope stability applications" by T.J. Oathes, R.W. Boulanger, and K. Ziotopoulou.

Chapter 3: This chapter presents the development of a regression model for predicting the onset of localization in plastic soils based on viscous tendencies and rate of strength loss developed using a numerical investigation. The development of the numerical database, regression, and validation of the regression against available laboratory data is presented. The content of this chapter has been submitted to the ASCE Journal of Geotechnical and Geoenvironmental Engineering for publication as "Effect of viscoplasticity on localization in viscous clays and plastic silts" by T.J. Oathes and R.W. Boulanger.

Chapter 4: This chapter presents a reexamination of the 2019 Feijão Dam 1 failure using alternative strength characterization methods and the newly developed viscoplastic constitutive model presented in Chapter 2. The past investigations, site characterization process, calibration procedure, and results of nonlinear analyses are presented alongside a discussion of lessons learned for practice. The contents of this chapter have been prepared for submission to the ASCE Journal of Geotechnical and Geoenvironmental Engineering for publication as "Nonlinear viscoplastic modeling of the Feijão Dam 1 failure" by T.J. Oathes and R.W. Boulanger.

Chapter 5: This chapter presents the results of nonlinear dynamic analyses (NDAs) of a set-back levee overlying a soft clay layer of varying sensitivity. The material calibration, model development, results of NDAs, and implications for practice are presented. The content of this chapter was published as "Seismic

deformations of a levee over soft clay of varying sensitivity" by T.J. Oathes and R.W. Boulanger in the conference proceedings of the 40th United States Society on Dams Annual Meeting and Conference in Denver, Colorado (2020).

Chapter 6: This chapter presents a comparison of the predicted seismic deformations of a set-back levee overlying a sensitive clay layer using simplified Newmark methods and NDAs. The development of the model, NDAs, Newmark sliding block analyses, and implications for practice are presented. The content of this chapter was published as "Influence of sensitivity and rate of strength loss on seismic deformations of a levee" by T.J. Oathes, R.W. Boulanger, and S. Friesen in the conference proceedings for Dam Safety 2021 by the Association of State Dam Safety Officials in Nashville, Tennessee.

Chapter 7: This chapter summarizes the research performed in this dissertation as well as future research directions.

Appendix A: Feijão Dam 1 FLAC FIS code

Chapter 2 : A Viscoplastic Constitutive Model for Plastic Silts and Clays in Slope Stability Applications

Original publication:

Oathes, T.J., Boulanger, R.W., and K. Ziotopoulou. (Under Review). "A viscoplastic constitutive model for plastic silts and clays for slope stability applications." ASCE Journal of Geotechnical and Geoenvironmental Engineering.

Abstract

A viscoplastic model for representing plastic silts and clays in geotechnical static slope stability applications is presented. The PM4SiltR model builds on the stress ratio-controlled, critical state-compatible, bounding surface plasticity model PM4Silt and is coded as a dynamic link library for use in the finite difference program FLAC 8.1. PM4SiltR incorporates strain rate-dependent shear strength, stress relaxation, and creep using a consistency approach combined with an internal strain rate and auto-decay process. The model does not include a cap, and as such cannot simulate strain rate-dependent consolidation under increasing overburden stress. Six parameters are introduced to control the viscous response for PM4SiltR while the parameters controlling the nonviscous components of the response are the same as for PM4Silt. Single element simulations are presented to illustrate the influence of viscoplasticity on the constitutive response in direct simple shear loading and undrained creep. Single element responses are shown to be consistent with observed experimental results. Simulations of a

hypothetical tailings dam constructed using the upstream method are performed to illustrate use of PM4SiltR at field scale. Results of field scale simulations show PM4SiltR can model undrained creep and progressive failure leading to delayed slope instability after relatively minor changes in loading conditions at field scale.

2.1 Introduction

Stability and deformation of slopes and embankments comprised in part of saturated, loose-of-critical-state, fine-grained soils are affected by a number of complex mechanisms including potential strain-softening and associated localization, pore pressure diffusion (consolidation), creep, and strength anisotropy. Analyses need to consider drained and undrained conditions and the large range of potential behaviors possible for each drainage condition. Observable behaviors in undrained loading may vary from undrained creep rupture in sensitive clays to static liquefaction in loose silty sands. Rates of pore pressure diffusion during various loading conditions can be difficult to evaluate confidently, particularly in highly heterogeneous deposits or hydraulically placed fills. The timing of a delayed slope instability after relatively minor changes in loading may be influenced by a combination of creep, diffusion, and progressive failure effects. For example, Robertson et al. (2019) concluded the sudden collapse of the Feijão Dam 1 near Brumadinho was attributable to a combination of creep and progressive failure effects in the hydraulically placed tailings following a loss of suction in unsaturated zones due to rainfall infiltration.

Plastic silts and clays exhibit viscous tendencies that can play a role in the static and dynamic performance of slopes and embankments. Most constitutive models do not directly incorporate viscous tendencies and instead rely on indirect allowances for their

effects. In dynamic analyses, viscous effects influence the peak shear strength and the potential for localizations to occur in strain-softening soils. Shear strength at earthquake loading rates is often selected from empirical correlations while the potential for localization is often accounted for by implementing a length scale at a user-specified strain level (e.g., Kiernan and Montgomery 2018). In static analyses, viscous effects can help explain delays in deformations and instability relative to imposed loading, thereby being a possible trigger for undrained failure conditions such as observed at Feijão Dam 1 (Robertson et al. 2019). The direct incorporation of viscous tendencies in constitutive models can help regularize strain-softening simulations (reduce mesh dependency) and better account for the mechanical behaviors observed in the laboratory and field (e.g., Needleman 1988 and Niazi et al. 2013). Recently developed models such as MIT-SR (Yuan and Whittle 2020) and the BS-EVP framework (Shi et al. 2019) directly incorporate viscoplasticity and provide an improved modeling of a broad range of strain rate-dependent behaviors. Nonetheless, there remains the need to have multiple models in software platforms that are commonly used in industry to help address model uncertainty when directly modeling viscoplasticity.

A viscoplastic bounding surface plasticity model (PM4SiltR) for representing strain rate-dependent shearing resistance in silts and clays in geotechnical static stability applications is presented. PM4SiltR builds upon the PM4Silt (Boulanger and Ziotopoulou 2019) model framework and is implemented as a dynamic link library (dll) for use in the finite difference program FLAC 8.1. PM4SiltR models strain rate-dependent shear strength, stress relaxation, and creep using a consistency approach combined with an internal strain rate and auto-decay process. The model does not include a cap and

therefore is not suited to simulate consolidation under increasing overburden stress. PM4SiltR utilizes the same monotonic parameters as PM4Silt and introduces six new parameters to control the viscoplastic behaviors. The development of the model, the calibration process, and the influence of the viscoplastic parameters are described herein. The model is shown to capture a range of viscoplastic behaviors in a manner consistent with literature. Simulations of a hypothetical tailings dam constructed using the upstream method are performed to illustrate use of PM4SiltR at field scale. These simulations show PM4SiltR can model undrained creep and progressive failure leading to delayed slope instability after relatively minor changes in loading conditions at field scale.

2.2 Time-Dependent Clay Behavior

2.2.1 Strain Rate-Dependent Clay Behavior

The undrained shear strength (s_u) of clays and plastic silts generally increases with the applied strain rate. Experimental results have shown that s_u increases approximately 5 to 15% per log cycle of strain rate (Graham et al. 1983, Lefebvre and LeBouef 1987, Sheahan et al. 1996). The undrained triaxial compression (TXC) test results shown in Fig. 2-1a (Lefebvre and LeBouef 1987) for normally consolidated (NC) B-6 clay samples at axial strain rates of 0.05, 0.5, and 5 %/hr showed that increasing the strain rate increased the shear resistance uniformly over the range of imposed strains. Kulhawy and Mayne (1990) compiled data for 26 saturated clays and showed that peak s_u increased by an average of 10% per log cycle of strain rate (Fig. 2-1b). The data in Fig. 2-1b showed that the s_u at the smallest strain rates examined (i.e., 0.001-0.01 %/hr) was generally 70-80% of the s_u at a standard laboratory strain rate of 1%/hr (i.e., su,1%/hr). Kutter and Sathialingam (1992) and Ladd and DeGroot (2004) concluded that the change in s_u per

log cycle of strain rate progressively increases with increasing strain rate. Rodriguez et al. (2009) provided an overview of the effect of different soil characteristics and loading conditions on the magnitude of strain rate dependency.

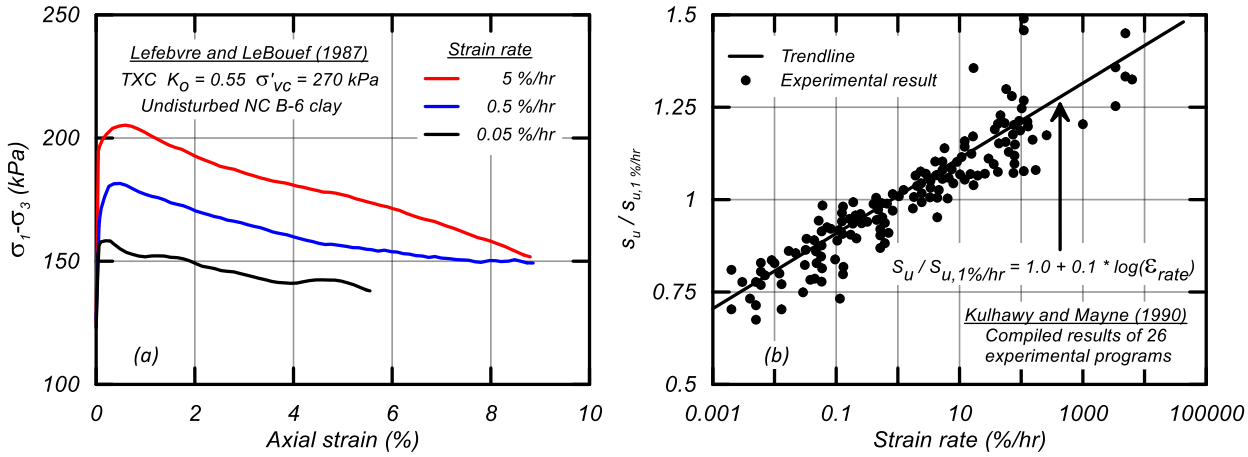

Figure 2-1: Strain rate effects on undrained monotonic loading response of clay: (a) undrained triaxial compression stress-strain responses of undisturbed NC B-6 clay samples at three strain rates (Lefebvre and LeBouef 1987), and (b) peak undrained shear strength

Experimental results have indicated a potential lower limit of applied strain rate below which the shear strength becomes independent of strain rate (Graham et al. 1983, Gylland et al. 2014, Rodriguez et al. 2009). Other researchers have postulated that this lower limit exists although experimental data does not clearly define the strain rate at which this occurs (Sheahan et al. 1996, Ladd and DeGroot 2004). Data from field vane tests at varying vane velocities supported a lower limit of strain rate dependency with a lower limit s_u of approximately 70% of the s_u at a reference rate (Peuchen and Mayne 2007).

The mechanisms causing strain rate-dependent shear strength have been postulated as changes in friction angle (or failure envelope) or suppression of shear-induced pore pressure. Triaxial compression (TXC) test data on compacted clay have suggested that the increased shear strength is due to suppression of shear-induced pore

pressures at high strain rates (Mun et al. 2016), whereas other results have shown shear induced pore pressures during undrained loading were uninfluenced by strain rate (Sorenson et al. 2006). Sheahan et al. (1996) and Lefebvre and LeBouef (1987) suggested that the fundamental mechanism may be a combination of the two mechanisms and vary depending on the overconsolidation ratio and other soil properties. Sorenson et al. (2006) found that the strain rate dependency of the bounding surface for isotropic compression and undrained shearing are of similar magnitude. Identification of the fundamental mechanism in experimental programs is complicated by limitations in pore pressure measurements during rapid undrained shearing.

2.2.2 Creep

Clays subjected to sustained shear stresses continue to creep (deform) over time. Results for five undrained TXC creep tests at sustained stress levels equal to 50, 70, 80, 90, and 95% of the peak s_u (for the reference strain rate) on undisturbed San Francisco (SF) Bay Mud (Lacerda 1976) are shown in Fig. 2-2 in terms of creep strain rate (Fig. 2-2a) and strain (Fig. 2-2b) versus time. Higher sustained stress levels resulted in larger creep strain (Fig. 2-2b). Creep strain rate initially decreased in time (Fig. 2-2a) for all sustained stress levels. Samples loaded at stress levels below 80% of peak s_u deformed with a continually decreasing creep strain rate throughout the duration of the test indicating a stable condition. Creep strain rates for samples loaded at 90% and 95% of peak s_u initially decreased before rapidly increasing to an undrained creep rupture (sample collapse). Vaid et al. (1996) related the observance of a minimum strain rate during a creep test as a sign of an impending rupture. Vaid et al. (1996) and Sheahan (1995) suggested the existence of a yield strength below which creep rupture will not occur and deformations

stabilize. Sheahan (1995) connected this behavior to the static yield surface introduced in elastic/viscoplastic models. Lacerda (1976) found that the peak s_u strain rate-dependency can be determined from creep parameters and that creep parameters can be used to predict the stress-strain curve in undrained shearing at low strain levels.

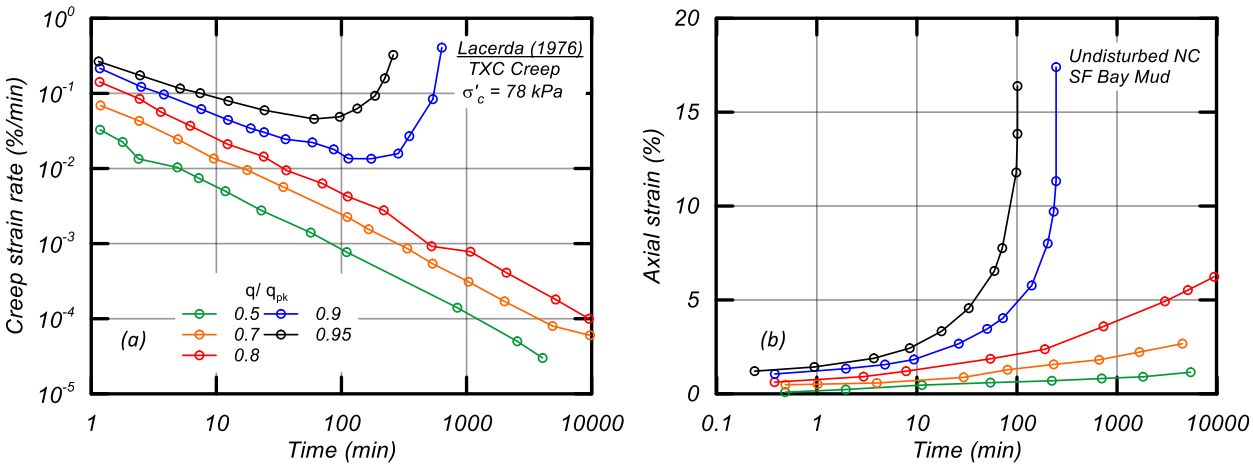

Figure 2-2: Triaxial creep tests by Lacerda (1976) on undisturbed NC SF Bay Mud: (a) strain rate, and (b) axial strain versus time

2.2.3 Stress Relaxation

Clays held at a constant strain after loading to a defined stress level shed stress over time, a process known as stress relaxation. The rate of stress relaxation was linear with the logarithm of time for three different clays in laboratory testing (Lacerda 1976). Experimental studies have shown the potential existence of a lower limit on stress levels below which further stress relaxation will not occur (Silvestri et al. 1988) as shown in Fig. 2-3. Silvestri et al. (1988) indicated that the time for stress relaxation may differ depending on loading conditions which is supported by Lacerda's (1976) observation that the time at which relaxation initiated is dependent on the strain level prior to relaxation. Lacerda (1976) asserted the rate of relaxation was independent of strain rate and strain prior to the relaxation stage. The slope of the strength versus logarithm of strain rate (e.g. Fig. 2-

1) has been shown to be equal to the slope of the stress relaxation curve (Lacerda 1976 – Fig. 2-2) and that creep parameters could be used to predict stress relaxation parameters.

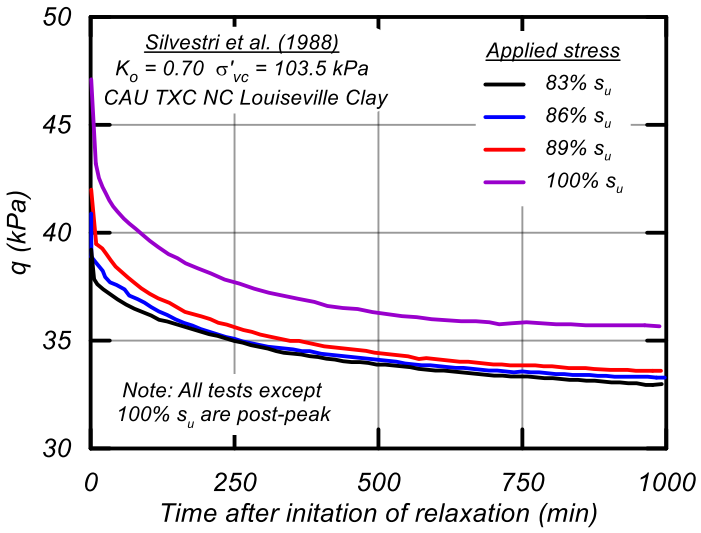

Figure 2-3: Four TXC stress relaxation tests by Silvestri et al. (1988) on NC Louiseville clay at different deviator stress levels showing the relaxation of deviator stress in time

2.2.4 1-D Compression

The apparent preconsolidation pressure in 1-D consolidation testing depends on the applied consolidation strain rate. Behavior at significant overconsolidation ratios (OCR) does not appear to be rate dependent with recompression curves being largely inviscid regardless of the applied consolidation strain rate. This behavior is consistent with peak strength rate dependency lessening during shear when the OCR is significant. Rate-dependency resulted in a preconsolidation pressure and virgin compression line that were unique for each applied consolidation strain rate, referred to as isotaches. Rate-dependency has been shown to become negligible at lower consolidation strain rates (Vaid et al. 1979). Compilations of data for various clays suggested this lower limit tends to be approximately 70% of the preconsolidation pressure for a reference consolidation

strain rate (Fig. 2-4; Leroueil et al. 1983 and Watabe et al. 2012). The rate-dependency of the preconsolidation pressure was shown to be approximately 5% per log cycle of applied consolidation strain rate near the reference strain rate (Leroueil 2006).

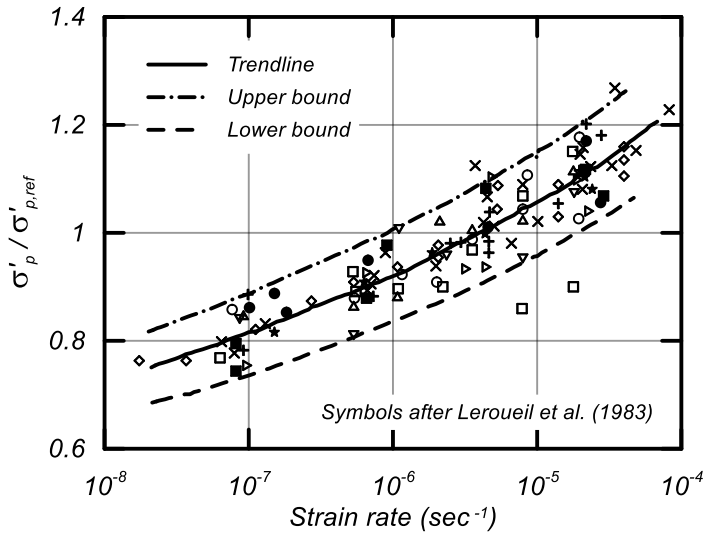

Figure. 2-4 Strain rate effects on the apparent preconsolidation pressure versus strain rate for a compilation of consolidation tests by Leroueil et al. (1983).

2.2.5 Rate-Dependent Constitutive Models

Constitutive models have been developed that can approximate the above-described, fundamentally-interrelated behaviors for a specific soil using a common set of calibrated input parameters. Perynza (1963) presented a constitutive framework that separated elastic and viscoplastic strains with a static yield condition; the viscous behavior of the material was dependent on the stress difference between the current loading state and static yield surface (known as over-stress) which was termed elastic/viscoplastic (EVP). A distinction was made between EVP and elastic-viscoplastic behavior which had viscous behavior in both the elastic and plastic regimes. Sheahan (1995) introduced a similar concept with a static yield surface that separates plastic and viscoplastic behaviors in a similar manner. Tatsuoka et al. (2002) described alternative approaches (i.e., TESRA and

isotache) for separating inviscid and viscous stress components and relating them to the elastic and irreversible components of strain rate.

Numerous constitutive models have been developed that incorporate viscoplasticity, including several that built on the Modified Cam Clay framework (Yin et al. 2006, 2011, 2015, Rezania et al. 2017) and several that used the bounding surface plasticity framework (Martindale et al. 2012, Shi et al. 2019, Kutter and Sathialingam 1992, and Jiang et al. 2017). Martindale et al. (2012) used a modified consistency approach which introduced strain rate-dependency by shifting the critical state line in e-log p' space. In a consistency approach, the strain rate-dependent features of a constitutive model do not shift instantaneously in response to a step change in the imposed strain rate, but rather shift over time after the change in strain rate. The term originates back in the consistency condition of constitutive models wherein the stress condition is always on the yield surface, which combined with the flow rule provides the final plastic strain increment experienced by the material. Internal strain rate parameters and auto-decay processes have been introduced in models to regulate the time-dependent response of internal variables to variations in the imposed strain rate (e.g., Clarke and Hird 2012, Yuan and Whittle 2018, 2020), which can be related to the natural decay of strain-rate concept described in Singh and Mitchell (1968).

2.3 Model Development

The model formulation for PM4SiltR builds directly on the PM4Silt model by Boulanger and Ziotopoulou (2019). Modifications were made to represent viscous effects in the form of a strain rate-dependent shear strength and the ability to model stress relaxation and creep. PM4SiltR is implemented as a dynamic link library in FLAC 8.1 (Itasca 2019) and

is thus a plane strain model. Its implementation in the explicit finite difference framework of FLAC is identical to PM4Silt except that the model was formulated for use with the creep module instead of the dynamic module.

The base model PM4Silt is a critical state-compatible, stress ratio-controlled, bounding surface plasticity model that builds upon the PM4Sand constitutive model described by Boulanger and Ziotopoulou (2017) and Ziotopoulou and Boulanger (2016). PM4Silt was developed to represent clays and plastic silts in geotechnical earthquake engineering applications. PM4Silt has three required input parameters: (1) the critical state strength or strength ratio under earthquake loading rates ($s_{u,cs,eq}$ or $s_{u,cs,eq}/\sigma'_{vc}$, where σ'_{vc} is the vertical effective consolidation stress), (2) the shear modulus coefficient (G_o), and (3) the contraction rate parameter (h_{po}). The model has an additional 20 secondary parameters that receive either default values or can be modified to account for site-specific data. Further discussion of the parameters and the model itself can be found in Boulanger and Ziotopoulou (2019). PM4Silt does not simulate viscous effects and the modeler must indirectly incorporate the effect of strain rate on strength during seismic analyses. Similarly, PM4Silt is unable to model stress changes or deformations in time due to stress relaxation or creep. PM4Silt does not include a cap and therefore is not suited to simulate consolidation under increasing overburden stress.

Viscoplasticity was added to the PM4Silt model using a consistency approach (Wang et al. 1997, Martindale et al. 2012) with transient responses and stress relaxation controlled through an internal strain rate and auto-decay process (Clarke and Hird 2012, Yuan and Whittle 2018, 2020). The consistency approach enables accounting for viscous effects by utilizing the formulation of the PM4Silt constitutive model without necessitating

reformulation of the model around a viscoplastic strain-rate and viscous material properties. Rate dependence is modeled by enforcing consistency with a rate-dependent yield surface controlled by the critical state line and plasticity surfaces, similar to Wang et al. (1997) and Martindale et al. (2012), rather than by including separate viscous resistance components. In addition, the details of the numerical implementation within the explicit finite difference framework of FLAC are fully described in Boulanger and Ziotopoulou (2019).

2.3.1 Rate-Dependent Plasticity Surfaces

The bounding, dilatancy, and critical state surfaces of the model were made strain rate-dependent using a consistency approach. The model defines critical state using a critical state stress ratio (M) and a linear critical state line (CSL) in void ratio (e) versus natural logarithm of mean effective stress (ln p′) space where the slope is λ and intercept e1kPa when p' = 1 kPa. This can be expressed as,

$$e_{cs} = e_{1kPa} - \lambda \ln\left(\frac{p'_{cs}}{1kPa}\right) \tag{2-1}$$

The p'_{cs} and M were made dependent on the internal strain rate ($\bar{\dot{\gamma}}$) as,

$$M = M_{ref}\left(1 + F_M \log\left(\frac{\bar{\dot{\gamma}}}{\dot{\gamma}_{ref}} + R_{\dot{\gamma},\min}\right)\right) \tag{2-2}$$

$$p'_{cs} = p'_{cs,ref}\left(1 + F_p \log\left(\frac{\bar{\dot{\gamma}}}{\dot{\gamma}_{ref}} + R_{\dot{\gamma},\min}\right)\right) \tag{2-3}$$

where $\dot{\gamma}_{ref}$ = reference strain rate, $p'_{cs,ref}$ = p'_{cs} at the reference strain rate, M_{ref} = M at the reference strain rate, F_M and F_p are rate parameters for M and p'_{cs} respectively, and $R_{\dot{\gamma},\min}$

is the minimum normalized strain rate producing a viscid response. The above equations utilize the base ten logarithm to be consistent with common experimental and empirical forms. $R_{\dot{\gamma},\min}$ determines the strain rate below which the behavior transitions from viscoplastic to inviscid, with the default value of 0.001 corresponding to a strain rate three orders of magnitude below the reference rate.

The rate dependency of the CSL is illustrated in Fig. 2-5a for an example set of calibration parameters (referred to as Calibration B and described in a later section). Strain rates are expressed as strain rate ratios (SRR) defined as:

$$SRR = \log\left(\frac{\bar{\dot{\gamma}}}{\dot{\gamma}_{ref}}\right) \tag{2-4}$$

The reference CSL (at SRR=0) is equivalent to the CSL without viscoplasticity. An increasing SRR shifts the CSL to the right in e-ln(p′) space by a magnitude controlled by the F_p parameter. A rightward shift in the CSL increases p' at critical state and thus decreases the state parameter. A decreasing SRR shifts the CSL to the left, with the leftward limit being the static CSL for a zero strain rate condition. CSLs for SRRs less than log($R_{\dot{\gamma},\min}$) are approximately equal to the static CSL. The effect of SRR on the CSL position is independent of the loading direction or current stress state.

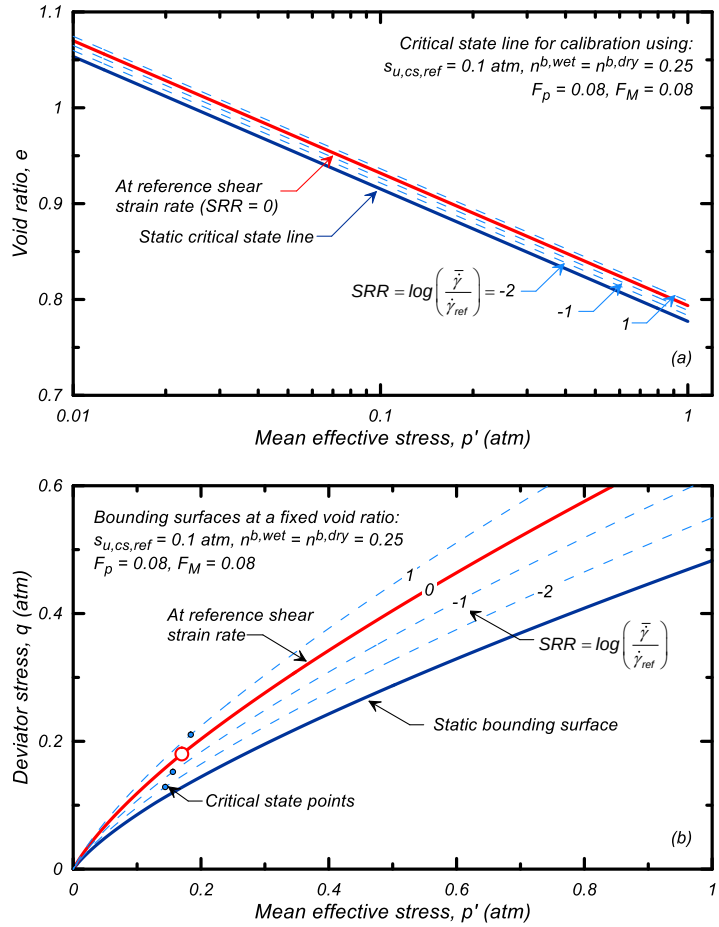

Figure 2-5: Rate dependent: (a) critical state lines in e-log(p′) space, and (b) bounding surfaces in q-p′ space at different SRRs

The rate dependency of the bounding surface is illustrated in Fig. 2-5b. The bounding surface for loose of critical state conditions is dependent on M and the state parameter ξ as,

$$M_b = M \cdot \exp\left(-n^{b,wet}\xi\right) \tag{2-5}$$

where $n^{b,wet}$ is a positive number so that M_b is smaller than M on the wet side of critical state. The bounding surface for dry of critical state conditions has a different functional form (Boulanger and Ziotopoulou 2019), but the key feature is that M_b is greater than M on the dry side of critical state. Rate-dependent bounding surfaces for different SRRs are illustrated in Fig. 2-5b for undrained loading (fixed void ratio) of a soil with an $s_{u,cs,ref}$ = 0.2

atm and $F_p = F_M = 0.08$. Increasing the SRR shifts the bounding surface upwards in q-p′ space due to the rightward shift in the CSL (Fig. 2-5a, Eq. 2-3) and increase in M (Eq. 2-2), as illustrated by the relative movements of the critical state points marked on the bounding surfaces for each SRR in Fig. 2-5b.

The static bounding surface ($M_{b,static}$) separating viscoplastic from inviscid behaviors is the bounding surface for a zero strain rate loading condition. The location of the static bounding surface is controlled by $R_{\dot{\gamma},\min}$, F_p, and F_M. The CSL and static bounding surface shown in Figs. 2-5a and 2-5b, respectively, are for simulations with $R_{\dot{\gamma},\min} = 0.001$ and $F_p = F_M = 0.08$. M and p'_{cs} for static loading conditions are,

$$p'_{cs,static} = p'_{cs,ref}\left(1-\log\left(R_{\dot{\gamma},\min}\right)F_p\right) \quad (2\text{-}6)$$

$$M_{static} = M_{ref}\left(1-\log\left(R_{\dot{\gamma},\min}\right)F_M\right) \quad (2\text{-}7)$$

For the parameters used to generate Fig. 5 (i.e., Calibration B), the result is that $M_{static} = 0.76M_{ref}$ and $p'_{cs,static} = 0.76p'_{cs,ref}$.

The rate dependency of peak shear strength (τ_{pk} or s_u) is illustrated in Fig. 2-6 showing $\tau_{pk}/\tau_{pk,SRR=0}$ versus SRR for single element simulations of undrained loading in direct simple shear (DSS), plane strain compression (PSC), and plane strain extension (PSE). These results were similarly based on Calibration B. Over a range of SRRs from -2 to 5 the trends were approximately linear for all loading conditions with an 10% change in s_u per log cycle of strain rate. The rate dependency is minimally affected by the loading direction and stress state, which is expected as the model is not dependent on the Lode angle, as seen by the similarity of the trends in Fig. 2-6. At higher SRRs the trend diverged

slightly for different loading conditions because the numerical implementation imposes upper limits on the bounding and dilation stress ratios. At SRRs < -2, the change in s_u with strain rate flattened with the lower bound corresponding to the static (inviscid) bounding surface.

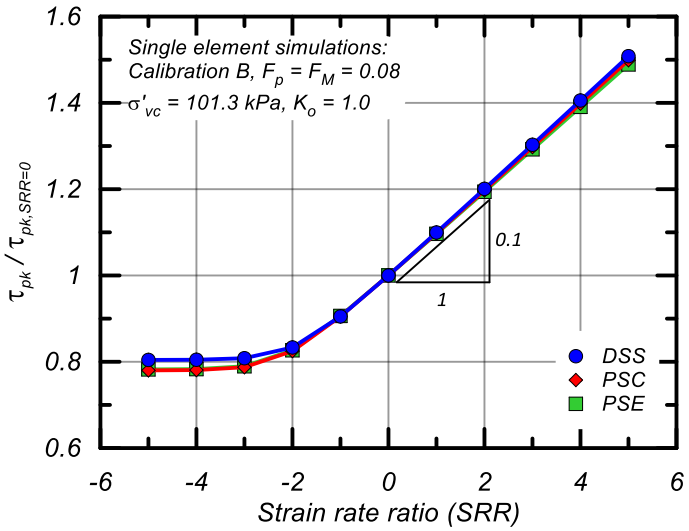

Figure 2-6. Variation in peak shear strength versus SRR for single element simulations of DSS (blue), PSC (red), and PSE (green)

2.3.2 Internal Strain Rate

Transient responses to changes in the external strain rate are controlled through updating the internal strain rate ($\bar{\dot{\gamma}}$) with the internal strain rate parameter θ_{ref}. At the end of each time step, the internal strain rate is updated based on the instantaneous external strain rate ($\dot{\gamma}$) and θ_{ref} as,

$$\bar{\dot{\gamma}}_{i+1} = \bar{\dot{\gamma}}_i \theta + \dot{\gamma}_{i+1}(1-\theta) \tag{2-8}$$

$$\theta = \theta_{ref} + (1-\theta_{ref})B \quad with \quad 0 \le \theta \le 0.99 \tag{2-9}$$

where B is a time smoothing factor based on the current time step size and a reference time step size,

$$B = 1 - \frac{\Delta t}{\Delta t_{ref}} \tag{2-10}$$

$$\Delta t_{ref} = \frac{m\, p'}{G\, \dot{\gamma}_{ref}} \tag{2-11}$$

where m = size of the elastic zone, p′ = current mean effective stress, and G = shear modulus. Larger θ_{ref} values result in a slower evolution of the internal strain rate toward the applied strain rate when the applied strain rate changes. θ_{ref} = 0.5 resulted in the internal strain rate adjusting to a step change in external strain rate over approximately 0.25% shear strain while θ_{ref} = 0.95 updated over approximately 2% shear strain, as illustrated by the example in Fig. 2-7. A larger θ_{ref} value increases the number of steps required for the internal strain rate to converge toward the external strain rate after a step increase in the external strain rate. The time smoothing factor (B) increases θ as the time step is reduced, increasing the number of steps needed for the internal strain rate to adjust to changes in external strain rate. This ensures that the evolution of internal strain rate occurs over a reasonable magnitude of strain. The reverse is true as the time step is increased, except θ goes to zero and the number of steps to adopt a new strain rate is reduced, while the strain increment required for evolution of internal strain rate remains approximately the same.

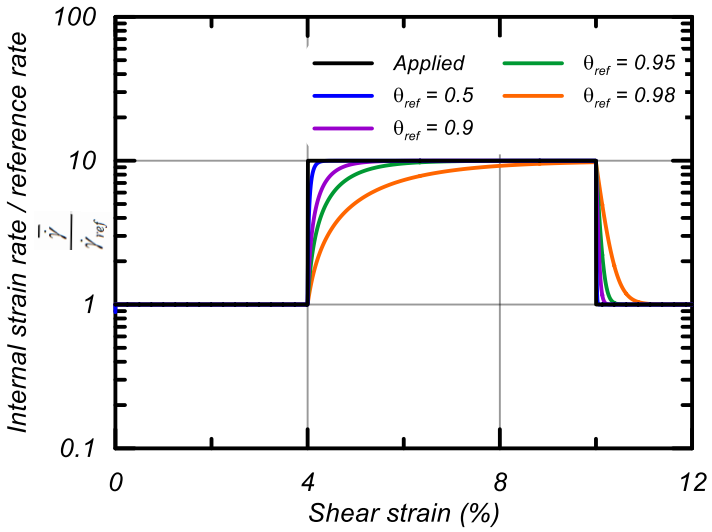

Figure 2-7: Internal strain rate evolution with varying internal strain rate parameter (θ_{ref})

2.3.3 Relaxation and Creep

Stress relaxation is imposed when the current stress ratio (η) is above the bounding surface, with the rate of relaxation proportional to the difference between η and M_b. A stress relaxation process is required for this situation because, when the imposed strain rate drops to zero and the operational bounding surface is equal to the static bounding surface, there is no other mechanism for the stresses to relax toward the static bounding surface. The relaxation process ceases when the current stress state has dropped to the static bounding surface, or when a strain rate is imposed and the bounding surface increases either to or above the current stress state. The deviator stress ratio tensor (**r**) and back-stress ratio tensor (α) are relaxed as:

$$\mathbf{r}_{i+1} = \mathbf{r}_i C_r \tag{2-12}$$

$$\boldsymbol{\alpha}_{i+1} = \boldsymbol{\alpha}_i C_r \tag{2-13}$$

Where the stress relaxation parameter C_r is computed as,

$$\beta = \beta_{ref} + \left(1 - \beta_{ref}\right) B \qquad (2\text{-}14)$$
$$0 \le \beta \le 1$$

$$C_r = \frac{M_b}{\eta} + \frac{\eta - M_b}{\eta} \beta \qquad (2\text{-}15)$$
$$C_r \le 1$$

The auto-decay parameter β_{ref} corresponds to the fraction of $\eta - M_b$ that remains after relaxation in a time increment equal to Δt_{ref}. This means that a $\beta_{ref} = 0.99$ corresponds to 1% of $\eta - M_b$ relaxed every Δt_{ref} increment of time. $\beta_{ref} = 1.0$ eliminates stress relaxation while $\beta_{ref} = 0.0$ results in instantaneous relaxation. The auto-decay parameter β is adjusted from the input β_{ref} with the time smoothing factor B to reduce the dependency on the time step size as done in the internal strain rate calculation. The parameter C_r reduces the current stress ratio toward M_b by an amount proportional to the difference between η and M_b, resulting in exponential relaxation. Stress relaxation ceases when η is reduced to or below the bounding surface.

The stress relaxation mechanism is illustrated in q – p′ space and time – stress ratio space in Fig. 2-8. The simulation in Fig. 2-8 shows an element that underwent DSS loading to point A, after which the strain rate was set to zero (i.e., displacements fixed). Upon cessation of straining, the bounding surface evolved from M_b (blue solid line) to $M_{b,static}$ (blue dashed line) over approximately 0.3 hours (Fig. 2-8b), the length of time is dictated by the evolution of the internal strain rate. The lowering of the bounding surface with a reducing internal strain rate resulted in η being larger than M_b at approximately 0.12 hours which induced the stress relaxation mechanism. The relaxation in stress ratio can be seen in the red line as a steady reduction until the stress ratio reached the static

bounding surface at approximately 1000 hours. This correlated to the reduction in deviator stress seen in the stress path in q- p′ space. For fixed-stress boundary conditions (as opposed to fixed displacement), this stress relaxation mechanism instead contributes to the accumulation of strain (i.e., creep) at a strain rate necessary to resist the imposed fixed-stress boundary condition.

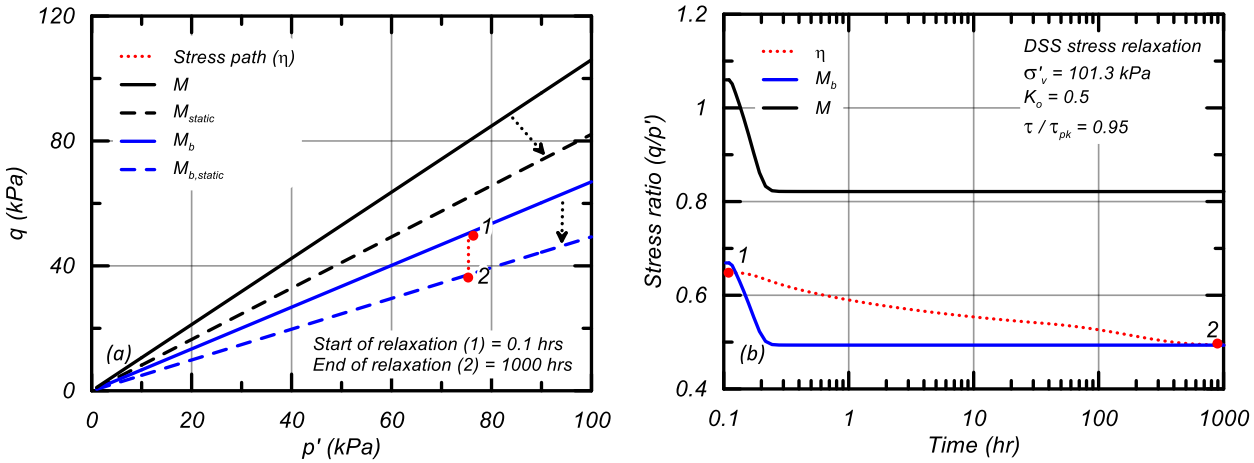

Figure 2-8: Stress relaxation mechanism shown as (a) stress path in q-p′ space, and (b) stress ratio reduction in stress ratio – time space for an undrained DSS simulation

2.3.4 Strain Rate Parameters

Six parameters control the viscous response of the model as shown in Table 2-1. F_p and F_M control the strain rate dependency of the CSL and M, respectively. $\dot{\gamma}_{ref}$ sets the reference rate for the base calibration. Placement of the static bounding surface and the corresponding distinction between inviscid and viscoplastic behavior is determined by $R_{\dot{\gamma},\min}$, F_p, and F_M. The transient response to external variations in strain rate is controlled by θ_{ref} while the rate of stress relaxation is controlled by β_{ref}.

Table 2-1: Input parameters for PM4SiltR model

Parameter	Description	Effect	Default Value
F_p	Rate parameter for p'$_{cs}$	Sets the rate dependency of the critical state line	0.0
F_M	Rate parameter for M	Sets the rate dependency of the M line	0.0
$\dot{\gamma}_{ref}$	Reference shear strain rate (per second)	Sets the reference rate for calculation of the SRR	5% per hour
$R_{\dot{\gamma},\min}$	Minimum normalized strain rate	Sets the placement of the static bounding surface	0.001
θ_{ref}	Internal strain rate parameter	Controls the transient response to changes in external strain rate	0.5
β_{ref}	Auto-decay parameter	Controls the rate of stress relaxation	0.999

2.4 Calibration Procedure

PM4SiltR is controlled by 24 parameters; out of those 12 are the parameters that control the monotonic response of PM4Silt, six control the viscous portion of the response, and six control cyclic aspects of the response. The preceding section focused on the viscous portions of the model; readers are referred to Boulanger and Ziotopoulou (2019) for full details of the PM4Silt model. The procedure outlined below can be used to calibrate the model with differing levels of site-specific soil information. Further information on calibration for rate effects can be found in Boulanger et al. (2021).

1) Select values for the critical state undrained shear strength ($s_{u,cs,ref}$) or undrained shear strength ratio ($s_{u,cs,ref}/\sigma'_{vc}$) and the corresponding reference shear strain rate ($\dot{\gamma}_{ref}$).
2) Select the shear modulus coefficient (G_o) and shear modulus exponent (n_g) to match the estimated small-strain shear modulus (G_{max}) and its variation with depth.
3) Select values for any secondary parameters that can be informed by soil-specific test data, such as e_o, λ, and ϕ'_{cv}.

4) Simulate undrained monotonic loading (DSS, PSC, or PSE) at the reference strain rate and iteratively adjust $n_{b,wet}$ to obtain the desired peak strength and compare to laboratory test data. Iteratively adjust the plastic modulus parameter (h_o) and contraction rate parameter (h_{po}) to adjust the stress-strain response as desired.
5) Simulate undrained monotonic loading for a range of strain rates and iteratively adjust F_p, F_M, and $R_{\dot{\gamma},\min}$ to obtain the desired variation in peak s_u with strain rate. Rate dependency for critical state strength may vary from that of peak strength and thus it should be evaluated separately for cases where it is important to the system response.
6) Simulate undrained creep rupture and compare the results to any site-specific laboratory test data or empirical correlations. The time to rupture for a given stress level depends on several factors including: h_{po} (rate of strain-softening), the F_p and F_M rate parameters, and the auto-decay parameter (β_{ref}).
7) Repeat steps 4 – 6 as needed.

The procedure above outlines increasingly complex calibrations that are dependent on the availability of site-specific data. Steps 1-4 largely follow the PM4Silt calibration procedure while steps 5-6 focus on the viscous behavior. The calibration process can be dependent on the types of analysis performed at the system level such that it is important to make choices during the calibration procedure that consider the behaviors of interest (i.e., the calibration process for drained versus undrained loading may differ). Model response should be examined for all loading paths that are expected to be important to the system level response.

2.5 Constitutive Responses

Single element simulations were performed to illustrate the constitutive response of PM4SiltR under a variety of loading conditions using different calibrations (Table 2-2). All calibrations had the same PM4Silt monotonic parameters that controlled the inviscid portion of the response. The inviscid response was calibrated to emulate a hypothetical, moderately sensitive, plastic clay or tailings material with common engineering properties. Calibration (A) was inviscid and illustrated the response in the absence of viscoplasticity. Calibration B was the baseline calibration and had a rate-dependency of 10% per log cycle. Calibrations C-G varied the six parameters controlling viscous responses. All parameters not indicated in Table 2-2 maintained their default values. The introduced viscous parameters allow for flexibility in the magnitude and function of the imposed viscous effects.

Table 2-2: PM4SiltR calibrations input parameters

	Calibration	A	B	C	D	E	F	G
PM4Silt	$s_{u,cs,ref}/\sigma'_{vc}$	0.09	-	-	-	-	-	-
	G_o	500	-	-	-	-	-	-
	h_{po}	250	-	-	-	-	-	-
	$n^{b,wet}=n^{b,dry}$	0.25	-	-	-	-	-	-
	h_o	0.1	-	-	-	-	-	-
PM4SiltR	F_p	0.0	0.08	0.08	0.08	0.05	0.1	0.0
	F_M	0.0	0.08	0.08	0.08	0.05	0.0	0.1
	$R_{\dot{\gamma},\min}$	0.0	0.01	0.001	0.1	0.001	0.001	0.001

2.5.1 Undrained Shear at Different Strain Rates

The variation of $\tau_{pk}/\tau_{pk,SRR=0}$ versus SRR is shown in Fig. 2-9 for six calibrations and undrained DSS loading with σ'_{vc} = 101.3 kPa, K_0 = 0.5, and SRRs ranging from -5 to 5. Responses for Calibrations B, C, and D, all used $F_p = F_M = 0.08$, are compared in Fig. 2-

9a to illustrate the effect of $R_{\dot{\gamma},\min}$. These three calibrations had the same 10% change in $\tau_{pk}/\tau_{pk,SRR=0}$ per log cycle of strain rate for SRR > -1, but had different lower limits on $\tau_{pk}/\tau_{pk,SRR=0}$. Calibrations B ($R_{\dot{\gamma},\min} = 10^{-2}$), C ($R_{\dot{\gamma},\min} = 10^{-3}$), and D ($R_{\dot{\gamma},\min} = 10^{-1}$) transitioned from viscoplastic to inviscid at SRRs of approximately -2, -3, and -1, respectively, and had lower limits on $\tau_{pk}/\tau_{pk,SRR=0}$ of 0.8, 0.7, and 0.9, respectively (Fig. 2-9a). These results illustrated how $R_{\dot{\gamma},\min}$ can be used to adjust the lower limit on $\tau_{pk}/\tau_{pk,SRR=0}$ (i.e., static undrained strength) after the values of F_p and F_M have been selected. Calibrations E, F, and G, all used $R_{\dot{\gamma},\min} = 0.001$, are compared in Fig. 2-9b to illustrate the effect of F_p and F_M. Calibration F ($F_p = 0.1$, $F_M = 0.0$) had a strength increase of 2.5% per log cycle while Calibration G ($F_p = 0.0$, $F_M = 0.1$) had a strength increase of 10% per log cycle as seen in Fig. 2-9b, illustrating how the peak s_u was more strongly influenced by F_M than F_p. Calibration E ($F_p = F_M = 0.05$) had an intermediate strength increase of 6.0% per log cycle (Fig. 2-9b). The lower limits on $\tau_{pk}/\tau_{pk,SRR=0}$ of 0.81, 0.92, and 0.70 for Calibrations E, F, and G, respectively, were directly related to their respective percent changes in strength per log cycle of strain rate because all three used the same $R_{\dot{\gamma},\min} = 0.001$.

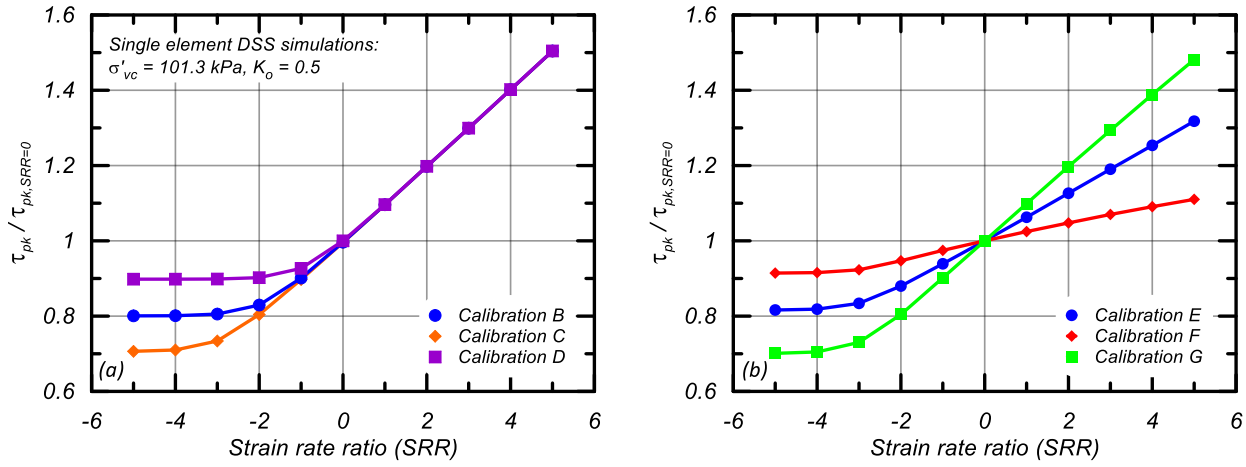

Figure 2-9: Peak shear strength rate dependency expressed as normalized peak shear strength versus SRR with varying: (a) $R_{\dot{\gamma},\min}$, and (b) magnitudes of Fp and FM

The stress-strain response at different SRRs is influenced by F_p, F_M, and $R_{\dot{\gamma},\min}$. Stress-strain responses in undrained DSS loading are shown for Calibrations A (inviscid case), E, F, and G at an SRR = 2 in Fig 2-10a. The shear strain at peak shear stress ($\gamma_{\tau,pk}$) increased with increasing peak strength, with $\gamma_{\tau,pk}$ increasing from 1.2% for the inviscid Calibration A to 1.4% to 1.6% for Calibrations E, F, and G. The simulations in Fig. 2-10a showed that including rate effects in Calibrations E, F, and G produced $\gamma_{\tau,pk}$ that were 15-35% greater than the $\gamma_{\tau,pk}$ for the inviscid Calibration A. Stress-strain responses for baseline Calibration B are shown for undrained DSS simulations loaded at SRRs = -4, -2, 0, 2, and 4 in Fig. 2-10b. The peak shear strength increased approximately 10% per log cycle of loading rate at SRR > -2, consistent with the summary of these results in Fig. 2-9a. The $\gamma_{\tau,pk}$ increased by about 20% per log cycle of loading rate (e.g., from $\gamma_{\tau,pk}$ = 1.15% at SRR = 0 to $\gamma_{\tau,pk}$ = 1.6% at SRR = 2) over the same range of SRR values. The shear strength ratio reached its lower (inviscid) limit of about 0.21 when the SRR was less than -2. In addition, the effect of strain rate on $\tau_{pk}/\tau_{pk,SRR=0}$ is independent of σ'_{vc} for the

same specified $s_{u,cs,ref}/\sigma'_{vc}$, but will vary with σ'_{vc} for the same specified $s_{u,cs}$ (i.e., with changing $s_{u,cs,ref}/\sigma'_{vc}$).

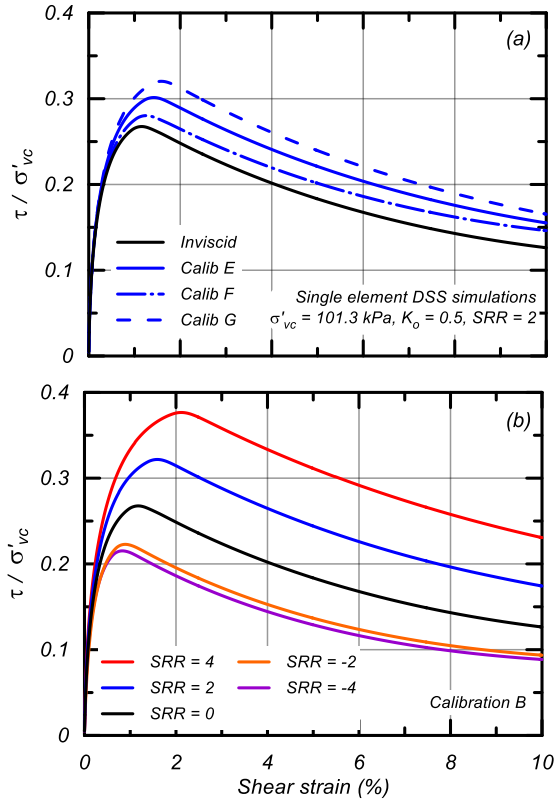

Figure 2-10: Influence of strain rate on the stress-strain response in undrained DSS loading: (a) Calibrations A, E, F, and G with SRR = 2, and (b) Calibration B with varying SRRs

2.5.2 Undrained creep under sustained stress

The undrained creep response under DSS shearing for Calibration B with σ'_{vc} = 101.3 kPa and K_0 = 0.5 is shown for five loading conditions in Fig. 2-11. For these five simulations, the horizontal shear stress (τ_h) was increased to 70, 75, 80, 85, or 90% of $s_{u,pk,ref}$, after which the shear stress was held constant. Undrained creep rupture occurred for shear stresses above approximately 80% of $s_{u,pk,ref}$ whereas stable conditions developed for shear stresses below approximately 75% of $s_{u,pk,ref}$. The time to creep rupture reduced from approximately 118 hours at $\tau_h/s_{u,pk,ref}$ = 0.8 to 2.3 hours for $\tau_h/s_{u,pk,ref}$ = 0.9. For

$\tau_h/s_{u,pk,ref}$ = 0.7 and 0.75, the stress ratio was below the static yield surface and thus the element exhibited no creep. For $\tau_h/s_{u,pk,ref} \geq 0.8$, the stress ratio was significantly above the static yield surface and thus the element began developing creep strains. These creep strains increased K_0 but produced large reductions in p′ such that the stress ratio remained above the static yield surface which resulted in accelerating creep rates over time and eventually led to rupture. The occurrence of creep strains did not indicate an imminent creep rupture as seen for $\tau_h/s_{u,pk,ref}$ = 0.79 where creep strains began to accumulate before stabilizing in time. In this condition the stress ratio was slightly above the static yield surface and thus the element began to develop creep shear strains. The creep strains led to an increase in K_0 and slight reduction in p′, the stress ratio eventually stabilized on the static bounding surface and creep deformations ceased. Sustained shear stresses near the static bounding surface stabilized or ruptured depending on the viscous properties, the sensitivity of material, and the rate of strain-softening.

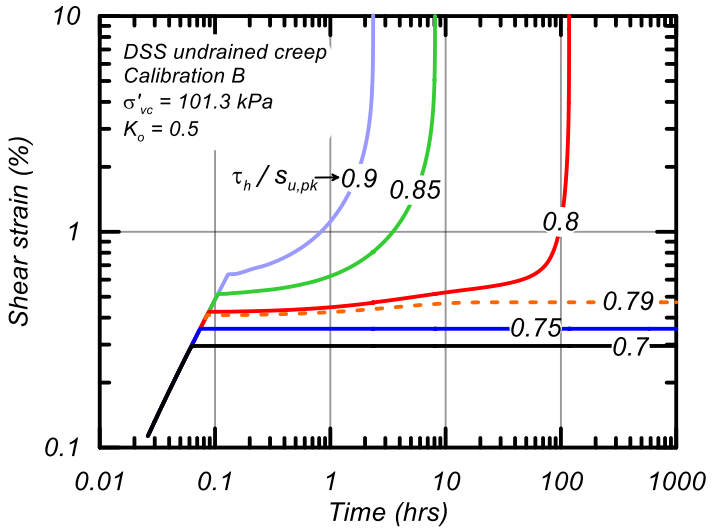

Figure 2-11: DSS undrained creep simulations of Calibration B with varying sustained stress levels in shear strain versus time space

2.5.3 Undrained Shear with Step Changes in Strain Rate

Stress-strain responses for undrained DSS loading with σ'_{vc} = 101.3 kPa and K_0 = 0.5 with step changes in strain rate (Fig. 2-12a) are shown in Figure 2-12(b) for Calibration B. Step-changed loading comprised ten intervals of 3% shear strain with constant SRRs of -1, 0, and 1 (a range of two orders of magnitude), two sets of simulations are shown where the only difference was the order of applied rate changes. Following a step change in strain rate, the stress-strain response transitioned towards a shear resistance consistent with the newly imposed SRR. The transition in shearing resistance following a step change in strain rate takes about 0.25 - 1.0% shear strain to fully develop depending on the magnitude of the change in strain rate, the strain level, and the model parameters. Dashed lines in Fig. 2-12 indicate an estimated fit of the intervals at unique SRRs. The steps did not directly fall onto the same line due to: (1) differences in internal strain rate evolution, (2) differences in the accumulation of plastic strain and the associated modulus reduction, and (3) the rate of post-peak strength loss. At larger strains (corresponding to lower shear resistances) the intervals corresponded more directly to the fit line because the magnitude of strength change per log cycle was smaller which led to smaller differences in the evolution of the plasticity surfaces. Pre-peak stress-strain responses are unchanged with changing strain rate until close to mobilization of peak strength (Fig. 2-10) as the evolving plasticity surfaces do not influence the initial stiffness of the calibration. Figure 2-12 shows an evolution in the stress-strain response with changing strain-rate that is consistent with observed stress-strain evolution for experimental results presented by Graham et al. (1983) for Winnipeg and Belfast clays subjected to similar strain-rate rate transitions.

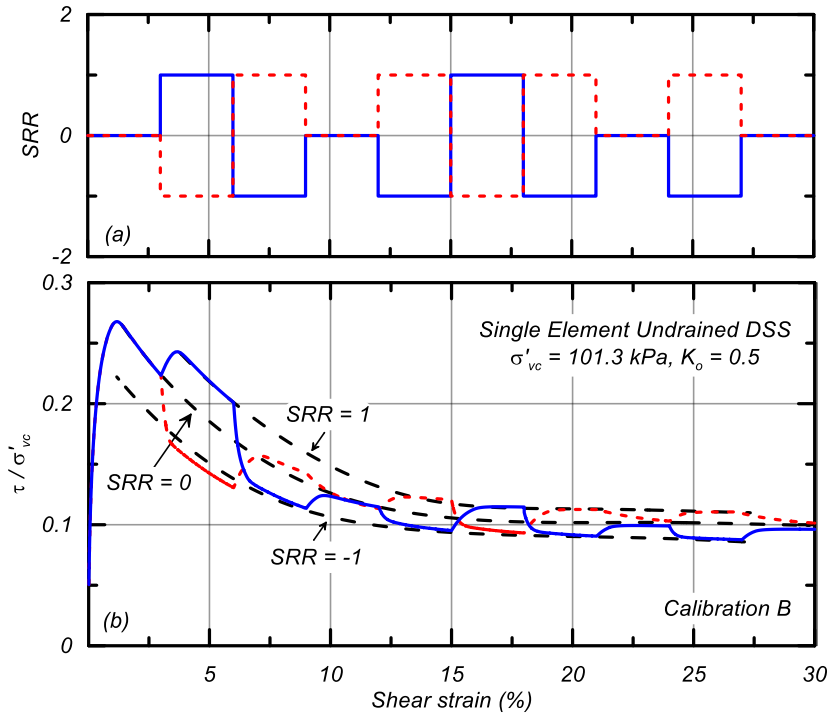

Figure 2-12: Variation in applied strain rate (a) and stress-strain response (b) in undrained DSS loading

2.6 Field Scale Response of a Hypothetical Tailings Embankment

The response of a hypothetical tailings embankment to wetting events was modeled using the finite difference program FLAC 8.1 (Itasca 2019). The tailings embankment of upstream construction was 50 m tall, had a 4:1 horizontal to vertical slope, and was underlain by a 20 m thick foundation layer (Fig. 2-13). Elements in the finite difference mesh were 0.5 m tall by 1.0 m wide except in areas near the dikes and toe where the mesh was adjusted to accommodate the more complex geometry. The water table was at the tailings surface starting at a distance ΔX_{pool} = 210 m from the head of the slope. Capillary rise was 6 m in the tailings and 1 m in the dikes. The hydraulic conductivity for the tailings and foundation were equal, while the conductivity for the dikes was 100 times larger. The horizontal conductivity was 10 times the vertical conductivity in all materials.

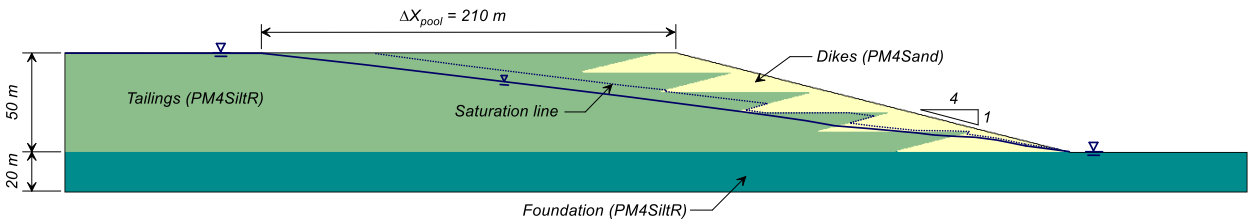

Figure 2-13: Tailings impoundment geometry with the phreatic surface and saturation surfaces from the steady seepage analysis case for Δx_{pool} = 210m.

The tailings and foundation were modeled using PM4SiltR. The tailings were assumed to have uniform engineering characteristics represented by Calibration B or C. The peak undrained shear strength in DSS loading at standard laboratory strain rates ($s_{u,pk,ref}/\sigma'_{vc}$) was 0.27 and the critical state strength ($s_{u,cs,ref}/\sigma'_{vc}$) was 0.09, resulting in a sensitivity (S_t) of 3.0. The shear wave velocity at a confining pressure of 1 atm (101.3 kPa) was 145 m/s. An initial void ratio of 0.95 and a dry unit weight of 13.6 kN/m^3 were assumed. Calibrations B and C produced a strain rate-dependence in $s_{u,pk,ref}$ of 10% per log cycle of strain rate, with the lower (inviscid) limit on $s_{u,pk}$ being about 80% of $s_{u,pk,ref}$ for Calibration B and about 70% of $s_{u,pk,ref}$ for Calibration C (Fig. 6). The foundation layer was modeled using the same parameters as for the tailings except with $s_{u,cs,ref}/\sigma'_{vc}$ = 0.50; this change produced a peak strength of $s_{u,pk,ref}/\sigma'_{vc}$ = 0.5 with no post-peak strain-softening (i.e., S_t =1.0).

The dikes were modeled as medium-dense silty sand using PM4Sand. The input parameters were an apparent relative density D_R = 55%, shear modulus coefficient G_o = 677, and contraction rate parameter h_{po} = 0.4; all other input parameters retained their default values. This calibration produced drained peak friction angles of 33-38 degrees in the dike depending on the loading path and effective confining stress.

Steady state seepage and initial static equilibrium conditions were established in a sequence of analysis steps as follows. Seepage and equilibrium conditions were first

established using Mohr-Coulomb material models, after which the materials were switched to PM4SiltR with inviscid parameters (Calibration A) and PM4Sand, and equilibrium conditions solved for again. The viscous parameters for PM4SiltR were then activated (i.e., F_p, F_M, and $R_{\dot{\gamma},min}$ values for Calibration B or C) and a creep analysis initiated with the tailings, foundation, and dikes fully drained. The creep analysis ended when creep deformations had ceased, corresponding to a long-term fully consolidated condition with all stress states either within or on the soil's static yield surface.

The embankment was then subjected to a wetting event with undrained conditions in the saturated tailings and foundation layers and drained conditions in the sand dikes. A wetting event comprised increasing the water content (Δw_c) in the tailings and dike soils above those already saturated by capillary rise (dashed line in Fig. 2-13), while simultaneously eliminating the suction (negative pore pressures) in the soils saturated by capillary rise. The wetting event was ramped to the final loading condition over a period of approximately 18 days. Horizontal displacement of the embankment face at mid slope is plotted versus time since the start of the wetting event in Fig. 2-14 for analyses using Calibration B with imposed Δw_c of 5%, 12%, 13%, and 15% and Calibration C with imposed Δw_c of 2% and 5%. For the analyses using Calibration B, wetting events with $\Delta w_c \leq 12\%$ caused less than 15 mm of horizontal displacement at the embankment face, with most of the deformation occurring as the wetting load was imposed. The analyses using Calibration B with $\Delta w_c = 13\%$ and 15% developed slope instability in 23 days and 7 days, respectively, after the end of the wetting event. For both of these unstable cases, face displacements remained less than about 50 mm until a day before the slope became unstable. For the analyses using Calibration C, the wetting events with $\Delta w_c = 2\%$ and 5%

developed instability in 168 and 20 days, respectively, after the end of the wetting event, with face displacements similarly remaining less than about 50 mm until a few days before the slope became unstable. The analyses using Calibration C ($R_{\dot{\gamma},\min}$ = 10^{-3}) developed instability under much smaller wetting loads (Δw_c = 2% versus 13%) compared to Calibration B ($R_{\dot{\gamma},\min}$ = 10^{-2}), taking an order of magnitude greater time to rupture after loading (168 days versus 23 days). These differences in responses were attributed to the order-of-magnitude smaller $R_{\dot{\gamma},\min}$ in Calibration C producing a 9% smaller static undrained shear strength at an order-of-magnitude smaller strain rates, such that undrained rupture at this lower strength required an order of magnitude more time to develop.

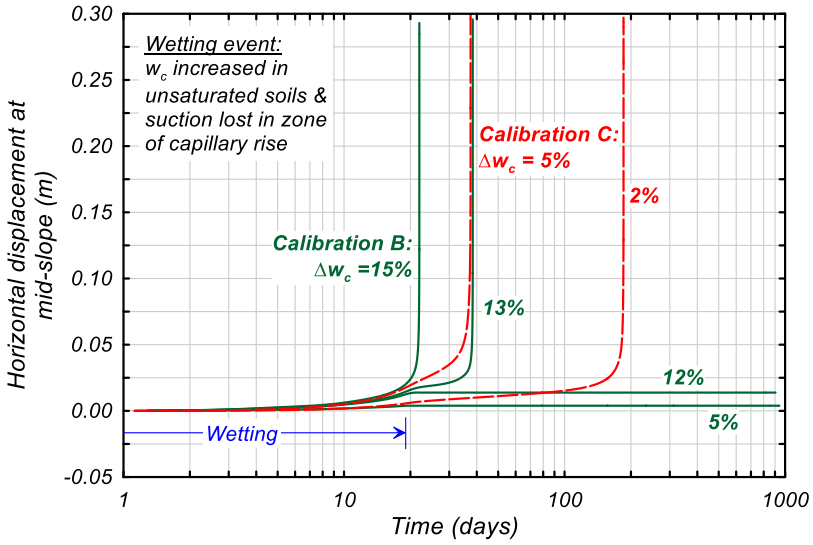

Figure 2-14: Horizontal displacement at mid-slope versus time after start of creep analysis for Calibrations B and C with different wetting events.

Wetting events that led to slope instability triggered progressive failure in the strain-softening tailings. Failure (post-peak softening) initiated in the tailings just above the foundation-tailings interface around mid-slope of the embankment (the initially highest stressed zone) for all wetting events leading to slope instability. The failure progression is illustrated in Fig. 2-15 showing shear strain contours for the simulation using Calibration

C with a Δw_c = 2% at different times and hence different mid-slope horizontal displacements. Mid-slope displacement was 5 mm at 18 days in Fig. 14 (i.e., end of wetting) gradually increasing to 15 mm at 100 days, 25 mm at 158 days, 50 mm at 181 days, and 75 mm at 184 days, followed by the rapid progression of rupture strains and slope instability in less than 24 hours (185 days). Zones of strain-softening, which corresponded approximately to the shear strain contours exceeding 1-2% in Fig. 2-15, developed in localized shear bands such that global displacements remained relatively small even as the shear strains in these localization zones became relatively large. The zone of strain-softening progressively grew in time, eventually developing along the full length of the eventual failure surface.

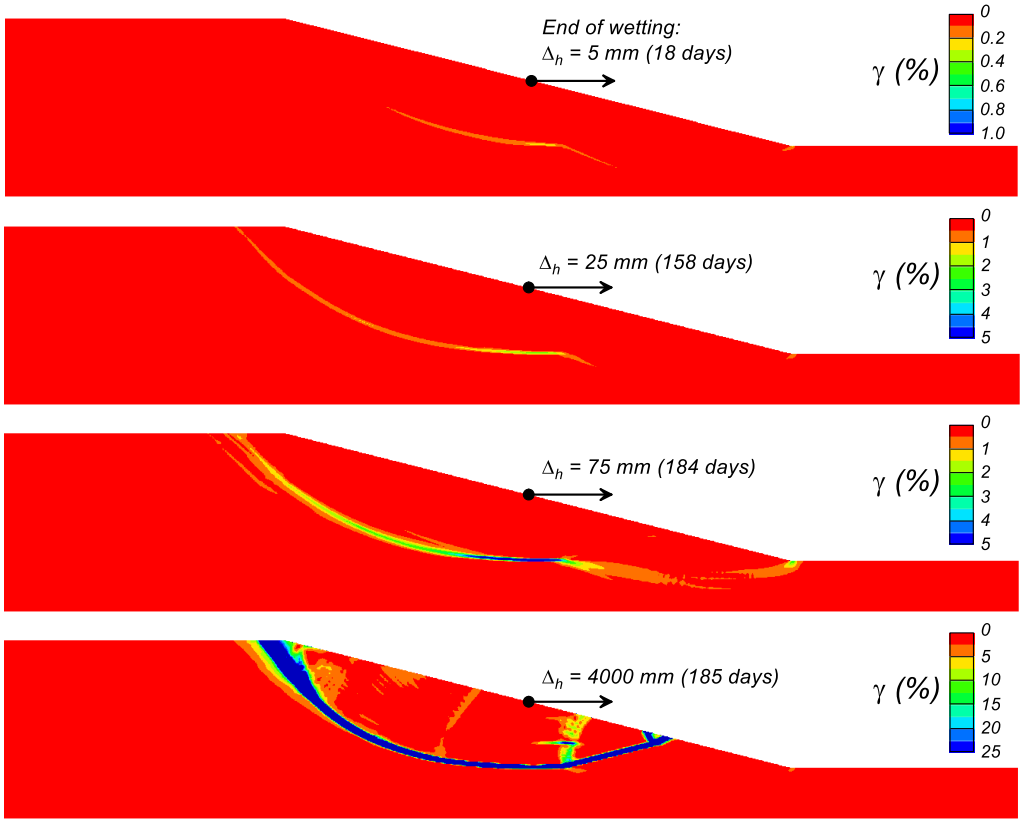

Figure 2-15: Contours of shear strain at different times using Calibration C with Δw_c = 2%.

The progressive nature of the failure and the associated shedding of shear stress from softening elements explains why the time to failure for the embankment (Fig. 2-14) was much longer than required for undrained creep rupture at the element level (Fig. 2-11). Softening elements shed shear stress into adjacent elements, which increased strain rates and hence increased shear resistances in all soils, thereby partially compensating for the reduced shear resistance in the softening elements. The elements adjacent to the strain-softening zones eventually developed enough creep-induced strain to begin strain-softening themselves. This process continued with the length of the softening zone progressively increasing over time, while slope displacements remained relatively small because the softening zone was relatively thin. This process progressed until further stress shedding led to instability with rapidly accelerating deformations.

The static stability of the slope in the absence of creep and progressive failure effects was evaluated using the strength reduction method with the same mesh and initial stress conditions and using non-strain softening Mohr Coulomb models. For long term drained stability, the dike, tailings, and foundation materials were assigned effective friction angles of 34, 32, and 32 degrees, respectively. The factor of safety was 2.6 with the critical failure mechanism being shallow surface slides; deeper failure mechanisms reaching the tailings would have even greater factors of safety. For long term (consolidated) undrained stability, the analyses assumed: (1) dike materials were drained with a friction angle of 34 degrees, (2) tailings were undrained where saturated with s_u/σ'_{vc} = 0.27 and drained where not saturated with a friction angle of 32 degrees, and (3) foundation clays were undrained with s_u/σ'_{vc} = 0.50. The factor of safety was 1.30 for this long-term consolidated, undrained loading condition, with the critical failure mechanism

being approximately the same as the mechanism that developed in the creep analyses (Fig. 2-15). This margin of safety, based on s_u at reference strain rates, was insufficient to maintain stability under the combined influences of undrained creep, progressive failure, and modest wetting loads. For the analyses using Calibration B, the margin of safety was overcome largely by the combination of the static s_u at the slowest strain rates (i.e., $s_{u,ref}/s_{u,static}$ = 1/0.82 = 1.22 per Fig. 2-6) and the Δw_c = 13% increasing the driving shear stresses in the tailings by about 7%. For the analyses using Calibration C, the smaller static s_u (i.e., $s_{u,ref}/s_{u,static}$ = 1/0.72 = 1.38) meant that only a nominal wetting induced load (e.g., Δw_c = 2%) was sufficient to trigger the start of undrained creep leading to instability. For both calibrations, the delay between wetting-induced loading and slope instability was controlled by the progressive failure processes and strain rate at which the static s_u is reached.

Additional analyses were performed for different pool locations (X_{pool} = 110 m, 160 m, 210 m, 260 m in Fig. 2-13), different calibrations, and a range of wetting induced loads. Reducing the pool's distance from the dam crest reduced the static factor of safety (based on the above-described strength reduction method), which reduced the amount of wetting induced load required to trigger instability for any given calibration. Reducing the static s_u via calibration of the rate parameters also reduced the amount of wetting-induced loading required to trigger instability. The delay between wetting-induced loading and slope instability was most strongly dependent on the material rate dependency, the ratio of the static s_u to the s_u at reference strain rates, the static factor of safety, and magnitude of wetting-induced loads. The results of these sensitivity analyses were consistent with those described above and are consistent with expectations.

Other sensitivity analyses were performed to evaluate sensitivity to the mesh size and time step constraints. The analysis cases with Calibration B and X_{pool} = 210 m (Fig. 2-13) were repeated with the element sizes reduced by a factor of two in both directions (four times as many elements). Delayed slope instability developed 3 days after a wetting event with Δw_c = 13% versus after 23 days with the coarser mesh. Delayed slope instability developed 8 days after a wetting event with Δw_c = 12% versus the slope remaining stable with the coarser mesh. The slope remained stable for $\Delta w_c \leq 10\%$, versus remaining stable for $\Delta w_c \leq 12\%$ with the coarser mesh. Thus, the finer mesh reduced the magnitude of the loading event required to trigger a delayed failure, which is consistent with expected mesh effects for systems with strain-softening materials. Sensitivity analyses using smaller strain increment limits for constraining the time steps within the explicit creep solution procedure of FLAC showed less effect than the mesh size, with smaller shifts in the timing of delayed failures and no significant effect on the loading limits for stability. The sensitivity of the simulation results to mesh size and time steps introduces an additional uncertainty that must be considered in practice and represents common limitations in analyses involving strain-softening materials.

2.7 Discussion

The field scale analysis introduced herein highlighted the capabilities of the PM4SiltR model in a boundary value problem, however it is important to be aware of potential limitations that may play a role in predicting the effects of undrained creep on slope stability. These creep analyses assumed fully undrained conditions in the tailings, which did not consider any potential beneficial effects from consolidation during creep. The potential for consolidation to progress fast enough to preclude undrained creep rupture

may be assessed by evaluating their relative time scales, each of which involves considerable uncertainty in practice. These analyses also exhibited mesh sensitivity due to the strain-softening tendency of the material and the progressive failure localizing along a narrow band. However, the inclusion of viscoplasticity can provide a measure of regularization to partially offset the mesh sensitivity (Needleman 1988, Niazi et al. 2013, Oathes and Boulanger 2019, 2020). Additional study is needed into procedures to account for mesh dependency and regularization, the modeling of coupled consolidation and creep, and laboratory and field testing to determine applicable creep properties. Nonetheless, application of these analysis procedures utilizing PM4SiltR in a reevaluation of the 2019 Feijão Dam 1 failure provide an additional measure of validation for their use in engineering practice (Oathes and Boulanger 2022).

Delayed failures of seemingly stable embankments, such as seen in Feijão Dam 1, highlights the need to consider internal creep and strain rate-dependent shear strengths in analyses. Consideration of internal creep and strain rate-dependent shear strengths involves the calibration of advanced constitutive models that capture the viscoplastic tendencies of plastic silts and clays. Accurately modeling the viscoplastic behavior requires more extensive testing, both field and laboratory, than is commonly performed. Estimates of rate-dependent material properties may be obtained from empirical correlations, but these correlations for creep behavior are not well defined for many soil types, including various tailings materials which have been shown to be susceptible to creep failures. Despite these challenges, the potential for undrained creep rupture needs to be considered in analysis or design. Recognizing the potential for creep and progressive failure can inform the selection of soil properties, assumptions for static

liquefaction triggering, and appropriate factors of safety when performing limit equilibrium analyses. Alternatively, directly simulating creep and progressive failure in numerical analyses can provide insights for specific projects and provide a framework for developing generalized guidance.

2.8 Conclusion

The PM4SiltR model was developed to represent strain rate dependent behaviors of clays and plastic silts in two-dimensional (plane strain) static slope stability applications. The model builds upon the stress ratio-controlled, critical state-compatible, bounding surface plasticity model PM4Silt. PM4SiltR was developed to simulate strain rate-dependent shear strength, stress relaxation, and creep; it is unable to simulate strain rate-dependent consolidation behavior because the model does not have a cap. The non-viscous behavior of PM4SiltR follows the monotonic behavior of PM4Silt. Six parameters were introduced to control the viscous behavior. The model utilizes a consistency approach wherein the critical state line and the critical state stress ratio are made strain rate dependent. A static yield surface separates the viscous and non-viscous behaviors at slow or zero loading rates. Transient responses and stress relaxation are controlled by an internal strain rate and auto-decay process.

Single element simulations of undrained DSS shearing and undrained creep illustrated the constitutive response of the model. The introduced viscosity was shown to increase the peak strength and the strain at the mobilization of peak strength as the applied strain rate increases. The peak strength became rate independent at strain rates smaller than the minimum strain defining the static bounding surface. Simulations of DSS undrained creep were either stable or ruptured depending on the magnitude of the

imposed stress level and the static bounding surface. Lower sustained shear stresses typically resulted in stable conditions and higher sustained stresses resulted in rupture, with the time to rupture decreasing with increasing sustained stresses. Simulations close to the bounding surface may result in small magnitudes of induced creep strain before becoming stable and deformations ceasing.

PM4SiltR was used to simulate undrained creep rupture in a hypothetical tailings dam with a strain-softening material. Small changes in loading were shown to be able to trigger a progressive failure due to undrained creep rupture in the strain-softening material resulting in delayed slope instability. Simulations showed that minor changes in phreatic surface elevation or pool length could transition an embankment from stable to unstable in the long term. Similarly, wetting events with a corresponding loss of suction were shown to be capable of causing sufficient internal strain to trigger undrained creep rupture, progressive failure, and slope instability.

The ability to incorporate viscous effects into analyses of earthen structures founded on or containing clays or plastic silts can improve confidence in analysis results by better representing the soil mechanics behaviors observed in the laboratory or in situ. Further advancing the modeling of creep and progressive failure in practice requires further investigation into mesh effects, site-specific testing, and empirical relations for viscous soil properties, as well as the relationship between creep and consolidation. Despite the remaining challenges, the numerical and constitutive modeling approach herein shows promise as a way for directly accounting for creep and progressive failure in practice.

2.9 Acknowledgements

Portions of the work were supported by the California Department of Water Resources under Contract 4600009751. Any opinions, findings, or recommendations expressed herein are those of the authors and do not necessarily represent the views of this organization. The authors appreciate the above support.

Chapter 3 : Effect of Viscoplasticity on Localization in Saturated Clays and Plastic Silts

Original publication:

Oathes, T.J., and Boulanger, R.W. (Under Review). "Effect of viscoplasticity on localization in saturated clays and plastic silts." ASCE Journal of Geotechnical and Geoenvironmental Engineering.

Abstract

A numerical study is presented of the effects that viscoplasticity has on localization processes in sensitive, saturated clays and plastic silts. Numerical simulations of laboratory specimens of sensitive, viscoplastic soil subjected to monotonic, undrained, direct simple shear loading were performed using a viscoplastic constitutive model. Parametric analyses evaluated the effects of soil sensitivity, post-peak strain-softening rate, and strain rate-dependency, as well as specimen size, mesh discretization, and loading rate. The numerical results showed that the global strain at which a localization forms primarily depends on the strain rate-dependency of the soil's shearing resistance relative to its rate of post-peak strain-softening. A regression model is subsequently presented that relates the global strain at the onset of localization to the soil's strain rate-dependency and post-peak strain-softening rate. The results indicate that the inclusion of reasonable levels of viscoplasticity significantly increases the strain that can develop before a localization develops in clays and plastic silts with modest strain-softening rates.

The consistency of the numerical results with available laboratory observations is discussed. Implications for practice and future research needs are discussed.

3.1 Introduction

Seismic deformations and stability of structures founded on or containing sensitive, saturated clays and plastic silts depend on numerous factors, including the rate and magnitude of potential strength loss with increasing deformation. The strength loss associated with fully remolded conditions (i.e., at large shear strains) may develop at modest global displacements if the shear strains are concentrated within narrow shear bands (localizations), which may be expected in strain-softening materials and can complicate numerical modeling (e.g., Schreyer and Chen 1986). Earthquake-induced landslides attributed to strength loss in sensitive clays are described by Seed and Wilson (1967), Lefebvre et al. (1992), Brooks (2014), Perret et al. (2017), and Abdellaziz et al. (2020). Predicting potential strength loss in sensitive clays and plastic silts during earthquake loading is complicated by challenges in (1) evaluating whether the deformations that develop during or after shaking are sufficient to cause formation of localizations, (2) predicting the "length scale" or thickness of any localization, (3) numerically approximating localization processes, and (4) estimating the soil's stress-strain response within a localization, wherein very large shear strains can both develop and be required for full remolding. Engineering practices for evaluating or numerically modeling strength loss in sensitive clays and plastic silts during earthquake loading are not uniformly established, although several approaches have been proposed or demonstrated (e.g., Kiernan and Montgomery 2018, Abdellaziz et al. 2020, Qiu and Elgamal 2020).

Numerical simulations of systems involving rate-dependent, strain-softening materials have shown that the rate dependence can significantly affect the localization process. Numerical simulations involving non-rate-dependent, strain-softening materials can be expected to exhibit mesh sensitivity wherein the degree of strain-softening and associated strength loss is dependent on the mesh discretization. Shear deformations tend to concentrate along single element-thick zones, such that smaller elements are likely to develop greater shear strains for similar levels of global deformation, unless the numerical analysis includes a specified length scale (e.g., D'Ignazio and Lansivaara 2015). The introduction of rate dependency or viscoplasticity in numerical models provides a measure of regularization that can reduce the mesh sensitivity (e.g., Needleman 1989, Wang et al. 1997, Armero 1997) as well as delay the onset of localization and increase the magnitude of deformation that occurs prior to significant strength loss.

This paper presents results of a numerical study of the effects that viscoplasticity has on localization processes in sensitive, saturated clays and plastic silts. Numerical simulations are presented for laboratory specimens of sensitive, viscoplastic soil subjected to monotonic, undrained, direct simple shear (DSS) loading. The simulations were performed using FLAC 8.1 (Itasca 2019) with the user-defined viscoplastic constitutive model PM4SiltR (Boulanger et al. 2022). Parametric analyses are used to evaluate the effects of soil sensitivity, post-peak strain-softening rate, and strain rate-dependency, as well as specimen size, mesh discretization, and loading rate. The numerical results show that the global (versus local) strain at which a localization forms primarily depends on the strain rate-dependency of the soil's shearing resistance relative

to its rate of post-peak strain-softening. A regression model is subsequently presented that relates the global strain at the onset of localization to the soil's strain rate-dependency and post-peak strain-softening rate. The results indicate that the inclusion of reasonable levels of viscoplasticity significantly increases the strain that can develop before a localization develops in clays and plastic silts with modest strain-softening rates. The consistency of the numerical results with available laboratory observations is discussed. Implications for practice and future research needs are discussed.

3.2 Prior Studies

Experimental studies have shown that sensitive clays with strain-softening tendencies are susceptible to the development of shear bands (or localizations) on the order of millimeters thick (Thakur 2006 and Gylland et al. 2014). Localizations can begin to develop at or near the mobilization of peak shear strength (Bernander et al. 1985, Atkinson and Richardson 1987, Sachan and Penumadu 2007, and Thakur 2018). Localizations continue to develop with increasing shear strain until they reach a minimum thickness that may be partly controlled by the dissipation of pore pressures from the localization. The thickness of the localization has been observed to decrease with increasing applied strain rate, which is consistent with drainage from the shear band being reduced at faster strain rates (Bernander et al. 1985, Thakur 2006, and Gylland et al. 2014). Conversely, Atkinson and Richardson (1987) reported that undrained triaxial tests on heavily overconsolidated, reconstituted clay specimens developed localizations when loaded slowly but did not develop localizations when loaded quickly, which is also consistent with local drainage given these soils were initial dense of critical state. The rate of post-peak strain-softening has been proposed as a parameter for quantifying the

tendency of saturated clays to localize (Bernander et al. 1985 and Gylland et al. 2014). Atkinson and Richardson (1987) stated that after the development of a localization, global strains of 10 to 20% are required to reach critical state. Thakur (2018) found that strains within a shear band were approximately three or four times larger than the applied global strain at the end of plane strain compression (PSC) tests on Norwegian quick clays. Sachan and Penumadu (2007) defined a localization as the difference of local and global strain greater than 4%.

The tendency of saturated clay specimens to localize in laboratory testing has been shown to depend on material properties and loading conditions. Fig. 3-1a shows stress-strain responses of TXC compression tests on normally consolidated (NC) B6 clay loaded at strain rates of 0.05%/hr, 0.5%/hr, and 5%/hr (Lefebvre and LeBouef 1987). Localization was not reported or discussed over the range of strain in the experiments. Fig. 3-1b shows the stress-strain response of undisturbed, lightly overconsolidated Tiller clay under triaxial loading, using a cell modified to allow for observing localization, loaded at strain rates of 3%/hr and 30%/hr (Gylland et al. 2014). Development of localizations (defined by base sled movement) was observed to occur over a range of displacements. Gylland et al. (2014) observed the initiation of localization nearly coincided with the mobilization of peak strength and that an additional axial strain of about 2% was necessary for the localization to fully develop.

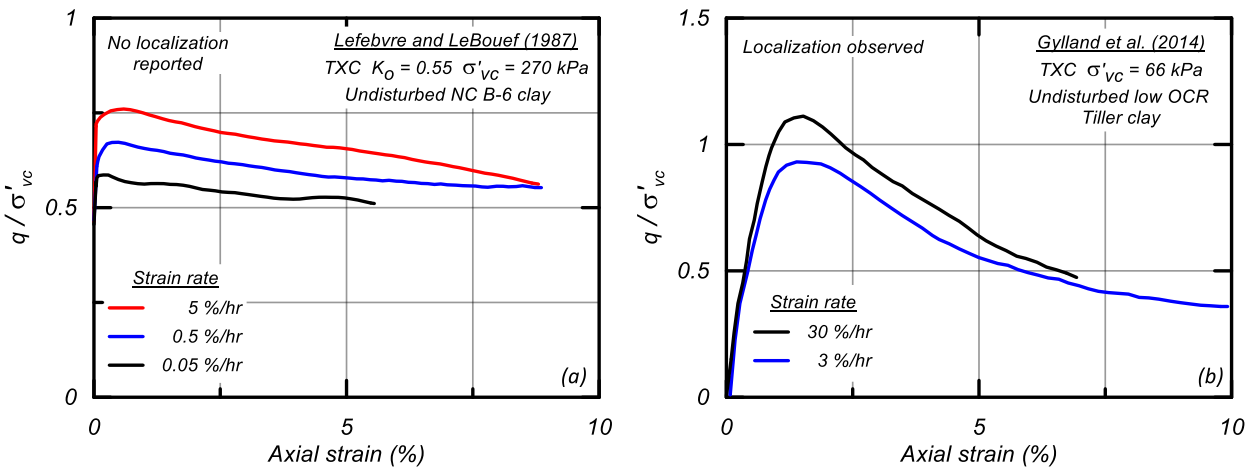

Figure 3-1: Undrained triaxial compression tests on: (a) NC B-6 clay by Lefebvre and LeBouef (1987) and (b) Tiller clay by Gylland et al. (2014)

Numerical modeling of strain-softening and associated localizations has been performed using several different methods in past studies. Some studies have used a coupled analysis with pore water flow and an elastic-plastic constitutive relationship that can simulate strain-softening. This method models pore pressure diffusion within and away from the localization zone in the soil body. The results are often mesh dependent, with the shear band narrowing to a single element due to continued strain-softening within the shear band (Thakur et al. 2006 and Thakur 2011). Thakur (2011) discussed an internal length parameter defined by the ratio of the permeability and the applied strain rate which controls the thickness of the shear band and can be used to prescribe the thickness of elements to account for the mesh dependency of common coupled and uncoupled mechanical - pore pressure solution schemes.

The inclusion of viscoplasticity (i.e., rate-dependent shearing resistance), through viscoplastic regularization, has been shown to reduce the mesh dependency of the solution: the concentration of shear strains within a narrow zone increases the local strain rate, which increases the viscoplastic material's shear stiffness and strength, which in

turn reduces the potential for shear strains to continue concentrating at that location (Niazi et al. 2013). This produces a viscoplastic length scale which relates the opposing effects of hardening (rate-dependency) and softening (damage). Needleman (1988) and Loret and Prevost (1990) showed that for a one-dimensional case, viscoplasticity and the associated regularization yielded a mesh independent response prior to the onset of localization, while the response remained mesh dependent after the localization developed. Viscoplastic regularization has also been shown to delay the onset of localization in other cases using different types of constitutive models (e.g., Needleman 1989, Oathes and Boulanger 2019, 2020).

3.3 Numerical Analyses of DSS Loading

Simulations of DSS loading were performed herein using the two-dimensional finite difference program FLAC 8.1 (Itasca 2019) with the creep module and the user defined constitutive model PM4SiltR (Chapter 2 and Boulanger et al. 2022). Single element and grid simulations were performed for a broad range of material properties to parametrically evaluate the effect of viscoplasticity on localizations in saturated, sensitive clays and plastic silts.

3.3.1 PM4SiltR

PM4SiltR is a viscoplastic, critical state-based, stress ratio-controlled, bounding surface plasticity model. The model builds upon the plane-strain PM4Silt (Boulanger and Ziotopoulou 2019) model with modifications that represent viscous effects using a consistency approach (e.g., Martindale et al. 2012) combined with an internal strain rate and auto-decay process (e.g., Clarke and Hird 2012, Yuan and Whittle 2020). PM4SiltR is implemented as a dynamic link library in FLAC 8.1 (Itasca 2019).

The critical state line and bounding surface are dependent on the strain rate (Fig. 3-2). An increase in strain rate shifts the critical state line to the right in e-log(p′) space (Fig. 3-2a) and the bounding surface upward in q-p′ space (Fig. 3-2b) by amounts that depend on independent input parameters. As the strain rate increases, the critical state strength and peak strength both increase. A static bounding surface separates viscous and inviscid plastic behavior as the strain rate is decreased (red lines in Fig. 3-2a and 3-2b). The static bounding surface sets the minimum strength for strain rates nearing zero. The transient response and stress relaxation are controlled with an internal strain rate and an auto-decay process, similar to the approaches by Clarke and Hird (2012) and Yuan and Whittle (2020). Rate-dependence is thereby modeled by enforcing consistency with the rate-dependent critical state line and bounding surfaces, similar to the consistency approach by Martindale et al. (2012), rather than by including separate viscous resistance components.

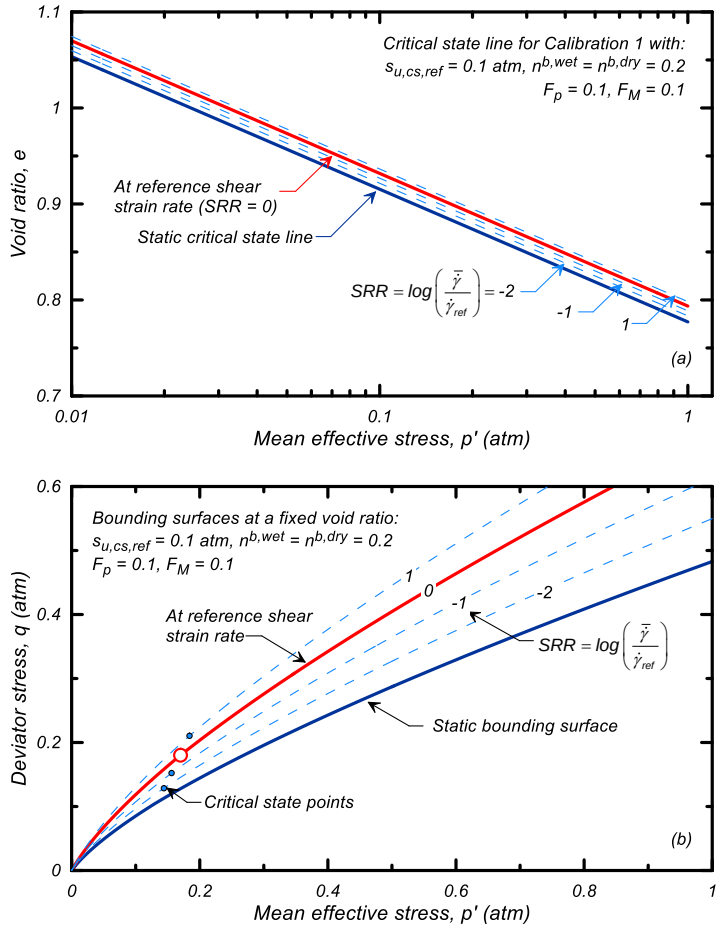

Figure 3-2: PM4SiltR (a) rate-dependent critical state lines and (b) bounding surfaces at varying SRRs for Calibration 1

PM4SiltR has 18 parameters; 12 parameters control the nonviscous monotonic response and six control the viscous portion of the response. The model has three required input parameters (similar to PM4Silt) which control the nonviscous behavior: (1) the critical state undrained strength or undrained strength ratio at the reference strain rate ($s_{u,cs,ref}$ or $s_{u,cs,ref}/\sigma'_{vc}$), (2) the shear modulus coefficient (G_o), and (3) the contraction rate parameter (h_{po}). The $s_{u,cs,ref}$ is not a model parameter itself, but rather is used internally to set the critical state line position given the other input parameters (i.e., Boulanger and Ziotopoulou 2018). The other nine parameters for the nonviscous response are assigned default values per the generalized calibration procedure in Boulanger et al. (2022). The

six parameters for the viscous portion of the model include (1) rate parameters for the critical state stress ratio (F_M) and mean effective stress at critical state (F_p), (2) the reference strain rate ($\dot{\gamma}_{ref}$) for which the critical state undrained strength was specified, (3) the minimum normalized strain rate that produces a viscid response ($R_{\gamma,min}$), and (4) the internal strain rate evolution parameter (θ_{ref}) and auto-decay parameter (β_{ref}). Input values are required for F_p and F_M, while the other parameters are assigned the following default values (as prescribed by PM4SiltR): $\dot{\gamma}_{ref}$ = 1.39 10^{-5}/s , $R_{\gamma,min}$ = 0.001 , θ_{ref} = 0.5, and β_{ref} = 0.999. Constitutive model responses for a range of loading conditions using the default calibration parameters are presented in Boulanger et al. (2022).

3.3.2 Calibrations

Six calibrations were developed with varying peak strengths, sensitivities, and rates of strain-softening at the reference strain rate. Stress-strain responses for single element simulations of DSS loading consolidated to a vertical effective stress (σ'_{vc}) = 101.3 kPa and a coefficient of earth pressure at rest (K_o) = 0.5 are shown in Fig. 3-3 for the six calibrations. Peak $s_{u,pk}/\sigma'_{vc}$ values ranged from 0.25 to 0.36 and the sensitivity (S_t = $s_{u,pk}/s_{u,rem}$) ranged from 2.4 to 6.2. Three calibrations (3,5, and 6) had the same $s_{u,pk}/\sigma'_{vc}$ and S_t with different strain-softening rates to isolate the effect of softening rate. Faster rates of strain-softening will herein be referred to as “brittle” or “more brittle” (i.e., Calibration 1 is more brittle than Calibration 2). The peak strength was mobilized prior to accumulation of 1% shear strain for all six calibrations (all calibrations were assigned the same small strain shear modulus and initial shear stiffness). The calibration process involved iteratively adjusting the $s_{u,cs,ref}/\sigma'_{vc}$ and bounding surface parameter ($n_{b,wet}$) to

obtain the target $s_{u,pk}/\sigma'_{vc}$ and S_t at the reference strain rate and the contraction rate parameter (h_{po}) to obtain the target rate of post-peak strain-softening. The nonviscous parameters for the six calibrations are shown in Table 3-1, while all parameters not indicated retained their default values. The range of strengths and sensitivities included in the analysis does not encompass the entire range possible but as illustrated later they are sufficient to investigate the interplay of viscous strength gain and strain-softening on the localization process.

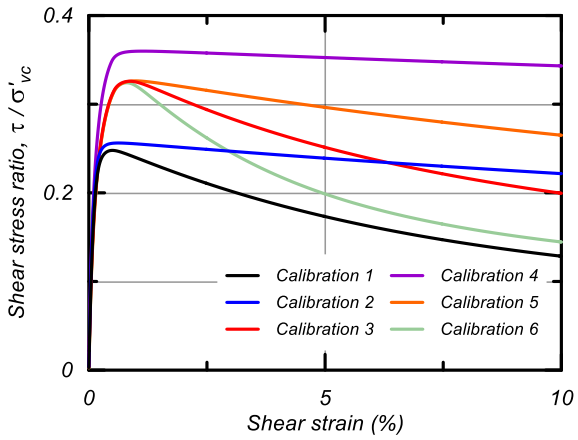

Figure 3-3: Six calibrations with varying sensitivities, softening rates, and peak strengths developed for use in the parametric analyses

Table 3-1: Soil properties and PM4SiltR parameters for the six calibrations

	Calibration	1	2	3	4	5	6
Properties	$s_{u,pk}/\sigma'_{vc}$	0.25	0.26	0.33	0.36	0.33	0.33
	S_t	6.2	3.7	5.5	2.4	5.5	5.5
Parameters	$s_{u,cs,ref}/\sigma'_{vc}$	0.04	0.07	0.06	0.15	0.06	0.06
	$n_{b,wet}$	0.2	0.25	0.1	0.1	0.1	0.1
	G_o	350	350	350	350	350	350
	h_{po}	5000	15000	5000	15000	15000	2000

3.3.3 DSS Simulations

Simulations of saturated specimens subjected to undrained DSS loading were performed using both single element and grid models. Single element simulations were used to

observe the constitutive response in the absence of localization (i.e., Fig. 3-3) whereas grid simulations were utilized to observe the response with localization. Stress conditions were initialized with σ'_{vc} = 101.3 kPa, σ'_{hc} = 50.7 kPa, and pore pressure (u_o) = 0.0. The grid simulations varied the discretization of the mesh, with results presented for a 10 x 10 mesh unless indicated otherwise (Fig. 3-4). The left and right side of the model were assigned attached boundary conditions which ensured the left and right side displaced identically, while not restricting the formation of localizations (Fig. 3-4). Stiff elastic caps with G = 600 MPa were placed above and below the soil mesh. The top boundary was assigned a constant horizontal velocity for shear loading, while applying a constant total vertical stress of 101.3 kPa. Time steps during loading were controlled to maintain a maximum strain increment per step of 10^{-7} throughout all zones, which sensitivity analyses showed was sufficient for convergence with FLAC's explicit formulation. Numerical damping was included using the default levels of FLAC's combined damping formulation, wherein damping forces are proportioned equally on the rate of change in forces and displacements. Simulations were run with flow off and as such did not consider the effect of pore pressure diffusion.

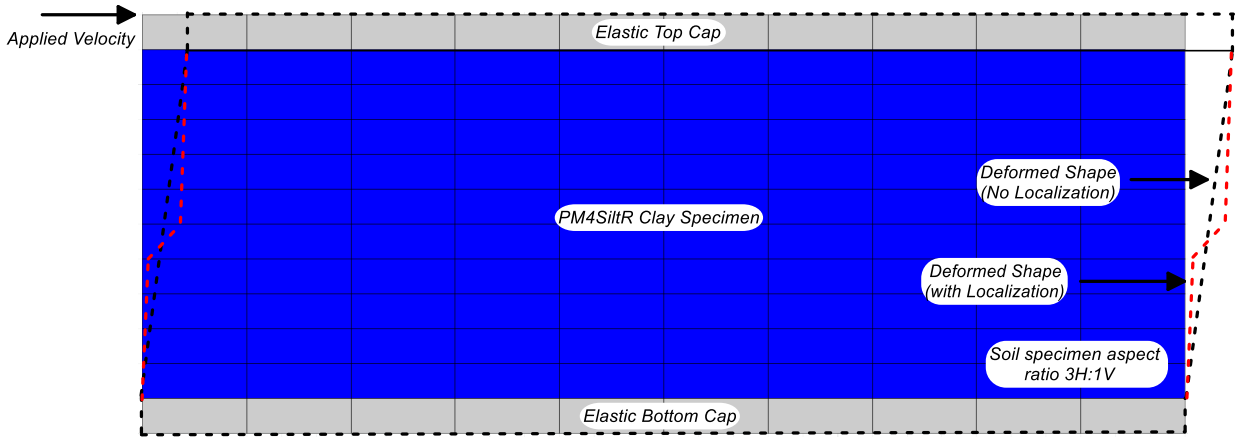

Figure 3-4: Mesh for a grid simulation with a 3:1 H:V ratio and schematic of deformation patterns from DSS shearing without localization (black dashed) and with localization (red dashed)

3.4 Simulations Results: Deformation Pattern and Onset of Localization

The inclusion of viscoplasticity delayed the onset of localization in the grid simulations of DSS loading, as illustrated by the global stress-strain responses shown in Fig. 3-5 for different rate parameters in combination with Calibrations 1 (Fig. 3-5a) and 2 (Fig. 3-5b). Global stress-strain responses for the grid simulations are shown for no rate dependence ($F_p = F_M = 0.0$), mild rate dependence ($F_p = F_M = 0.05$), and moderate rate dependence ($F_p = F_M = 0.10$). Stress-strain responses from single element simulations (black dashed lines) are shown for comparison. Without rate dependency, localizations developed immediately upon mobilization of peak strength for both calibrations. In addition, the post-peak strain-softening was far more rapid in the grid simulations than in the single element simulation, which is a direct consequence of the local shear strains within the localization being far greater than the global (average) shear strain for the grid simulations. Inclusion of rate dependence for the more brittle (faster strain-softening) Calibration 1 delayed the onset of localization from approximately 0.3% shear strain (without rate dependence) to 1.8% and 3.3% for $F_p = F_M = 0.05$ and $F_p = F_M = 0.1$, respectively. For the less brittle

(slower strain-softening) Calibration 2 the onset of localization was further delayed, from approximately 0.5% shear strain (without rate dependence) to 6.2% and >10% strain, respectively.

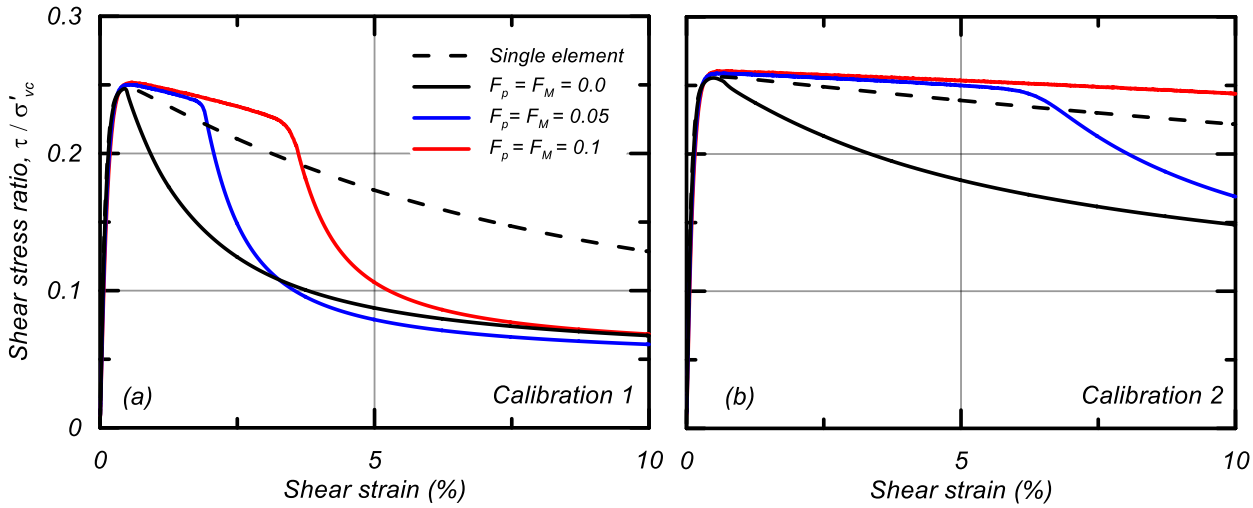

Figure 3-5: Effect of viscoplasticity on the onset of localization with varying levels of implemented viscoplasticity for (a) Calibration 1 and (b) Calibration 2

The delay in onset of localization from the inclusion of viscoplasticity is due to the continued dispersion of shear strain throughout the grid model prior to strains becoming concentrated within a single row of elements. Local shear strain contours are shown in Fig. 3-6 for grid simulations of Calibration 1 without rate dependency (Fig. 3-6a-d) and with $F_p = F_M = 0.1$ (Fig. 3-6e-h) at global shear strains of 1%, 2%, 3%, and 5%. At 1% global shear strain, the shear band was fully developed in the simulation without rate dependency as seen by the single row of elements having approximately 5% shear strain whereas the other nine rows have less than 1% shear strain. At 1% global shear strain, there was no distinct shear band in the simulation with $F_p = F_M = 0.1$, all elements had approximately 1% shear strain (nearly uniform deformation). As the global shear strain increased, the displacement accumulated solely within the localized band for the

simulation without rate dependency (Fig. 3-6a-d). In the simulation with rate dependency (Fig. 3-6e-h), shear strains continued to accumulate nearly uniformly until the global shear strain reached approximately 3%, after which the strains began to accumulate in fewer bands until the localization was observed to be fully developed by approximately 5% shear strain. The full development of a localization was accompanied by a sharp increase in the global rate of strain-softening, as show in Fig. 3-6a.

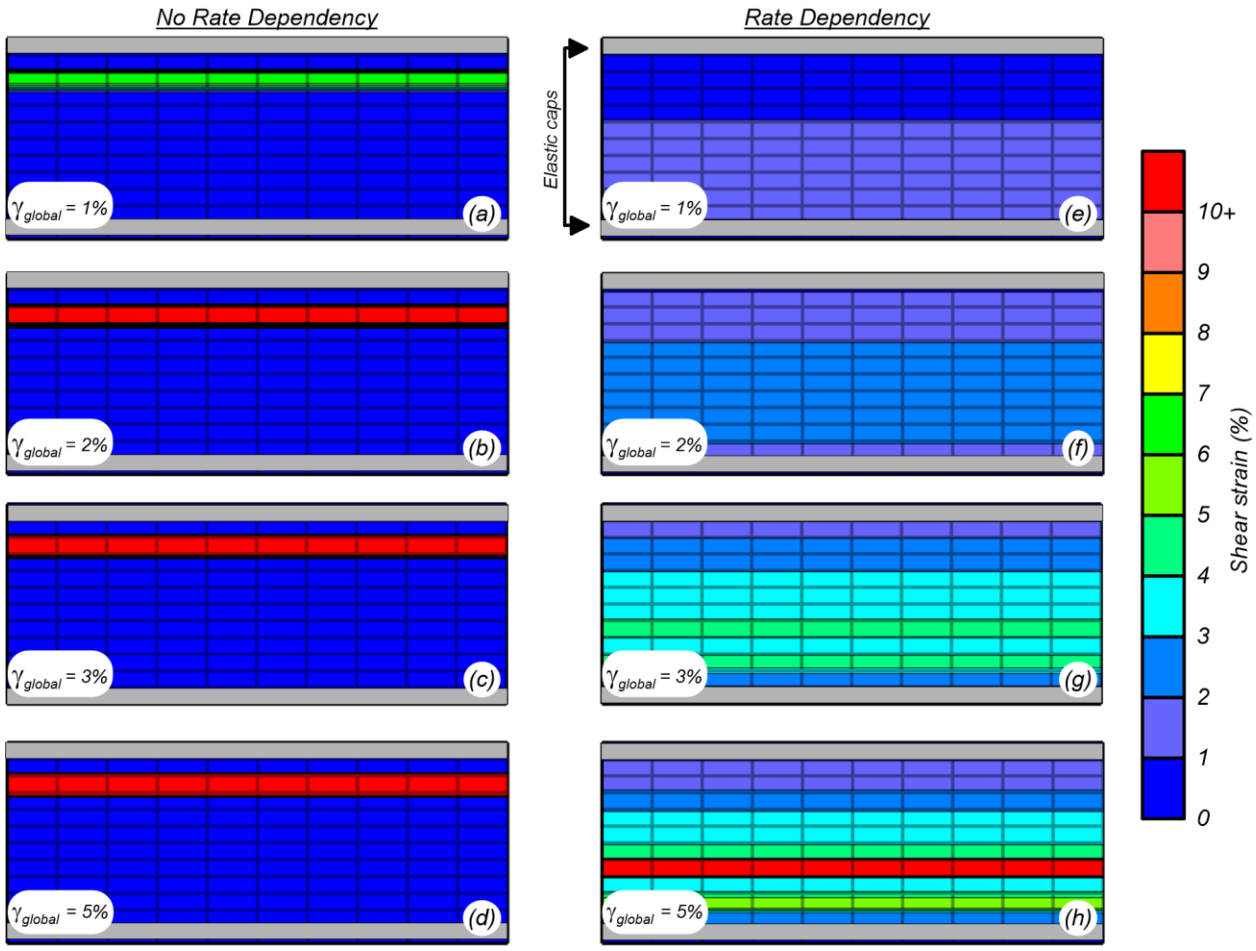

Figure 3-6: Local shear strain distributions at different global (average) shear strains for Calibration 1: (a-d) without rate dependency, $F_p = F_M = 0.0$, and (e-h) with moderate rate dependency, $F_p = F_M = 0.1$.

These results showed that the magnitude of global strain prior to the onset of localization was dependent on the rate of strain-softening and the degree of rate

dependency. The global shear strain required for a localization to fully form increases with (1) a decreasing rate of strain-softening and (2) an increasing degree of rate dependency. Results of parametric analyses presented later are used to develop a regression model relating the onset of localization to these two primary factors.

3.4.1 Other Influences

Mesh dependency of the stress-strain responses before and after the onset of localization is illustrated by the stress-strain responses for varying meshes (8x8, 10x10, 12x12, 16x16, 20x20, and 30x30 grids) shown in Fig. 3-7 for Calibrations 1 (Fig. 3-7a) and 2 (Fig. 3-7b) with $F_p = F_M = 0.05$. Simulations using Calibration 1 localized at 1.7% to 2% shear strain for all meshes whereas simulations using Calibration 2 localized at 6.5% to 10% shear strain. The rate of strain-softening after the onset of localization increased with decreasing element height for both calibrations due to the more rapid accumulation of strain within the narrower localization band (i.e., along a single row of elements). Simulations using Calibrations 1 and 2 without viscoplasticity ($F_p = F_M = 0.0$) localized immediately after reaching the peak shear resistance (0.3% shear strain for Calibration 1 and 0.5% shear strain for Calibration 2; results for 10x10 grid shown in Fig. 3-5), after which the rates of strain-softening showed mesh dependencies similar to those with viscoplasticity effects (e.g., Fig. 3-7). Thus, the inclusion of viscoplasticity increased the effective length scale (thickness) of the localization zone (e.g., Fig. 3-6) which increased the global strain at which localizations fully formed for all meshes (Fig. 3-7), although the results still exhibit a degree of mesh dependency both before and after the onset of a localization. The more brittle Calibration 1 showed less mesh sensitivity than the less brittle Calibration 2 with the same levels of viscoplasticity (Fig. 3-7a versus 3-7b), but it

also developed localizations at much smaller shear strains (e.g., 1.7-2.0% versus 6.5-10%). Similar analyses using different numbers/sizes of elements in the horizontal and vertical directions showed that the results are controlled by the element thicknesses in the vertical direction.

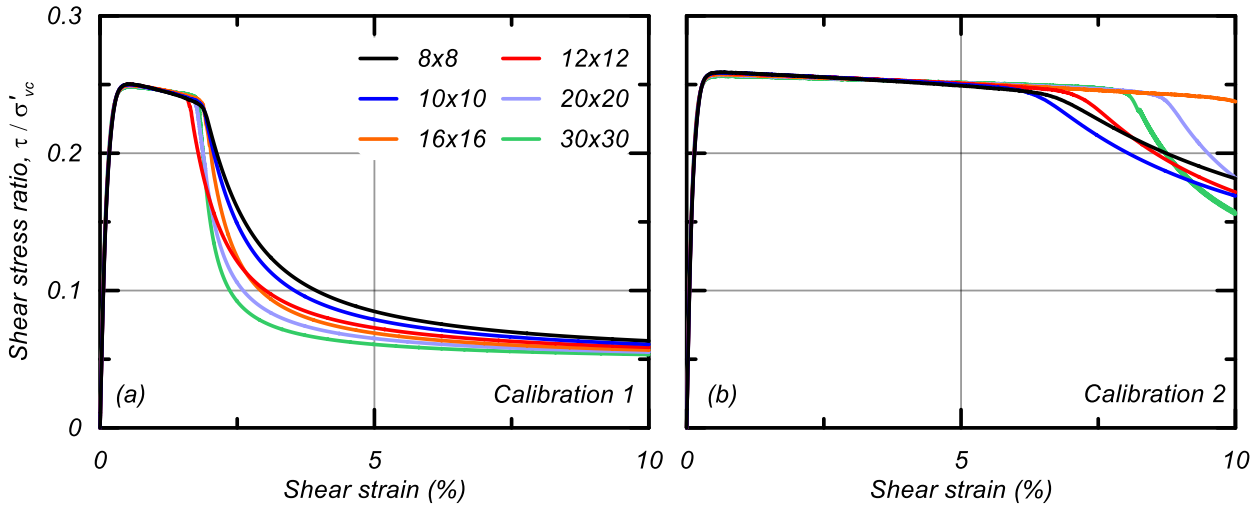

Figure 3-7: Stress-strain responses illustrating mesh dependency of (a) Calibration 1 and (b) Calibration 2

The dependency of the stress-strain responses on the rate of stress relaxation and the evolution of the internal strain rate is illustrated in Fig. 3-8 for simulations of Calibration 1 with a 10x10 mesh consolidated to a σ'_{vc} = 101.3 kPa and K_o = 0.5 loaded in DSS with varying θ_{ref} (Fig. 3-8a) and β_{ref} (Fig. 3-8b) values. The global shear strain at the onset of localization decreases slightly with an increasing θ_{ref} value, decreasing from about 2% shear strain for θ_{ref} values of 0.5 and 0.9 to about 1.7% for θ_{ref} values of 0.95 and 0.98 (Fig. 3-8a). This change in global strain at the onset of localization is similar to the change observed for the different mesh sizes in Fig. 7. The global strain at the onset of localization decreased with an increasing β_{ref} (Fig. 3-8b). Increasing β_{ref} from 0.99 to 0.999 decreased the shear strain at localization from approximately 2.8% to 1.8%. The above ranges for

θ_{ref} and β_{ref} values envelop the ranges previously found to produce constitutive responses consistent with observed experimental results for a range of loading conditions.

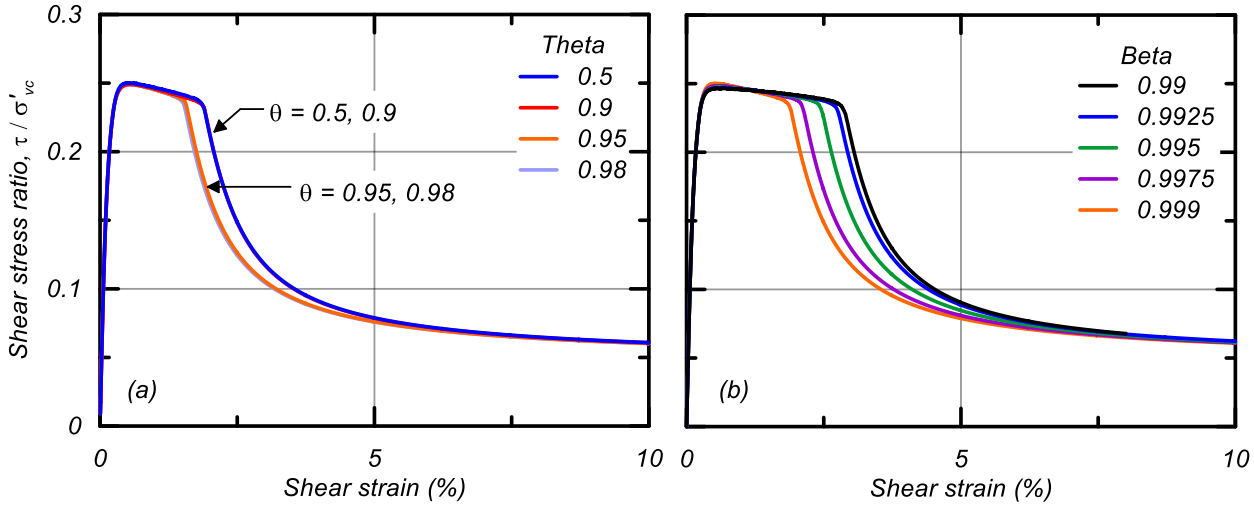

Figure 3-8: Stress strain responses of 10x10 grid simulations of Calibration 1 with varying (a) θ_{ref} values and (b) β_{ref} values

These results illustrate that the solution has some degree of sensitivity to the numerical methods, although the effects are small enough that parametric analyses can still be expected to provide insights on response patterns. Subsequent parametric analyses are based on a 10 x 10 square grid, θ_{ref} = 0.5, and a β_{ref} = 0.999. The impacts of potential uncertainties on the overall findings are discussed later.

3.4.2 Relating Effects of Viscoplasticity and Strain-Softening

The global strain at the onset of localization in a uniform specimen is dependent on the offsetting effects of the soil's viscoplastic and strain-softening behaviors, as illustrated conceptually in Fig. 3-9. The local stress-strain response can be idealized as three distinct phases: (1) prior to global peak strength mobilization, (2) during localization development, and (3) after the onset of localization. In the first phase, the stress-strain response in the potential localization is the same as the global stress-strain response as

the deformation is uniform within the specimen (Figs. 3-6 and 3-9). In the second phase, which begins at the mobilization of global peak strength, the strains begin to concentrate within the eventual localization zone, which increases the local strain rate and produces an associated increase in shear resistance. This increase in shear resistance due to the increased strain rate offsets the concurrent decrease in shear resistance due to post-peak strain-softening. These offsetting effects allow the soil to continue shearing at approximately the same global shear stress. The second phase continues until the increase in shearing resistance from the increased strain rate is no longer sufficient to offset the loss of shearing resistance due to strain-softening (damage), at which point the localization fully develops and the third phase begins. In the third phase, all displacements accumulate within the localization, and the global stress-strain response is controlled by the local stress-strain response within the localization.

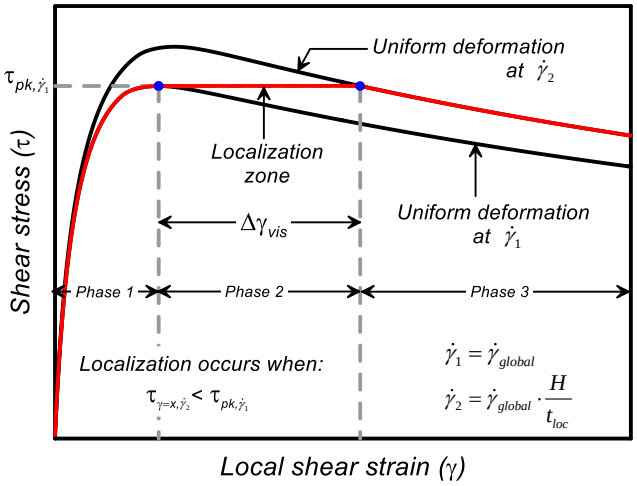

Figure 3-9: Framework for predicting the onset of localization and the idealized stress – strain response of a potential shear band

The global strain at the onset of localization can be approximately estimated by equating the offsetting effects illustrated in Figs. 3-9 and 3-10 (herein expressed for DSS loading). A strength increase (SI) parameter is used to describe the strain rate

dependency, expressed in a linearized form over an order of magnitude increase in strain rate as:

$$SI = \frac{\tau_{pk,10\cdot\dot{\gamma}_1} - \tau_{pk,\dot{\gamma}_1}}{\tau_{pk,\dot{\gamma}_1}} \cdot \frac{1}{\log 10\dot{\gamma}_1 - \log \dot{\gamma}_1} \cdot 100\% = \frac{\tau_{pk,10\cdot\dot{\gamma}_1} - \tau_{pk,\dot{\gamma}_1}}{\tau_{pk,\dot{\gamma}_1}} \cdot 100\% \quad (3\text{-}1)$$

where $\tau_{pk,10\cdot\dot{\gamma}_1}$ is the peak shear stress mobilized when sheared at a strain rate one order of magnitude greater than the global (average) applied rate and $\tau_{pk,\dot{\gamma}_1}$ is the peak shear stress when sheared at the global applied strain rate. The SI is defined using base-10 logarithm so the reported value is consistent common practice for describing rate effects; i.e., SI = 9% means a 9% increase in undrained strength per order of magnitude increase in strain rate. A post-peak strain-softening rate (SR) parameter is used to describe the soil's (local) average reduction in shearing resistance per 1% shear strain averaged over the first five percent shear strain after mobilization of peak shear stress as:

$$SR = \left(\frac{\tau_{pk} - \tau_{\gamma_{\tau_{pk}}+5\%}}{\tau_{pk}} \right) \cdot \frac{100\%}{5\%} \quad (3\text{-}2)$$

where τ_{pk} is the peak shear stress at the applied rate (i.e., local response from single element simulation) and $\tau_{\gamma_{\tau_{pk}}+5\%}$ is the shear stress after an additional 5% shear strain. The difference in the global strains at peak shear resistance versus at the onset of localization is the delay due to viscoplasticity ($\Delta\gamma_{vis}$), as shown in Fig. 3-10b,

$$\Delta\gamma_{vis} = \gamma_{Lz} - \gamma_{\tau_{pk}} \quad (3\text{-}3)$$

where $\gamma_{\tau_{pk}}$ is the shear strain (global) at peak shear resistance and γ_{Lz} is the shear strain (global) at the onset of localization. When the localization fully forms (end of phase two) with thickness t_{loc}, the incremental shear strains and shear strain rate in the localization will be greater than the applied global shear strain and shear strain rate values by a factor of approximately H/t_{loc} where H is the specimen thickness. The end of phase 2 can be estimated by equating the increase in shearing resistance from strain rate effects with the decrease in shearing resistance at localization due to strain-softening, which has the following solution if the ratio of local to global incremental strains remains equal to H/t_{loc} throughout phase two:

$$\frac{\tau - \tau_{pk,\dot{\gamma}_1}}{\tau_{pk,\dot{\gamma}_1}} = SI \cdot \log\left(\frac{\dot{\gamma}_{loc}}{\dot{\gamma}_1}\right) - SR \cdot \Delta\gamma_{loc} = 0 \tag{3-4}$$

$$SI \cdot \log\left(\frac{H}{t_{loc}}\right) - SR \cdot \left(\Delta\gamma_{vis} \cdot \frac{H}{t_{loc}}\right) = 0 \tag{3-5}$$

$$\Delta\gamma_{vis} = \frac{SI}{SR} \cdot \frac{\log\left(H/t_{loc}\right)}{H/t_{loc}} = f\left(\frac{SI}{SR}\right) \tag{3-6}$$

where $\Delta\gamma_{loc}$ is the additional local strain within the localization. This functional form illustrates how $\Delta\gamma_{vis}$ is expected to depend on SI and SR, but it does not account for the more complex evolution of local and global incremental strains and strain rates throughout loading or the progressive change in rate of strain-softening (i.e., SR is a secant value, whereas the slopes of the stress-strain curves decrease with increasing shear strain during softening). Consequently, alternative versions of this functional form are shown later to better fit the parametric analysis results described below.

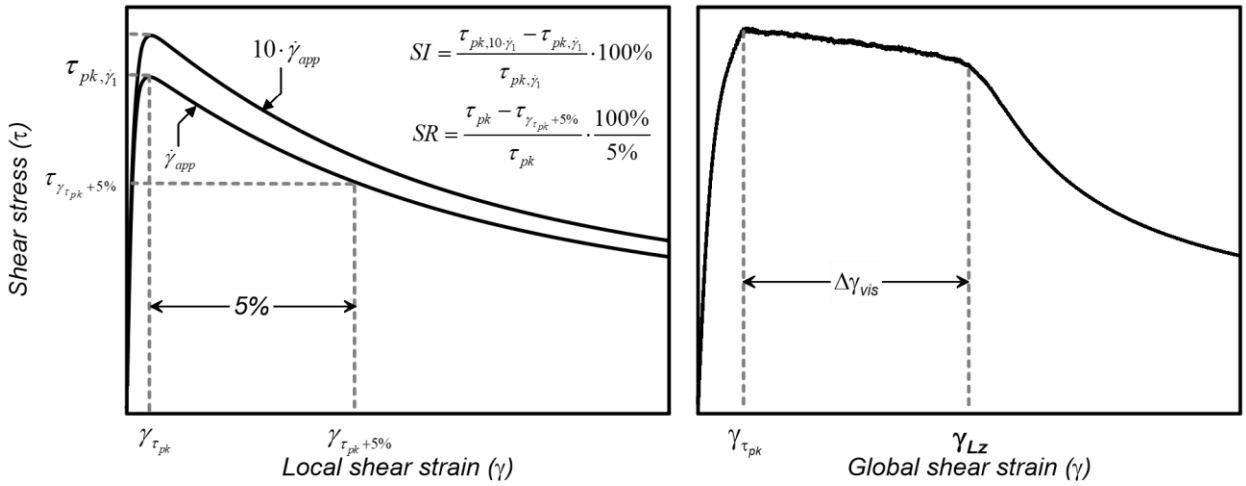

Figure 3-10: Schematic of (a) SR and SI and (b) $\Delta\gamma_{vis}$

3.5 Parametric Analyses

Parametric analyses were performed to observe the influence of SI and SR on $\Delta\gamma_{vis}$ over a broad range of conditions. SI for the simulated responses was varied using PM4SiltR's rate dependency parameters (F_p and F_M). The viscous parameters F_p and F_M were varied from 0.0 to 0.175 in increments of 0.025. For each value, simulations were performed with rate dependence mechanisms of F_p only, F_M only, and $F_M = F_p$ to investigate the influence of the mechanism of induced rate dependency. A range of SR values was provided by the six PM4SiltR calibrations shown in Fig. 3-3. Applied strain rates of 1, 100, and 10,000 times the reference strain rate were used (i.e., SRR of 0, 2, and 4). A total of 378 parametric combinations (21 SI values, 6 SR values, 3 loading rates) were used.

Each parametric combination was used in two single element simulations and one 10x10 grid simulation. Grid simulations were performed to global shear strains of up to 50% to extract $\gamma_{\tau_{pk}}$ and γ_{loc} to obtain $\Delta\gamma_{vis}$. The two single element simulations were performed at SRR=N and SRR=N+1 (with N = 0, 2 and 4) to obtain the SI for each

parametric combination; The single element simulation at SRR=N was also used to obtain the SR and $\tau_{pk,\dot{\gamma}_{app}}$.

The parametric combinations produced SR of 0 – 10% and SI of 0 – 25%, as shown by the plot of SI versus SR for the six calibrations in Fig. 3-11. Each calibration produced SR values that generally fell in narrow separate bins, although there was some overlap across bins from simulations with large F_p and F_M values. The points that correlate with a vertical line for each calibration in Fig. 3-11 represent simulations with an SRR = 0 as the stress-strain response is identical for all simulations loaded at the reference rate (SRR=0). With SRR = 2 and 4, simulations with only $F_p > 0$ produced smaller SR while simulations with only $F_M > 0$ produced larger SR. The SR for simulations with both F_p and $F_M > 0$ depended on the magnitude of the parameters and imposed strain rate. Fig. 3-11 illustrates the broad range of SI and SR values produced by the parametric analysis.

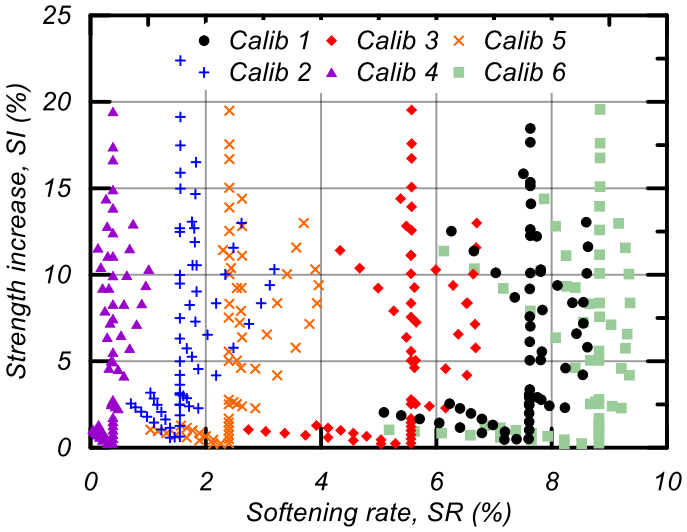

Figure 3-11: SI versus SR from parametric analyses

The global strain at the onset of localization in grid simulations can be visually determined with reasonable accuracy by the sharp break in the global stress-strain

response (e.g., Fig. 3-7), but numerical criteria were nonetheless established to eliminate subjectivity. Two indices that compared the strain accumulation rates within individual rows of the DSS grid were computed; strain rates in each element were approximately equal along each row, so the middle element was used as representative of its row. First, shear strain rates were computed over windows of 0.05% global shear strain. The first index identified the onset of localization as the first global strain-step at which more than three rows were elastically unloading (i.e., the local strain rates were opposite to the global strain rate). The second index identified the onset of localization as the first global strain step at which only one row had a local strain rate greater than 90% of the global applied strain rate. The global shear strain at the onset of localization was selected to be the smaller of the shear strains identified by these two indices. Generally, the first index governed except for those cases with the very small SR values. Visual observation of the simulated stress-strain responses confirmed that the combination of these two indices provided accurate and repeatable values for the global strain at the onset of localization.

The $\Delta\gamma_{vis}$ from the simulations ranged from approximately 0 – 50%. Figure 3-12 shows $\Delta\gamma_{vis}$ versus SR (Fig. 3-12a) and SI (Fig. 3-12b) for each of the six calibrations. These plots illustrate that $\Delta\gamma_{vis}$ can vary widely for any given SI and SR, although $\Delta\gamma_{vis}$ generally decreased with increasing SR (Fig 3-12a). Simulations using Calibration 4 with large SI values did not localize before reaching 50% shear strain in 22 cases, such that these cases only provide a lower limit on the possible value for $\Delta\gamma_{vis}$. These non-localized cases are plotted at the lower limits they imply for $\Delta\gamma_{vis}$ in Figs 3-12a and 3-12b, where there are identified by the gray shaded zones.

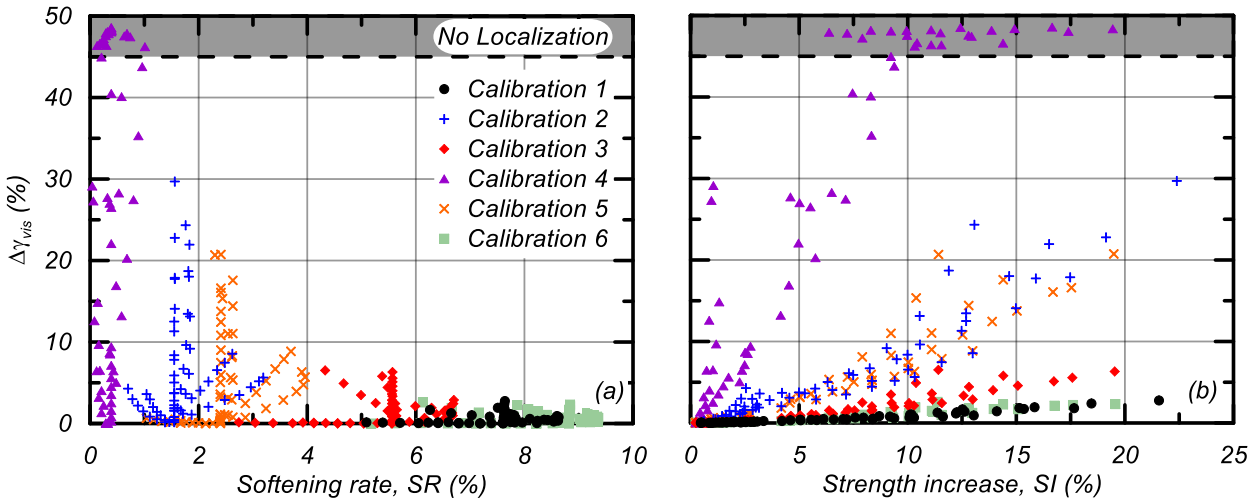

Figure 3-12: $\Delta\gamma_{vis}$ versus (a) SR and (b) SI

3.6 Relating Softening Rate and Strength Increase with Delay in Onset of Localization

A regression model for $\Delta\gamma_{vis}$ was developed using the simulation dataset for cases with $0.1\% \leq \Delta\gamma_{vis} \leq 20\%$. Cases with $\Delta\gamma_{vis}$ smaller than 0.1% or greater than 20% were evaluated against the regression model, but the emphasis was optimizing the model for $\Delta\gamma_{vis}$ in the 0.1% to 20% range. Several regression models with alternative functional forms, number of constants, and transformations were evaluated. The best results were obtained using a version of the functional form in Eq. 6 as:

$$\Delta\gamma_{vis} = C_1 \cdot \left(\frac{SI}{SR}\right)^{C_2} \tag{3-7}$$

where C_1 and C_2 are fitting parameters. Regression was performed using natural logarithmic transforms of SI and SR as,

$$\ln\left(\Delta\gamma_{vis}\right) = \ln\left(C_1\right) + C_2 \ln\left(SI\right) - C_2 \ln\left(SR\right) \tag{3-8}$$

with the result being $C_1 = 0.8$ and $C_2 = 1.5$. The predicted $\Delta\gamma_{vis}$ (regression model results) are plotted versus the observed $\Delta\gamma_{vis}$ (grid simulation results) in Fig. 3-13, along with lines for the regression model best fit and at plus/minus one or two standard deviations (σ). The residuals in $\ln(\Delta\gamma_{vis})$ (i.e., observed minus predicted values) are plotted versus the observed $\Delta\gamma_{vis}$ and the predictor variables SI and SR in Figs. 3-14a, 3-14b, and 3-14c, respectively. The residuals are approximately normally distributed with $\sigma = 0.33$ as shown by the cumulative distribution function shown in Fig. 3-15 and have no significant trends with regard to the predictor variables. The regression lines at $\pm\sigma$ in Fig. 3-13 therefore correspond to the expected value for $\Delta\gamma_{vis}$ multiplied/divided by a factor of 1.39 (i.e., e^{σ}). The data points for $\Delta\gamma_{vis}$ smaller than 0.1% or greater than 20% are also reasonably predicted by the regression model, as shown in Figs. 3-13 and 3-14, despite being excluded from the dataset used for regression.

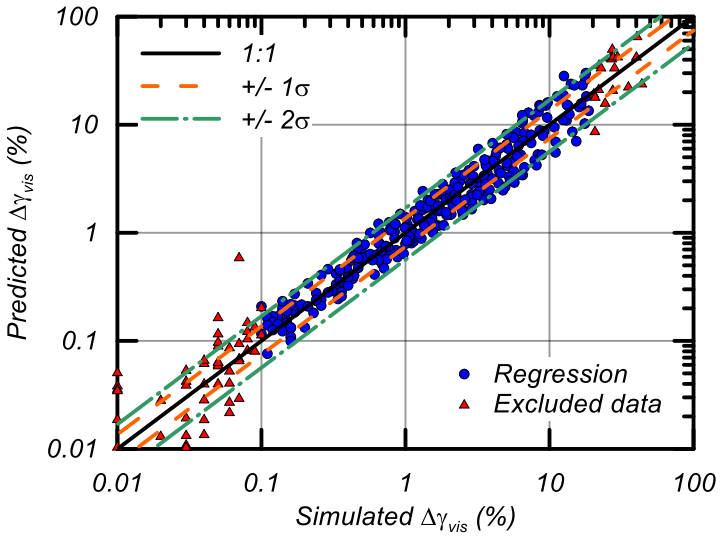

Figure 3-13: Predicted versus simulated $\Delta\gamma_{vis}$

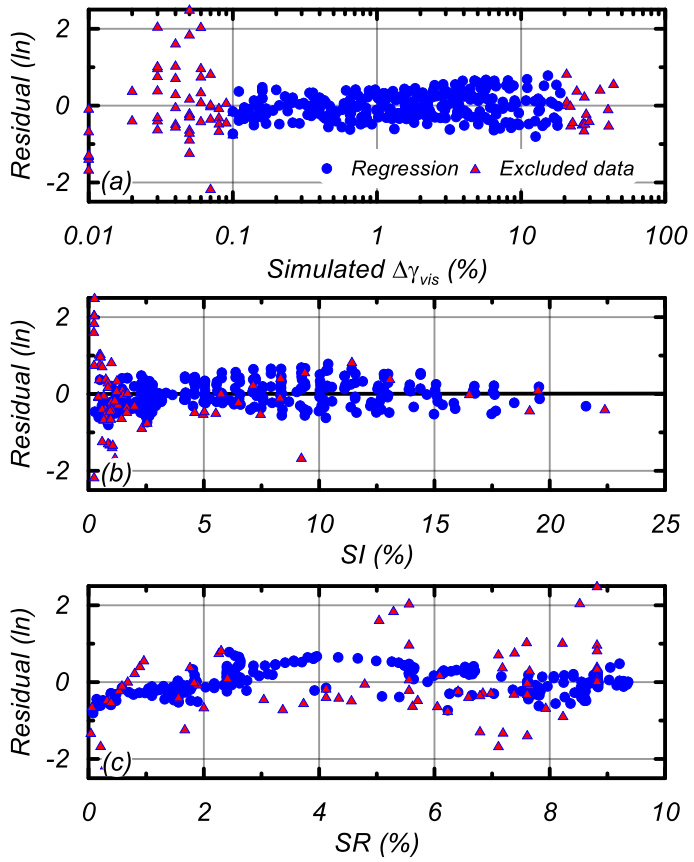

Figure 3-14: Residuals versus (a) $\Delta\gamma_{vis}$, (b) SI, and (c) SR

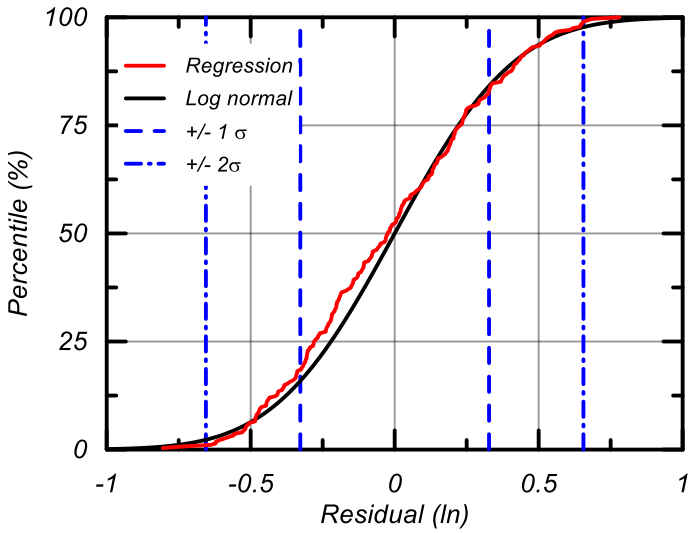

Figure 3-15: Cumulative density function of logarithmic transformed residuals

3.7 Discussion

The regression model inherits the assumptions and limitations of the numerical simulations. The analyses considered a perfectly uniform material which is unlikely to be encountered in the field. In a uniform specimen, the concentration of strain does not begin until the entire specimen has mobilized the peak strength. In a non-uniform specimen, strain concentration begins when the weakest material reaches its peak strength. Depending on the strength of the weak layer and the stiffness of the stress-strain response, strain concentration may begin to occur at a strain level lower than the strain at which a uniform deposit would mobilize peak strength. The influence of these potential imperfections in natural deposits on the onset of localization must be assessed (Oathes and Boulanger 2020). In practice, this assessment should be performed prior to both setting the mesh discretization and determining how localization length scales will be accounted for.

Predictions using the regression model appear to compare favorably with observations of laboratory tests with and without observed localization. The experiments on NC B-6 clay in Fig. 3-1a (Lefebvre and LeBouef 1987) extend to approximately 9% axial strain for all applied loading rates without exhibiting signs of a localization developing and the test descriptions did not discuss any occurrence of localizations. Applying the regression with SI = 15% and SR = 2.4%/% (based on the experiments) predicts a $\Delta\gamma_{vis}$ ~12.5% which is consistent with the lack of localization being reported or discussed in these experiments. The experiments on Tiller clay in Fig. 3-1b (Gylland et al. 2014) developed localizations. For the test loaded at 3%/hr the localization initiated at ~1.25% global axial strain and fully developed at a global axial strain of ~4.25%. Applying the

regression with SI = 4% and SR = 10% (from the experiments) predicts the onset of localization at 1.7% which is reasonably consistent with the observed results (~3%). Similar comparisons for the Gylland et al. (2014) test loaded at 30%/hr showed initiation of localization at 2% axial strain and full development of the localization at 4.5% axial strain. The regression predicts onset of localization at ~2.75% axial strain for this experiment with an associated SI = 15% and SR = 11%, consistent with reported experimental results (~2.5%). These three comparisons illustrate that the regression appears consistent with experimental observations for the onset of localization, although a more systematic compilation of experimental data is required to adequately assess the regression model.

Pre-existing shear bands or weak layers within a soil deposit from depositional history, landslides, or other loading events, can be relatively thin in comparison to the overall deposit thickness. The identification of pre-existing shear bands tends to rely on investigations into historical records or site investigation data. Common site investigation tools provide either visual identification of small portions of the soil column (i.e., SPT) or continuous logging of the entire soil column without visual identification of the soil (i.e., CPT). Both methods may not identify the weakest layers as the weakest layer may fall between samples in the SPT or thin layer effects may mask the weakest layer in a CPT. Other site investigation tools allow for the visual identification of the entire soil column (i.e., sonic logging) but do not provide the sample quality required for strength testing. An overlooked shear band can result in strength loss occurring at displacements smaller than would be expected in the absence of a shear band.

The developed regression model for $\Delta\gamma_{vis}$ provides an estimate for when a localization may develop, however the results must still be implemented in a dynamic analysis using a length scale or similar methodology given practical limitations on mesh dimensions for many applications. Applying the regression necessitates assessing SI and SR, which can be complicated by limitations in laboratory and field testing as well as natural variability. Experimental programs to obtain these values are likely to be more expensive than traditional testing programs. Despite these and other practical challenges, the regression model provides an initial basis for estimating or evaluating the range of strains over which localizations may be expected to develop in strain-softening, rate-dependent soils.

There are relatively few case histories of failures resulting from earthquake-induced ground deformation in soft clays suggesting that fully remolded strength losses and associated localizations may not be easily triggered in the field depending on the soil characteristics. The compensating factors that affect dynamic response and contribute to the accumulation of deformation in geotechnical structures affected by cyclic softening of clays during earthquakes complicate the development of approaches for estimating potential strength losses. Further work is needed to develop and validate methodologies for modeling strain-softening clays and plastic silts under earthquake loading.

3.8 Conclusion

The effects that viscoplasticity has on localization processes in sensitive, saturated clays and plastic silts were evaluated by numerically simulating monotonic, undrained, direct simple shear tests using FLAC 8.1 (Itasca 2019) with the user-defined viscoplastic constitutive model PM4SiltR (Boulanger et al. 2022). Parametric analyses demonstrated

that the global strain at which a localization forms in a strain-softening clay is primarily dependent on the magnitude of the soil's strain rate-dependency relative to its rate of post-peak strain-softening. The parametric results were used to develop a regression model that relates the global strain at the onset of localization to the soil's strain rate-dependency and post-peak strain-softening rate. The regression model appears consistent with experimental observations, although a systematic compilation of experimental data for localization processes is required to assess its accuracy. Nonetheless, the results indicate that the inclusion of reasonable levels of viscoplasticity can be expected to significantly increase the global strain that can develop before a localization forms in clays and plastic silts with modest strain-softening rates.

Evaluating the potential for strength loss and localization in sensitive, saturated clays and plastic silts is complicated by numerical issues (e.g., dependency on mesh discretization, numerical solution parameters, internal length scales), experimental challenges (e.g., boundary conditions, stress and pore pressure non-uniformity, internal local drainage), and practical issues (e.g., spatial variability, sample disturbance, competing effects of creep and consolidation). The potential for strength loss during earthquake loading is further complicated by the effects of cyclic degradation, initial static shear stresses, and ground motion variability. The results of the present study suggest that viscoplastic characteristics of saturated clays and plastic silts are another important factor influencing their responses to earthquake loading and should be considered in future efforts toward developing and validating design methodologies.

3.9 Acknowledgements

The work described herein was supported by the California Department of Water Resources under Contract 4600009751. Any opinions, findings, or recommendations expressed herein are those of the authors and do not necessarily represent the views of this organization. The authors appreciate the above support.

Chapter 4 : Nonlinear Viscoplastic Modeling of the Feijão Dam 1 Failure

Original publication:

Oathes, T.J., and Boulanger, R.W. (To be submitted). "Nonlinear viscoplastic modeling of the Feijão Dam 1 Failure." ASCE Journal of Geotechnical and Geoenvironmental Engineering.

Abstract

Two-dimensional viscoplastic nonlinear analyses of the 2019 Feijão Dam 1 failure in Brazil are performed using the finite difference program FLAC 8.1 with the user-defined constitutive models PM4SiltR and PM4Sand. A brief history of Feijão Dam 1, its failure, and the conflicting findings from two previous independent failure investigations are summarized. The present study uses the site characterization from those prior studies to develop the dam cross section, obtain material index properties, and establish groundwater conditions, but uses alternative techniques for characterizing undrained shear strengths. Simulations show that the dam was marginally stable against long-term consolidated, undrained conditions and that modest loading changes were sufficient to trigger failure with deformation patterns consistent with the observed failure. Simulations further show that collapse could have been triggered by a modest wetting event causing an increase in water contents and loss of suction above the phreatic surface, by ongoing drilling activities causing a localized loss of shear strength in the tailings, or a combination of both mechanisms. Sensitivity of the results to choices in the calibration process and the numerical solution scheme are discussed. The implications of these results on the

interpretation of the Feijão Dam 1 failure and long-term slope stability assessment procedures in practice are discussed.

4.1 Introduction

Feijão Dam 1 was an 86-meter tall tailings impoundment located at the Córrego de Feijão Mine in Brumadihno, Minas Gerais, Brazil that suffered a catastrophic failure on January 25th, 2019. The impoundment was constructed using the upstream construction method. By-products of mine operations (tailings) were placed behind the embankment using the hydraulic fill method. The embankment was primarily composed of compacted tailings and the structure was founded on native clayey soil. Negligible deformations were observed prior to the failure. Collapse of the dam occurred within approximately 5 seconds of initial deformations being observed. The failure surface appeared to develop within the impounded tailings and did not go through the foundation. The failure resulted in more than 250 deaths and significant economic and environmental costs (Vergilio et al. 2020). Characteristics of the tailings impoundment and subsequent investigations into the failure are provided in two reports (Robertson et al. 2019 and Arroyo and Gens 2021). Robertson et al. (2019) concluded that (1) the failure was triggered by a combination of internal creep and loss of suction in the unsaturated zone due to heavy rainfall in late 2018, and (2) the drilling that was in progress at the time of the failure could not have triggered the collapse. Arroyo and Gens (2021) concluded that (1) internal creep and the effects of increased precipitation, alone or in combination, would not have triggered collapse, and (2) drilling of borehole B1-SM-3 potentially triggered the collapse. Thus, these two studies reached opposing conclusions regarding mechanisms that may or may not have triggered the collapse.

Performing stability assessments of earthen structures, such as dams and tailings impoundments, requires accounting for all potential loading conditions and failure modes as well as understanding potential limitations of the analyses. However, Shewbridge (2019) noted that several significant texts do not consider long-term, consolidated, undrained static conditions in stability assessments, although several significant failures have occurred under these conditions (e.g., Feijão Dam 1). Analysis methods range from limit equilibrium methods (LEM) to more complex nonlinear analyses using finite element or finite difference methods depending on system complexity and the consequences of a failure. LEMs can provide an assessment of structure stability but are generally unable to identify potential failure mechanisms as those depend on complex soil behaviors such as strain-softening, viscous effects, and progressive failure. Systems in which the failure mechanism is critical or whose failures have the potential for major consequences often necessitate the use of nonlinear analyses. Zabolotnii et al. (2022) highlighted the importance of nonlinear analyses in capturing the progressive failure observed in the Mount Polley Tailings Storage Facility failure and the influence of localization in the analyses of systems involving strain-softening materials. Nonlinear analyses of long-term, undrained stability rely on advanced constitutive models capable of approximating soil behaviors important to a specific system's performance. There remains a need for further development, implementation, and validation of constitutive models to account for complex aspects of undrained, plastic soil behavior. The development of PM4SiltR (Oathes et al. 2022) and its ability to evaluate the static stability of plastic silts and clays provides an opportunity to reevaluate the possible role of creep in the Feijão Dam 1 failure.

This paper presents the results of two-dimensional (2D) viscoplastic nonlinear analyses of the 2019 Feijão Dam 1 failure in Brazil using the finite difference program FLAC 8.1 with the user-defined constitutive models PM4SiltR and PM4Sand (Boulanger et al. 2022, Ziotopoulou and Boulanger 2016). A brief history of Feijão Dam 1, its failure, and the subsequent failure investigations as described by Robertson et al. (2019) and Arroyo and Gens (2021) are summarized. The present study uses the site characterization by Robertson et al. (2019) to develop the dam cross section, obtain material index properties, and establish groundwater conditions, but uses alternative techniques for characterizing undrained shear strengths. Simulations showed that the dam was marginally stable against long-term consolidated, undrained conditions and that modest loading changes were sufficient to trigger failure with deformation patterns consistent with the observed failure. Simulations further show that collapse could have been triggered by a modest wetting event causing an increase in water contents and loss of suction above the phreatic surface, by the ongoing drilling activities causing a localized loss of shear strength in the tailings, or a combination of both mechanisms. Sensitivity of the results to choices in the calibration process and the numerical solution scheme are discussed. The implications of these results on the interpretation of the Feijão Dam 1 failure and long-term slope stability assessment procedures in practice are discussed.

4.2 History and Failure of Feijão Dam 1

Feijão Dam 1 was an approximately 86-meter tall tailings impoundment with a 720-meter long crest located in Brumadihno, Minas Gerais, Brazil at the Córrego de Feijão Mine. The dam was constructed over 37 years beginning in 1976 in ten raises with heights varying from 5-meter to 18-meter using the upstream construction method (Robertson et

al. 2019). The fourth raise was setback relative to the first three raisings which reduced the overall slope of the dam but moved the upper portion of the dam over weaker, finer tailings. The dam was constructed by multiple construction companies and designed by five engineering firms. Construction was completed in 2013 and tailings deposition ceased in July 2016 with the final constructed slope shown in Fig. 4-1a. The dam slope ranged from 1.5H:1V to 2.5H:1V with most raisings having a 2H:1V slope. The impoundment was founded on a native clay layer and the raisings generally consisted of compacted tailings behind which tailings were deposited using the hydraulic fill method (Robertson et al. 2019). Deposited tailings consisted of interbedded fine and coarse tailings near the face of the dam and a very soft slime in the pond region.

Figure 4-1: Feijão Dam 1 (a) looking north prior to failure (Google Earth via Robertson et al. 2019) and (b) after failure (Robertson et al. 2019)

On January 25, 2019, Feijão Dam 1 suffered a rapid collapse resulting in the release of approximately 9.7 million cubic meters of retained tailings, nearly 75% of the

total retained material. The dam after failure is shown in Fig. 4-1b. The failure resulted in more than 250 deaths and environmental impacts that reached nearly 300 km downstream (Vergilio et al. 2020) and contributed to the development of the Global Industry Standard on Tailings Management (Oberle et al. 2020). The failure surface extended from the crest to just above the toe (near the top of the first raising). Full collapse occurred within seconds of the first observed deformations. The initial failure surface appeared to be relatively shallow with retrogressive slip-surfaces developing further into the retained materials.

Negligible deformations were observed prior to the failure based on survey, inclinometer, ground-based radar, satellite (InSAR), and drone video data (Robertson et al. 2019). The survey and inclinometer data indicated no discernable trends in the measurements. Analyses of InSAR data indicated that downward deformations near the crest and mid-slope of the dam were no greater than 30 mm/year increasing to approximately 36 mm/year in the lower central region of the dam. InSAR analysis paired with rainfall data indicated that deformations may have increased slightly during the wet season. Robertson et al. (2019) concluded that the tailings were fully consolidated and that the observed deformations were likely the result of ongoing internal creep and not indicative of an imminent failure.

The Expert Panel Report (EPR) prepared by Robertson et al. (2019) summarized their investigations, analyses, and findings. The EPR utilized a stochastic state parameter-based approach for estimating strengths of the fine and coarse tailings in their analysis. Critical state properties were established through laboratory testing, generally on reconstituted samples, and state parameter distributions were developed from CPT

profiles using three different methodologies for the tailings (Jefferies and Been 2016, Robertson 2009, and Plewes 1992). Forty stochastic realizations of state parameter distributions in the dam were developed. The static Factors of Safety (FS) for these forty realizations ranged from 0.5 to 2.2 using peak undrained shear strengths ($s_{u,pk}$) with the Shear Strength Reduction Method (SSRM). Four stochastic realizations with FS of 1.0 to 1.16 were selected for further analyses. The shear strengths in these selected realizations were further reduced to obtain a FS of 1.0. Potential failure triggers were applied to the modified, marginally stable realizations in nonlinear analyses using FLAC 2D and 3D. Results indicated that the failure was due to brittle strengths in the tailings coupled with ongoing internal creep and a loss of suction due to seasonal wetting. The EPR eliminated ongoing drilling operations as a potential mechanism for triggering the collapse. The EPR further eliminated tailings deposition, dam construction, earthquakes, blasting, fatigue loading, internal erosion and piping, human interaction, and underground springs.

A second report by CIMNE (Arroyo and Gens 2021) was commissioned by Vale (mine operator) in conjunction with Brazilian authorities. Their analyses also utilized a state-parameter based approach for estimating strengths of the fine and coarse tailings. Critical state properties were developed from laboratory testing, generally on reconstituted samples, and state parameter variability was developed using two CPT methodologies (Shuttle and Cunning 2007 and Jefferies and Been 2015). The state parameter distributions were developed using weighted averaging of CPT data. Additionally, CIMNE performed a series of nine triaxial compression tests at varying strain rates (0.002 mm/min, 0.02 mm/min, and 0.2 mm/min) on reconstituted tailings specimens to investigate the strain rate dependency over three orders of magnitude of strain rate.

The average change in undrained strength per order of magnitude change in strain rate was 2%. The foundation was modeled as elastic. Nonlinear analyses were performed in PLAXIS (PLAXIS 2019) using the rate-independent Clay and Sand Model (CASM) that was modified to capture viscous effects (CASM-visco). Analysis results indicated that ongoing drilling operations caused the failure. CIMNE eliminated internal creep and wetting induced loss of suction as the potential trigger mechanism. CIMNE also eliminated blasting, earthquakes, loss of support, and construction traffic as potential triggers.

4.3 Material Characterization

The analyses presented herein utilized the subsurface cross-section shown in Fig. 4-2, as developed in the EPR. The cross-section includes five materials: coarse tailings, fine tailings, slime, embankment, and foundation. Index properties and drained strengths were generally taken as reported in the EPR. Undrained strengths were reexamined using the available laboratory test and CPT data, as discussed below. Material properties used in the present analyses are listed in Table 4-1.

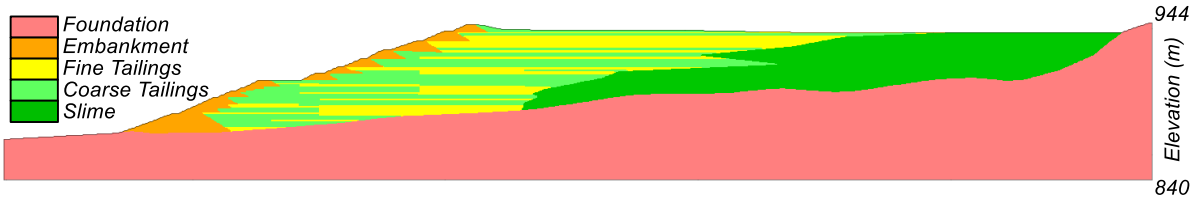

Figure 4-2: Feijão Dam 1 Section 3-3' after Robertson et al. (2019)

Table 4-1: Selected soil properties

Properties	Coarse Tailings	Fine Tailings	Slime	Embankment	Foundation
$s_{u,pk}/\sigma'_{vc}$	0.29	0.21	0.16	N/A	0.5
$s_{u,rem}/\sigma'_{vc}$	0.09	0.05	0.04	N/A	0.5
ρ (kg/m^3)[1]	2265	1898	2014	1863	1898
K_h (cm/sec) [1]	$5.0 \cdot 10^{-4}$	$1.0 \cdot 10^{-5}$	$1.0 \cdot 10^{-6}$	$1.2 \cdot 10^{-4}$	$9.3 \cdot 10^{-5}$
K_v (cm/sec) [1]	$1.0 \cdot 10^{-4}$	$2.0 \cdot 10^{-6}$	$2.0 \cdot 10^{-7}$	$1.2 \cdot 10^{-4}$	$9.3 \cdot 10^{-5}$
PI[1]	0	4	18	4	18
Porosity[1]	0.5	0.59	0.49	0.30	0.31

[1]Taken as characterized in Robertson et al. 2019

The interlayering and distinct differences of the coarse and fine tailings are illustrated by the data for B1-CPTU-01 from the EPR in Fig. 4-3, showing profiles for (a) cone tip resistance (q_t), (b) friction ratio (R_f), (c) pore pressure behind the tip (u_2), and (d) interpreted stratigraphic units. The fine tailings are identified by their smaller q_t values and larger R_f and u_{bt} values, which results in a clay-like soil behavior classification (Robertson 2016). The q_t values in the fine tailings increase approximately linearly with depth, which is consistent with a normally consolidated profile of clay-like soil. The coarse tailings are identified by their larger q_t values and smaller R_f and u_{bt} values, which results in a sand-like soil behavior classification.

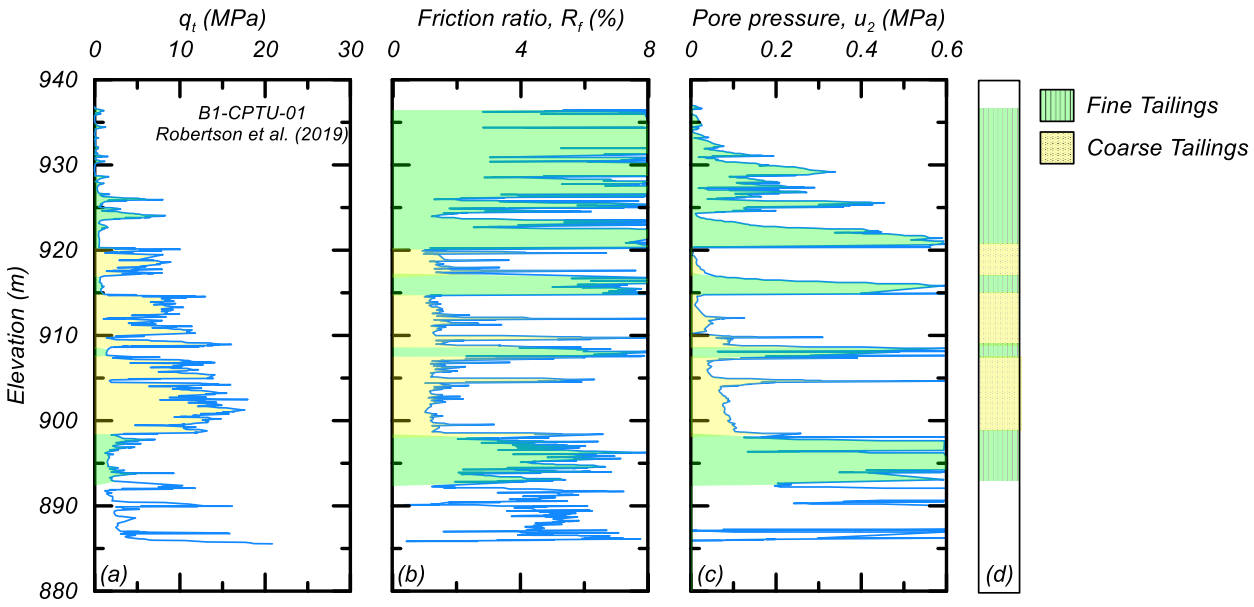

Figure 4-3: Profile of B1-CPTU-01 showing (a) cone tip resistance (q_t), (b) friction ratio (R_f), (c) pore pressure (u_2), and (d) delineation of materials (after Robertson et al. 2019)

The fine tailings properties were characterized using data from the EPR and analysis of CPT data. The undrained strength (s_u) of the fine tailings was estimated through a combination of CPT data interpretation, laboratory test data, and empirical correlations for low plasticity silts and clays. CPT data digitized from the EPR is summarized in Fig. 4-4 showing profiles of (a) q_t, (b) u_{bt}, (c) total vertical stress (σ_v), (d) $s_{u,pk}$, (e) peak undrained strength ratio ($s_{u,pk}/\sigma'_{vc}$), and (f) sensitivity (S_t). The $s_{u,pk}$ was estimated using an N_{kt} of 9 based on correlations for brittle soils and N_{kt} values from other studies on tailings (Martin et al. 2002, Mayne and Peuchen 2018, and Paniagua et al. 2019). The S_t was estimated using sleeve friction correlations (Nader et al. 2015) and the limited number of field vane results showing a S_t of approximately 4. The $s_{u,pk}/\sigma'_v$ of the fine tailings for DSS loading was characterized as 0.21 with a S_t of 4. Larger N_{kt} values that are often used for less brittle, sedimentary materials (~12-14) would result in $s_{u,pk}/\sigma'_{vc}$ of approximately 0.15 to 0.17, which is lower than expected for most low plasticity fine-

grained materials. The small-strain stiffness was taken as characterized in the EPR based on dilatometer data. The fine tailings had a density of 1898 kg/m^3, a porosity of 0.59, a plasticity index (PI) of 4, a liquid limit (LL) of 21, a fines content (FC) of 71%, and generally a USCS classification of ML. The vertical (k_y) and horizontal (k_h) hydraulic conductivities were $2.0 \cdot 10^{-6}$ and $1.0 \cdot 10^{-5}$ cm/sec respectively.

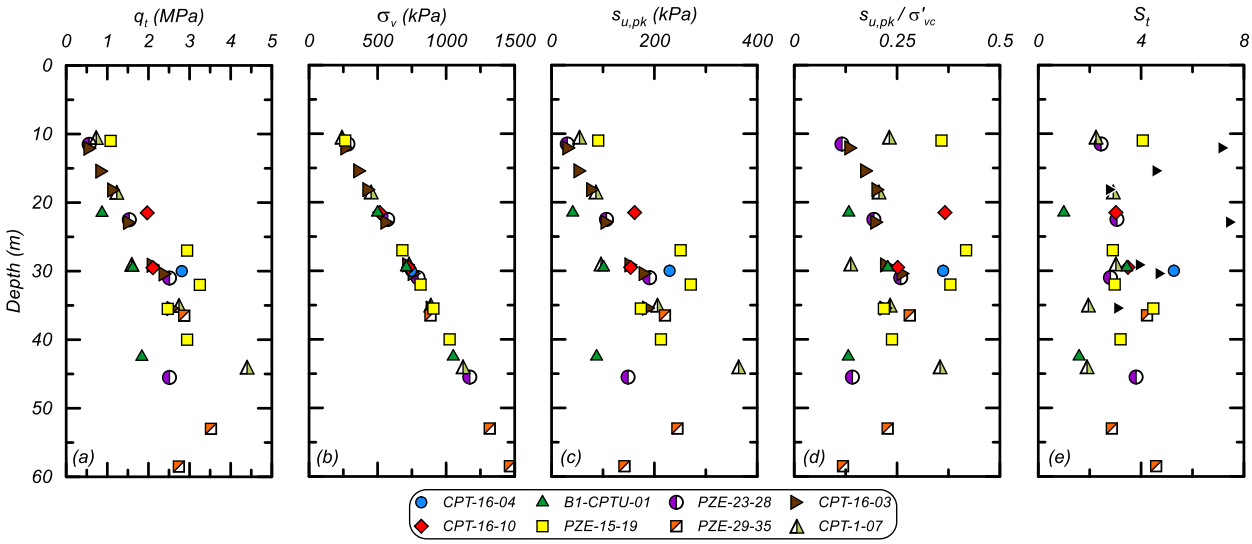

Figure 4-4: Figure 4: Profiles for the fine tailings based on CPT data: (a) representative cone tip resistance (q_t), (b) total vertical stress (σ_v), (c) peak undrained strength ($s_{u,pk}$), (d) normalized peak undrained strength ratio ($s_{u,pk}/\sigma'_{vc}$), and (e) sensitivity (S_t)

The coarse tailings properties were characterized using data from the EPR and analysis of CPT data. Strength was characterized using CPT correlations common for sand-like materials. Digitized CPT data and correlation results are shown in Fig. 4-5 which contains profiles of (a) q_t, (b) u_{bt}, (c) vertical effective stress (σ'_v), (d) relative density (D_r) using the Idriss and Boulanger (2008) correlation, (e) D_r using the Jamiolkowski (2003) correlation, and (f) the residual undrained strength ratio (s_{ur}/σ'_{vc}) using Idriss and Boulanger (2008). The average D_r was about 35% from these two correlations and the average s_{ur}/σ'_v was 0.09, with the Jamiolkowski (2003) method generally predicting higher

D_r compared to the Idriss and Boulanger (2008) method. The EPR estimated an average $s_{u,pk}/\sigma'_v$ of 0.29 (from CPT correlations), which is consistent with estimates based on the CPT data in Fig. 4-5 and relationships by Olson and Stark (2003). Limited field vane test results indicated a large strain strength loss consistent with the estimated s_{ur}/σ'_v and $s_{u,pk}/\sigma'_v$ from CPT relationships. The small-strain stiffness was characterized using the dilatometer data from the EPR and was found to be similar to the small-strain stiffness of the fine tailings. The coarse tailings had a density of 2265 kg/m^3, a porosity of 0.5, a PI of 0, a FC of 33%, and generally a USCS classification of SM. The k_y and k_h were $1.0 \cdot 10^{-4}$ and $5.0 \cdot 10^{-4}$ cm/sec respectively.

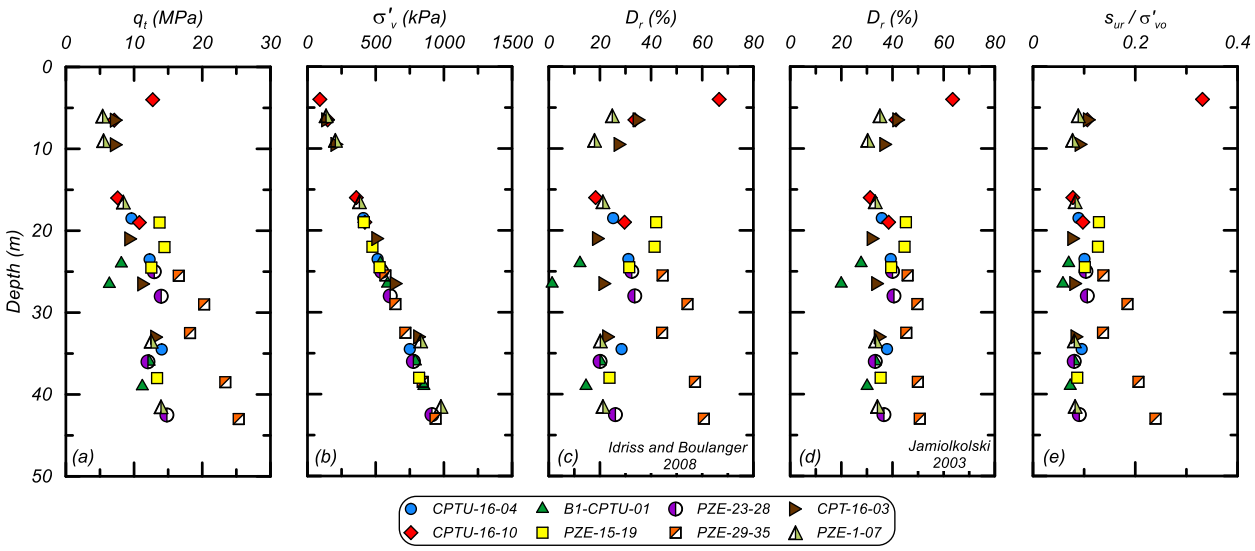

Figure 4-5: Profiles for the coarse tailings based on CPT data: (a) representative cone tip resistance (q_t), (b) vertical effective stress (σ'_v), (c) relative density (D_r) using Idriss and Boulanger (2008), (d) D_r using Jamiolkowski et al. (2003), and (e) residual strength ratio (s_{ur} /σ'_{vo})

The slime properties were characterized using the limited data from the EPR and comparisons to the properties of the fine tailings, while also recognizing that the slime is located far enough from the dam face to not affect the anticipated failure mechanisms. The limited CPT data indicates that the slime is weaker than the fine tailings, especially

at shallow depths. For simplicity, the slime was assumed to have an undrained strength that was 80% of the fine tailings resulting in an $s_{u,pk}/\sigma'_{vc}$ of 0.16 and a S_t of 4. Similarly, the small-strain stiffness was assumed to be 80% of the fine and coarse tailings' small-strain stiffness. The slime had a density of 2014 kg/m^3, a porosity of 0.49, a PI of 18, a LL of 42, and generally a USCS classification of CL. The k_y and k_h were $5.0 \cdot 10^{-7}$ and $1.0 \cdot 10^{-6}$ cm/sec respectively.

The foundation soils were characterized as a residual or colluvial soil of gneiss saprolite (CIMNE). The EPR presented DSS laboratory tests that had an average $s_{u,pk}/\sigma'_{vc}$ = 0.33 without strain-softening but it is not apparent which strength was used in their analyses. CIMNE discussed the possibility of the available laboratory tests and CPT data not being representative of the overall foundation unit as they were from relatively shallow depths; they subsequently modeled the foundation as elastic, precluding failure surfaces from developing in the foundation. Whittle et. al (2022) modeled the foundation as drained with a friction angle of 30 degrees and a cohesion of 8.5 kPa. The analyses herein subsequently modeled the foundation with a $s_{u,pk}/\sigma'_{vc}$ = 0.5 and a S_t = 1. Parametric analyses considered lower foundation strengths and the influence of the foundation strength is discussed later. The foundation as identified and tested by the EPR had a density of 1898 kg/m^3, a porosity of 0.31, a PI of 18, a LL of 60, and generally a USCS classification of MH. The k_y and k_h were $9.3 \cdot 10^{-5}$ cm/sec.

The embankment properties were characterized using data from the EPR. The embankment was assumed to have an average drained friction angle of 36 degrees. The embankment had a density of 1863 kg/m^3, a porosity of 0.3 a PI of 4, a LL of 20, and generally a USCS classification of SM. The k_y and k_h were $1.2 \cdot 10^{-4}$ cm/sec.

4.4 Constitutive Model Calibration

The user-defined constitutive models PM4SiltR (version 1.0) and PM4Sand (version 3.1) were used for all materials. PM4SiltR was used to model the fine tailings, slime, and foundation materials. PM4Sand was used to model the coarse tailings and embankment materials.

PM4SiltR is a modified version of PM4Silt (Boulanger and Ziotopoulou 2019) that incorporates viscoplasticity and is intended for slope stability applications. Viscoplasticity was implemented in the model using a consistency approach coupled with an internal strain rate and an auto-decay mechanism. The model has six required input parameters: (1) the critical state undrained strength or strength ratio ($s_{u,cs}$ or $s_{u,cs}/\sigma'_{vc}$), (2) the shear modulus coefficient (G_o), (3) the contraction rate parameter (h_{po}), (4) the rate dependency factor for the critical state stress ratio (F_M), (5) the rate dependency factor for the critical state line (F_p), and (6) the minimum normalized strain rate producing a viscid response ($R_{\dot{\gamma},\min}$). The model has an additional 12 parameters that are assigned default values based on generalized calibrations and can be modified at the user's discretion (Boulanger et al. 2022).

PM4Sand is a critical state based, stress-ratio controlled, bounding surface plasticity model for sands that builds on the framework of the plasticity model developed by Dafalias and Manzari (2004). PM4Sand has three primary (required) input parameters: (1) relative density (D_r), (2) the shear modulus coefficient (G_o), and (3) the contraction rate parameter (h_{po}). The model has an additional 21 parameters that are assigned default values based on generalized calibrations and can be modified at the user's discretion (Ziotopoulou and Boulanger 2016).

4.4.1 Fine Tailings, Foundation, and Slime

The calibration process for the fine tailings, slime, and foundation materials involved: (1) establishing $s_{u,cs}/\sigma'_{vc}$ and G_o based on the material characterization, (2) adjusting the $n^{b,wet}$ parameter to obtain the desired $s_{u,pk}/\sigma'_{vc}$ and hence S_t, (3) adjusting h_{po} to obtain reasonable rates of post-peak strain-softening, (4) adjusting F_p, F_M, and $R_{\dot{\gamma},\min}$ to obtain the desired viscous response, and (5) iteratively repeating steps 1-4 as warranted. The input parameters for the baseline calibrations are presented in Table 4-2; parameters not listed retained their default values. Sensitivity to selected input parameters is discussed in the results section.

Table 4-2: PM4SiltR input parameters for the base calibration of fine tailings, foundation, and slime

Parameter[1]	Fine Tailings	Slime	Foundation
G_o	994	800	645
$s_{u,cs}/\sigma'_{vc}$	0.05	0.04	0.5
h_{po}	100	100	100
$n_{b,wet} = n_{b,dry}$	0.32	0.28	-
n_g	0.5	-	0.68
h_o	0.02	0.05	0.05
F_M	0.04	0.05	0.0
F_p	0.04	0.05	0.0
$R_{\gamma,min}$	0.01	0.01	0.01

[1]Parameters not indicated retain default values

Stress-strain responses for single element simulations of undrained DSS loading consolidated to a σ'_{vc} of 1 atm and K_o of 0.5 are shown in Fig. 4-6 for the fine tailings with varying static stress ratios (α) of 0.0, 0.05, 0.1, 0.15, and 0.2 (Fig. 4-6a) and varying applied strain rate ratios (SRR, $\log(\dot{\gamma}_{app}/\dot{\gamma}_{ref})$) of -4 -2, 0, 2, and 4 (Fig. 4-6b). Increasing α increased the initial stiffness of the stress-strain response and increased the $s_{u,pk}$. The stress-strain responses exhibit post-peak, strain-softening consistent with the imposed S_t

of 4. The $s_{u,pk}$ increases by approximately 5% per log cycle of loading rate. Stress-strain responses for SRRs of -2 and -4 mobilize approximately the same $s_{u,pk}$, which is approximately 90% of $s_{u,pk,ref}$. The minimum mobilized $s_{u,pk}$ is determined by the location of the static bounding surface which is controlled by F_M, F_p, and $R_{\dot{\gamma},\min}$. The stress-strain responses for the slime with varying α and SRRs are similar to those of the fine tailings but the slime has a reference peak strength ratio of 0.16 (80% of the fine tailings).

The undrained creep response in DSS loading at different sustained stress ratios is shown for the fine tailings (Fig. 4-6c) for single element simulations consolidated to a σ'_{vc} = 1 atm, $K_0 = 0.5$, and $\alpha = 0$. After initial consolidation, a shear stress (τ_h) was applied under undrained loading at a fixed rate until reaching target percentages of $s_{u,pk}$, after which τ_h was held constant. Stable conditions developed for $\tau_h/s_{u,pk} < 0.88$ and undrained creep rupture occurred for $\tau_h/s_{u,pk} > 0.9$. The distinction between stable and rupture conditions is dependent on the placement of the static bounding surface. The time to rupture decreases with increasing sustained stress levels. The undrained creep response of the slime is similar to that of the fine tailings.

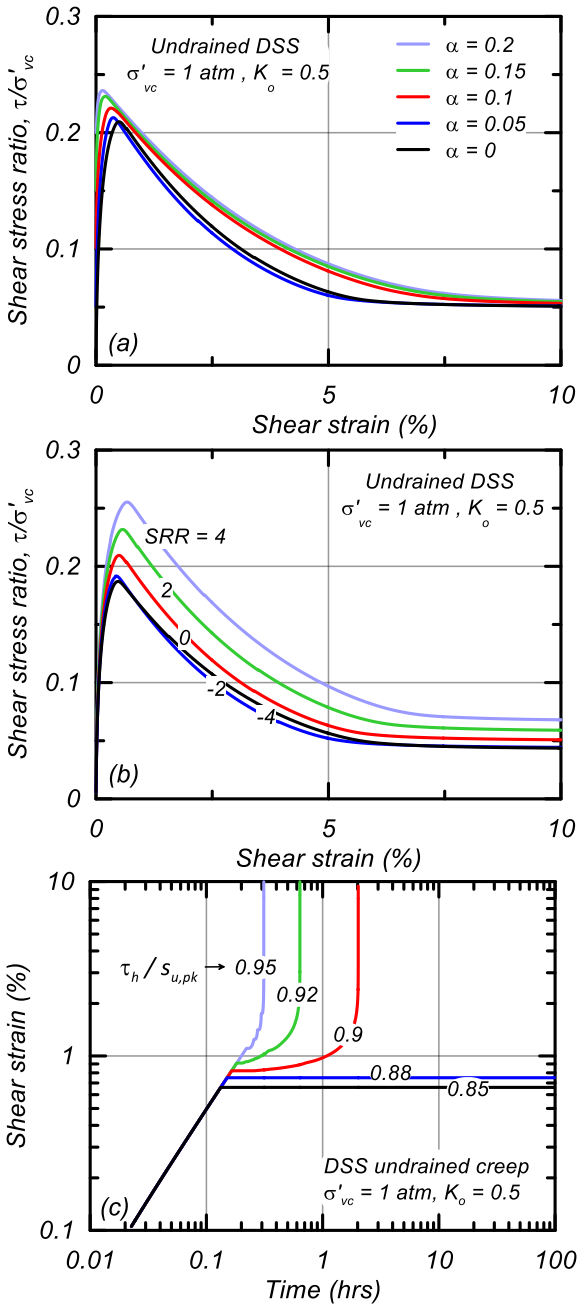

Figure 4-6: Simulations of DSS loading with (a) varying sustained static shear stress ratios, (b) varying applied strain rates, and (c) undrained creep simulations with varying sustained shear stresses for the fine tailings

Stress-strain responses for single element simulations of the foundation material subjected to undrained DSS loading after consolidation to σ'_{vc} of 0.5, 1, 2, 3, and 4 atm and K_o of 0.5 are shown in Fig. 4-7. Peak strength is mobilized at larger shear strains with

increasing σ'_{vc} and the $s_{u,pk}/\sigma'_{vc}$ is 0.5. Post-peak, the stress-strain response strain-hardens and does not lose strength, consistent with the characterized S_t of 1. The foundation F_p and F_M parameters are 0 and as such the baseline calibration does not have the potential for creep to occur and the strength does not vary with the SRR.

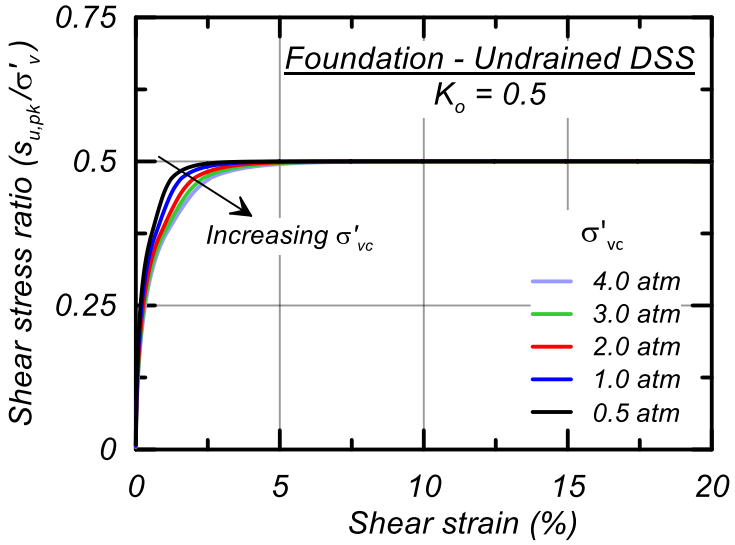

Figure 4-7: Simulations of undrained DSS loading with varying static shear stress ratios for the foundation

4.4.2 Coarse Tailings and Embankment

The calibration of PM4Sand for the coarse tailings and embankment materials was performed as follows: (1) establishing D_r and G_o based on material characterization, (2) adjusting R to position the critical state line to produce the target $s_{u,r}/\sigma'_{vo}$, (3) adjusting n_b, h_{po}, and h_o to obtain desired $s_{u,pk}$ and reasonable rates of strain-softening, and (4) iteratively repeating steps 1-3 until no further adjustments are warranted. The value of R computed in step (2) is a function of the initial effective stress state and thus varies across elements. The value of R is computed as (Boulanger and Ziotopoulou 2018),

$$R = D_R \cdot \left(Q - \ln\left(\frac{2 \cdot s_{u,cs}}{M} / P_a \right) \right) \tag{4-1}$$

Calibrated input parameters for the coarse tailings and embankment materials are shown in Table 4-3. All other parameters retained their default values.

Table 4-3: PM4Sand input parameters for the coarse tailings and embankment

Parameter[1]	Coarse Tailings	Embankment
G_o	994	667
D_r	0.35	0.55
h_{po}	7.5	0.4
n_b	0.5	-
h_o	0.1	-
R	Varies[2]	-

[1]Parameters not indicated retain default values

[2]Computed from initial effective stress state and target $s_{u,cs}$

Single element simulations of monotonic DSS loading are shown for the coarse tailings (undrained and drained loading, Fig. 4-8a) and embankment material (drained loading, Fig. 4-8b) consolidated to varying σ'_{vc} of 0.5, 1, 2, 3, and 4 atm and K_o of 0.5. The coarse tailings are stronger drained than undrained as the they are initially loose of critical state. Drained loading of the coarse tailings mobilizes a shear strength ratio slightly larger than 0.5 while undrained loading mobilizes a $s_{u,pk}/\sigma'_{vc}$ of 0.29. Post peak, the coarse tailings strain-soften when undrained to the s_{ur}/σ'_{vc} of 0.09 whereas the coarse tailings strain-harden when loaded under drained conditions. The influence of drained versus undrained coarse tailings behavior is discussed in the results section. The embankment material mobilizes a drained friction angle between 32 and 36 degrees depending on σ'_{vc} and exhibits only minor post-peak strain-softening.

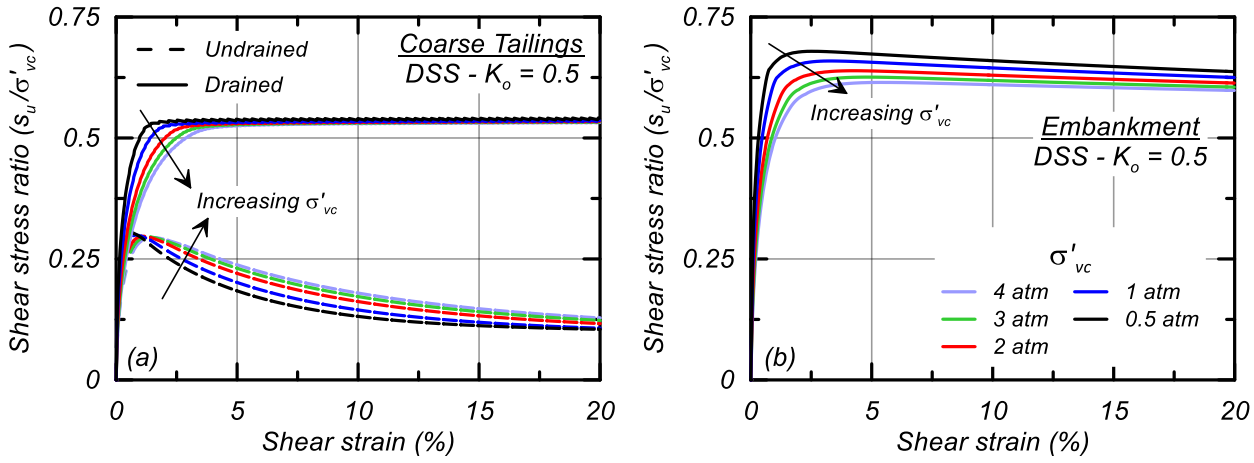

Figure 4-8: Stress-strain responses for DSS loading with varying confining stresses for (a) undrained and drained loading for the coarse tailings and (b) drained loading for embankment material

4.5 Model Development and Initial Stress Conditions

Two-dimensional nonlinear analyses were performed using the finite difference program FLAC 8.1 (Itasca 2019) with the creep module. The analysis cross-section and stratigraphy are shown in Fig. 4-2. Elements were generally 1 m thick by 2 m wide for a total of approximately 45,000 elements. The initial static stress and seepage conditions were established with the following sequence.

The initial seepage conditions were established first using an uncoupled analysis calibrated to produce results consistent with the EPR. The EPR examined seepage under 2D and 3D conditions and accounted for seepage in partially saturated soils. The FLAC seepage analyses did not account for seepage in partially saturated soils, such that material property adjustments were made to obtain consistency with the EPR results. The pore fluid tensile stress controls the height to which soils are saturated by capillary rise above the phreatic surface; pore fluid tensile stresses of 29.4 kPa, 9.8 kPa, and 9.8 kPa were assigned to the fine tailings, coarse tailings, and embankment materials to produce capillary saturation to heights of 3.0 m, 1.0 m, and 1.0 m above the phreatic surface,

respectively. Hydraulic conductivities of the materials were initially assigned the values in Table 4-1 and then iteratively adjusted to obtain a phreatic surface consistent with the EPR. The final calibrated analysis included two adjustments: (1) the isotropic conductivity of the foundation was reduced to $1 \cdot 10^{-6}$ cm/sec, and (2) the coarse tailings conductivity was made isotropic with a reduced conductivity of $1 \cdot 10^{-5}$ cm/sec. The results of the steady state seepage analysis are illustrated in Fig. 4-9 which shows saturation and pore pressure contours. The calibrated phreatic surface, like in the EPR, is high near the face of the dam due to a lack of internal drainage in the lower portion of the dam.

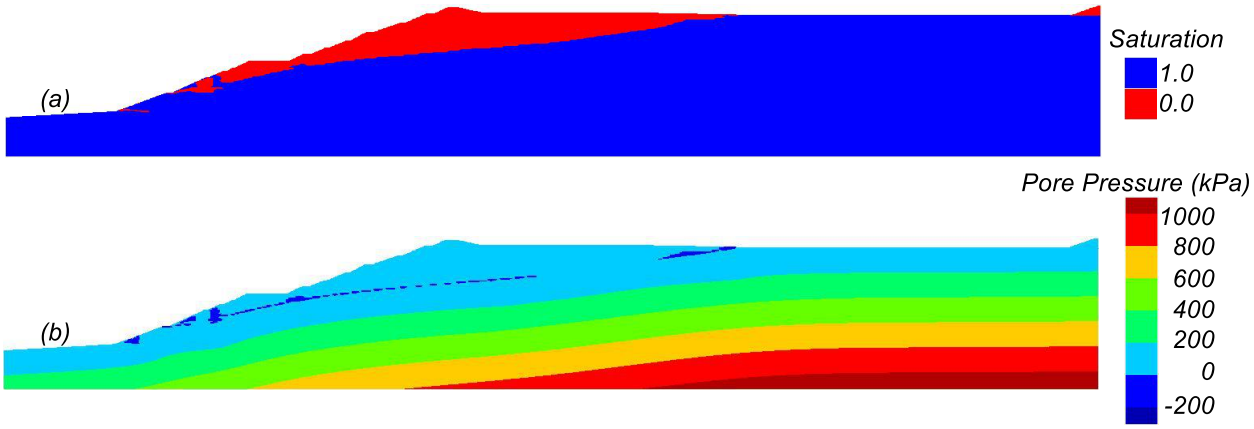

Figure 4-9: Contours of (a) saturation and (b) pore pressure at the end of consolidation

Initial stress conditions were computed with another uncoupled analysis (using pore pressures based on the preceding step) in which: (1) vertical stresses were based on overlying soils, (2) horizontal stresses assigned based on a $K_o = 0.5$, and (3) all zones assigned a Mohr Coulomb constitutive model and a stress-dependent secant shear modulus. After solving for equilibrium, the material models were then switched to PM4Sand and PM4SiltR (without viscous parameters) and equilibrium was again solved for.

Viscous parameters in PM4SiltR were then initiated and a coupled creep analysis performed with all materials fully drained. The final "initial" stress conditions were established when creep deformations had ceased, corresponding to a long-term fully consolidated condition. The initial stress conditions are illustrated in Fig. 4-10 in terms of (a) σ'_v, (b) α, and (c) K_o. The σ'_v increases with depth from the ground surface. The α values range from 0.1 to 0.3 in the tailings and foundation under the embankment and approaches 0.4 near the dam face. Large α values are expected due to the relatively steep slope of the embankment and the placement of the set-back relative to the dam face. K_o is generally 0.5 in the tailings below the dam face except in narrow bands where K_o is decreased due to rotation of principal stresses in the fine tailings.

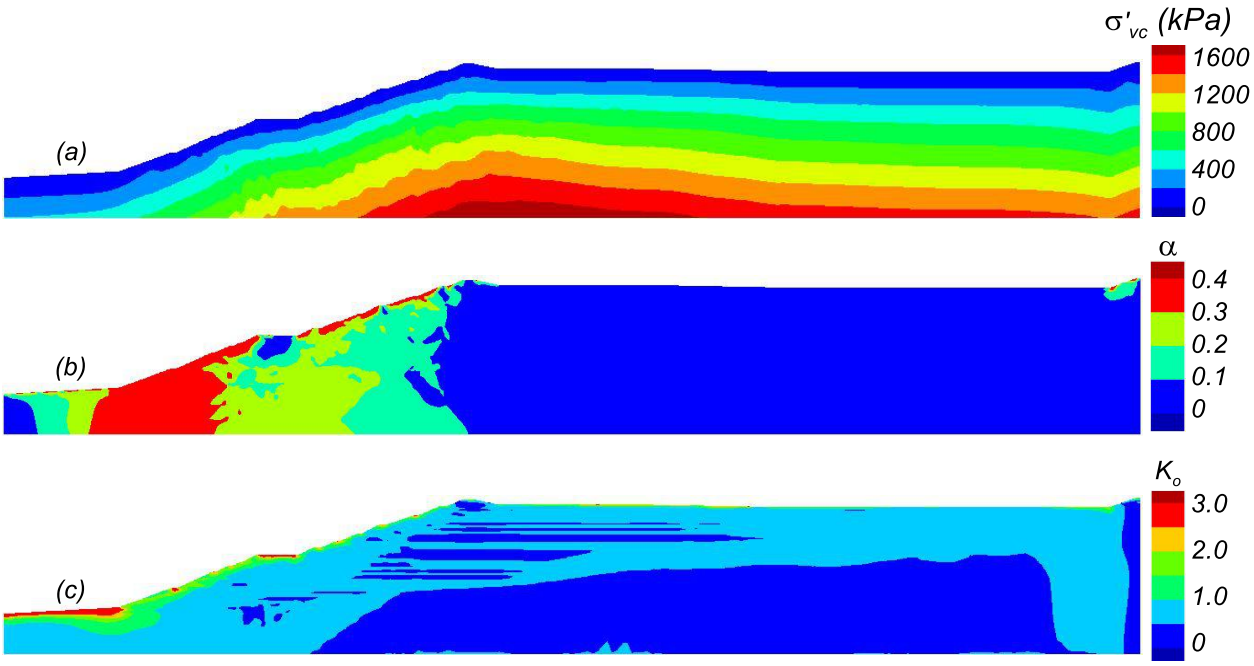

Figure 4-10: Initial static stress conditions at the end of consolidation: (a) vertical effective stress (σ'_{vc}), (b) horizontal static shear stress ratio (α), and (c) at-rest lateral earth pressure coefficient (K_0)

4.6 Static Factor of Safety by SSRM

The static FS against slope instability, evaluated using the SSRM, is presented first to provide context for the viscoplastic nonlinear analyses results presented next. The SSRM analyses used non-strain-softening Mohr Coulomb models (i.e., neglects progressive failure effects) and assigned strengths based on the initial stress conditions and strength properties described previously. For long-term drained stability, materials were assigned the following drained friction angles: (1) 34˚ for the coarse tailings and foundation materials, (2) 33˚ for the fine tailings, (3) 30˚ for the slime, and (4) 36˚ for the embankment materials. The FS was 1.54 for this long-term drained condition. For long-term (consolidated) undrained stability, the analyses assumed: (1) the embankment was drained with a friction angle of 36˚, (2) the foundation was undrained with an $s_u/\sigma'_{vc} = 0.5$, (3) the coarse tailings were undrained with an $s_u/\sigma'_{vc} = 0.29$ where saturated, and drained with a friction angle of 34˚ where unsaturated, (4) the fine tailings were undrained with an $s_u/\sigma'_{vc} = 0.21$ where saturated, and drained with a friction angle of 33˚ where unsaturated, and (5) the slime was undrained with an $s_u/\sigma'_{vc} = 0.16$. The FS for this long-term consolidated undrained condition was 1.06. The low FS for long-term undrained loading indicates that the dam was only marginally stable, such that, when combined with progressive failure effects, it is reasonable to expect instability may be triggered by some combination of a relatively small increase in loading or reduction in shear strengths. The low FS is consistent with recent analyses by Whittle et al. (2022) that calculated the FS to be between 1.11 – 1.16 using 2D numerical limit analyses. The small difference in FS can be attributed to their slightly higher characterized strength ($s_{u,pk}/\sigma'_{vc} = 0.22$ versus

0.21) of the fine tailings and differences in geometries, imposed drainage conditions, and stratigraphy.

4.7 Nonlinear Viscoplastic Deformation and Stability Analysis

Nonlinear viscoplastic analyses were performed for two different loading/disturbance scenarios applied after establishment of the initial stress conditions (i.e., long-term, fully consolidated condition). The two loading scenarios are (1) wetting events and (2) borehole disturbance events. These coupled analyses imposed fully undrained conditions (i.e., no flow) and thus do not account for the potentially beneficial effects of consolidation during creep. Parametric analyses are used to evaluate how the responses to different loading intensities are affected by reasonable variations in input parameters and analysis procedures.

4.7.1 Response to Wetting Events

Wetting events were modeled as a progressive uniform increase in the degree of saturation (ΔS) in the unsaturated materials above the phreatic surface while simultaneously eliminating suction (negative pore pressures) in the soils saturated by capillary rise. Increasing ΔS increases the weight of the potential slide mass through increased water contents and unit weights and reduces the resisting force with the loss of suction, both of which decrease the stability of the dam. The water content changes (Δw_c) in the fine tailings, coarse tailings, and embankment materials due to the imposed ΔS are shown in Table 4-4. The Δw_c is different for each material because they have varying porosities and specific gravities. For example, imposing ΔS = 15% produces Δw_c of 4.7%, 3.3%, and 2.4% in the fine tailings, coarse tailings, and embankment materials above the phreatic surface, respectively. These Δw_c affect only a portion of the eventual

slide mass, as shown later, such that an imposed ΔS = 15% increases the slide mass weight and average driving shear stress along the eventual failure surface by only 2.2%. This increase in driving stresses is combined with a concurrent reduction in shear strength within the zone of capillary rise (due to the imposed loss of suction), but the increase in driving stress has the greater influence because the zones of capillary rise are not large relative to the dimensions of the slope. In all cases, wetting events are imposed by linearly increasing the degree of saturation and simultaneously linearly reducing capillary suction pressures in applicable zones over a period of approximately 4 days.

Table 4-4: Changes in saturation, water content, and average slide mass weight

ΔS (%)	Δw_c (%)			Average slide mass increase %[1]
	Fine Tailings	Coarse Tailings	Embankment	
5	1.6	1.1	0.8	0.7
10	3.1	2.2	1.6	1.5
15	4.7	3.3	2.4	2.2
20	6.2	4.4	3.2	2.9
30	9.3	6.6	4.8	4.4
50	15.5	11	8.1	7.3

[1]Average assumes equal weight of fine tailings, coarse tailings, and embankment

Horizontal displacement at the mid-slope setback is plotted versus time since the start of wetting in Fig. 4-11 for ΔS of 5, 10, 12, 14, 15, and 30%. Simulations with $\Delta S \leq$ 12% accumulated less than 10 mm of horizontal displacement at the set-back with most of the deformation occurring as the wetting load was imposed (a period of 4 days). The simulation with ΔS = 30% failed during the wetting event. The simulations with ΔS = 14% and 15% developed slope instability in approximately 24 days and 6 days, respectively, after the end of the wetting event. For both these cases, displacements at the set-back remained small (less than approximately 20 mm) until just prior to the failure occurring.

Imposing ΔS = 14% or 15% increased the average driving shear stresses along the eventual failure surface by only about 2.2%, which might not be expected to trigger failure on its own given the static FS = 1.06, but it was sufficient to trigger failure because it initiated the onset of progressive failure.

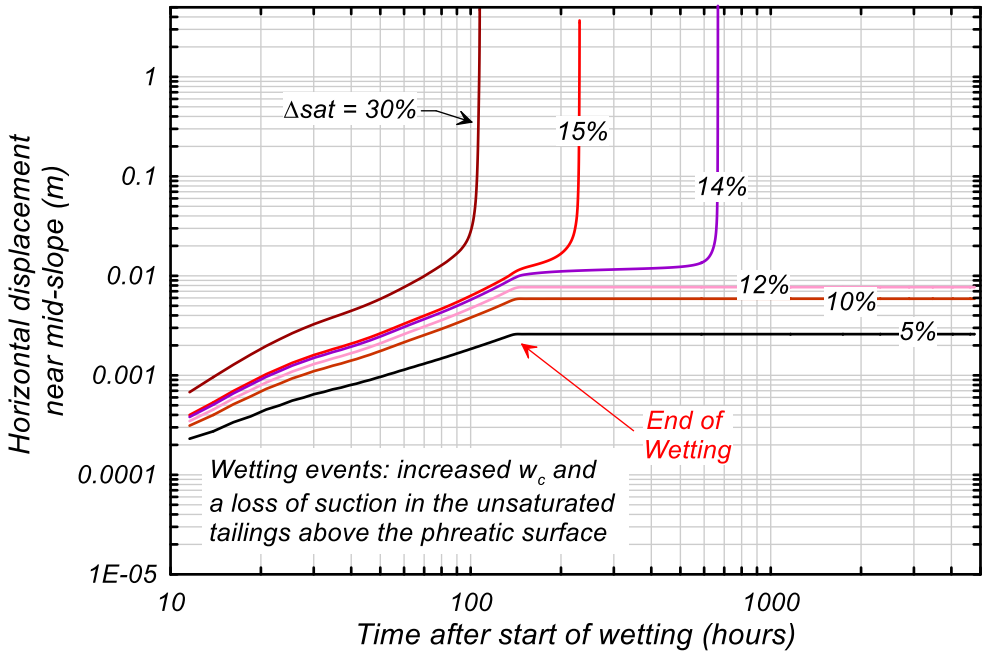

Figure 4-11: Horizontal deformations at the set-back versus time after the start of a wetting event causing an increase in the percent saturation (ΔS) and loss of suction in unsaturated tailings above the phreatic surface

Wetting events that resulted in slope instability involved progressive failure as the failure surface (or shear zone) developed over time in the strain-softening tailings. The progressive development of the eventual failure surface is shown in Fig. 4-12 which shows shear strain contours (capped at 15%) for the simulation with a ΔS = 14% at set-back displacements of 2, 5, 20, 40, and 500 cm. The failure surface initially developed in a thin fine tailings layer that approaches the dam face near the top of the first raising; this region had initial α values close to the $s_{u,pk}/\sigma'_{vc}$ and thus required only a minor shear stress increase before beginning to strain-soften. Set-back displacements were 2 cm at

an elapsed time of 648 hours (27 days) and 5 cm at 663 hours (28 days), followed by the rapid increase of displacements and slope instability over the next four hours (elapsed time = 667 hours). The fully developed failure surface is illustrated in Fig. 4-13 which shows contours of x-displacement and y-displacement at the end of the simulation (set-back displacement of 500 cm). The failure surface daylights on the dam face near the top of the first raise and at the crest behind the final raising. The simulated failure surface is similar to the failure observed in the video. Collapse and runout of slide materials above this relatively shallow failure surface would likely be followed by retrogressive slip-surfaces as the remaining slopes are too steep to remain stable.

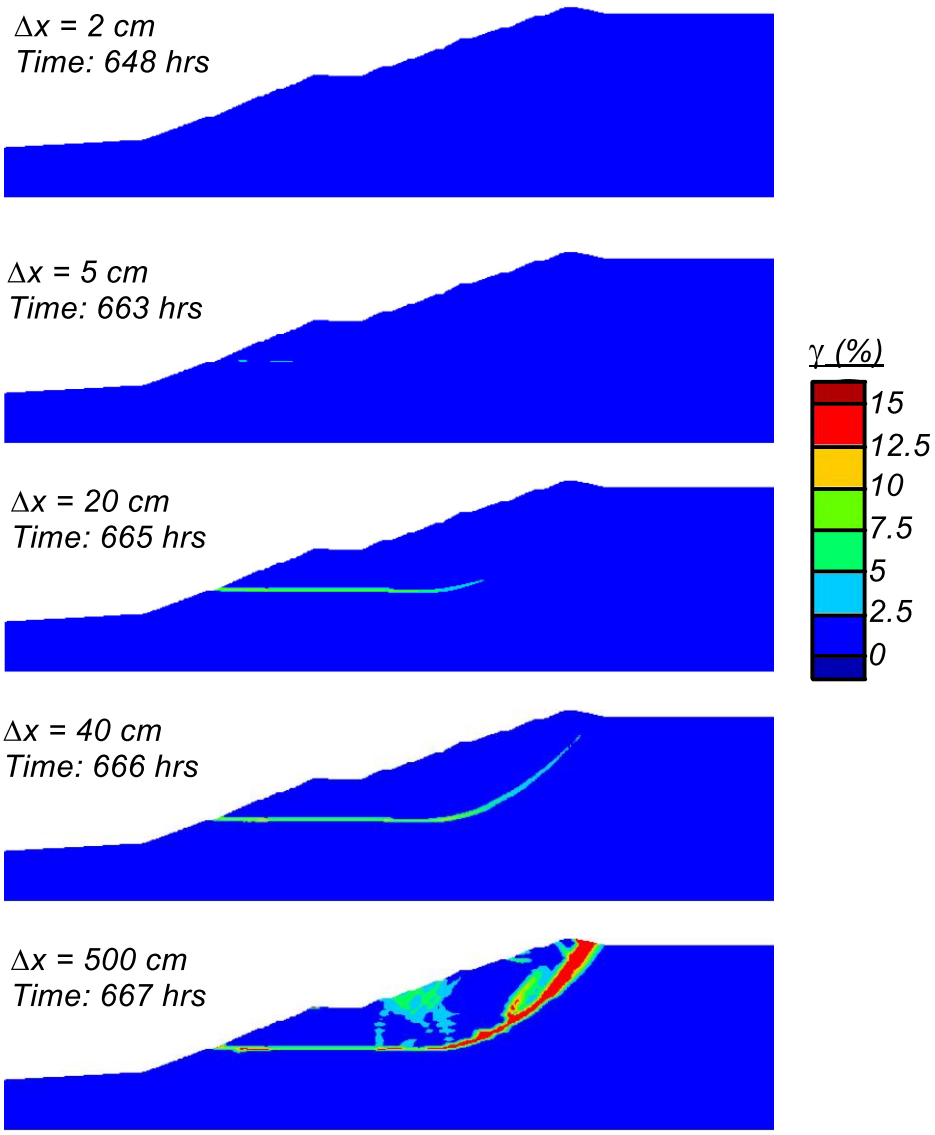

Figure 4-12: Shear strain contours (capped at 15%) at slope deformations of 2 cm, 5 cm, 20 cm, 40 cm, and 500 cm for the simulation with a ΔS = 14%

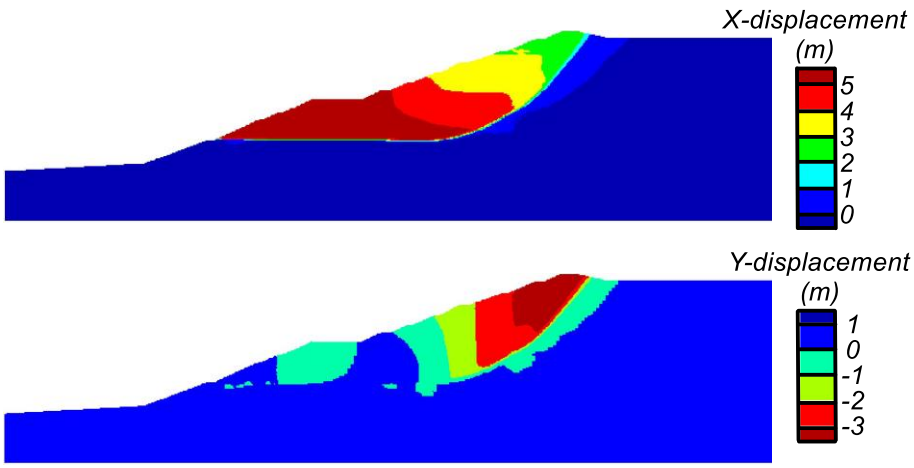

Figure 4-13: Contours of X-displacement and Y-displacement at the end of the simulation with a $\Delta S = 14\%$

The EPR modeling of the wetting event assumed a uniform strength reduction of 15 kPa in all of the unsaturated tailings due to a loss of suction. The analyses herein assumed a strength reduction in the tailings with suction due to capillary rise (3 m in the fine tailings and 1 m in the coarse tailings). These different approaches amount to different magnitudes of reduction in the overall resisting force. The approximate total resisting force of the simulated failure band (based on a piecewise averaging of strengths along the failure band) is approximately 75,000 kN/m. The unsaturated tailings accounted for approximately 60 m of the failure band in the analyses herein. The EPR approach would result in a reduction of approximately 900 kN/m or approximately 1.2% of the total resisting force. The approach herein resulted in a reduction in resisting force of approximately 100 kN/m or 0.13% of the total resisting force. If the loss of suction in the present analyses were on the same magnitude as the EPR, the magnitude of wetting necessary to trigger slope instability would be smaller than shown.

Parametric analyses were performed that varied the fine tailings strength, rate of strain-softening, and viscous parameters as well as the foundation strength and the

drainage conditions in the coarse tailings. The maximum ΔS sustainable prior to creep failure are shown in Table 4-5 for the parameters varied which also illustrates the effect of the parameter variation on $s_{u,pk}$ and $s_{u,static}$. Decreasing the fine tailings $s_{u,pk}$ by 10% caused the system to be unstable in undrained conditions without a change in loading (i.e., $\Delta S = 0\%$); this result is consistent with the static FS = 1.06 and the eventual failure surface passing predominantly through fine tailings. Increasing the fine tailings $s_{u,pk}$ by 10% increased the ΔS that can be withstood prior to creep failure to about 60% compared to 14% with the baseline $s_{u,pk}$. These results indicate that the magnitude of ΔS required to trigger instability is very sensitive to s_u/σ'_{vc} because the FS is already close to unity. Decreasing the rate of strain-softening (by setting $h_{po} = 1000$) increased the ΔS prior to failure to approximately 26%, whereas increasing the rate of strain-softening (by setting $h_{po} = 10$) decreased the ΔS prior to failure to approximately 1%, indicating that the brittleness of the tailings is critical to the development of the progressive failure. Increasing the fine tailings $s_{u,static}$ (either through F_p and F_M or $R_{\dot{\gamma},\min}$) while keeping $s_{u,pk}$ constant, increased the ΔS that can be incurred prior to loading. Conversely, decreasing $s_{u,static}$ caused the system to be unstable in undrained conditions without a change in loading as the lower static strength of the fine tailings was sufficient to initiate progressive failure. Decreasing the foundation material's $s_{u,pk}/\sigma'_{vc}$ to ≤ 0.4 resulted in the failure surface going through the foundation at the toe of the dam which was not observed in the failure. Modeling the coarse tailings as drained increased the ΔS prior to failure to 19% compared to 14% when the coarse tailings were undrained. The small dependency of ΔS to failure seen with the coarse tailings drainage variation relative to the sensitivity to the

fine tailings calibration indicates that the fine tailings characterization was more critical to the stability of the structure.

Table 4-5: ΔS needed to initiate slope instability with variation in fine tailings calibration

Condition Investigated	Parameter Varied	$s_{u,pk} / \sigma'_{vc}$	$s_{u,static} / \sigma'_{vc}$	ΔS prior to slope instability
Baseline	N/A	0.21	0.19	14%
Rate of strain-softening	$h_{po} = 10$	0.21	0.19	1%
	$h_{po} = 1000$	0.21	0.19	26%
Rate dependency	$F_p = F_M = 0.0$	0.21	0.21	40%
	$F_p = F_M = 0.02$	0.21	0.2	27%
	$F_p = F_M = 0.06$	0.21	0.18	0%
	$R_{y,min} = 0.1$	0.21	0.2	27%
	$R_{y,min} = 0.001$	0.21	0.18	0%
$s_{u,pk}$	$n_{b,wet} = 0.27$	0.23	0.21	60%
	$n_{b,wet} = 0.37$	0.19	0.17	0%

Simulations were performed with $F_p = F_M = 0.0$ to investigate the stability of the slope in the absence of creep which had two primary effects. The first effect is that the static strength is the same as the characterized peak strength which increased the ΔS prior to slope instability to 40%. The second effect is that there was no delayed failure as stress reduction and creep in time were unable to occur. The failure occurs during the wetting event due to only the increased driving stresses. The absence of viscous effects did not alter the predicted failure surface. These simulations showed that nonviscous models could predict the failure mechanism but were unable to capture a delayed failure and estimates different magnitudes of loading necessary to trigger the failure

Additional analyses were performed to evaluate the sensitivity to numerical implementation including mesh size and time step constraints. Sensitivity analyses using smaller strain increment limits for constraining time steps within the explicit creep solution

of FLAC showed minimal effect on ΔS prior to instability (~1%) and had a minor effect on the timing of the failure. The influence of mesh size and time step are additional factors that must be accounted for when analyzing results of analyses on strain-softening materials. Further refining the mesh (decreasing the mesh size) reduced the magnitude of deformation needed for the system to become unstable. The mesh refinement also influenced the timing of the failure as the reduced deformations do not take as long to accumulate which allows failure to occur more rapidly. Additionally, due to the low viscosity of the tailings material, the system did not largely benefit from the regularization (reduced mesh dependency) that is associated with the inclusion of viscous effects in analyses and as such the solution remained mesh dependent. The mesh dependency would be expected to decrease in systems with more viscous materials.

4.7.2 Response to Drilling-Induced Disturbances

Drilling-induced slope instability was investigated by simulating large strength loss in a localized zone due to the hypothetical occurrence of a hydraulic fracture or over-pressurized zone along borehole (B1-SM-13) which was being drilled at the time of failure. Fig. 4-14 shows the approximate location of borehole B1-SM-13 along Section 3-3′. Available records indicate that borehole B1-SM-13 was advanced using rotary drilling methods with water recirculation in casing to native soil on the day prior to the failure (Robertson et al. 2019). No drilling log is available for this activity, and thus the potential for hydraulic fracturing and fluid loss to have occurred during drilling is speculative for the purpose of exploring the potential impacts of such an event. The potential extent of strength loss due to a hydraulic fracture was crudely estimated by equating an estimate of possible fluid loss with the volume of a fracture; e.g., a borehole water level drop of

approximately 30 m (down to the phreatic surface) in a 100 mm diameter hole could fill a 5 mm thick, circular fracture with a diameter of almost 8 m. The plan area of such a fracture would be equivalent to a 1.0 m wide zone over a 50-m long reach. Alternatively, the elevated water levels inside the borehole could have over-pressurized zones around the borehole, possibly triggering local strength losses or yielding. In this regard, CIMNE assumed that liquefaction was triggered in a local zone near the base of the tailings during drilling of borehole B1-SM-13. Boring-induced liquefaction was imposed on a 1 m wide by 3 m tall zone around the borehole in their 2D analyses and as 1 m wide, 1 m long, and 3 m tall zone around the borehole in their 3D analyses of a 15-meter wide slice of the slope. The actual size of any borehole disturbance zone is highly uncertain, but the above discussion suggests a 2D analysis should consider borehole disturbance as having relatively small dimensions. The baseline 2D mesh has elements that are generally 1 m tall by 2 m wide, such that the disturbance zone was modeled as being one element tall and a varying number of elements wide.

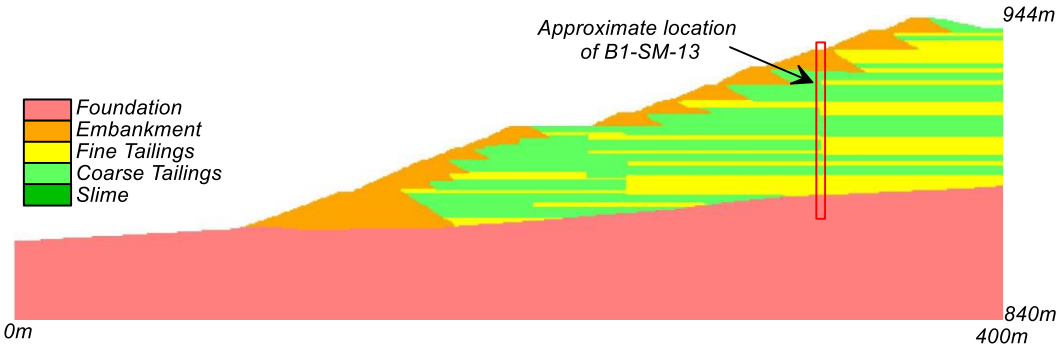

Figure 4-14: Approximate location of borehole B1-SM-13 along Section 3-3'

Parametric analyses varied the horizontal and vertical dimensions, depth, and strength loss for the potential borehole disturbance zone. The location of the borehole disturbance zone had a strong effect on the potential for drilling to trigger slope instability.

Simulations with the borehole disturbance zone near the bottom of the tailings (just above the foundation surface) resulted in minimal deformations regardless of the vertical and horizontal dimensions examined (up to a zone of 1 m tall by 12 m wide). Simulations with the borehole disturbance zone at a depth of 45 m, which is close to the depth where the failure surface formed in the prior analyses for wetting events, were most susceptible to having slope instability being triggered by a borehole disturbance. Possible disturbances at these intermediate depths would have occurred when drilling reached this depth the day before the slope failure.

The results of a simulation with a borehole disturbance zone 12 m wide by 1 m tall at a depth of 45 m in borehole B1-SM-13 are presented in Fig. 4-15 showing the location of the borehole disturbance zone (Fig. 4-15a) and contours of shear strain (Fig. 4-15b) and horizontal displacement (Fig. 4-15c) at the end of the analysis. The displacement and shear strain contours illustrate a rotational failure with a slide mass that resembles the observed failure. The failure occurs approximately 35 hours after the borehole disturbance which is qualitatively consistent with drilling at that depth having occurred the day before the slope failure. The 12 m length of the disturbance zone represents about 4.7% of the total failure surface length, which would increase average driving shear stresses elsewhere along the eventual failure surface by a similar percentage. This change in shear stresses might not be expected to trigger failure on its own given the static FS = 1.06, but it was sufficient to trigger failure because it initiated the onset of progressive failure as noted for the wetting event scenarios and discussed below.

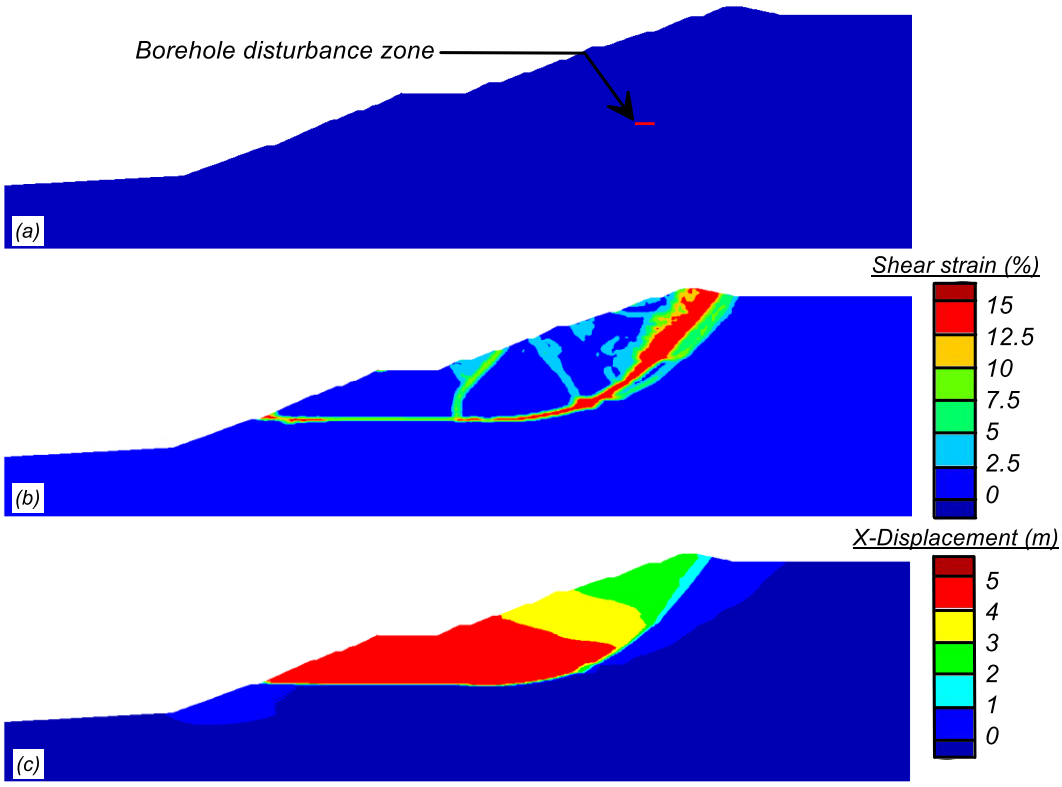

Figure 4-15: Results of simulation of borehole disturbance causing slope instability: (a) borehole disturbance zone, (b) shear strain (capped at 15%) and (c) horizontal displacement

Borehole disturbances that trigger failure involve a progressive failure within the impoundment. Fig. 4-16 shows shear strain contours (capped at 15%) when the horizontal displacements at the mid-slope setback are 5 cm, 10 cm, 20 cm, 40 cm, and 500 cm. Only 5 cm of displacement developed over the first 33.4 hours after the borehole disturbance occurs, with no observed localized shear band. Over approximately the next 1.5 hours (elapsed time 34.9 hours) the displacement increased to 10 cm and the failure surface began to develop along the fine tailings layer near the dam face and to the left of the imposed borehole disturbance. At an elapsed time of 35.4 hours, 500 cm of displacement had developed with full collapse underway. While the details and timing of the progressive failure may slightly differ, the similarity in shape and size of the failure

surfaces from both a wetting event and from a borehole disturbance indicates that the critical failure surface is similar regardless of the triggering mechanism.

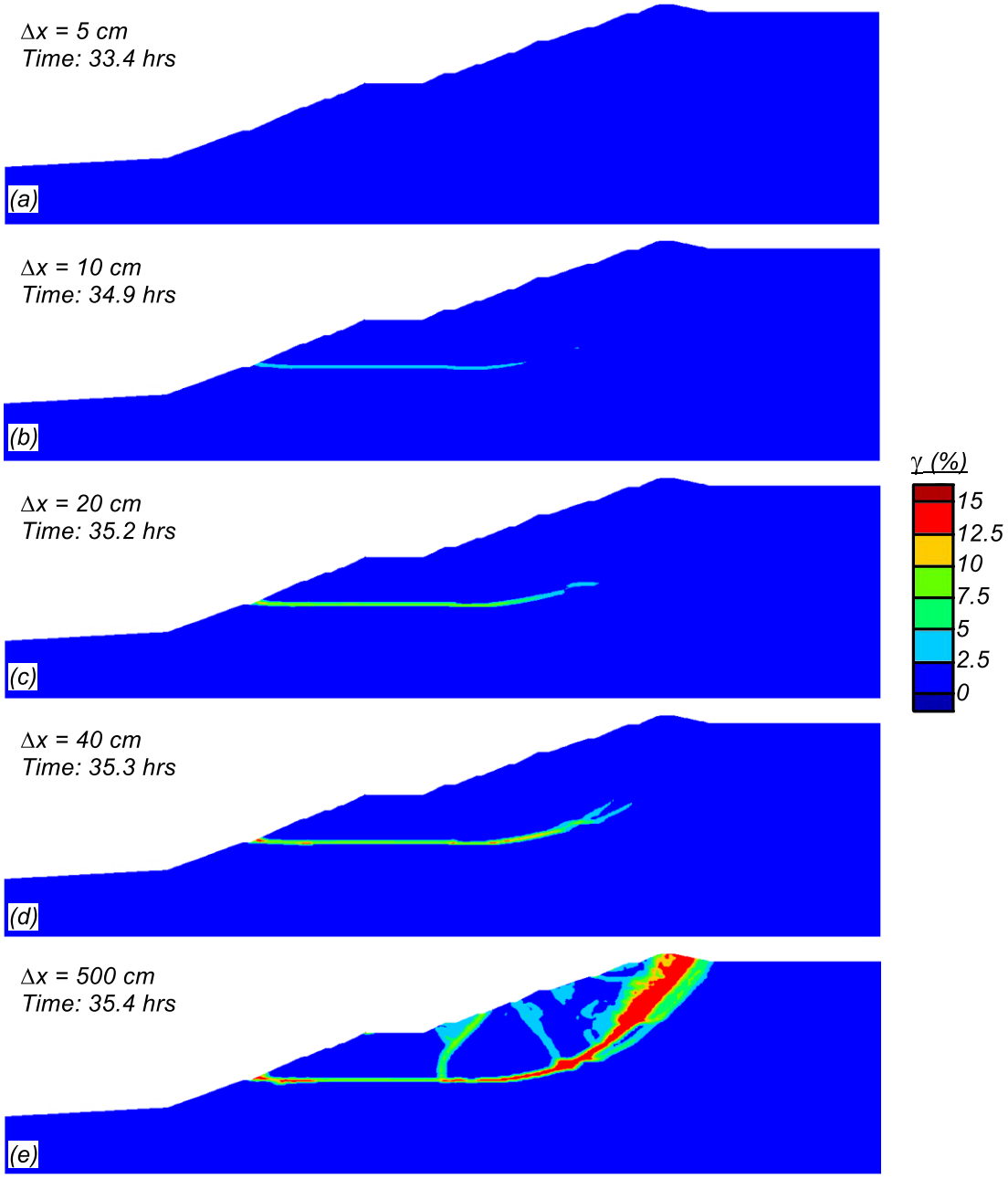

Figure 4-16: Contours of shear strain (capped at 15%) at horizontal embankment deformations of (a) 5 cm, (b) 10 cm, (c) 20 cm, (d) 40 cm, and (e) 500 cm

Similar parameter variations were performed to identify the influence of critical fine tailings parameters on the disturbance width necessary to initiate undrained failure. As

seen in wetting induced displacements analyses; decreasing the $s_{u,pk}$ by 10% and decreasing $s_{u,static}$ (through either mechanism) caused the system to be unstable undrained without any external changes in loading. The smallest disturbance width that initiates undrained failure are shown in Table 4-6 for the parameters varied. Increasing the fine tailings $s_{u,pk}$ by 10% increased the disturbance width necessary to induced undrained failure to >40m compared to 12m with the baseline $s_{u,pk}$. These results indicate that the disturbance width required to trigger instability is very sensitive to $s_{u,pk}/\sigma'_{vc}$. Decreasing the rate of strain-softening (by setting h_{po} = 1000) increased the disturbance width prior to failure to 18m, whereas increasing the rate of strain-softening (by setting h_{po} = 10) decreased the disturbance width prior to failure to 2 m. Increasing the fine tailings $s_{u,static}$ (either through F_p and F_M or $R_{\dot{\gamma},\min}$) while keeping $s_{u,pk}$ constant, increased the disturbance width that can be incurred prior to loading to 16 m.

Generally, the failure mechanism mobilized through the tailings and did not involve the foundation (consistent with the observed failure) regardless of the disturbance size and location. One exception was a simulation with the baseline properties and a disturbance width of 10 m which initiated a failure surface through the foundation which was inconsistent with the observed failure. The same analysis with a disturbance width of 8 m remained stable with deformations less than 1 cm while a disturbance width of 12 m mobilized a failure through the tailings (Fig. 4-15). These simulations highlight the sensitivity of the dam stability to the width of the imposed disturbance. They also highlight the sensitivity to the foundation strength as a slightly higher foundation strength would have precluded failure through the foundation.

Table 4-6: Disturbance width necessary to initiate slope instability with variation in fine tailings calibration

Condition Investigated	Parameter Varied	$s_{u,pk} / \sigma'_{vc}$	$s_{u,static} / \sigma'_{vc}$	Disturbance width to initiate slope instability
Baseline	N/A	0.21	0.19	12m
Rate of strain-softening	$h_{po} = 10$	0.21	0.19	2m
	$h_{po} = 1000$	0.21	0.19	18m
Rate dependency	$F_p = F_M = 0.02$	0.21	0.2	16m
	$F_p = F_M = 0.06$	0.21	0.18	0m
	$R_{y,min} = 0.1$	0.21	0.2	16m
	$R_{y,min} = 0.001$	0.21	0.18	0m
$s_{u,pk}$	$n_{b,wet} = 0.27$	0.23	0.21	> 40m
	$n_{b,wet} = 0.37$	0.19	0.17	0m

4.8 Discussion

Feijão Dam 1 was marginally stable against undrained loading such that only minor loading changes were required to trigger undrained failure. Relatively small changes in shear stress were sufficient to initiate post-peak strain-softening and progressive failure in the fine tailings. Results showed that either a modest wetting event or borehole induced disturbance could provide a large enough change in shear stresses to initiate progressive failure. Parametric analyses indicated that the time to failure may range from a few hours to upwards of two months. It is unlikely however that the longer times to failure would occur in the field as it is likely that the fine tailings would consolidate over that time scale. The estimated time to 50% consolidation for the fine tailings is about 2 days and 35 days for drainage lengths of 1 m and 4 m respectively, based on the estimated hydraulic conductivity and compressibility for these soils. The coarse tailings would consolidate in considerably less time than the fine tailings as they behaved drained during CPT penetration. This indicates that wetting from rainfall events months earlier was unlikely to

be the sole cause of the failure although more recent rainfall events may have been a contributing factor.

The characterization of the fine tailings was critical to the overall stability of the dam as it was the weakest material near the dam face and laterally continuous over large distances in regions with high initial static shear stresses. These analyses showed that relatively simple site characterization techniques common in geotechnical practice were sufficient to predict the undrained failure. The $s_{u,pk}/ \sigma'_{vc}$ of 0.2 to 0.22 for the fine tailings was supported by a synthesis of results from procedures common in geotechnical practice for fine-grained (cohesive) materials including: (1) interpretation of CPT data using an N_{kt}, (2) limited data from laboratory tests and in-situ vane shear tests, and (3) empirical expectations for DSS loading mode of normally consolidated, plastic silts. This method of strength characterization resulted in similar strengths to those characterized by CIMNE which utilized a state parameter-based approach. Estimates of undrained strength (and other critical geotechnical properties) are best supported by a synthesis of different applicable approaches while recognizing the limitations and biases of each approach.

The present analyses illustrate the need to consider consolidated, undrained strengths when evaluating stability of earthen structures. However, as noted by Shewbridge (2019), significant books (Duncan et al. 2014) and manuals (USACE 2003) do not consider long-term, consolidated, undrained strengths when assessing stability. Other texts (e.g., Ladd 1991) recommend considering consolidated, undrained strengths when evaluating long-term stability recognizing that failures in low OCR clays are rapid and can occur without notable changes in loading. Based on present results and other

recent slope failures in fine-grained soils, evaluations of long-term stability should always consider undrained shear strengths in fine-grained (cohesive) soils.

4.9 Conclusion

Two-dimensional nonlinear analyses of the 2019 Feijão Dam 1 failure were performed using the finite-difference program FLAC 8.1 with the user defined constitutive models PM4SiltR and PM4Sand. Feijão Dam 1 was an 86-meter tall tailings impoundment built with upstream construction that occurred on January 25th, 2019. Negligible deformations were observed prior to the failure. Two prior investigations into the failure utilized a state parameter-based approach for strength characterization and found that the failure was due to either wetting induced internal creep (Robertson et al. 2019) or drilling induced strength loss (Arroyo and Gens 2021). The present analyses primarily utilized the characterized index properties and drained strengths from the EPR. The undrained strengths were reevaluated using other methods commonly used in geotechnical practice including analysis of CPT data using an N_{kt}, limited laboratory data, and empirical correlations for DSS loading in low plasticity silts and clays for the fine tailings and a CPT based D_r and remolded strength ratio approach for the coarse tailings. The strength characterization resulted in undrained strengths similar to the strengths obtained with the state parameter-based approach used by CIMNE.

Simulation results indicated that the dam was marginally stable against undrained loading and that both wetting induced internal creep and drilling induced strength loss were potential failure triggers. The failure initiated in a fine tailings layer with high static shear stresses and the failure band progressively developed in time. Drilling-induced strength loss triggered slope instability when the idealized strength loss occurred along the critical

failure surface. Sensitivity analyses indicated that increased rates of strain-softening and increased magnitude of viscous effects increases the potential for a progressive undrained failure to develop in the strain-softening tailings. Undrained stability was further assessed in a FS framework using the SSRM method and the FS against undrained failure was 1.06.

The results of these analyses indicate that nonlinear stability analyses using this combination of tools (FLAC with PM4SiltR and PM4Sand) and characterization methods were in reasonable agreement with the observed field behavior. The analyses were shown to capture the shape and pattern of the failure mechanism, the susceptibility to instability due to minor loading changes, and the small deformations and minimal pore pressure changes prior to the collapse. However, assessing the magnitude of deformations necessary to induce undrained long-term instability is complicated by issues surrounding modeling strain-softening and localization.

4.10 Acknowledgements

The work described herein was supported by the California Department of Water Resources under Contract 4600009751. Any opinions, findings, or recommendations expressed herein are those of the authors and do not necessarily represent the views of this organization. The authors appreciate the above support.

Chapter 5 : Seismic Deformations of a Levee Over Soft Clay of Varying Sensitivity

Original publication:

Oathes, T.J., and Boulanger, R.W. (2020). "Seismic deformations of a levee over soft clay of varying sensitivity." Proc. 40th USSD Annual Meeting and Conference, United States Society on Dams, Denver, CO, 1-15.

Abstract

Nonlinear dynamic analyses are used to investigate how seismic deformations of a 6-m tall levee founded on a deposit of normally consolidated clay may vary with the sensitivity of the clay. The results are used to evaluate how strain-softening and associated strength loss affects the seismic response and deformation pattern under different conditions. The analyses considered cases with clay layers of 6 m and 16 m thick and input ground motions scaled to three intensity levels. The PM4Silt constitutive model was calibrated to provide sensitivities (ratio of peak to remolded undrained shear strength) of 1, 2, and 4. The analysis results showed that strain-softening and associated strength loss in the clay layer increased with increasing clay sensitivity, but it did not result in increased levee deformations for the conditions examined. Instead, the results showed that increasing clay sensitivity slightly reduced the levee deformations, which was attributed to the strength loss in the clay also causing a reduction in the accelerations that developed at the levee level. These findings are only applicable to the conditions examined, wherein the models remained statically stable at the end of strong shaking.

5.1 Introduction

Seismic performance of levees, dams or embankments founded on normally-consolidated (NC) clays is commonly evaluated based on the estimated deformations during anticipated earthquake loading (Beaty and Perlea 2015). Analysis of these structures commonly starts with simple methods (such as Newmark's) and progresses to more involved methods including non-linear dynamic analyses (NDAs). The numerous details and limitations of the NDA procedures used to model the complex behavior of NC clays need to be well-documented to facilitate interpretation and review of the results (Boulanger and Beaty 2016). One important source of uncertainty is the constitutive model and its calibration.

The calibration process for constitutive modeling of NC clays or plastic silts requires decisions about what soil behaviors to emphasize, including details of the shear strength, strain-softening, cyclic mobility and dynamic properties. Decisions regarding one soil behavior can have large impacts on other simulated soil behaviors, as seen in the relationship between strain-softening and cyclic mobility. For these behaviors, a decision may need to be made regarding whether the monotonic or dynamic behavior is more critical to the current analysis. An additional complication is that strain-softening cannot be simulated using simple elastic-plastic constitutive models, such as Mohr-Coulomb models, without modifications.

The purpose of this paper is to investigate how seismic deformations of a levee founded on a deposit of NC clay may vary with sensitivity of the clay. NDAs with the finite difference program FLAC 8.0 (Itasca 2016) and user-defined constitutive model PM4Silt (Boulanger and Ziotopoulou 2019) are used to evaluate how strain-softening and

associated strength loss affects the seismic response and deformation pattern under different conditions. Strain-softening characteristics of sensitive clays are reviewed briefly. The NDA modeling procedures, two model geometries (varying the clay layer thickness), and input ground motions are described. The constitutive models and calibration procedures are described, followed by results showing the simulated material responses for three alternative calibrations that correspond to sensitivities (ratio of peak to remolded undrained shear strength) of 1, 2, and 4. NDA results are presented for the three calibrations, two model geometries, and three shaking intensities to illustrate various aspects of how the strain-softening behavior affected the dynamic responses, strain concentrations, and levee deformations. The results show that strain-softening and associated strength loss in the clay did not increase the levee deformations for the conditions examined, since the loss of strength in the clay also caused a reduction in the accelerations that developed at the levee level.

5.2 Strain-softening in Sensitive Clays

Experimental studies have shown that strain-softening can occur over a large range of strains in sensitive clays. Triaxial compression tests on sensitive Norwegian clays have shown strength drops of approximately 50% prior to the accumulation of 10% shear strain (Bjerrum and Landva 1966). Other experimental studies on highly sensitive clays have shown that strength degradation is relatively modest over the range of strains seen in laboratory element tests (Lefebvre and LeBoeuf 1987). The difference in these behaviors may be partly attributed to both material differences and test limitations (e.g., boundary conditions). Field vane shear tests can measure strength loss at large strains but generally do not assess the rate or strain range over which the strength loss occurs,

although limited research has investigated the potential for using the field vane to assess the rate of strain-softening (Ansari et al. 2014). The interpretation of strain-softening rates from laboratory and field test data is an important consideration when calibrating constitutive models to strain-softening behaviors.

To account for strain-softening and sensitivity of clays in NDAs, relatively complex modeling procedures are required (Kiernan and Montgomery 2019). One difficulty in modeling strain-softening clays is the strength degradation (or remolding) that occurs under both monotonic and cyclic loading, including the complex strain histories that can develop beneath a slope under seismic loading (Beaty and Dickenson 2015). More complex modeling procedures, such as plasticity and bounding surface constitutive models, often require more inputs and user choices to implement. The additional inputs and choices require greater emphasis on transparency and documentation for ensuring that the calibration captures the desired behavior reasonably well.

Further complicating the numerical modeling of clays is the tendency for strain-softening clays to localize, as well as the strain-rate dependency of clay behavior. Clays have been shown to have an increase in shear strength of approximately 9% to 15% per logarithmic cycle of strain-rate depending on the soil (Graham et al. 1983); a 10% percent strength increase per logarithmic cycle is commonly used in practice (Kulhawy and Mayne 1990). The strain-rate dependence also influences the strains at which the soil tends to develop localizations during shearing. Strain-rate dependency has been shown to delay the onset of localizations (Needleman 1988; Oathes and Boulanger 2019) to larger accumulated global shear strains or displacements. Both these clay behaviors are important considerations when modeling strain-softening clays.

5.3 Non-linear Dynamic Analyses

5.3.1 Model and Simulated Geometries

Two-dimensional NDAs of a set-back levee overlying a soil profile with a thick deposit of normally consolidated clay, as shown in Fig. 5-1, were performed using the finite difference program FLAC 8.0 (Itasca 2016). The NC clay layer is overlain by a 2-m thick sand layer and underlain by a dense sand layer. The levee is 6.0 m tall with a 6.0 m wide crest and upstream and downstream slopes of 2.5H:1V. Two model geometries, as shown in Fig. 5-1, are used to investigate the effect of the thickness of the clay layer on the dynamic performance of a dry levee. Geometry 1 contains a 16-m-thick clay layer underlain by a 10-m-thick base layer, whereas Geometry 2 has a 6-m-thick clay layer underlain by a 20-m-thick base layer. The water level is at the interface between the crust and the clay layer (2 m below the ground surface). The levee and crust were modeled dry to model a set-back levee during non-flood stage loading. The horizontal expanse of the model was 180 m to mitigate the effect of the lateral boundaries on the simulation results. The mesh for the analysis contains soil elements 0.5 meters tall by 0.6 meters wide. This element thickness corresponds to $1/8^{th}$ of a wavelength at 25 Hz with a small strain V_s of 100 m/s, or $1/8^{th}$ of a wavelength at 12.5 Hz with a degraded or effective V_s of 50 m/s. The base was modeled with rigid boundary conditions while the sides were free and attached together to move uniformly.

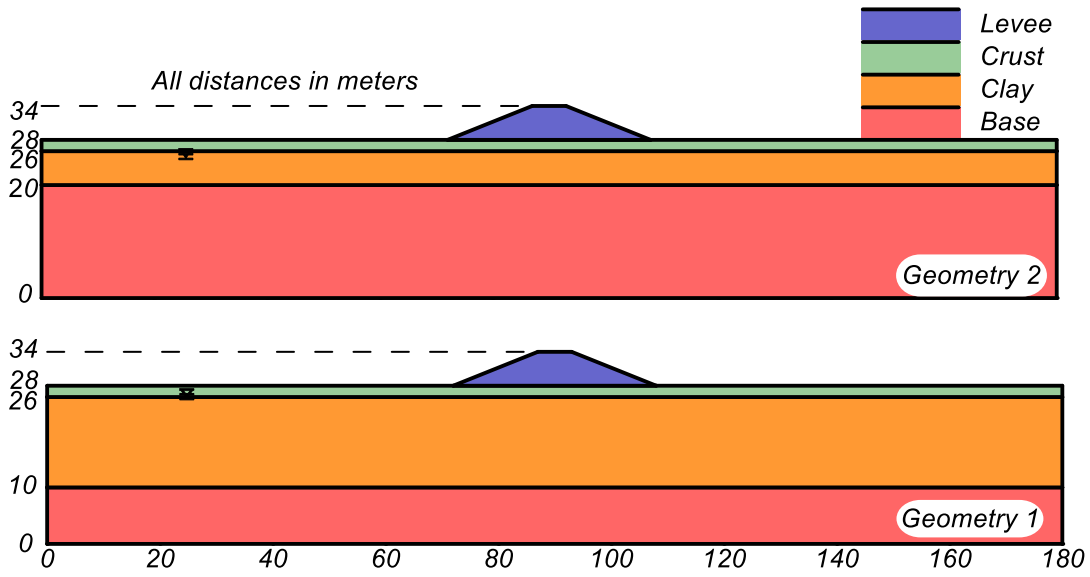

Figure 5-1: Levee geometry for NDAs with a 16-m thick clay layer (Geometry 1, bottom) and a 6-meter-thick clay layer (Geometry 2, top)

5.3.2 Ground Motions and PGA

The models were subjected to horizontal and vertical acceleration time series that were linearly scaled to produce peak horizontal ground accelerations (PGA) of 0.2 g, 0.4 g, and 0.6 g. The motions were linearly scaled recordings from the Corralitos station during the 1989 Loma Prieta Earthquake. The scaled vertical and horizontal motions for a PGA = 0.6 g are shown in Fig. 5-2 (left). The motion has a significant duration (defined as duration of motion containing between 5% and 95% of the Arias Intensity) of approximately 8 seconds lasting from 2 to 10 seconds. The response spectrum for the vertical and horizontal motions (Fig. 5-3 right) have different predominant frequencies (approximately 5 Hz and between 1-2 Hz, respectively). The scaled accelerations were applied as within motions directly to the base of the model. Rayleigh damping of 0.5% at a frequency of 1.0 Hz was used to provide nominal damping at small strains.

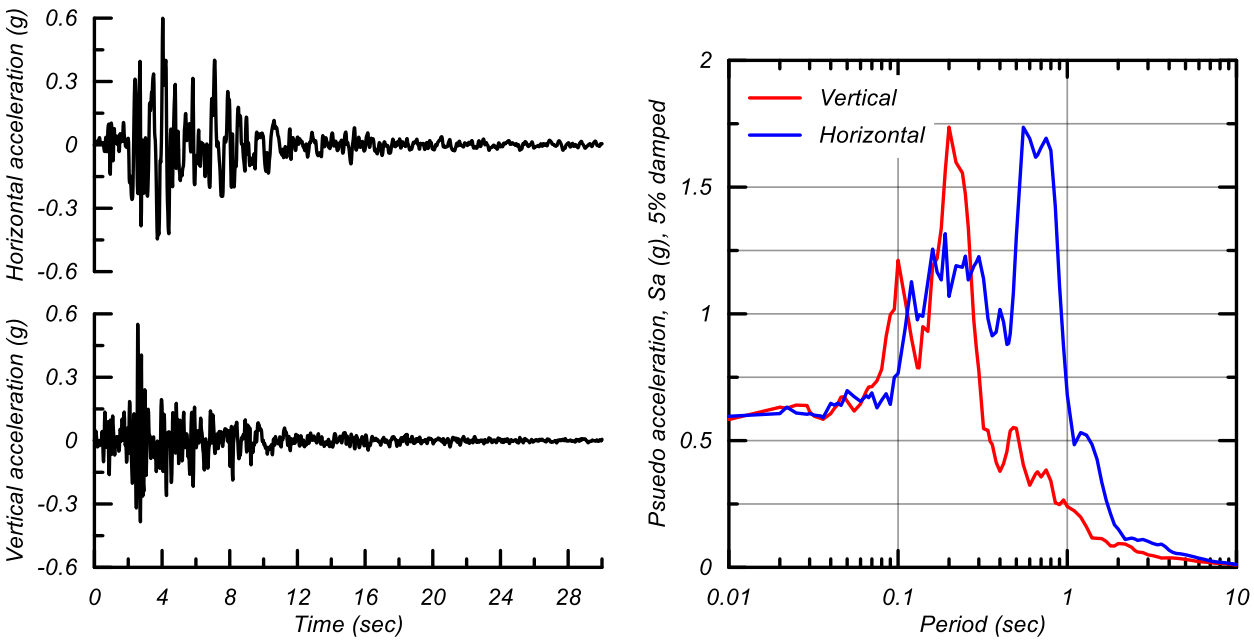

Figure 5-2: Linearly scaled acceleration time histories with a PGA = 0.6g (left) and pseudo acceleration spectrum (right)

5.4 Constitutive Models and Material Properties

The user-defined constitutive models PM4Silt and PM4Sand were used for the NC clay and levee/crust/base materials, respectively. The two models are described below, followed by details of their calibrations.

PM4Sand (version 3.1; Ziotopoulou and Boulanger 2016, Boulanger and Ziotopoulou 2017) is a critical state compatible, stress-ratio controlled, bounding surface plasticity model which follows the framework of the plasticity model developed by Dafalias and Manzari (2004) and was developed for geotechnical earthquake engineering applications. The model has 3 primary (required) inputs: (1) the apparent relative density (D_R), (2) the shear modulus coefficient (G_o), and (3) the contraction rate parameter (h_{po}). PM4Sand has an additional 21 secondary parameters with default values based on a generalized calibration, although they may be modified at the user's discretion.

PM4Silt (version 1; Boulanger and Ziotopoulou 2018, 2019) is a plasticity model that builds upon the PM4Sand constitutive model with adaptations to better approximate the response of silts and clays that follow stress-normalized behavior. PM4Silt has 3 primary (required) inputs: (1) the critical state undrained strength or undrained strength ratio (s_u or s_u/σ'_{cs}), (2) the shear modulus coefficient (G_o), and (3) the contraction rate parameter (h_{po}). The model has 20 secondary parameters that similarly have default values based on a generalized calibration or can be adjusted based upon site-specific data.

5.4.1 Base, Crust, and Levee

The base, crust, and levee materials were modeled using the PM4Sand model with the primary input parameters shown in Table 5-1. All secondary parameters were given their default values. The levee was modeled as a dense sand with a relative density of 75% while the crust is modeled as a medium dense sand with a relative density of 55%. The base is a very dense sand with a relative density of 87%. The permeability for these three materials is 10^{-5} cm/sec with a dry density of 1.64 Mg/m^3.

Table 5-1: PM4Sand input parameters for the levee, crust, and base materials

Layer	D_R	G_o	h_{po}
Levee	0.75	890	0.63
Crust	0.55	677	0.4
Base	0.87	1025	0.63

5.4.2 Clay Layer

The clay layer was modeled using the PM4Silt constitutive model. Three calibrations with varying sensitivities (1, 2, and 4) were developed with the goal of retaining similar peak undrained shear strengths and similar cyclic strengths. The three calibrations produce a peak undrained strength ratio ($s_{u,pk}/\sigma'_{vc}$) = 0.25 and similar cyclic strength ratios for different numbers of loading cycles, as demonstrated below. The calibration process for

the different calibrations largely follow the procedures outlined in Boulanger and Wijewickreme (2019).

The input parameters for the three calibrations are listed in Table 5-2. All parameters retained default values except for the primary input parameters and the secondary bounding surface parameter $n^{b,wet}$. For Calibration 1, the critical state undrained strength ratio ($s_{u,cs}/\sigma'_{vc}$) was set to 0.25 and then $n^{b,wet}$ was set to 1.0 which eliminates any post-peak softening. For Calibrations 2 and 3, $s_{u,cs}/\sigma'_{vc}$ was reduced because it represents the strength after full remolding, and then $n^{b,wet}$ was reduced (which raises the bounding surface) to obtain the target $s_{u,peak}$. The shear modulus coefficient (G_o) was the same for all three calibrations to ensure the models exhibited similar small strain behavior. The contraction rate parameter (h_{po}) was adjusted to produce similar cyclic strength ratios for different numbers of uniform loading cycles. The clay had a permeability of 10^{-8} cm/sec and a dry density of 1.48 Mg/m^3.

Table 5-2: PM4Silt input parameters for three calibrations with varying sensitivities

Calibration	S_t	$s_{u,cs}$ / σ'_{vc}	$n^{b,wet}$	G_o	h_{po}
1	1	0.25	1	250	75
2	2	0.125	0.41	250	300
3	4	0.0625	0.25	250	800

5.4.2.1 Monotonic Behavior

The stress-strain and stress path responses for the three calibrations are shown below in Fig. 5-3 for single element simulations subjected to monotonic undrained Direct Simple Shear (DSS) loading. Models were consolidated at a confining pressure of 50 kPa with a K_o = 0.5. The simulated stress strain responses are the same for all three calibrations until the peak shear stress is mobilized. Post-peak, Calibration 1 only slightly strain-hardens while Calibrations 2 and 3 begin to strain-soften immediately. At 10%

engineering shear strain (i.e., twice the shear strains reported in FLAC), Calibration 2 has lost approximately 1/3 of its peak strength while Calibration 3 has lost over ½ of its peak strength (Fig. 5-3 left). The progressive reduction in shear resistance with Calibrations 2 and 3 coincides with a progressive reduction in effective vertical stress as shear strains increase (Fig. 5-3 right). Shear strains of about 41% and 28% are required for Calibrations 2 and 3, respectively, to reach 90% of their eventual strength losses.

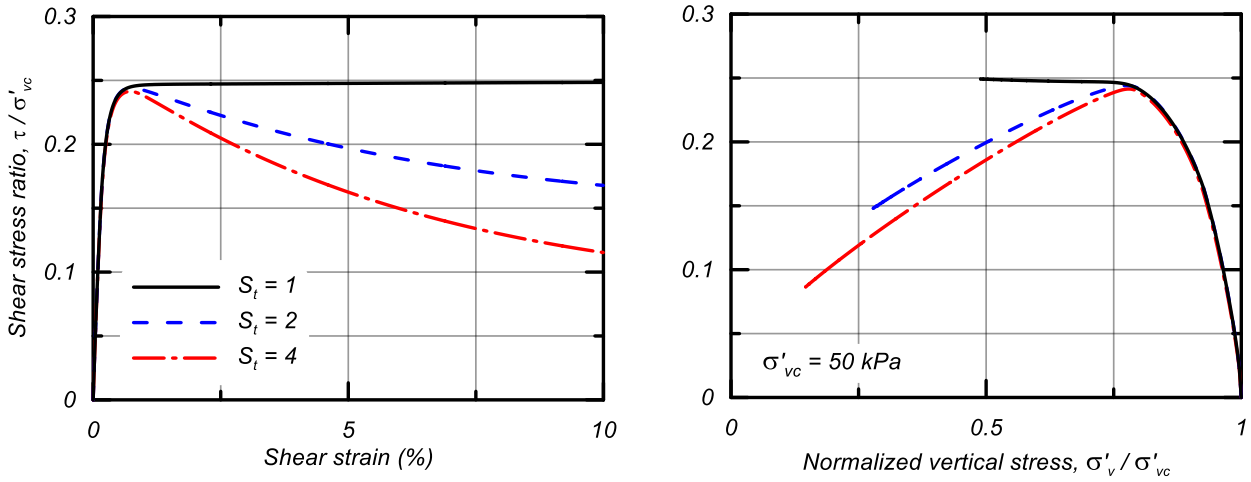

Figure 5-3: Stress-strain (left) and stress path (right) responses for undrained DSS monotonic loading for calibrations with sensitivities of 1 (black), 2 (blue), and 4 (red)

5.4.2.2 Modulus Reduction and Damping

Undrained, strain controlled cyclic DSS simulations were used to develop shear modulus reduction and equivalent damping ratio curves for the three calibrations. The results of these simulations are shown below for consolidation with K_o = 1.0 (for better consistency with empirical relationships) in Fig. 5-4 and are compared to the empirical relationships by Vucetic and Dobry (1991). Loading consisted of three cycles of loading at each strain level and the data presented consists of the secant shear modulus and damping ratio from the last cycle at each strain level.

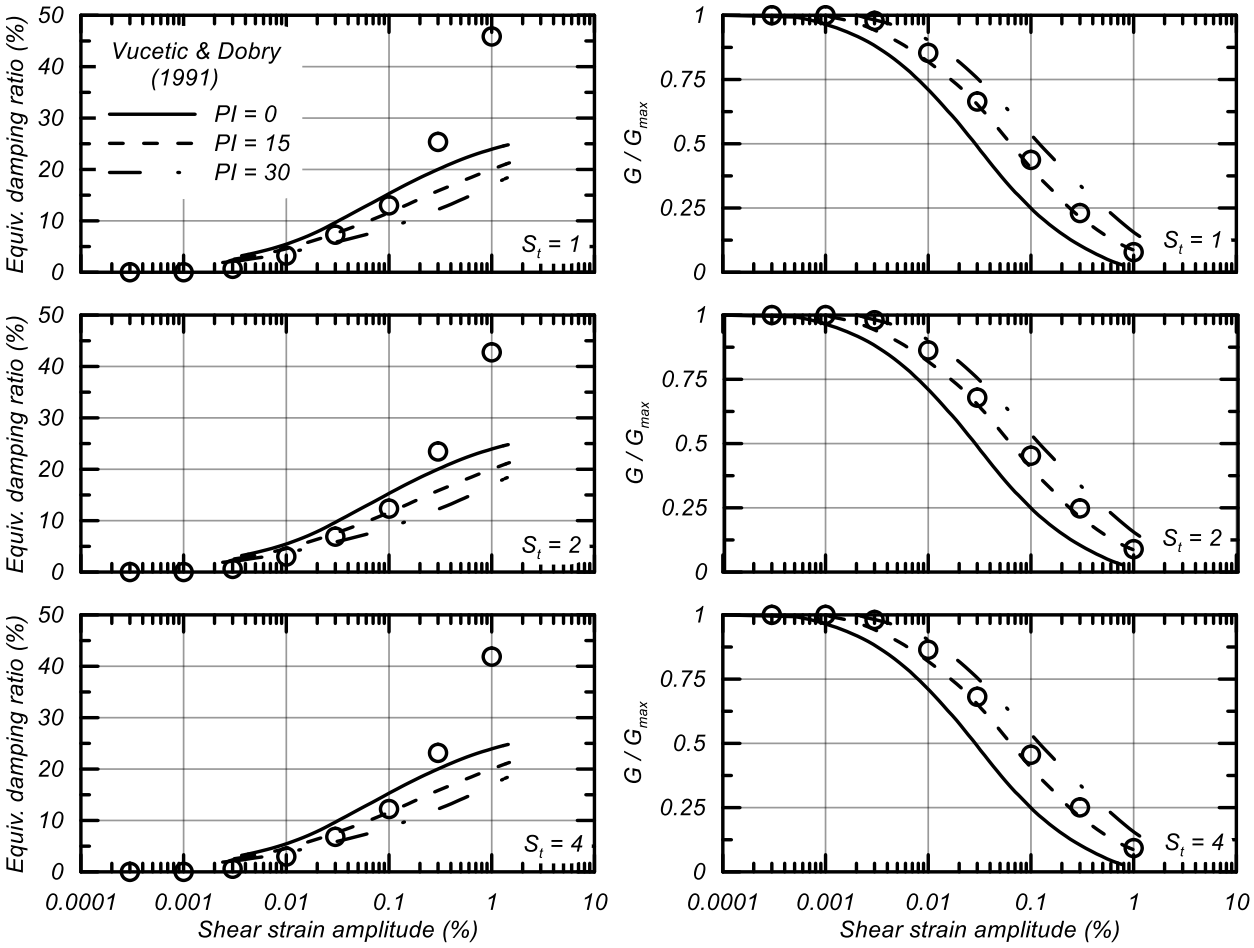

Figure 5-4: Equivalent damping ratio (left) and shear modulus reduction (right) curves for the three calibrations compared with relationships by Vucetic and Dobry (1991)

The modulus reduction and equivalent damping ratios for the three calibrations are relatively similar. This is anticipated because the secondary parameters that control shear modulus reduction and equivalent damping ratios were set to the default values for all three calibrations, leading to the similar behaviors. The results of the simulations agree reasonably well with the PI = 15 empirical curve from Vucetic and Dobry (1991) for the shear modulus reduction curves. Similarly, at strain levels below 0.1% the equivalent damping ratio curves agree reasonably well with the PI = 15 empirical data. At larger strain levels the simulated equivalent damping ratio curves are larger than seen in the empirical data, which is a common limitation of elastic-plastic constitutive models.

5.4.2.3 Cyclic Behavior

Simulations of stress ratio controlled cyclic undrained DSS loading were performed for the three calibrations. Single element models loaded with different cyclic stress ratios were used to provide a basis for adjusting the parameters controlling cyclic strengths. The contraction rate parameter (h_{po}) was iterated upon to develop calibrations that had reasonably similar cyclic strengths and similar mobility when possible. Increasing h_{po} slows the accumulation of cyclic shear strains, and thus larger h_{po} values are needed for calibrations with larger sensitivities and increased rates of strain-softening.

Results of the simulations with a vertical consolidation stress of 50 kPa and $K_o = 0.5$ are presented in Fig. 5-5 showing the cyclic strength ratio ($\tau_{cyc}/s_{u,pk}$) versus the number of uniform stress cycles to cause 3% peak single amplitude shear strain. The calibrations have similar cyclic strength ratios across the full range in number of uniform loading cycles, as desired. The cyclic strength ratio near a single loading cycle is similar for all three calibrations because it is controlled by the peak undrained shear strength, which is approximately the same for all three calibrations as shown previously. The cyclic strength ratio at larger numbers of loading cycles is controlled by the h_{po} values, which needed to be increased as the sensitivity increased (Table 5-2) to provide similar number of cycles to 3% single amplitude shear strain at a given $\tau_{cyc}/s_{u,pk}$ for all three calibrations to isolate the effect of sensitivity on the dynamic response.

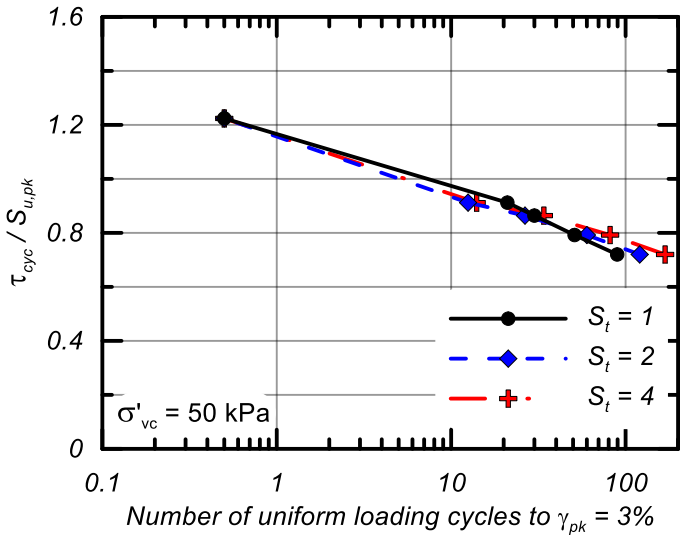

Figure 5-5: Cyclic strength ratio versus number of uniform cycles to 3% peak single amplitude shear strain for calibrations with sensitivities of 1 (black), 2 (blue), and 4 (red)

The simulated stress–strain and stress path responses for cyclic loading at a $\tau_{cyc}/s_{u,pk}$ = 0.92 are shown in Fig. 5-6. This $\tau_{cyc}/s_{u,pk}$ requires approximately 15 cycles to reach 3% peak single amplitude strain. The three calibrations have similar stress-strain responses until the peak shear strain reaches about 0.7% (corresponds to the stress paths reaching the bounding surfaces), after which the rate of shear strain accumulation varies with the sensitivity. For Calibration 1, the shear strains accumulate exponentially with increasing cycles after shear strains exceed about 0.7%. For Calibrations 2 and 3, the specimen begins to strain soften and becomes unstable once shear strains exceed about 0.7%, which is consistent with their sensitivities. For these cases, the stress-strain responses at larger strains essentially follow a monotonic path toward full remolding. This is due to the strain-softening tendencies of a sensitive soil that is subjected to stress-ratio controlled loading, wherein the material eventually cannot resist the imposed shear stress.

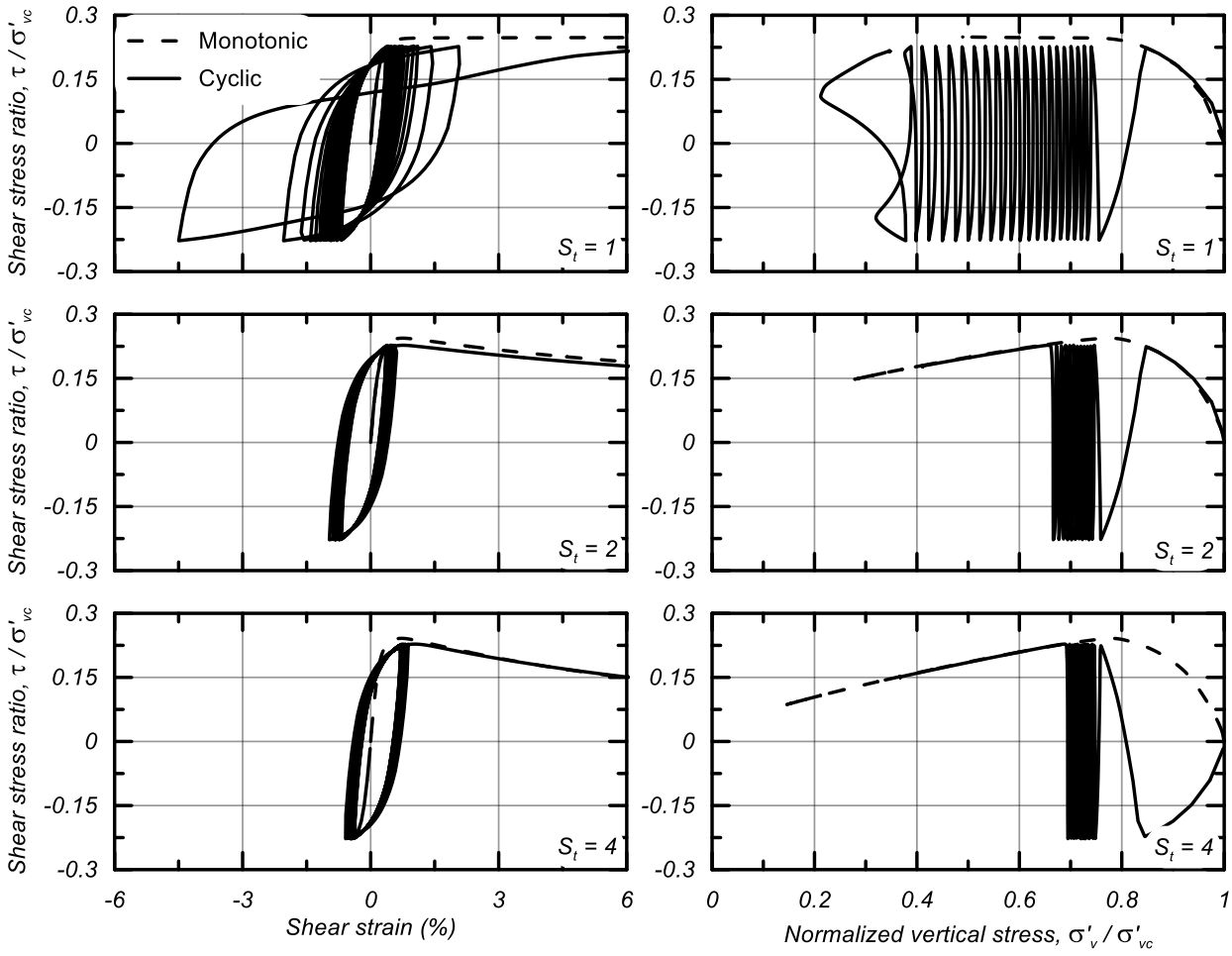

Figure 5-6: Simulations of cyclic undrained DSS loading for the three calibrations subjected to $\tau_{cyc}/s_{u,pk}$ = 0.92: stress-strain (left) and stress path (right)

5.5 NDA Results

Results for NDAs with different combinations of model geometry, sensitivity, and input motion PGA are presented below. Simulations with Geometry 1 were performed using all three calibrations and three different input motion PGA's. Simulations with Geometry 2 were performed with all three calibrations at a PGA = 0.6 g.

The deformed levees with contours of shear strain are shown in Fig. 5-7 for both geometries and all three calibrations (total of six cases), subjected to the input motion scaled to a horizontal PGA = 0.6 g. The contours in Fig. 5-7, show that the shear strains

concentrated in the bottom row of elements in the clay layer, just above the stronger base layer, for all six cases. Note that shear strains in excess of 60% develop in these zones for some cases, but all shear strains greater than 15% are plotted with the same color to retain resolution at the smaller strain levels. Shear strains can be expected to localize (or concentrate) where the ratio of the shear demand to shear resistance was greatest. This occurs at the base of the clay layer because the undrained shear strength is proportional to effective consolidation stress, the seismic shear stresses are more proportional to total stresses, and the ratio of total to effective stress increases with depth in the model. Shear strains greater than 15% developed in the bottom row of elements in the clay layer for all six cases, with the extent of these larger shear strains being least for the thicker clay layer (Geometry 1) with the least sensitive clay (Calibration 1). Shear strains in the rest of the clay layer were generally less than 15% for Geometry 1 with all three calibrations, but did exceed 15% in shear zones that formed up through the clay layer beneath the levee for Geometry 2 with all three calibrations. For either geometry, the strain contours for all three calibrations are relatively similar despite the differences in clay sensitivity.

The levee crest settlement and maximum shear in the clay layer for both geometries and all three calibrations for the input motion PGA = 0.6 g are shown in Fig. 5-8. The crest settlements progressively reduced as the clay sensitivity increased. For Geometry 1, the crest settlements were about 67, 65, and 51 cm for Calibrations 1, 2, and 3, respectively. For Geometry 2, the crest settlements were about 56, 48, and 42 cm for Calibrations 1, 2, and 3, respectively. The crest settlements for Geometry 2 with its thinner clay layer are about 70-85% of those for Geometry 1.

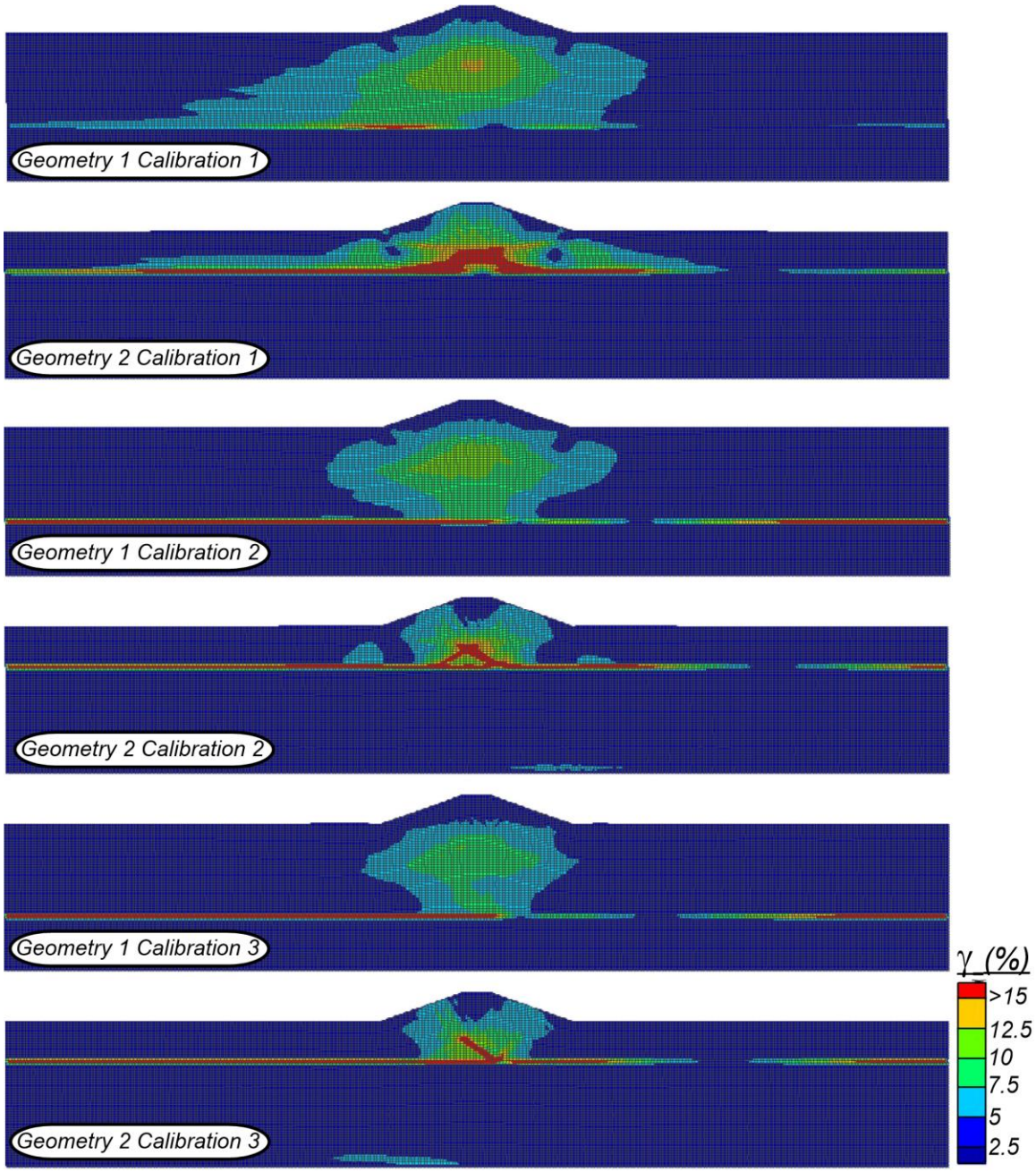

Figure 5-7: Shear strain contours for simulations with both geometries and all three calibrations for the input motion PGA = 0.6g

The maximum shear strains in the clay layer did not follow the same trends as the crest settlements (Fig. 5-8), and instead showed a stronger dependence on the clay layer thickness. For the thicker clay layer of Geometry 1, maximum shear strains were about 12% with Calibration 1, increasing to about 36-39% with Calibrations 2 and 3. For the

thinner clay layer of Geometry 2, significantly larger shear strains of 60-64% were obtained for all three calibrations.

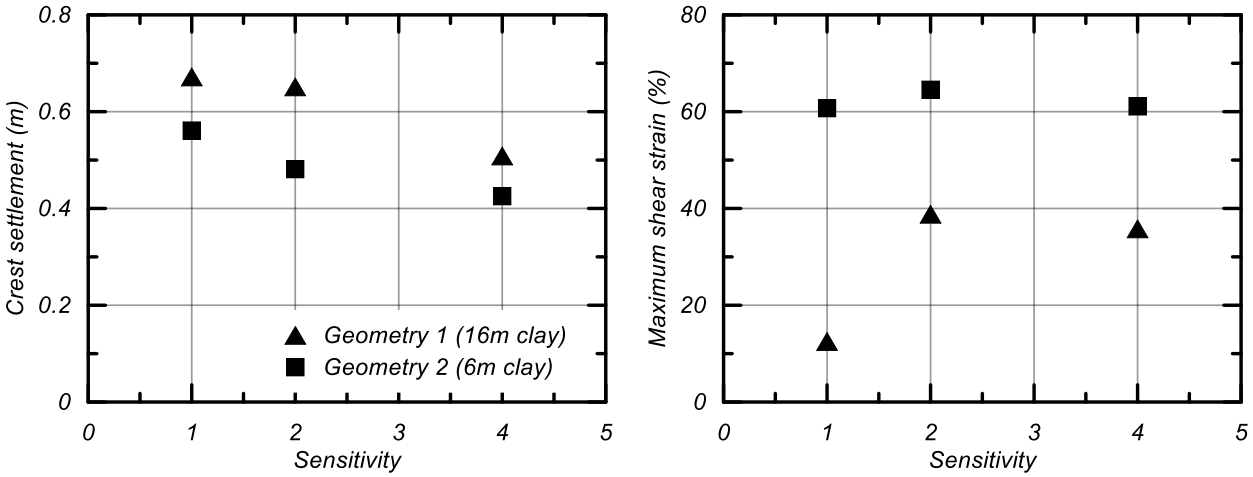

Figure 5-8: Crest settlement (left) and maximum shear strain in the clay layer (right) versus sensitivity for simulations with a PGA = 0.6g

Levee crest settlements at lower input motion PGAs were relatively insensitive to the different calibrations. The crest settlements for all three calibrations were about 24-25 cm for an input motion PGA = 0.2 g and about 48-50 cm for an input motion PGA = 0.4 g. The maximum shear strains in the clay layer for all three calibrations were about 2.5% for an input motion PGA = 0.2 g and about 5-16% for an input motion PGA = 0.4 g. The zones of strain concentration for the PGA = 0.2 g and 0.4 g motions were also significantly smaller than observed for the PGA = 0.6 g motion.

The effect of clay sensitivity on dynamic and stress-strain responses is examined in Fig. 5-9 showing time series of acceleration at the levee crest (bottom row) and shear stress (middle row) and shear strain (top row) in the clay just above the base layer for Calibrations 1 (left column) and 3 (right column). The levee crest accelerations for Calibration 3 (sensitivity of 4) are significantly smaller than those for Calibration 1

(sensitivity of 1), other than one acceleration pulse early in strong shaking. Fig. 5-10 shows the response spectra of the horizontal input motion (scaled to PGA = 0.6g) and the crest acceleration time histories from Fig. 5-9. Yielding of the clay results in deamplification of the spectral accelerations in the period range of 0.2 to 0.9 sec. At periods shorter than 0.2 seconds, amplification is observed due to high frequency acceleration pulses and possibly high frequency numerical noise. At periods larger than 1 second the S_t = 4 simulation results in lower spectral accelerations than the S_t =1 simulation. The peak shear stress ratios in the clay for Calibration 3 progressively decreases from absolute values of about τ/σ'_{vc} = 0.25 (the negative values in the Fig. are because this point is located left of the levee centerline) at about 3 seconds into strong shaking to fully remolded values of about τ/σ'_{vc} = 0.06 after about 5 seconds of strong shaking. The peak absolute shear stress ratios for Calibration 1 remain much higher, which shows that the insensitive clay continued transmitting greater shear stresses and that produced greater accelerations at the levee elevation. The shear strains for Calibration 3 increase to about 60% at the end of strong shaking versus about 50% for Calibration 1. The final shear strains are not significantly greater for Calibration 3 despite the remolding and loss of shear strength in the bottom row of clay elements. The small difference in final shear strains is generally consistent with the small differences in levee crest settlements, as shown previously in Fig. 5-8.

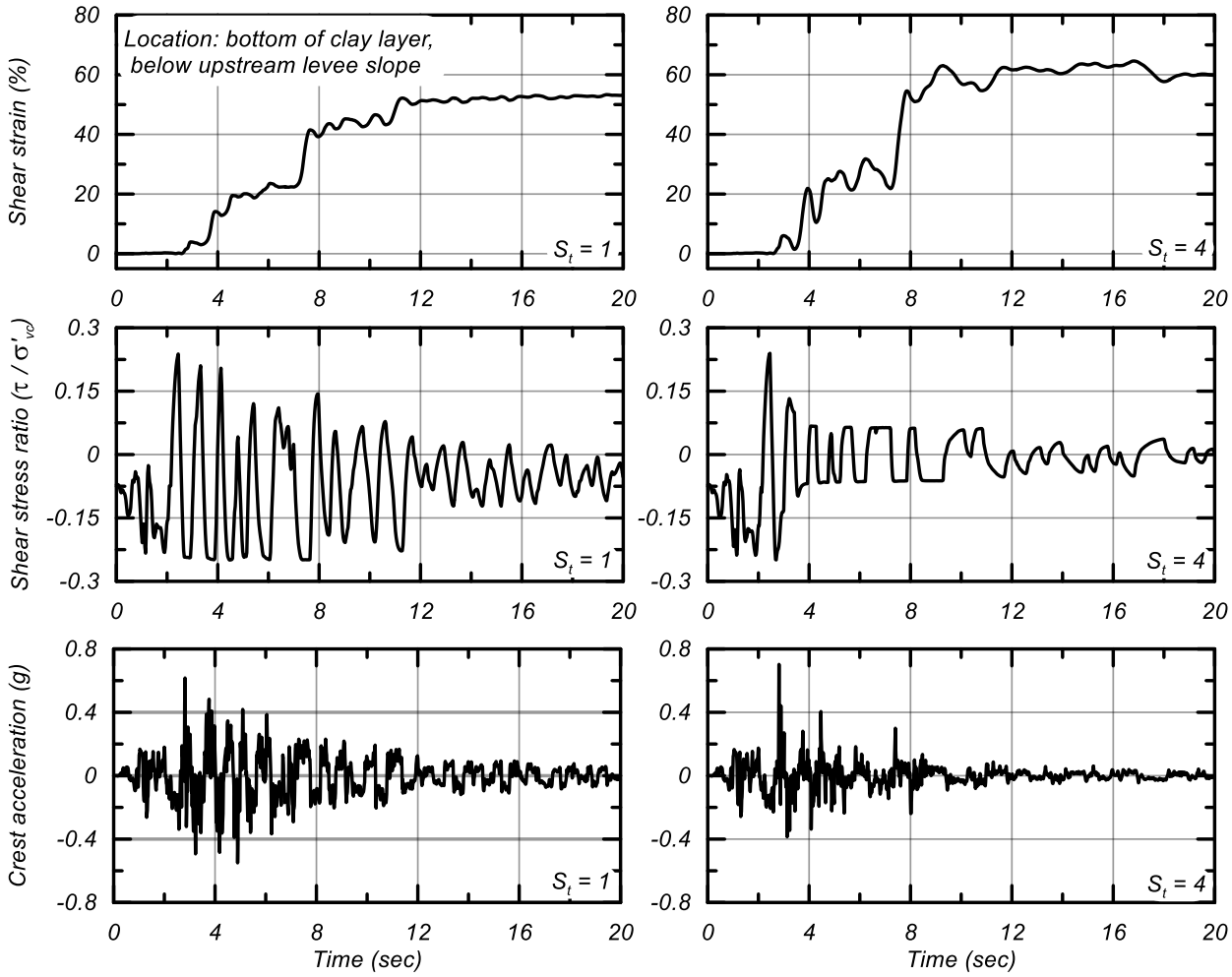

Figure 5-9: Shear stress and shear strain in an element at the base of the clay layer and acceleration at the levee crest for Geometry 2 and PGA = 0.6g: Calibration 1 (left side) and Calibration 3 (right side)

The relatively small effect that clay sensitivity had on levee deformations and maximum strains in the clay layer for these levee geometries, as shown in Figs. 5-7 and 5-8, is attributed to two compensating effects. The strength loss due to remolding with Calibration 3 (sensitivity of 4) lowers the factor of safety against static instability, which would be expected to increase levee deformations if the seismic loading was unchanged. However, the progressive strength loss along the bottom of the clay layer also reduced the accelerations transmitted to the levee level, which would be expected to reduce levee deformations if the clay strengths were unchanged. The compensating effects of reduced

strengths and reduced seismic loads resulted in the levee deformations actually decreasing slightly as the clay sensitivity was increased from 1.0 to 4.0 (Fig. 5-8).

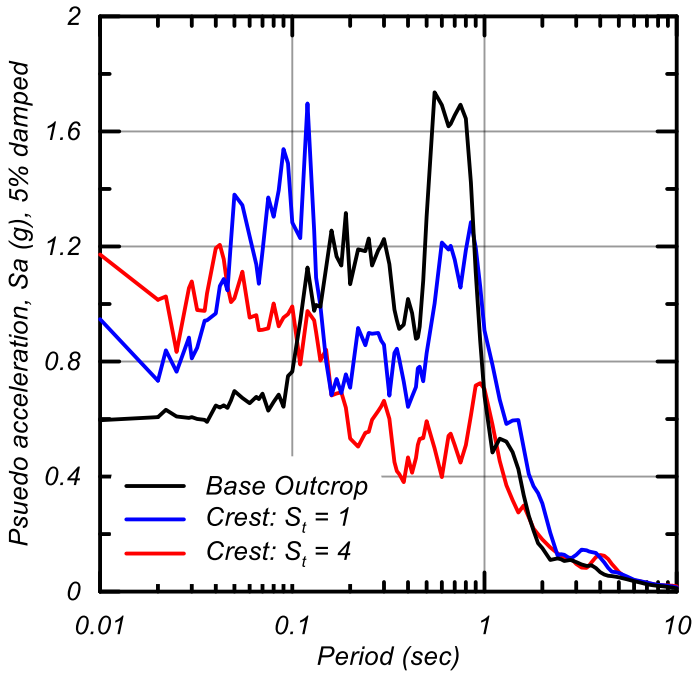

Figure 5-10: Acceleration response spectrums of horizontal input and crest acceleration time histories from Fig. 5-9

5.6 Conclusions

Nonlinear dynamic analyses were used to investigate how seismic deformations of a 6-m tall levee founded on a deposit of normally consolidated clay may vary with the sensitivity of the clay. The analyses, performed using the finite difference program FLAC 8.0 with the user-defined constitutive models PM4Silt and PM4Sand, were used to evaluate how strain-softening and associated strength loss affected the seismic response and deformation pattern under different conditions. The analyses considered two model geometries (clay layers of 6 m and 16 m thickness) and an input ground motion scaled to three intensity levels. Three calibrations for the clay were developed with PM4Silt, which corresponded to sensitivities (ratio of peak to remolded undrained shear strength) of 1, 2,

and 4. The analysis results showed that strain-softening and associated strength loss in the clay layer increased with increasing clay sensitivity, but it did not result in increased levee deformations for the conditions examined. Instead, the results showed that increasing clay sensitivity slightly reduced the levee deformations, which was attributed to the strength loss in the clay also causing a reduction in the accelerations that developed at the levee level. These findings are only applicable to the conditions examined, wherein the models remained statically stable at the end of strong shaking. In other situations, the progressive strength loss associated with clay sensitivity can lead to instability and thus the results of the present study should not be generalized to other conditions; a greater effect of clay sensitivity can be expected if the progressive strength loss results in a loss of stability.

Future research is expected to include further simulations examining the influence of ground motion selection, mesh dependency, and the rate of strain-softening within the clay layer. The goal is an improved understanding of the effect that strain-softening and associated strength loss can have on the seismic performance of dams and levees founded on sensitive, normally consolidated clays.

5.7 Acknowledgments

The work described herein was supported by the California Department of Water Resources under Contract 4600009751. Any opinions, findings, or recommendations expressed herein are those of the authors and do not necessarily represent the views of this organization. The authors appreciate the above support.

Chapter 6 : Influence of Sensitivity and Rate of Strength Loss on Seismic Deformations of a Levee

Original publication:

Oathes, T.J., Boulanger, R.W., and Friesen, S. (2021). "Influence of sensitivity and rate of strength loss on seismic deformations of a levee." Proc. Dam Safety 2021. ASDSO, Nashville, Tennessee, Sept. 12-15, 2021.

Abstract

Evaluating the seismic deformation of levees can require accounting for a wide range of soil types, including liquefiable sands and silts, soft organics and peats, and soft clays. In some situations, the potential for earthquake-induced strength loss in soft clays of medium or greater sensitivity can be a significant concern and source of uncertainty. Additionally, the rate of strength loss can vary greatly and strongly affect seismic deformation. This paper presents the results of nonlinear dynamic analyses (NDAs) of an idealized levee founded on soft clays to evaluate the influence of sensitivity and strain-softening on the estimated seismic deformations. Results of NDAs are compared with simplified procedures that combine limit equilibrium (LE) and Newmark sliding block methods. The tendency for simplified procedures to underestimate or overestimate seismic deformations compared with NDA results is shown to depend on the specific conditions (e.g., soil sensitivity and brittleness, ground motion intensity, margin of safety against instability) and how potential strength loss is accounted for in the simplified

methods. Limitations of the NDA and simplified methods for use with strain-softening, sensitive materials and the implications of these findings for practice are discussed.

6.1 Introduction

The Sacramento – San Joaquin Delta contains 1100 miles of levees (Burton and Cutter 2008) which overly a wide range of soil types, including liquefiable sands and silts, soft organics and peats, and soft clays. The delta is a significant source of fresh water to agriculture and urban users. Since much of the delta land is below channel water levels, levee failures draw in water, which can degrade water quality near delta pumping plants and inhibit the export of water. Earthquake induced levee failures are a scenario that has raised particular concern among delta water users. An earthquake near the delta could induce multiple levee failures, resulting in saltwater intrusion and extended outages at pumping plants and agriculture diversions. The large consequences highlight the need to accurately evaluate static and seismic stability of levees. Assessing stability in high seismicity regions requires accounting for potential earthquake induced strength loss in soft, sensitive clays and the potential for it to cause destabilization and deformation.

Evaluating seismic performance of levees typically involves simplified methods (such as limit equilibrium (LE) combined with Newmark sliding block methods), with more complex analysis procedures (such as nonlinear dynamic analyses (NDAs)) typically reserved for systems with higher potential consequences of failure. Simplified methods are unable to directly capture more complex soil behaviors such as liquefaction or strain-softening. In normally consolidated (NC) clays the potential for strain-softening and associated localization complicates the analysis regardless of the chosen method. When using simplified methods, the selection of clay shear strength needs to consider the

anticipated strength loss during earthquake shaking. Inclusion of strain-softening in NDA analyses introduces an inherent mesh dependency wherein the element size influences the rate of post-peak strength loss due to the concentration of shear strains within a narrow band. Often strength loss and localization are accounted for by implementing a localization length scale in NDA elements (Kiernan and Montgomery 2018*)* whereby internal strains depend on the element size and user-specified localization length scale. However, this approach requires the modeler to make the determination on when and how to invoke the length scale, which can vary widely from modeler to modeler.

This paper presents the results of nonlinear dynamic analyses (NDAs) of an idealized levee founded on soft clays to evaluate the influence of sensitivity and strain-softening on estimated seismic deformations. Results of NDAs using FLAC (Itasca 2019) with the user-defined constitutive models PM4Sand and PM4Silt are compared with a common simplified procedure that combines limit equilibrium (LE) with Newmark sliding block methods (or simplified method for brevity). The tendency for the simplified method to underestimate or overestimate seismic deformations in comparison with NDA results is shown to depend on the specific conditions and how potential strength loss is accounted for in the simplified method. Limitations of NDAs and simplified methods for estimating seismic deformations of earthen structures founded on or containing strain-softening, sensitive materials and the implications of these findings for practice are discussed.

6.2 Model and Ground Motions

This work investigates the deformations of an idealized set-back levee overlying a deposit of sensitive NC clay as shown in Fig. 6-1. Set-back levees are engineered levees placed

behind existing levees as secondary protection and are typically dry unless the existing levee fails. The levee is founded on a 2m thick over-consolidated (OC) clay crust, underlain by a 12m thick NC clay layer, underlain by a deep deposit of very dense sand (i.e., the base layer in Fig. 6-1). Two levees are modeled: one with a height of 6m and one with a height of 10m, with both having 2.5H:1V upstream and downstream slopes. The water level is located at the interface between the OC clay crust and the NC clay layer at a depth of 2m below the ground surface.

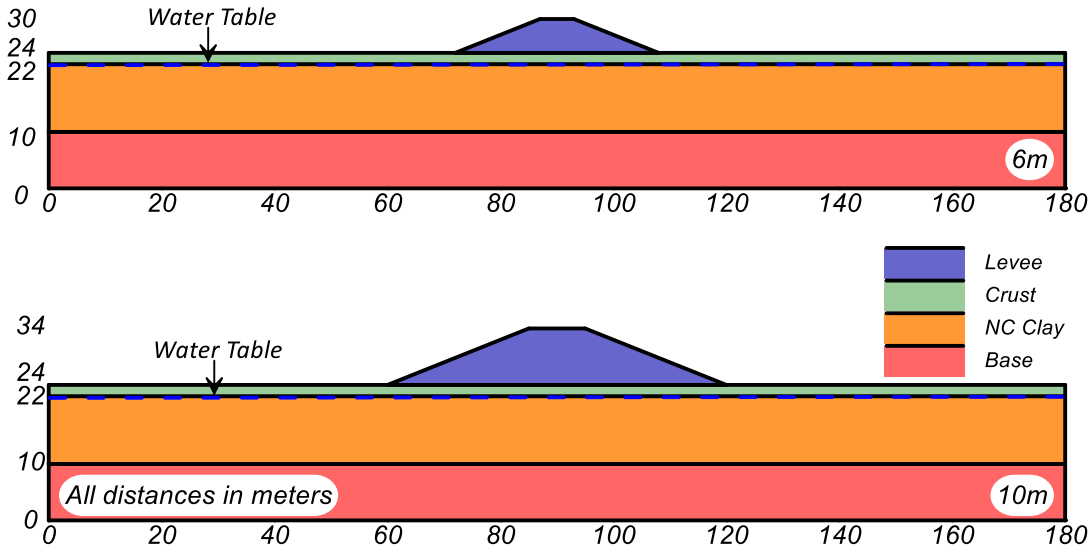

Figure 6-1: Model geometry and water table

The input motions were modified versions of the horizontal and vertical acceleration time series from the 2001 Nisqually earthquake recorded at the Gig Harbor Fire Station. The horizontal time series was spectrally matched to a target spectrum for a specific hazard scenario approximately corresponding to an M_w=7.0 earthquake at a rupture distance of 80 km, and then linearly scaled to a PGA = 0.6g. The vertical time series was linearly scaled to produce a peak acceleration of 0.5g. The response

spectrums of the horizontal and vertical motions have predominant frequencies of approximately 3-4 Hz and 10-17 Hz, respectively, as shown in Fig. 6-2.

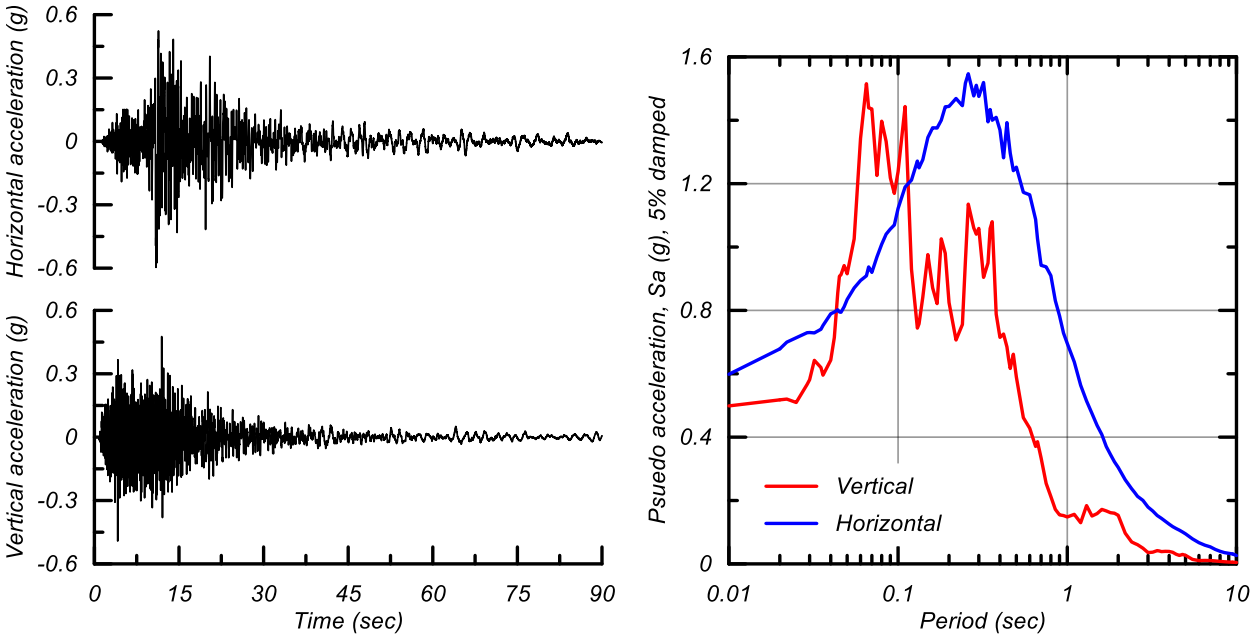

Figure 6-2: Vertical (top left) and horizontal (bottom left) acceleration time series and response spectra (right) for the input motions

The levee was assumed to be a well compacted, dense sand with a relative density of 75% and a peak friction angle of 40 degrees. The deep deposit of very dense sand (base layer) was assumed to have a relative density of 87% and peak friction angle of 43 degrees. Both materials were assigned a permeability of 10^{-5} cm/sec and a dry density of 1.64 Mg/m^3.

The NC clay layer was assumed to have a peak undrained strength ratio ($s_{u,pk}/\sigma'_{vc}$) = 0.25 and a sensitivity (S_t) of 4 which resulted in a critical state strength ratio ($s_{u,cs}/\sigma'_{vc}$) = 0.0625 when fully remolded. The crust layer was assumed to be OC with a uniform peak undrained shear strength of 50 kPa and a S_t = 1 (i.e. no strain-softening). Both materials were assigned a permeability of 10^{-8} cm/sec and a dry density of 1.48 Mg/m^3.

Table 6-1: Material properties

Layer	D_r (%)	Friction Angle	$s_{u,pk}/\sigma'_{vc}$ or $s_{u,pk}$	S_t
Levee	75	40	N/A	N/A
Crust	N/A	N/A	50 kPa	1
NC Clay	N/A	N/A	0.25	4
Base	87	43	N/A	N/A

6.3 Nonlinear Dynamic Analyses

Two-dimensional NDAs were performed using the finite difference program FLAC 8.1 (Itasca 2019). Elements in the mesh were 1m wide by 1m thick in the base and generally 1m wide by 0.5m thick in the NC clay, crust, and levee. The base was assigned a quiet (compliant) boundary while the sides were “attached” so the horizontal motion was the same at both sides of the model. Acceleration time series were converted to stress time series and applied to the compliant base. The bottom four meters of the base were modeled as elastic with the element thickness increased to 2m.

6.3.1 Soil Calibrations

The NC clay and OC clay crust were modeled with PM4Silt. The $s_{u,cs}/\sigma'_{vc}$ for the NC clay was determined from the $s_{u,pk}/\sigma'_{vc} = 0.25$ and $S_t = 4$. The peak strength was then obtained by reducing the value of $n^{b,wet}$ until the desired peak strength ratio was achieved. Parameter G_o was selected to result in a shear wave velocity at a vertical effective stress of 1 atm ($V_{s,1}$) of approximately 150 m/s. The undrained strength of the crust was assigned directly, and the shear modulus coefficient was selected to have a $V_{s,1}$ of approximately 200 m/s. Parameter h_{po} for each material was selected to approximate reasonable cyclic strength ratios versus number of uniform loading cycles. Assigned model parameters are shown in Table 6-2; all other parameters maintained their default values.

Table 6-2: PM4Silt input parameters for OC clay crust and NC clay

Material	$s_{u,cs}$ or $s_{u,cs}/\sigma'_{vc}$	$n^{b,wet}$	G_o	h_{po}
NC Clay	0.0625	0.25	350	800
Crust	50 kPa	1	600	50

The stress-strain and stress path of the OC clay crust and NC clay are shown below in Fig. 6-3 for single element simulations subjected to monotonic undrained direct simple shear (DSS) loading. Simulations were consolidated at a vertical consolidation stress of 1 atm with a K_o = 0.5. The initial stress strain response for the OC crust is stiffer than the NC clay due to the larger small strain shear modulus and corresponding higher $V_{s,1}$ value. Mobilization of peak strength occurs for the OC crust and NC clay at approximately 5% and 1% shear strain, respectively. The OC crust exhibits no post-peak strain-softening, consistent with a calibration for S_t = 1. The NC clay exhibits strong post-peak strain-softening, with the shear resistance dropping 50% at 10% shear strain. The shear resistance drops to its fully remolded value after more than 100% shear strain (beyond axis limits in Fig. 6-3).

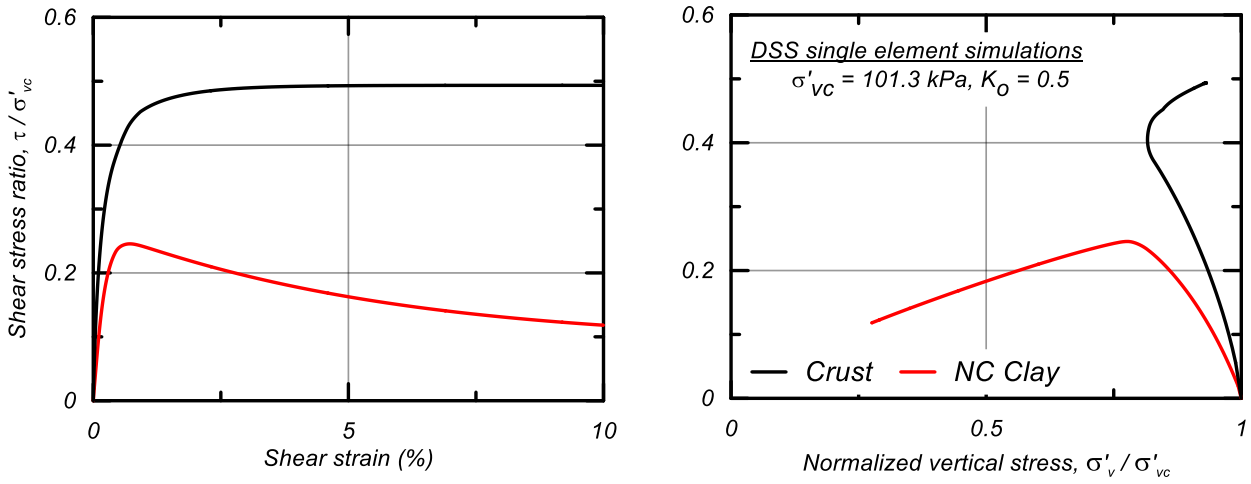

Figure 6-3: Stress-strain response and stress path of OC clay crust and NC clay layer in undrained monotonic DSS loading

Results of stress ratio controlled cyclic undrained DSS loading is shown for the OC clay crust and NC clay in Fig. 6-4 which shows the cyclic strength ratio, CSR, (τ_{cyc}/σ'_{vc}) versus the number of uniform stress cycles to 3% peak single amplitude shear strain. Results are shown for simulations with a vertical consolidation stress of 101.3 kPa and K_o = 0.5. The cyclic strength at one cycle is the same as the monotonic undrained strength resulting in a CSR versus number of cycles curve for the crust that is at higher CSR values than the curve for the NC clay. The cyclic strength ratio at larger numbers of cycles is controlled by the contraction rate parameter (h_{po}). The larger h_{po} value for the NC clay creates a flatter slope than for the crust. At small number of cycles, the difference in CSR between the crust and NC clay is large; the difference gets smaller as the number of cycles increases due to the steeper slope of the crust curve.

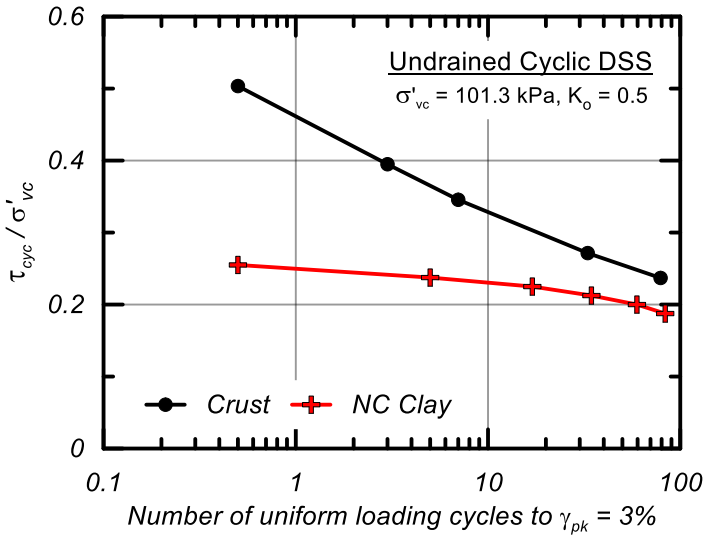

Figure 6-4: Cyclic strength versus number of uniform cycles for OC clay crust and NC clay

The levee and base layer were modeled with PM4Sand. Table 6-3 below shows the input parameters; all other parameters maintained their default values. The bottom

four meters of the base layer were modeled as elastic, with a shear modulus equal to the small strain shear modulus of the deep dense sand at that depth.

Table 6-3: PM4Sand input properties for Levee and Base Layer

Material	D_R	G_o	h_{po}
Levee	0.75	890	0.63
Base	0.87	1025	0.63

6.3.2 NDA Results

Results from NDAs are shown below. Simulations used large deformation mode. If crest settlements greater than 20% of the levee height occurred, the levee was essentially unstable and simulations would have required repeated re-meshing to arrive a stable deformed shape. Thus, once crest settlement exceeded 20% of the levee height, the analysis was categorized as an instability.

Strain contours for the 10m tall levee are shown in Fig. 6-5 at crest settlements equivalent to 2%, 4%, 6%, 8%, and 10% of the levee height (20cm, 40cm, 60cm, 80cm, and 100cm, respectively). The strain contours show the progressive development of a localized shear band. At a crest settlement = 20cm (11.5 seconds into the dynamic analysis) a shear band is observed at the base of the NC clay layer just above the interface with the very dense base under the upstream slope. The shear band developed at onset of strong shaking in the ground motion. As strong shaking continued and crest settlements increased, the shear band continued to develop. The soils in this localization began to lose strength due to strain-softening and began to shed shear stress to the surrounding soils which further elongated the shear band. After further development of the shear band along the base of the NC clay, the strain band began to propagate vertically through the clay layer towards the crust and approached the base of the levee

(t=12.5-13.5 seconds). The shear band began to go vertical as the clays above the shear band lost strength due to strain-softening and became the path of least resistance. At a crest settlement of 80 cm, the shear band was fully developed through the upstream slope and a progressive failure was underway. The location of the strain contours at the far edge of the model are affected by the side boundary.

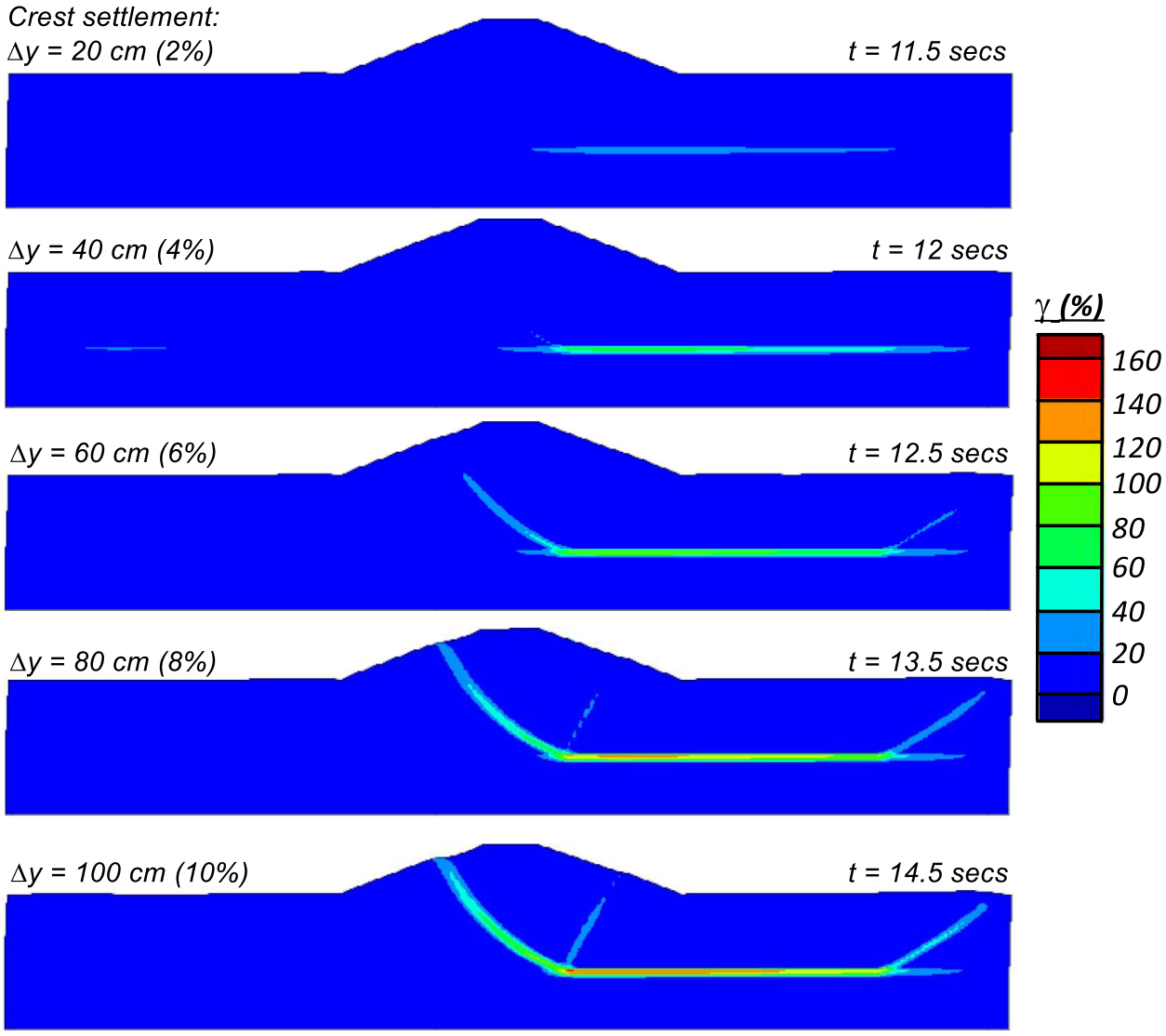

Figure 6-5: Development of localized shear band with increasing crest deformations for the 10m tall levee

The deformations continued to accumulate following the development of the failure mechanism until the crest settlement was 2m for the 10 m levee (i.e., 20% of the levee height) at an elapsed time of approximately 23 seconds. Fig. 6-6 shows contour plots of x-displacement (top), y-disp (middle), and shear strains (bottom) for the 10m levee at a elapsed time of 23 seconds. Shear strains concentrations are plotted where strains greater than 15% are the same color to maintain resolution at lower strain levels. The x-displacement shows a sliding mass that translates from left to right with the maximum displacement of approximately 2.5m near the right toe. The slide mass follows the strain concentrations shown in Fig. 6-6 (bottom) and the progressive shear band that developed in Fig. 6-5. Y-displacements decreased from left to right in the levee as expected with a rotating failure mass. After crest settlement reached 20% of the levee height, displacements continued to rapidly accumulate which confirmed the levee was unstable.

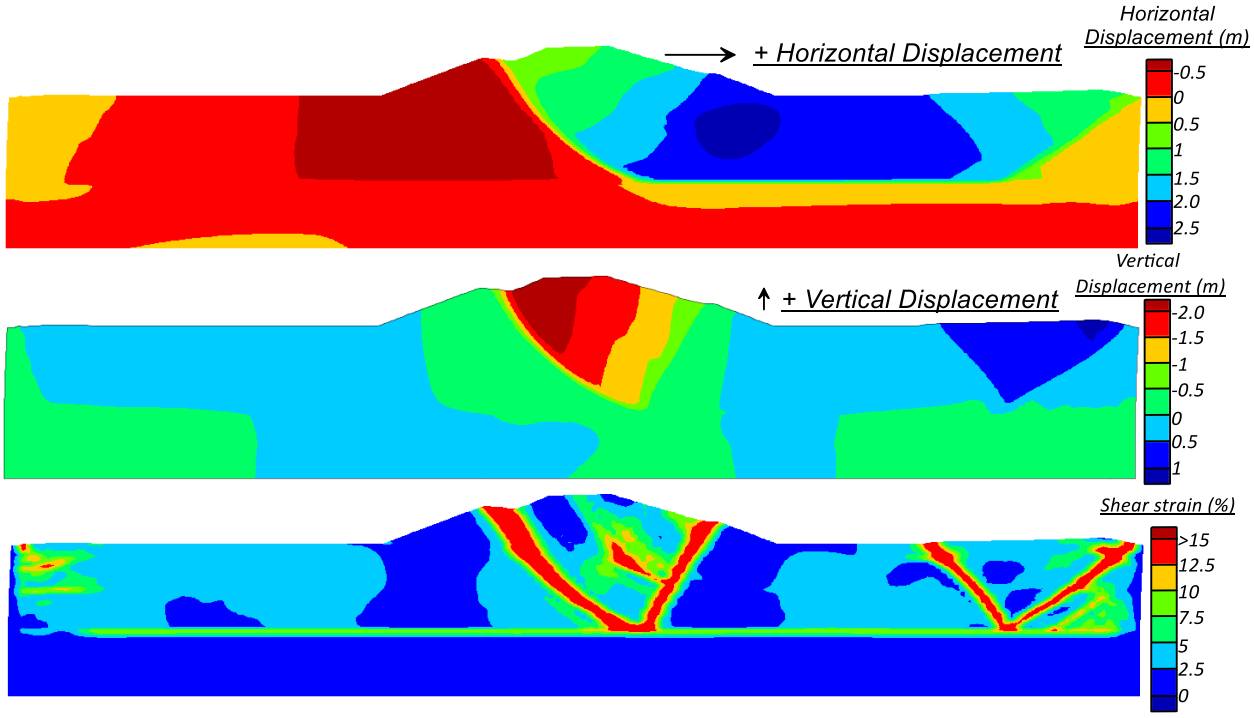

Figure 6-6: Horizontal displacement (top), vertical displacement (middle), and shear strain (bottom) for the 10m levee at a crest settlement of 2m (t = 23 seconds)

The 6m tall levee settled 79 cm at the end of shaking, which was less than 20% of the levee height. Contour plots are shown in Fig. 6-7. for horizontal displacement (top), vertical displacement (middle), and shear strains (bottom) for the 6m levee at the end of shaking. The horizontal displacements indicated a left to right translational sliding block similar to the 10m levee. The shear strain contours (Fig. 6-7 bottom) did not daylight at the ground surface on the right side of the model as was observed for the case with a 10m tall levee. The lack of a daylighting shear band indicated the failure surface was not fully developed, consistent with the levee remaining stable during the shaking event.

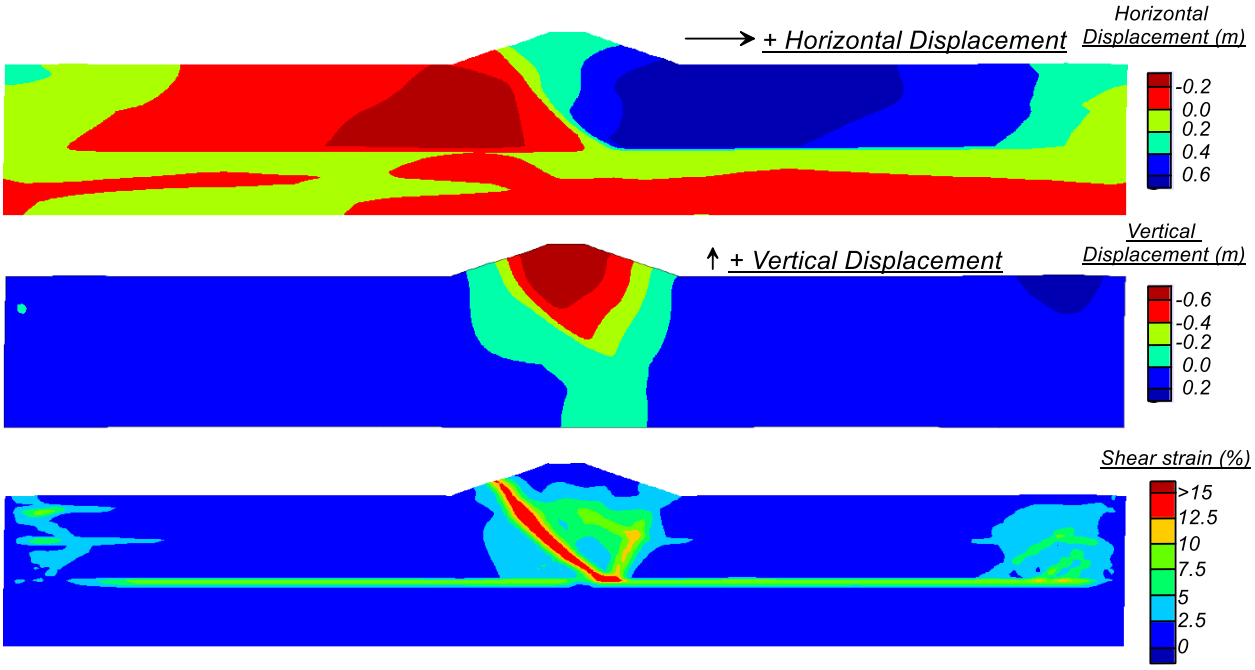

Figure 6-7: Horizontal displacement (top), vertical displacement (middle), and shear strains (bottom) for the 6m tall levee at end of shaking

6.4 Simplified Method

The simplified method included LE analyses performed using Slide2 8.0 (RocScience 2018) to obtain static factors of safety (FS) and yield accelerations (k_y), and a Newmark sliding block method to estimate deformations. Results shown for FS and k_y were obtained using Spencer's method and Newmark displacements were obtained using the SLAMMER (Jibson et al. 2013) program in Slide2. The sliding mass was assumed to be a rigid block. The applied ground motion for the Newmark methods was the acceleration time series extracted at the top of the base layer from the NDA analyses. This motion was selected because the critical failure surface in the LE models was observed to be similar in depth and size of the failure surface from the NDAs. This is a relatively common approach for selecting input motions for the Newmark sliding block calculation. Alternatively, equivalent linear dynamic analyses can be used to obtain an inertial loading

history for the potential slide mass. Regardless, the displacement from Newmark methods is best viewed as only an index of expected deformation.

The sensitivity of the Newmark displacement to the NC clay's undrained strength ratio (allowing for strength loss during deformation) was evaluated using effective undrained strength ratios of 0.125, 0.156, 0.188, 0.219, and 0.25, which correspond to strength losses of 50%, 37.5%, 25%, 12.5% and 0% relative to the peak undrained strength, respectively. The levee and base layer were modeled with a Mohr Coulomb material model in the LE analyses. The crust was applied a uniform undrained strength in the LE analyses.

The LE static factor of safety progressively decreased with decreasing effective undrained shear strength ratio for both levee heights. Fig. 6-8 (top) shows static factor of safety versus NC clay undrained strength ratio for the 6m (red) and 10m (blue) tall levees. Without consideration of strength loss (s_u/σ'_{vc} = 0.25) the static FS is 1.58 for the 6m tall levee and 1.24 for the 10m tall levee. The 10m tall levee becomes statically unstable (defined as having a static factor of safety below 1.0) with an s_u/σ'_{vc} = 0.188 or a strength reduction of 25%. The 6m tall levee remains statically stable until the s_u/σ'_{vc} = 0.125 or a strength reduction of 50%. The smaller levee can absorb more strength loss than the large levee before static instability occurs, consistent with the lower initial shear stress demands on the NC clay layer below the smaller levee.

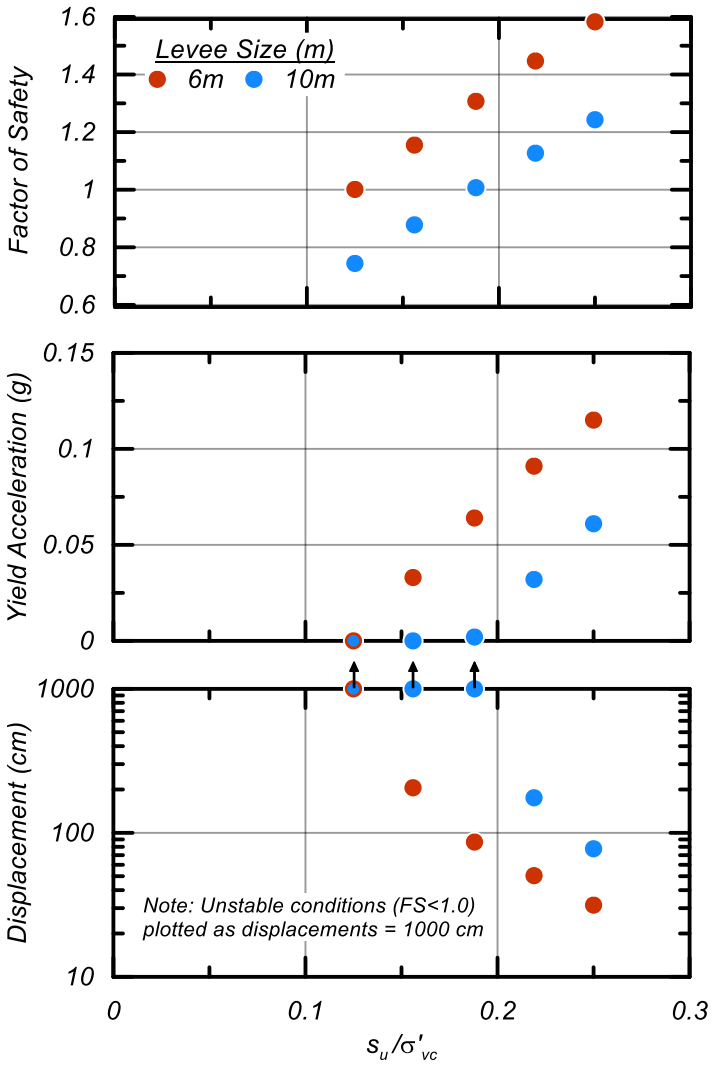

Figure 6-8: Factor of safety, yield acceleration, and deformations versus undrained strength ratio obtained using LE and Newmark methods

Fig. 6-8 (middle) shows K_y versus the NC clay's undrained shear strength ratio. K_y reduces towards 0 for both levee sizes as the strength ratio decreases with K_y equal to 0 coinciding with the static factor of safety being less than 1.0. Without remolding, K_y was 0.115 for the 6m tall levee and 0.061 for the 10m tall levee. The linear decrease in yield acceleration with reducing shear strength ratio results in an exponential increase in predicted deformations. Fig. 6-8 (bottom) shows displacements versus NC clay undrained strength ratio for both levees. Without remolding, predicted deformations were 31cm

(~5% of levee height) for the 6m tall levee and 78cm (~8% of levee height) for the 10m tall levee (less than predicted by the respective NDA analysis). With a 25% loss in strength, the estimated deformations rose to 86 cm for the 6 m tall levee and unstable (>1000 cm) for the 10m tall levee. Settlements > 20% of the crest height occurred for the 6m tall levee with an undrained strength ratio between 0.156 and 0.188 (between 25% and 37.5% strength loss) and for the 10m tall levee with an undrained strength ratio between 0.188 and 0.219 (between 12.5 and 25% strength loss).

6.5 Discussion

Newmark displacements for both the 6m and 10m tall levees were sensitive to the assumed level of strength loss in the NC clays. Newmark displacements were lower than predicted by the NDAs if there was no assumed strength loss in the NC clay but were greater than predicted by the NDAs if the assumed strength loss was 25% or greater. For the evaluated cases, a 20% reduction in the NC clay strength produced similar displacements to those predicted by the NDAs. However, the levee displacements in the NDAs reflect the compensating effects of strain-softening on stability and dynamic response (i.e., strain-softening reduced both the resistance to deformation and the inertial forces driving deformation). As a result, different combinations of ground motion, rate of strength loss, and sensitivity may result in different appropriate strength reductions for the sensitive clay in a simplified method. Further work is needed to develop guidance on how to account for strength degradation in seismic loading.

Selection of analysis method often depends on the structure in question, the consequence of failure, the magnitude of uncertainty in the analysis, and the available resources. Analysis effort is lowest for simplified methods and significantly greater for

NDAs. Simplified methods, while quicker to perform, require the modeler to externally estimate the degree of strength loss in any NC or nearly NC clays, which is strongly affected by assumptions regarding potential strain-localization in post-peak strain-softening materials. The use of more complicated NDA methods with constitutive models that can model the strain-softening tendencies introduces other complexities that need to be accounted for such as mesh dependency and localization.

In practice, levees, such as those in the delta, have primarily been evaluated using simplified methods. Previous evaluation studies have concluded that the delta may experience significant levee failures during a large earthquake and that significant disruption to the water supply may follow. Given the wide range of site conditions in the delta, it is difficult to make general conclusions based on 2D models, however behaviors like strain-softening and strain localization are likely to play an important role in the performance of some levees.

6.6 Conclusion

Nonlinear dynamic analyses of idealized 6m- and 10m-tall levees founded on a 12-m thick deposit of soft sensitive clay were used to evaluate the influence of the clay sensitivity and strain-softening on estimated seismic deformations. The NDAs were performed using FLAC (Itasca 2019) with the user-defined constitutive models PM4Sand and PM4Silt. The NDA analyses showed strain localization and strength loss initiating in the soft clay near its lower contact with an underlying stronger stratum, after which the strain localization zone grew progressively upward through the soft clay, overlying crust, and levee, for the imposed ground motions. Strength losses within the strain localization zone reduced

levee stability but also reduced dynamic motions within the slide mass, which had a compensating effect on final levee deformations and crest settlements.

Simplified analyses using limit equilibrium (LE) analyses with a Newmark sliding block method to estimate levee displacements were also performed. The results of both types of analyses gave similar results when a small reduction in the strength (~20%) was accounted for in the simplified method, but this finding is only applicable to the conditions examined and should not be generalized to other conditions. Other analysis results have shown that the tendency for simplified methods to underestimate or overestimate seismic deformations compared to NDA methods depend on the specific site conditions and ground motion characteristics.

Further work is underway to develop generalized guidance on how to account for sensitivity and the rate of strength loss when predicting the seismic deformations of earthen structures over normally consolidated clay using either simplified methods or NDAs.

6.7 Acknowledgment

The work described herein was supported by the California Department of Water Resources under Contract 4600009751. Dr. Rambod Hadidi provided the spectrally matched ground motions. Any opinions, findings, or recommendations expressed herein are those of the authors and do not necessarily represent this organization. The authors appreciate the above support.

Chapter 7 : Conclusions and Future Research Directions

This chapter presents the primary conclusions and outcomes of this dissertation. They are discussed in three overarching categories: (1) accounting for viscous behavior (Chapters 2 and 3), (2) static slope stability (Chapters 2 and 4), (3) and seismic stability assessments (Chapters 5 and 6). In addition, future research directions and needs are discussed.

7.1 Conclusions

7.1.1 Accounting for Viscous Behaviors

The constitutive model PM4SiltR was developed to account for viscous effects in plastic silts and clays in static slope stability applications. It was developed as a user-defined constitutive model for use in FLAC 8.1 with the creep module. PM4SiltR expanded on the PM4Silt constitutive model to simulate rate-dependent shear strength, creep, and stress relaxation through the implementation of a consistency approach combined with an auto-decay process and an internal strain rate. The model introduced six parameters that control the viscous behavior. Single elements simulations of undrained DSS were presented to illustrate the constitutive response of the model. The introduction of viscous effects was shown to increase the peak strength as the applied strain rate increases. Additionally, simulations with sustained stress conditions were shown to accumulate shear strains through undrained creep, with higher sustained stress levels leading to larger accumulated shear strains and potentially creep rupture.

A numerical parametric analysis was performed to develop a relationship that predicts the onset of localization (and associated large strength loss) in strain-softening plastic materials that directly incorporates viscous effects. The analysis used the recently developed constitutive model PM4SiltR in FLAC 8.1 with single element and grid simulations of undrained DSS. Six calibrations with varying peak strength ratios, sensitivities, and rates of strain-softening were used in a parametric analysis that varied the loading rate and viscous properties. The onset of localization was found to depend on the magnitude of viscous peak strength increase and the rate of post-peak strain-softening. A regression was performed to develop a relationship that predicted the onset of localization based on these dependencies. The relationship was shown to predict the onset of localization at shear strains that were consistent with experimental results, although a systematic compilation of experimental data on the localization process is required to fully assess its accuracy.

7.1.2 Static Slope Stability

PM4SiltR was used to assess the undrained, long-term, static stability of a hypothetical tailings impoundment to validate the PM4SiltR model at the system level. The hypothetical impoundment was subjected to wetting events that increased the saturation and reduced the suction in the unsaturated tailings above the phreatic surface. The wetting events increased the driving force and reduced the resisting force which induced displacements in the dam over time. Depending on the magnitude of the wetting event the displacements developed during wetting (due to the change in loading and resistance) and/or in the time following the end of the wetting event (due to creep in the tailings). Small changes in loading were shown to be sufficient to trigger undrained creep rupture

in the strain-softening material which resulted in delayed slope instability (progressive failure). The PM4SiltR model was shown to be capable of assessing long-term, undrained, static stability of slopes.

Additionally, a re-examination of the Feijão Dam 1 failure was presented. On January 25th, 2019, Feijão Dam 1 in Brumadinho, Minas Gerais, Brazil underwent a catastrophic failure that resulted in the release of almost 10 million cubic meters of retained tailings. It was an 86-meter-tall dam with a 720-meter crest length and was constructed in a series of 10 raises over 37 years using upstream construction. Past investigations utilized critical state properties obtained from laboratory samples on reconstituted samples and assessed state parameter variability using CPT correlations. The failure trigger has been proposed to be either seasonal wetting leading to an increased saturation level and a loss of suction above the phreatic surface inducing internal creep or a drilling-induced disturbance.

The re-examination primarily used the site stratigraphy and index properties developed in the prior investigations. The tailings strengths were characterized using a combination of methods common in geotechnical practice and the distinct materials were assigned uniform material properties. The dam was shown to be marginally stable against undrained loading (FS = 1.06). Nonlinear analyses were performed using PM4SiltR and PM4Sand in FLAC 8.1 to evaluate the proposed failure triggers. Results showed that wetting induced internal creep, drilling-induced disturbances, or a combination of both mechanisms could trigger the failure. Both failure mechanisms induced internal strains which were sufficient to trigger progressive failure and eventually slope instability.

The results of these analyses indicated that Feijão Dam 1 was marginally stable against long-term undrained loading and that only a minor change in loading was necessary to induce slope instability. The system stability was most influenced by the fine tailings as it was the weakest material and there was a thin, laterally continuous layer that approached the dam face. The re-examination showed that strength characterization methods common in geotechnical practice and uniform material properties were sufficient to model the failure. The results show that long-term, consolidated, undrained slope stability should be considered in practice, although several significant texts do not recommend considering this condition.

7.1.3 Seismic Stability Assessments

Nonlinear dynamic analyses were used to investigate how seismic deformations of a setback levee founded on a normally consolidated clay layer varied with the sensitivity of the underlying clay layer. The analyses were performed in FLAC 8.0 with the user-defined constitutive models PM4Silt and PM4Sand. The analyses considered two clay layer thicknesses and three sensitivities. Strain-softening and associated strength loss in the clay layer increased as the sensitivity increased, although increasing the sensitivity did not increase the levee deformations for the conditions examined. The crest deformations generally decreased with increasing clay sensitivity which was attributed to base isolation as the weakened clay layer reduced the accelerations transmitted through the clay layer to the crest. These observations were only valid for the conditions examined where the models remained statically stable at the end of shaking; in other conditions it is expected that the progressive strength loss will result in instability and slope failure.

Additionally, results of nonlinear dynamic analyses of two idealized levees (with different crest heights) over a 12-meter-thick sensitive clay layer were compared with seismic deformations predicted using simplified limit equilibrium analyses in conjunction with Newmark sliding block methods. The results showed that the simplified methods under predicted deformations compared with the NDA results when strength loss was not considered in the simplified methods. The results of the two methods compared favorably when a strength loss of approximately 20% was considered in the simplified methods. Additional analyses indicated that the tendency for simplified methods to underestimate or overestimate deformations compared to NDA methods depends on the specific site conditions and ground motion characteristics.

7.2 Future Research Directions

The research performed in this dissertation investigated several questions involving the numerical modeling of viscous effects and strain-softening in static and dynamic analyses. However, there remains additional questions that should be investigated to further understand viscous effects and strain-softening in nonlinear analyses. These future research directions are broadly broken into three categories: (1) numerical, (2) experimental, and (3) methodological.

7.2.1 Numerical

One complication when modeling strain-softening behavior in numerical analyses is the tendency for strains to localize along a single row of elements and the influence this has on the global response. The research presented herein attempted to address some of the complexities related to numerical localization. However, it did not address several additional issues including the influence of pore pressure dissipation away from shear

zones. Further work is needed to investigate the influence of pore pressure dissipation and permeability on the development of localizations in fully coupled numerical analyses of strain-softening materials.

Additionally, the influence of pore pressure dissipation on progressive failure development at the system level needs to be further investigated. The accumulation of strains within a localized band generates pore pressure during undrained loading which can lead to strength loss and progressive failure. However, the strength loss may be offset by the beneficial effects of consolidation due to the dissipation of the generated pore pressure away from the shear band into the surrounding soil delaying or negating the development of a progressive failure. Additional work is needed to investigate the influence of pore pressure dissipation on the development and timing of progressive failures in systems containing strain-softening soils.

Further research is needed to investigate the potential base isolation effect observed in nonlinear dynamic analyses of strain-softening materials where an increasing sensitivity in the soil layer reduced the predicted deformations. Additional simulations are necessary to develop a robust database of different combinations of model geometries, ground motions, and material properties to understand which conditions could potentially benefit from base isolation and when strength loss in the underlying layer increases deformations.

7.2.2 Experimental

The development of numerical tools for use in practice relies on robust data sets from which models, empirical relationships, and fundamental understanding can be based. The research herein used the existing laboratory and field data available however additional

data is needed to further validate numerical tools and improve understanding of soil behavior.

The viscous behaviors of rate-dependent shear strength, creep, and stress relaxation are postulated to be related through a single governing equation. However, there is limited experimental data that investigates all these behaviors in the same soil during the same experimental program. There is a need for the development of a robust database of experimental results for a range of plastic soil types (i.e., silt, clays, and tailings) with different material properties that are systematically tested under consistent conditions to investigate the relationship between these soil behaviors and identify the critical material properties that control them.

The tendency of a plastic soil to localize in experimental tests has been shown to depend on the soil properties and loading conditions. Several research programs have discussed localization in soil specimens, although relatively few researchers have discussed the development, onset, and geometry of localizations in a systematic manner. There is a need to systematically investigate the localization process and tendency for a range of plastic soils under different loading conditions including at a wide range of loading rates. PIV technology can be used to track the strain accumulation throughout loading and evaluate the development of a localization. This can lead to improved implementation of length scales and large strain strength loss, and their possible dependence on loading rate, at the system level.

The modeling of progressive failure is complicated by the localization process such that modeling these failures can often only provide estimates of failure trigger magnitude and timing due to a lack of available data, site variability, and modeling limitations. There

is a need for a controlled set of physical model (e.g., centrifuge) experiments that induce progressive failures in plastic slopes under defined loading (static and dynamic) and boundary conditions to develop numerical methods that can predict both failure trigger magnitude and failure timing. The use of PIV technology, pore pressure transducers, and strain gauges, amongst other experimental tools, may provide the data necessary to develop new and evaluate existing models and numerical solution schemes against.

7.2.3 Methodological

Seismic stability assessments of earthen structures founded on or containing strain-softening plastic materials often require the implementation of a length scale to account for localization and associated strength loss. Currently, there is not a standard methodology that is used in practice, instead individual modelers and engineers apply their judgement to determine how to properly implement a length scale for their project. Future engineers should work to establish a standard-length scale methodology that incorporates our understanding of viscous tendencies, strain-softening, and localization. A standardized methodology would increase the replicability and transparency of numerical models.

Several significant texts (including design manuals) do not discuss the consideration of the long-term, consolidated, undrained condition in static stability assessments. However, recent failures have occurred under these conditions and other texts suggest that this condition should be considered. There remains a need for a methodology or standard that addresses when this condition needs to be accounted for and how to model it in order to avoid future high consequence failures like those that have occurred recently (i.e., Feijão Dam 1).

References

Abdellaziz, M., Karray, M., Hussein, M.N., Delisle, M., Ledoux, C., Locat, P., Mompin, R., and Chekired, M. 2020. “Experimental and numerical investigation of the Saint-Adelphe landslide after the 1988 Saguenay earthquake.” *Can. Geotech. J.* 57(12), 1936-1952. https://doi.org/10.1139/cgj-2018-0629.

Ansari, Y., Pineda, J., Kouretzis, G., and Sheng, D. (2014). “Experimental and Numerical Investigation of Rate and Softening Effects on the Undrained Shear Strength of Ballina Clay” *Australian Geomechanics,* Volume 49(4).

Armero, F. 1997. “Large-scale modeling of localized dissipative mechanisms in a local continuum: application to the numerical simulation of strain localization in rate-dependent inelastic solids.” *Mechanics of Cohesive-Frictional Materials.* 4, 101-131

Arroyo, M., and Gens, A. 2021. “Computational analyses of Dam 1 failure at the Corrego de Feijão mine in Brumadihno.”

Atkinson, J.H., and Richardson, D. 1987. “The effect of local drainage in shear zones on the undrained strength of overconsolidated clay.” *Géotechnique.* 37(3), 393-493.

Beaty, M. H., and Dickenson, S. E. 2015. “Numerical Analysis for Seismically-Induced Deformations in Strain-Softening Plastic Soils.” *6th Internation Conference on Earthquake Geotechnial Engineering*, Christchurch, New Zealand.

Beaty, M. H., and Perlea, V. G. 2015. “Several Observations on Advanced Analyses with Liquefiable Materials.” *Proc., 31st USSD Annual Meeting and Conference*, San Diego, CA, 1369-1397.

Bernander, S., Svensk, I., Holmberg, G., Bernander, J., and Isacsson, K. 1985. “Shear strength and deformation properties of clays in direct shear tests at high strain rates.” *In Proc. 11th International Conference on Soil Mechanics and Foundation Engineering.* 978-990.

Bjerrum, L., and Landva, A. 1966. “Direct simple-shear tests on a Norwegian quick clay.” *Geotechnique*, Volume 16(1), 1–20.

Boulanger, R. W., and Beaty, M. H. 2016. “Seismic Deformation Analyses of Embankment Dams: A Reviewer's Checklist.” *Proceedings, Celebrating the Value of Dams and Levees – Yesterday, Today and Tomorrow, 36th USSD Annual Meeting and Conference*, Denver, CO, 535–546.

Boulanger, R. W., and Wijewickreme, D. 2019. “Calibration of a constitutive model for the cyclic loading responses of Fraser River Delta Silt.” *Earthquake Geotechnical Engineering for Protection and Development of Environment and Constructions: Proceedings of the 7th International Conference on Earthquake Geotechnical Engineering*, F. Silvestri and N. Moraci, eds., Associazione Geotecnica Intaliana, Rome, Italy, 121–137.

Boulanger, R. W., and Ziotopoulou, K. 2017. PM4Sand (Version 3.1): A sand plasticity model for earthquake engineering applications." Report No. UCD/CGM-17/01, *Center for Geotechnial Modeling*, Department of Civil and Environmental Engineering, University of California, Davis,CA, 108 pp.

Boulanger, R. W., and Ziotopoulou, K. 2018. “PM4Silt (Version 1): A silt plasticity model for earthquake engineering applications.” Report No. UCD/CGM-18/01, *Center for*

Geotehcnical Modeling, Department of Civil and Environmental Engineering, University of California, Davis, CA, 108 pp.

Boulanger, R.W. and Oathes, T.J. 2020. “Modeling slope instability due to undrained creep”. *Proc. Tailings and Mine Waste 2020*, Colorado State University.

Boulanger, R.W. and Ziotopoulou, K. 2019. “A constitutive model for clays and plastic silts in plane-strain earthquake engineering applications.” *Soil Dynamics and Earthquake Engineering*, 127(2019): 105832, 10.1016/j.soildyn.2019.105832

Boulanger, R.W., and Montgomery, J. 2016. “Nonlinear deformation analyses of an embankment dam on a spatially variable liquefiable deposit.” *Soil Dynamics and Earthquake Engineering*. 91(2016): 222-233. https://doi.org/10.1016/j.soildyn.2016.07.027

Boulanger, R.W., and Ziotopoulou, K. 2018. “On NDA practices for evaluating liquefaction effects.” *Proc., Geotechnical Earthquake Engineering and Soil Dynamics V, Geotechnical Special Publication 290*, S. J. Brandenberg and M. T. Manzari, eds., ASCE, 1-20. https://doi.org/10.1061/9780784481455.001

Boulanger, R.W., Ziotopoulou, K., and Oathes, T.J. (In Preparation). “PM4SiltR (Beta Version): A silt plasticity model with rate effects for slope stability applications.” Report No. UCD/CGM-21/0X, *Center for Geotechnical Modeling*, University of California, Davis.

Boulanger, R.W., Ziotopoulou, K., and Oathes, T.J. In Preparation. “PM4SiltR (Beta Version): A silt plasticity model with rate effects for slope stability applications.” Report

No. UCD/CGM-21/0X, *Center for Geotechnical Modeling*, University of California, Davis.

Brooks, G.R. 2014. “Prehistoric sensitive clay landslides and paleoseismicity in the Ottawa Valley, Canada.” Landslides in Sensitive Clays: From Geosciences to Risk Management. J.-S. L'Heureux, A. Locat, S. Leroueil, D. Demers, and J. Locat (eds). Springer.

Burton, C. and Cutter, S.L. 2008. “Levee Failures and Social Vulnerability in the Sacramento-San Joaquin Delta Area, California.” *Natural Hazards Review,* 9(3): 136-149, 10.1061/(ASCE)1527-6988(2008)9:3(136)

Campanella, R.G. and Vaid, Y.P. 1974. “Triaxial and plane strain creep rupture of an undisturbed clay.” *Canadian Geotechnical Journal*, 11(1): 1-10.

Clarke, S.D. and Hird, C.C. 2012. “Modelling of viscous effects in natural clays.” *Canadian Geotechnical Journal*, 49: 129-140.

D’Ignazio, M. and Lansivaara, T. 2015. “Shear bands in soft clays: strain softening behavior in finite element method.” *Journal of Structural Mechanics,* 48(1): 83-98.

Dafalias, Y.F., and Manzari, M.T. 2004. “Simple plasticity sand model accounting for fabric change effects.” *Journal of Engineering Mechanics*. 130(6), 622-634. DOI: 10.1061/(ASCE)0733-9399(2004)130:6(622)

Diaz-Rodriguez, J.A., Martinez-Vasquez, J.J., and Santamarina, J.C. 2009. “Strain rate effects in Mexico City soil.” *ASCE Journal of Geotechnical and Geoenvironmental Engineering*, 135 (2), 300 – 305.

Duncan, J.M., Wrights, S.G., and Brandon, T.L. 2014. Soil strength and slope stability. 2nd ed, New York: Wiley

Fodil, A., Aloulou, W., and Hicher, P.Y. 1997. “Viscoplastic behaviour of soft clay.” *Géotechnique*, 47 (3), 581-591.

Graham, J., Crooks, J. H. A., and Bell, A. L. 1983. "Time effects on the stress-strain behaviour of natural soft clays." *Géotechnique*, 33(3), 327–340.

Gylland, A.S., Jostad, H.P., and Nordal, S. 2014. “Experimental study of strain localization in sensitive clays.” *Acta Geotechnica,* 9, 227-240

Idriss, I.M., and Boulanger, R.W. 2008. “Soil Liquefaction During Earthquakes.” Monograph MNO-12, Earthquake Engineering Research Institute, Oakland, CA, 261 pp.

Itasca 2016. FLAC - Fast Lagrangian Analysis of Continua, Version 8.0, *Itasca Consulting Group, Inc*, Minneapolis, Minnesota.

Itasca. 2019. “Fast Lagrangian Analysis of Continua (FLAC), release 8.1.” *Itasca Consulting Group,* Inc., 566 Minneapolis, MN.

Jamiolkowski, M., Lo Presti, D.C.F., and Manassero, M. 2003. “Evaluation of relative density and shear strength of sands from CPT and DMT.” *Soil Behavior and Soft Ground Construction. ASCE GSP 119*. https://doi.org/10.1061/40659(2003)7

Jefferies, M., Morgenstern, N.R., Zyl, D.V., and Wates, J. 2019. “Report on NTSF Embankment Failure Cadia Valley Operations for Ashurst Australia.”

Jiang, J., Ling, H.I., Kaliakin, V.N., Zeng, X., and Hung, C. 2017. “Evaluation of an anisotropic elastoplastic-viscoplastic bounding surface model for clays.” *Acta Geotechnica*, 12:335-348.

Jibson, R.W., Rathje, E.M., Jibson, M.W., Lee, Y.W. 2013. “SLAMMER – Seismic Landslide Movement Modeled using Earthquake Records, Version 1.1, November 2014.” *U.S. Geological Survey Techniques and Methods,* book 12, chap. B1, unpaged.

Jefferies, M., and Been, K. (2015). “Soil liquefaction: a critical state approach.” *CRC press.*

Kiernan, M. and Montgomery, J. 2018. “Numerical simulations of the Fourth Avenue landslide considering 570 strain-softening.” Proc., Geotechnical Earthquake Engineering and Soil Dynamics V, Geotechnical 571 Special Publication 290, S.J. Brandenberg and M.T. Manzari, eds., ASCE, 67–78.

Kulhawy, F. H., and Mayne, P. W. 1990. Manual on Estimating Soil Properties for Foundation Design, Report EPRI EL-6800, *Electric Power Research Inst*., Palo Alto, CA.

Kutter, B.L. and Sathialingam, N. 1992. “Elastic-viscoplastic modelling of the rate-dependent behaviour of clays.” *Géotechnique,* 42 (3): 427-441.

Lacerda, W. 1976. “Stress-relaxation and creep effects on soil deformation.” University of California, Berkeley.

Ladanyi, B. and Melouki, M. 1993. “Determination of creep properties of frozen soils by means of the borehole stress relaxation test.” *Canadian Geotechnical Journal*, 30, 170-186.

Ladd, C.C. 1991. “Stability evaluation during staged construction.” *Journal of Geotechnical Engineering*. 117 (4). https://doi.org/10.1061/(ASCE)0733-9410(1991)117:4(540)

Ladd, C.C. and DeGroot, D.J. 2004. “Recommended Practice for Soft Ground Site Characterization: Arthur Casagrande Lecture.” *12th Panamerican Conference on Soil Mechanics and Engineering*, MIT, Cambridge, MA.

Lefebvre, G. and LeBoeuf, D. 1987. “Rate Effects and Cyclic Loading of Sensitive Clays.” *J. Geotech. Engr.* 113 (5): 476-489.

Lefebvre, G., Leboeuf, D., Hornych, P., and Tanguay, L. 1992. “Slope failures associated with the 1988 Saguenay earthquake, Quebec, Canada.” Can. Geotech. J. 29 (1): 117–130. https://doi.org/10.1139/t92-013.

Leroueil, S. 2006. “The isotache approach. Where are we 50 years after its development by Professor Suklje?” 2006 Prof. Suklje’s Memorial Lecture.

Leroueil, S., Tavenas, F., Samson, L., and Morin, P. 1983. “Preconsolidation pressure of Champlain clays. Part II. Laboratory determination.” *Canadian Geotechnical Journal*, 20, 803-816.

Loret, B. and Prevost, J.H. 1990. “Dynamic strain localization in elastic-(visco-)plastic solids. Part 1. General formulation and one-dimensional examples. *Computer Methods in Applied Mechnaics and Engineering,* 83, 247-273

Martin, T.E., McRoberts, E.C., and Davies, M.P. 2002. “A tale of four upstream tailings dams.” Proceedings Tailings Dams, 2002.

Martindale, H., Chakraborty, T., and Basu, D. 2012. “A rate dependent constitutive model for clay.” In Proc*. GeoCongress* 2012. 859-868.

Mayne, P.W., and Peuchen, J. 2018. “Evaluation of CPTU Nkt cone factor for undrained strength of clay.” Cone Penetration Testing, Delft University of Technology.

McRoberts, E.C. and Sladen, J.A. 1992. “Observations on static and cyclic sand-liquefaction methodologies.” *Canadian Geotechnical Journal*, 29: 650-665.

Morgenstern, N.R., Vick, S.G., Viotti, C.B., and Watts, B.D. 2016. “Report on the immediate causes of the failure of the Fundão dam.”

Mun, W., Teixeira, T., Balci, M.C., Svoboda, J., and McCartney J.S. (2016). “Rate effects on the undrained shear strength of compacted clay.” *Soils and Foundations*, 56 (4), 719-731.

Nader, A., Fall, M., and Hache, R. 2015. “Characterization of sensitive marine clays by using cone and ball penetromenters examples of clays in eastern Canada.” *Geotechn Geol Eng* 33:841-864. DOI 10.1007/s10706-015-9864-x

Needleman, A. 1988. “Material rate dependence and mesh sensitivity in localization problems.” *Computer Methods in Applied Mechanics and Engineering*, 67, 69-85.

Needleman, A. 1989. “Dynamic shear band development in plane strain.” *Journal of Applied Mechanics,* 56, 1-9.

Niazi, M.S., Wisselink, H.H., and Meinders, T. 2013. “Viscoplastic regularization of local damage models: Revisited.” *Computational Mechanics*, 51(2), 203–216.

Oathes, T. J., and Boulanger, R. W. 2019. “Numerical Evaluation of Strain-Rate Effects

on Strain-Softening and Localization in Saturated Clays." *Second City - Second Chances: Stories of Rehabilitation, Modification, and Reviatalization, 39th USSD Annual Meeting and Conference*, United States Society of Dams, Chicago, IL, 1–15.

Oathes, T.J. and Boulanger, R.W. 2020. "Influence of strain rate on localization and strain-softening in normally consolidated clays with varying strength profiles". *Geo-Congress 2020: Modeling, Geomaterials, and Site Characterization*, Geotechnical Special Publication 317, J. P. Hambleton, R. Makhnenko, and A. S. Budge (eds), ASCE, 247-255.

Oathes, T.J. and Boulanger, R.W. 2022. "Nonlinear viscoplastic modeling of the Feijão Dam 1 failure." *Geo-Congress 2022: State of the Art and Practice in Geotechnical Engineering*, ASCE, Charlotte, North Carolina, March 20-23, 2022.

Oathes, T.J., Boulanger, R.W., and Ziotopoulou, K. (Under Review). "A viscoplastic constitutive model for plastic silts and clays for static slope stability applications." *Journal of Geotechnical and Geoenvironmental Engineering*.

Oberle, B. 2020. "Global Industry Standard on Tailings Management."

Olson, S.M., and Stark, T.D. 2003. "Yield strength ratio and liquefaction analysis of slopes and embankments." *ASCE Journal of Geotechnical and Geoenvironmental Engineering*. 129 (8): 727-737. https://doi.org/10.1061/(ASCE)1090-0241(2003)129:8(727)

Paniagua, P., D'Ignazio, M., L'Heureux, J.S., Lunne, T., and Karlrud, K. 2019. "CPTU correlations for Norwegian clay: an update." *AIMS Geoscience*, 5(2): 82-103. DOI: 10.3934/geosci.2019.2.82

Paul, N.A., Boulanger, R.W., and DeJong, J.T. 2020. “Accounting for spatial variability in nonlinear dynamic analyses of embankment dams on liquefiable deposits.” *ASCE Journal of Geotechnical and Geoenvironmental Engineering*. 146(11): 04020124. https://doi.org/10.1061/(ASCE)GT.1943-5606.0002372

Perret, D., Pugin, A., Mompin, R., and Demers, D. 2017. “The possible role of topographic and basin-edge effects in triggering the Mulgrave and Derrylandslide during the 2010 Val-des-Bois earthquake, Québec (Canada)”. In Proceedings of the 70th annual Canadian Geotechnical Conference GeoOttawa, Ottawa, Canada.

Perynza, P. 1963. “The constitutive equations for rate sensitive plastic materials.” *Quarterly Applied Mathematics*, 20, 321-332.

Perynza, P. 1966. “Fundamental problems in viscoplasticity.” *Advances in Applied Mechanics*, 9, 243-377.

Peuchen, J., Mayne, P.W. 2007. “Rate effects in vane shear testing.” *6th Intl. Offshore Site Investigation and Geotechnics Conference: Confronting New Challenges and Sharing Knowledge*, 259-265

PLAXIS. (2019). “PLAXIS 2D Reference Manual.” Bentley Systems International Limited, Dublin.

Plewes, H.D., Davies, M.P., and Jefferies, M.G. (1992). “CPT based screening procedure for evaluating liquefaction susceptibility.” *Proceedings of the 45th Canadian Geotechnical Conference, Totronto, Ont.*

Prevost, J. H. 1976. “Undrained stress-strain-time behavior of clays.” *Journal of Geotechnical Engineering*, 102(12). 1245-1259.

Qiu, Z. and Elgamal, A. 2020. “Three-dimensional modeling of strain-softening soil response for seismic-loading applications.” *ASCE Journal of Geotechnical and Geoenvironmental Engineering.* 146:(7).

Rezania, M., Taiebat, M., and Poletti, E. 2016. “A viscoplastic SANICLAY model for natural soft soils.” *Computer and Geotechnics*, 73, 128 - 141

Robertson, P.K. (2009). “Interpretation of cone penetration tests – a unified approach.” *Canadian Geotechnical Journal,* 46(11), 1337-1355.

Robertson, P. K. 2016. “Cone penetration test (CPT)-based soil behaviour type (SBT) classification system – an update.” *Canadian Geotechnical Journal* 53:1910-1927. dx.doi.org/10.1139/cgj-2016-0044

Robertson, P.K., de Melo, L., Williams, D.J., and Wilson, G.W. 2019. “Report of the Expert Panel on the Technical Causes of the Failure of Feijão Dam 1.” http://www.b1technicalinvestigation.com. Accessed: 12/18/2019.

Rocscience. 2018. “Slide2 Version 8.”

Sachan, A. and Penumadu, D. 2007. “Strain localization in solid cylindrical clay specimens using digital image analysis (DIA) technique.” *Soils and Foundations,* 47(1), 67-78.

Schreyer, H.L. and Chen, Z. 1986. “One-dimensional softening with localization.” *Journal of Applied Mechanics.* 53, 791-797.

Seed, H. B. and Wilson, S. D. 1967. The Turnagain heights landslide in Anchorage, Alaska. Berkeley, CA: Dept. of Civil Engineering, Institute of Transportation and Traffic Engineering, Univ. of California, Berkeley.

Sheahan, T.C. 1995. “Interpretation of undrained creep tests in terms of effective stresses.” *Canadian Geotechnical Journal*, 32, 373-379.

Sheahan, T.C., Ladd, C.C., and Germaine, J.T. 1996. “Rate-dependent undrained shear behavior of saturated clay.” *Journal of Geotechnical Engineering*, 122 (2), 99-108.

Shewbridge, S. 2019. “Undrained strengths and long-term stability of slopes.” *ASCE Journal of Geotechnical and Geoenvironmental Engineering*. 145 (11). https://doi.org/10.1061/(ASCE)GT.1943-5606.0002140

Shi, Z. and Hambleton, J.P. 2019. “Bounding surface elasto-viscoplasticity: a general constitutive framework for rate-dependent geomaterials.” *Journal of Engineering Mechanics*, 145 (3): 04019002

Shuttle, D.A., and Cunning, J. (2007). “Liquefaction potential of silts from CPTu.” *Canadian Geotechnical Journal,* 44(1), 1-19.

Silvestri, V., Soulie, M., Touchan, Z., and Fay, B. 1988. “Triaxial relaxation tests on a soft clay.” Advanced Triaxial Testing of Soil and Rock, ed. R. Donaghe, R. Chaney, and M. Silver West Conshohocken, PA: *ASTM International*, 321-337. https://doi.org/10.1520/STP29084S

Singh, A., and Mitchell, J.K. 1968. “General stress-strain-time function for soils.” *Journal of the Soil Mechanics and Foundations Division*, 94(1): 21-46.

Sladen, J.A., D'Hollander, R.D., and Krahn, J. 1985. "The liquefaction of sands, a collapse surface approach." *Canadian Geotechnical Journal*, 22: 564-578.

Sorenson, K. K., Baudet, B.A., and Simpson, B. 2006. "Influence of structure on the time-dependent behaviour of a stiff sedimentary clay." *Géotechnique*, 57 (1), 113-124.

Tatsuoka, T., Masanori, I., Di Benedetto, H., and Kuwano, R. 2002. "Time-dependent shear deformation characteristics of geomaterials and their simulation." *Soils and Foundations*, 42(2): 103-129.

Thakur, V. 2011. "Numerically observed shear bands in soft sensitive clays." *Geomechanics and Geoeningeering: An International Journal,* 6(2): 131-146.

Thakur, V., Grimstad, G., and Nordal, S. 2006. "Instability in soft sensitive clays." *In Proc. ECI Congerence on Geohazards.*

Thakur, V., Nordal, S., Viggiani, G, and Charrier, P. 2018. "Shear bands in undrained plane strain compression of Norwegian quick clays." *Can. Geotech. J.,* 55, 45-56.

USACE. 2003. Slope stability, engineer manual 1110-2-1902. Washington, D.C: USACE.

Vaid, Y.P., Robertson, P.K., and Campanella, R.G. 1979. "Strain rate behaviour of Saint-Jean-Vianney Clay." *Canadian Geotechnical Journal*, 16, 34-42.

Vergilio, C.d.S., Lacerda, D., Oliveira, B.C.V.d., Sartori, E., Campos, G.M., Pereira,L.d.S., Aguiar, D.B.d., Souza, T.d.S., Almeida, M.G.d., Thompson, F., and Rezende, C.E.d. 2020. "Metal concentrations and biological effects from one of the largest mining disasters in the world (Brumadinho, Minas Gerais, Brazil)." Scientific Reports 10, 5936 (2020). https://doi.org/10.1038/s41598-020-62700-w

Vucetic, M., and Dobry, R. 1991. “Effect of Soil Plasticity on Cyclic Response.” *Journal of Geotechnical and Geoenvironmental Engineering*, 117(1), 89–107.

Wang, W.M., Sluys, L.J., and De Borst, R. 1997. “Viscoplasticity for instabilities due to strain softening and strain-rate softening.” *International Journal for Numerical Methods in Engineering.* 40, 3839-3864.

Watabe, Y., Udaka, K., Nakatani, Y., and Leroueil, S. 2012. “Long-term consolidation behavior interpreted with isotache concept for worldwide clays.” *Soils and Foundations*, 52 (3): 449-464.

Whittle, A.J., El-Naggar, H.M., Akl, S.A.Y., and Galaa, A.M. 2022. “Stability analysis of upstream tailings dam using numerical limit analyses.” *ASCE Journal of Geotechnical and Geoenvironmental Engineering*. 04022035-1. https://doi.org/10.1061/(ASCE)GT.1943-5606.0002792

Yin, Z.Y., Hicher, P.Y., Riou, Y., and Huang, H.W. 2006. “An elasto-viscoplastic model for soft clay.” *Proc. GeoShanghai International Conference 2006*, 312-319.

Yin, Z.Y., Karstunen, M., Chang, C.S., Koskinen, M. and Lojander, M. 2011. “Modeling time-dependent behavior of soft sensitive Clay.” *Journal of Geotechnical and Geoenvironmental Engineering,* 137(11): 1103-1113.

Yin, Z.Y., Xu, Q., and Yu, C. 2015. “Elastic-viscoplastic modeling for natural soft clays considering nonlinear creep.” *Int. J. Geomech*, 15 (5): A6014001.

Yuan, Y. and Whittle, A.J. 2018. “A novel elasto-viscoplastic formulation for compression behaviour of clays.” *Géotechnique*, 68(12): 1044-1055

Yuan, Y. and Whittle, A.J. 2020. “Formulation of a new elastoviscoplastic model for time-dependent behavior of clay.” *International Journal for Numerical and Analytical Methods in Geomechanics*. https://doi.org/10.1002/nag.3173

Zabolotnii, E., Morgenstern, N.R., and Wilson, G.W. 2022. “Mechanism of failure of the Mount Polley Tailings Storage Facility”. *Canadian Geotechnical Journal*. https://doi.org/10.1139/cgj-2021-0036

Ziotopoulou, K., and Boulanger, R. W. 2016. “Plasticity modeling of liquefaction effects under sloping ground and irregular cyclic loading conditions.” *Soil Dynamics and Earthquake Engineering*, 84 (2016), 269-283, 10.1016/j.soildyn.2016.02.013.

Appendix A: Feijão Dam 1 FLAC FIS code

This appendix contains nine sequential codes that are an example of those used for the analyses in Chapter 4 of Feijão Dam 1.

A.1: Mesh Generation

```
;*********************************************************************
;  Feijao - Section 3-3'
;  - This file generates mesh and groups lower berm, upper berm and bedrock
;  baseed on the digitized profile of section 3-3' from Robertson et al. 2019
;  Tyler Oathes May 2022
;*********************************************************************
; Congfigure the set-up in FLAC

config creep gw cppudm ex 20

; Generate the mesh

grid 450,160
gen  0,820 0,980 900,980 900,820 i=1,451 j=1,161
model mohr

;;;;;;;; Tables for boundary conditions and seperate groups ;;;;;;
; profiles generated through a plot digitizer
; Bedrock Profile
table 1 0,852 &
90, 857 &
100.362, 858.182 &
118.134, 856.445 &
142.350, 856.965 &
166.566, 856.992 &
190.782, 858.880 &
214.998, 860.580 &
239.214, 862.735 &
263.430, 864.475 &
287.646, 867.531 &
311.862, 869.989 &
335.883, 870.903 &
360.294, 872.089 &
380.565, 873.003 &
407.618, 874.679 &
421.145, 876.152 &
434.671, 878.130 &
448.198, 880.003 &
461.724, 882.058 &
475.251, 884.240 &
488.777, 886.317 &
515.830, 887.576 &
542.883, 887.376 &
569.936, 888.243 &
583.462, 889.757 &
596.989, 890.993 &
610.515, 891.777 &
637.568, 889.784 &
651.095, 888.964 &
664.621, 889.514 &
678.148, 891.146 &
691.674, 893.372 &
705.201, 895.201 &
718.727, 897.190 &
732.254, 898.934 &
759.307, 900.122 &
772.833, 899.188 &
786.360, 897.705 &
799.886, 898.708 &
826.939, 906.054 &
853.660, 917.829 &
877.054, 936.534 &
884.086, 939.085 &
893.296, 942.233 &
898, 943.557 &
900, 943.557


```

```
  table 2 90, 857 &
  106.884, 862.909 &
  131.159, 872.000 &
  135.870, 872.000 &
  164.855, 885.091 &
  167.029, 885.091 &
  177.899, 889.818 &
  180.797, 889.818 &
  186.594, 892.727 &
  188.043, 892.727 &
  200.000, 898.545 &
  232.246, 898.182 &
  244.203, 904.000 &
  250.362, 904.000 &
  262.319, 909.091 &
  265.217, 909.091 &
  280.072, 915.273 &
  283.333, 915.273 &
  296.377, 922.182 &
  302.536, 922.182 &
  323.551, 929.455 &
  327.536, 929.455 &
  345.290, 937.091 &
  351.449, 937.091 &
  362.681, 942.182 &
  372.101, 942.182 &
  391.874, 938.077 &
  418.927, 937.985 &
  459.507, 937.985 &
  486.560, 937.979 &
  513.613, 937.987 &
  540.666, 937.548 &
  567.718, 936.998 &
  594.771, 936.443 &
  621.824, 936.003 &
  662.404, 935.970 &
  689.457, 935.970 &
  716.510, 935.970 &
  743.563, 935.970 &
  770.616, 935.970 &
  797.669, 935.970 &
  824.722, 935.970 &
  851.775, 935.970 &
  874.508, 935.970

  ;Upper Berms
  table 3 368.841, 942.182 &
  379.710, 936.0 &
  353.623, 936.000 &
  367.029, 929.0 &
  330.072, 929.0 &
  345.290, 920.000 &
  303.623, 921.455 &
  316.304, 915.0 &
  286.957, 915.0 &
  298.188, 908.727 &
  268.478, 908.727 &
  274.275, 905.818 &
  278.623, 905.818 &
  282.609, 903.273 &
  253.623, 903.273 &
  263.406, 898.182 &
  232.609, 898.182 &

  ;Lower Berm
  table 4 207.971, 898.545 &
  217.754, 893.455 &
  200.362, 893.455 &
  204.348, 891.273 &
```

```
195.290, 891.273 &
197.101, 890.182 &
189.130, 890.182 &
191.304, 889.0 &
184.783, 889.0 &
193.116, 885.0 &
173.551, 885.0 &
185.507, 879. &
174.638, 879 &
180.072, 876.000 &
165.217, 876.000 &
171.014, 873.0 &
155.072, 873.0 &s
179.348, 857.818

; Slime boundary
table 5 745.726, 935.745 &
658.547, 932.340 &
617.949, 924.681 &
542.735, 917.872 &
611.111, 910.638 &
481.624, 905.106 &
468.803, 900.000 &
423.077, 891.064 &
413.675, 887.660 &
419.658, 885.532 &
407.692, 880.426 &
407.692, 877.021 &
405.128, 875.745

;;;; Generate different groups and regions

;Bedrock and dam region
gen table 2
gen table 1

unmark i=438 j=116
unmark i=49 j=38,39
unmark i=48 j=38

group 'Space' region 1,160
model null group 'Space'

mark i=438 j=116
mark i=49 j=38,39
mark i=48 j=38

unmark i=48 j=40
unmark i=47,48 j=39
unmark i=49,50 j=40
unmark i=438 j=117
group 'Bedrock' region 1,1

mark i=48 j=40
mark i=47,48 j=39
mark i=49,50 j=40
mark i=438 j=117

;Slime boundary
gen table 5

group 'Slime' region 327,76
group 'Coarse Tailings' region 260,100

; Upper berms
gen table 3

unmark i=153 j=102
group 'Berm' region 173,112
```

```
208
209 ;Lower berms
210 gen table 4
211
212 unmark i=106,107 j=79
213 group 'Berm' region 85,61
214
215 mark i=106,107 j=79
216
217 ;;;;;;;Fix zones and grid points that are in wrong groups or wrong area
218
219 ; Change assigned group of elements that were assigned wrong
220
221 group 'Coarse Tailings' i=79 j=53
222 group 'Coarse Tailings' i=89 j=59
223 group 'Coarse Tailings' i=94 j=69
224 group 'Coarse Tailings' i=129 j=83
225 group 'Coarse Tailings' i=136 j=89
226 group 'Coarse Tailings' i=145  j=95
227 group 'Coarse Tailings' i=154 j=101
228 group 'Coarse Tailings' i=186 j=122
229 group 'Berm' i=149 j=90
230 group 'Berm' i=158 j=96
231 group 'Berm' i=190 j=117
232
233 group 'Slime'    i=274,275 j=98
234 group 'Coarse Tailings' i=303 j=91
235
236 ; Adjust position of grid points to account for bad geometries
237
238 ini x=547 y=917.5 i=274 j=98
239 ini x=605 y=910.5 i=304 j=91
240 ini x=297 y=909.5 i=150 j=91
241 ini x=315 y=915.5 i=159 j=97
242 ini x=379 y=936.5 i=191 j=118
243 ini x=282 y=903.273 i=142 j=84
244
245 ini x=202 y=891.273 i=102 j=72
246 ini x=202 y=892 i=102 j=73
247 ini x=204 y=892.2 i=103 j=73
248
249 ini x=217 y=893.455 i=109 j=74
250
251 ;unmark
252
253 ; Fix boundary conditions
254
255 fix x y j = 1
256 fix x   i = 1
257 fix x   i = 451
258
```

A.2: Fine and Coarse Tailings Delineation

```
;**********************************************************************
;  Feijao - Section 3-3
;  - This file dilineates the interbeded tailings layer by layer
;
;  Tyler Oathes May 2022
;**********************************************************************

; From the bottom to the top generation of digitized interbedding
; Typically table is generated and laters assigned and then individual
; elements are adjusted and grid points moved to have good geomeetry

table 6 173.078, 861.690 &
227.139, 861.690

gen table 6

group 'Fine Tailings' region 93,41
group 'Berm' i=89 j=39

table 7 284.203, 867.324 &
208.857, 867.324 &
208.877, 865.915 &
273.299, 865.915

gen table 7
group 'Fine Tailings' region 123,47
group 'Coarse Tailings' i=133,136 j=46



table 8 322.531, 870.423 &
247.45, 870.423 &
247.45, 871.549 &
156.693, 871.549 &
154.717, 872.676 &
247.434, 872.676 &
247.378, 876.620 &
178.747, 876.620

gen table 8

table 9 406.731, 878.592 &
247.071, 878.592 &
247.082, 877.746 &
231.392, 877.746 &
231.392, 879.718 &
183.469, 879.718

gen table 9

group 'Fine Tailings' region 130,55
group 'Fine Tailings' region 109,59

group 'Berm' i=92 j=60
group 'Coarse Tailings' i=80 j=52
group 'Berm' i=85 j=54
group 'Coarse Tailings' i=90 j=57
group 'Coarse Tailings' i=155,156 j=51
group 'Coarse Tailings' i=150,154 j=50
group 'Coarse Tailings' i=154 j=51

ini x=246 y=871 i=124 j=52
ini x=246 y=876 i=124 j=57
ini x=247.45 y=871 i=125 j=52

table 10 415.623, 883.944 &
247.276, 883.944 &
247.296, 882.535 &
413.122, 882.535
```

```
70
71  gen table 10
72  group 'Fine Tailings' region 145,64
73  group 'Coarse Tailings' i=206 j=63
74
75  table 11 412.783, 886.761 &
76  326, 886.761 &
77  326, 887.324 &
78  231.25, 887.324 &
79  231.250, 888.451 &
80  326, 888.451 &
81  326, 893 &
82  231.2, 893 &
83  231.2, 894.930 &
84  214.633, 894.930
85
86  gen table 11
87
88  table 12 431.743, 892.958 &
89  408.5, 892.958 &
90  408.5, 894.085 &
91  325.845, 894.085 &
92  325.845, 894.930 &
93  247.122, 894.930 &
94  247.122, 896. &
95  212.096, 896
96
97
98  gen table 12
99  group 'Fine Tailings' region 203,70
100 group 'Fine Tailings' region 159,75
101 group 'Berm' i=108 j=74
102 group 'Coarse Tailings' i=108 j=75
103
104 table 13 474, 902.817 &
105 325.845, 902.817 &
106 325.845, 905.634 &
107 273.303, 905.634 &
108 267.941, 908.451 &
109 550, 908.451
110
111 gen table 13
112
113 table 14 488.190, 905.070 &
114 407.764, 905.070 &
115 407.737, 906.479 &
116 491.890, 906.479
117
118 gen table 14
119
120 group 'Fine Tailings' region 257,88
121 group 'Fine Tailings' region 226,85
122 group 'Coarse Tailings' i=205,245 j=86
123 group 'Coarse Tailings' i=237,238 j=83
124
125 table 15 564, 915 &
126 325.545, 915 &
127 325.526, 917.0 &
128 546, 917.0 &
129
130 gen table 15
131 group 'Fine Tailings' region 275,97
132 group 'Coarse Tailings' i=273 j=98
133 group 'Slime' i=274,275 j=98
134
135 table 16 559.380, 919.718 &
136 344.814, 919.718 &
137 341.141, 921.972 &
138 580.029, 921.972
```

```
139
140  gen table 16
141  group 'Fine Tailings' region 175,102
142  group 'Coarse Tailings' i=276,280 j=100
143
144  table 17 602, 923.944 &
145  337.752, 923.944
146
147  table 18 359.194, 932.958 &
148  664.155, 932.958
149
150  gen table 17
151  gen table 18
152
153  group 'Fine Tailings' region 187,112
154
155  table 19 712.00, 934.930 &
156  354.965, 934.930 &
157  352.428, 936.00 &
158  590, 936.0
159
160  gen table 19
161  group 'Fine Tailings' region 299,116
162  group 'Coarse Tailings' i=345,357 j=115
163  group 'Coarse Tailings' i=273,296 j=117
164  group 'Coarse Tailings' i=179 j=115
165
166
167  group 'Berm' i=183 j=110
168  group 'Coarse Tailings' i=171 j=104
169  group 'Berm' i=172 j=101
170  group 'Coarse Tailings' i=139,140 j=86
171
172  ;;;; Adjust grid points that got weird with table generations
173  ini x=272 y=908 i=137 j=89
174  ini x=272 y=907 i=137 j=88
175  ini x= 278.5 y=905.3 i=140 j=86
176  ini x=276.5 y=905.5 i=139 j=86
177  ini x=272.5 y=906 i=137 j=87
178
179  ini x=232 y=895 i=117 j=76
180  ini x=232 y=894 i=117 j=75
181
182  ini x=246 y=876.62 i=124 j=58
183  ini x=247.45 y=876.62 i=125 j=58
184
185  group 'Coarse Tailings' i=124 j=57
186
187  ini x=247.45 y=871.55 i=125 j=53
188  ini x=246 y=871 i=124 j=52
189  ini x=246 y=871.55 i=124 j=53
190  ini x=247.45 y=870.45 i=125 j=51
191  group 'Coarse Tailings' i=124 j=52
192  ini x=326 y=916 i=164 j=97
193
194  ini x=231.392 y=877.746 i=117 j=59
195  ini x=247.45  y=877.746 i=125 j=59
196  ini x=247.45  y=878.592 i=125 j=60
197
198  ini x=408.5 y=894.085 i=205 j=75
199  ini x=325.845 y=902.817 i=164 j=84
200
201  ini x=408 y=906.479 i=205 j=87
202
203  group 'Slime' i=370 j=116
204
205  ini x = 740 y=935.22 i = 371 j = 116
206
207  ; Top right of mesh - grid fix
```

```
208
209   group 'Space' i=450 j=124
210   model null group 'Space'
211
212   ini x=898 y = 943.56 i=450 j=124
213   ini x=900 y = 943.56 i=451 j=124
214
215   ; Fix slime area to account for low stress conditions
216   group 'Coarse Tailings' i=353,357 j=116
```

A.3: Mohr Coulomb Properties

```
;*********************************************************************
;  Feijao - Section 3-3
;  - This file assigns static properties and initializes stresses
;  - No solving
;  Tyler Oathes May 2022
;*********************************************************************


; Definition of static properties (both model and soil)

def $properties static
    $Pa = 101.3e3     ; atmospheric pressure (Pa)
    $grav = 9.81      ; gravity constant (m/s2)

    $rho w = 1000     ; water density (kg/m^3)
    $Kwater = 2.0e9   ; Water bulk modules is 2e9 Pascal
    $Kwater low = $Kwater/10000 ; Small bulk modulus for use during initialization

    ; Water tensile limits for different materials
    $watTensBerm       = -1.0 * $rho w * $grav
    $watTensTailCoarse = -1.0 * $rho w * $grav
    $watTensTailFine   = -3.0 * $rho w * $grav

    $Ko min = 0.5     ; minimum value to try to maintain during initialization

    $Go MC = 400

    ; Permeabilities - Pulled from Table 4 Appendix G (seepage)
    ; FLAC uses permeability k = Kh / gammawater
    ;  k m^2/(Pa*sec) = Kh (cm/s) / 980700 (Pa/m) = Kh(cm/s)*1.02e-06
    ; Original as taken from Robertson et al. 2019
    ; Upscaled as changed to account for seepage condition


    $permBase x   = 1.0e-6 * 1.02e-6
    $permBase y   = 1.0e-6 * 1.02e-6

    ; $permCoarse x = 5.0e-4 * 1.02e-6 ; original
    $permCoarse x = 1.0e-5 * 1.02e-6 ; upscaled
    ; $permCoarse y = 1.0e-4 * 1.02e-6 ; original
    $permCoarse y = 1.0e-5 * 1.02e-6 ; upscaled

    $permFine x   = 1.0e-5 * 1.02e-6 ; original
    ; $permFine x   = 5.0e-5 * 1.02e-6  ; upscaled
    $permFine y   = 2.0e-6 * 1.02e-6 ; original
    ; $permFine y   = 2.0e-5 * 1.02e-6 ; upscaled

    $permSlime x  = 1.0e-6 * 1.02e-6
    $permSlime y  = 2.0e-7 * 1.02e-6

    $permBerm x   = 1.2e-4 * 1.02e-6     ;
    $permBerm y   = 1.2e-4 * 1.02e-6

    ; Porosity - from Table 2 Appendix G (seepage)

    $porosBase =   0.31
    $porosFine =   0.59
    $porosCoarse = 0.50
    $porosSlime  = 0.49
    $porosBerm   = 0.30

    ; Densities - Confirm later
    $densBase   = 1898
    $densCoarse = 2265
    $densFine   = 1898
    $densSlime  = 2014
    $densBerm   = 1863

    ; Containment berms MC properties - Section 3.1.3.2 Appendix H
```

```
70      $phiBerm   = 36   ; degree
71
72      $cohBerm   = 0    ; Pa
73      $bulkBerm  = 28e6 ; 28 MPa
74      $shearBerm = 21e6 ; 21 MPa
75
76      ; Tailings properties
77      $phiCoarse = 0.9 * 33 ; Page 35 - 38 Appendix E - Lab Testing
78      $phiFine   = 0.8 * 32 ; Page 35 - 38 Appendix E - Lab testing
79      $phiSlime  = 0.7 * 32 ; from nowhere - find real number
80      $phiBase   = 0.9 * 32 ; from nowhere - find real number
81
82      $cohCoarse = 0
83      $cohFine   = 0
84      $cohSlime  = 0
85      $cohBase   = 0
86
87  end
88
89  $properties static
90
91  ; Assign properties of water and gravity
92
93  water density $rho w bulk $Kwater ; tens 1e10
94  set grav $grav
95
96  ini ftens $watTensBerm group 'Berm'
97  ini ftens $watTensTailFine group 'Fine Tailings'
98  ini ftens $watTensTailCoarse group 'Coarse Tailings'
99  ini ftens $watTensTailCoarse group 'Bedrock'
100 ini ftens $watTensTailFine group 'Slime'
101 ;
102
103
104 ; Initialize internal water pressures
105 ; Assigned based on piece wise function fit to Robertson et al. 2019 seepage surface
106
107 def $initialize pp working
108     loop $i (1,igp)
109         loop $j (1,jgp)
110
111                 loop $p (1,jzones)          ; set zw at surface for the right edge
112                 $ii = min($i,izones)
113                     if model($ii,$p) # 1
114                         $zw = min(y($ii,$p+1),937)  ; 937 is used to keep right edge
                            stable
115                     else
116                         $zw = min($zw,937)
117                     endif
118                 endloop
119
120             if x($i,$j) < 616                                   ; Segment 7
121                 $zw = 934 + 0.0577 * (x($i,$j) - 564)
122             endif
123
124             if x($i,$j) < 564                                   ; Segment 6
125                 $zw = 918 + 0.4444 * (x($i,$j) - 528)
126             endif
127
128             if x($i,$j) < 528                                   ;Segment 5
129                 $zw = 909 + 0.0625 * (x($i,$j) - 384)
130             endif
131
132             if x($i,$j) < 384                                   ; Segment 4
133                 $zw = 904 + 0.2083 * (x($i,$j) - 360)
134             endif
135
136             if x($i,$j) < 360                                   ; Segment 3
137                 $zw = 899 + 0.049 * (x($i,$j) - 258)
```

```
            endif

            if x($i,$j) < 258                                   ; Segment 2
                $zw = 888 + 0.2292 * (x($i,$j) - 210)
            endif

            if x($i,$j) < 210                                   ; Segment 1
                $zw = 886 + 0.0526 * (x($i,$j) - 172)
            endif

            if x($i,$j) < 172                                   ; Surface for left edge
                loop $p (1,jzones)
                $ii = min($i,izones)
                    if model($ii,$p) # 1
                        $zw = y($ii,$p+1) ; -1.0 ; 1 m below the face
                    else
                        $zw = $zw
                    endif
                endloop
            endif

            $zw rise = 0.0

            if y($i,$j) > $zw + $zwrise
                sat($i,$j) = 0.0
            else
                sat($i,$j) = 1.0
                gpp($i,$j) = ($zw-y($i,$j)) * $rho w * $grav
            endif

        endloop
    endloop

    loop $i (1,izones)
        loop $j (1,jzones)
            if model ($i,$j) # 1
                pp($i,$j)=0.25*(gpp($i,$j)+gpp($i,$j+1)+gpp($i+1,$j+1)+gpp($i+1,$j))
            endif
        endloop
    endloop

end
$initialize pp working

;
;  Set boundary conditions for seepage
;
def $fixboundary
    command
        ; left boundary and toe
        fix sat  i= 1
        fix pp  i=1

        ; toe surface
        fix sat  i= 1,5 j=33
        fix sat  i=6,15 j=34
        fix sat  i=16,24 j=35
        fix sat  i=25,32 j=36
        fix sat  i=33,41 j=37
        fix sat  i=42,47 j=38

        fix pp  i= 1,5 j=33
        fix pp  i=6,15 j=34
        fix pp  i=16,24 j=35
        fix pp  i=25,32 j=36
        fix pp  i=33,41 j=37
        fix pp  i=42,47 j=38

        ; pool surface
```

```
        fix sat from 275,118 to 297,118
        fix pp  from 275,118 to 297,118
        fix sat i=297,439 j=117
        fix pp  i=297,439 j=117


        ;right boundary
        fix sat  i= 451
        fix pp  i= 451

        ; Only fix pp on the free face where we will let S<1
        ; Face above toe
        ini sat 0.0 from 47,38 to 86,68
        fix sat from 47,38 to 86,68
        fix pp  from 47,38 to 86,68

        ini sat 0.0 from 87,68 to 182,123
        fix sat from 87,68 to 182,123
        fix pp  from 87,68 to 182,123

    end command
end
$fixboundary

; Assign internal drainage conditions

def $fixdrain

; Lower drain line
    command
        ini sat 0.0 i=78,85 j=57
        fix sat     i=78,85 j=57
        ini pp  0.0 i=78,85 j=57
        fix pp      i=78,85 j=57


        ini sat 0.0 i = 69 j = 53
        fix sat     i = 69 j = 53
        ini pp  0.0 i = 69 j = 53
        fix pp      i = 69 j = 53

        ini sat 0.0 i = 70 j = 53
        fix sat     i = 70 j = 53
        ini pp  0.0 i = 70 j = 53
        fix pp      i = 70 j = 53

        ini sat 0.0 i = 71 j = 53
        fix sat     i = 71 j = 53
        ini pp  0.0 i = 71 j = 53
        fix pp      i = 71 j = 53

        ini sat 0.0 i = 72 j = 54
        fix sat     i = 72 j = 54
        ini pp  0.0 i = 72 j = 54
        fix pp      i = 72 j = 54

        ini sat 0.0 i = 73 j = 55
        fix sat     i = 73 j = 55
        ini pp  0.0 i = 73 j = 55
        fix pp      i = 73 j = 55

        ini sat 0.0 i = 74 j = 55
        fix sat     i = 74 j = 55
        ini pp  0.0 i = 74 j = 55
        fix pp      i = 74 j = 55

        ini sat 0.0 i = 75 j = 56
        fix sat     i = 75 j = 56
        ini pp  0.0 i = 75 j = 56
```

```
276           fix pp      i = 75 j = 56
277
278           ini sat 0.0 i = 76 j = 56
279           fix sat     i = 76 j = 56
280           ini pp  0.0 i = 76 j = 56
281           fix pp      i = 76 j = 56
282
283           ini sat 0.0 i = 77 j = 57
284           fix sat     i = 77 j = 57
285           ini pp  0.0 i = 77 j = 57
286           fix pp      i = 77 j = 57
287
288   ; middle drain line
289
290           fix sat     i=87,89 j=66
291           fix sat     i=87,89 j=66
292           ini pp  0.0 i=87,89 j=66
293           fix pp      i=87,89 j=66
294
295
296           ini sat 0.0 i = 81 j = 63
297           fix sat     i = 81 j = 63
298           ini pp  0.0 i = 81 j = 63
299           fix pp      i = 81 j = 63
300
301           ini sat 0.0 i = 82 j = 63
302           fix sat     i = 82 j = 63
303           ini pp  0.0 i = 82 j = 63
304           fix pp      i = 82 j = 63
305
306           ini sat 0.0 i = 83 j = 64
307           fix sat     i = 83 j = 64
308           ini pp  0.0 i = 83 j = 64
309           fix pp      i = 83 j = 64
310
311           ini sat 0.0 i = 84 j = 64
312           fix sat     i = 84 j = 64
313           ini pp  0.0 i = 84 j = 64
314           fix pp      i = 84 j = 64
315
316           ini sat 0.0 i = 85 j = 65
317           fix sat     i = 85 j = 65
318           ini pp  0.0 i = 85 j = 65
319           fix pp      i = 85 j = 65
320
321           ini sat 0.0 i = 86 j = 65
322           fix sat     i = 86 j = 65
323           ini pp  0.0 i = 86 j = 65
324           fix pp      i = 86 j = 65
325
326
327   ; upper drain line
328
329           ini sat 0.0 i=91,99 j=71
330           fix sat     i=91,99 j=71
331           ini pp  0.0 i=91,99 j=71
332           fix pp      i=91,99 j=71
333
334
335
336   ; base drain
337           ini sat 0.0 i=48,49 j=38
338           fix sat     i=48,49 j=38
339           ini pp  0.0 i=48,49 j=38
340           fix pp      i=48,49 j=38
341
342           ini sat 0.0 i=49,55 j=39
343           fix sat     i=49,55 j=39
344           ini pp  0.0 i=49,55 j=39
```

```
345          fix pp      i=49,55 j=39
346
347          ini sat 0.0 i=55,60 j=38
348          fix sat     i=55,60 j=38
349          ini pp  0.0 i=55,60 j=38
350          fix pp      i=55,60 j=38
351
352
353      ; additional drains from fig 7
354          ini sat 0.0 i=79,86 j=54
355          fix sat     i=79,86 j=54
356          ini pp  0.0 i=79,86 j=54
357          fix pp      i=79,86 j=54
358
359          ini sat 0.0 i=85,90 j=57
360          fix sat     i=85,90 j=57
361          ini pp  0.0 i=85,90 j=57
362          fix pp      i=85,90 j=57
363
364          ini sat 0.0 i=90,96 j=66
365          fix sat     i=90,96 j=66
366          ini pp  0.0 i=90,96 j=66
367          fix pp      i=90,96 j=66
368      end command
369  end
370  $fixdrain
371
372  ; Desaturate the foundation slope
373
374  def $found slope desat
375      command
376          ini sat 0.0 i=439,451 j=117
377          fix sat     i=439,451 j=117
378          ini pp  0.0 i=439,451 j=117
379          fix pp      i=439,451 j=117
380
381          ini sat 0.0 i=440,451 j=118
382          ini pp  0.0 i=440,451 j=118
383
384      end command
385  end
386  $found slope desat
387  ;-------------------------------------------------------
388  ; Assign soil properties - except for shear and bulk modulus
389
390  def $assign prop
391
392      command
393          prop dens=$densBase por=$porosBase &
394              coh=$cohBase    fri=$phiBase   &
395              k11=$permBase x  k22=$permBase y     group 'Bedrock'
396
397          prop dens=$densBerm por=$porosBerm &
398              coh=$cohBerm    fri=$phiBerm   &
399              k11=$permBerm x  k22=$permBerm y     group 'Berm'
400
401          prop dens=$densFine por=$porosFine &
402              coh=$cohFine    fri=$phiFine   &
403              k11=$permFine x  k22=$permFine y      group 'Fine Tailings'
404
405          prop dens=$densCoarse por=$porosCoarse &
406              coh=$cohCoarse    fri=$phiCoarse   &
407              k11=$permCoarse x  k22=$permCoarse y  group 'Coarse Tailings'
408
409          prop dens=$densSlime por=$porosSlime &
410              coh=$cohSlime    fri=$phiSlime   &
411              k11=$permSlime x  k22=$permSlime y    group 'Slime'
412      end command
413  end
```

```
$assign prop

;-------------------------------------------------
; these are total stresses
;-------
;  Initialize vertical stress
def $initialize_syy_sxx ; have to start at top and then go down (stresses are additive)

    loop $i (1,izones)
        $dsyy_last = 0.0
        $syy_last  = 0.0

            loop $j (1,jzones)

            $dens_use = 0.0

                $jrev = jzones + 1 -$j ; make the zone of interest start at top and
                decrease
                if model ($i,$jrev) # 1   ; if model is not null
                    $dz = (y($i,$jrev+1)+y($i+1,$jrev+1) - y($i,$jrev)  -y($i+1,$jrev))/2


                    $dens_use = density($i,$jrev)+sat($i,$jrev)*porosity($i,$jrev)*$rho_w
                    $dsyy = -1 * $dens_use * $grav * $dz / 2

                    syy($i,$jrev) = $syy_last + $dsyy_last +$dsyy

                    $syy_last  = $syy_last + $dsyy_last +$dsyy
                    $dsyy_last = $dsyy

                    sxx($i,$jrev) = -pp($i,$jrev) + $Ko_min*(syy($i,$jrev)+pp($i,$jrev))
                    szz($i,$jrev) = sxx($i,$jrev)
                end if
            endloop
    endloop


end
$initialize syy sxx

; Assign bulk and shear modulus

def $assign_moduli
    $K_G_ratio = 2*(1+0.3)/(3*(1-2*0.3))
    loop $i (1,izones)
        loop $j (1,jzones)
            if model($i,$j) # 1
                $p_stress = 0.75*(-syy($i,$j)-pp($i,$j))
                $shear = $Go_MC*$Pa*max(1,$p_stress/$Pa)^0.5
                $bulk  = $K_G_ratio * $shear
                command
                    prop shear = $shear bulk = $bulk i=$i j=$j
                end command
            endif
        endloop
    endloop
end
$assign moduli


;-------------------------------------------------------
; Cohesion for shallow elements

def $shallow_cohesion

$esyy_cut = $Pa / 2 ; Cutof at 0.25 atm or ~2.5 m of soil coverage
$Coh_add = $Pa / 10 ; Add 0.1 atm or 10 kPa of cohesion

```

```
loop $i (1,izones)
    loop $j (1,jzones)
        if model ($i,$j) # 1
            $esyy temp = -1* syy($i,$j) - pp($i,$j)
                if $esyy temp < $esyy cut
                    command
                        prop coh = $Coh add i=$i j=$j
                    end command
                end if
        end if
    end loop
end loop

end
$shallow cohesion

;-----------------------------------------------------------
;  Extra variables for plotting
;
;  ex 1:    x relative displacement
;  ex 2:    Ko
;  ex 3:    alpha
;
def $extras
    loop $i (1,izones)
        loop $j (1,jzones)
            if model($i,$j) # 1
                ex 1($i,$j) = xdisp($i,$j)-xdisp(110,1)
                ex 2($i,$j) = (sxx($i,$j)+pp($i,$j))/(syy($i,$j)+pp($i,$j))
                ex 3($i,$j) = abs(sxy($i,$j)/(syy($i,$j)+pp($i,$j)))
                ex 3($i,$j) = min(ex 3($i,$j),0.4) ; Max of 0.4 for plotting
            endif
        endloop
    endloop
end
$extras

```

A.4: Seepage Solution

```
;*************************************************************************
;  Feijao Dam Section 3-3
;
;  T.J. Oathes - May 2022
;   - Solving seepage only
;
;*************************************************************************
;
set mech off

his 60 unbalance

; initializing uncoupled analysis so can use funsat and fastwb
set flow on

set funsat on
set fastwb on
set sratio 1e-2
solve

$extras

```

A.5: Mohr Coulomb Static Solution

```
;**************************************************************************
;  Brumadihno - Section 3-3
;  - Solves for MC static equilibrium
;
;  Tyler Oathes May 2022
;**************************************************************************
;
;  Function to keep Ko from falling outside reasonable ranges
def $Ko limits
    $Ko min  = 0.45
    $Ko max  = 3.0
    loop $i (1,izones)
        loop $j (1,jzones)
            if model($i,$j) # 1
                $sxx = sxx($i,$j) + pp($i,$j)
                $syy = syy($i,$j) + pp($i,$j)
                $Ko this = $sxx / min($syy,-$Pa/100)
                if $Ko this < $Ko min
                    sxx($i,$j) = $Ko min * $syy - pp($i,$j)
                endif
                if $Ko this > $Ko max
                    sxx($i,$j) = $Ko max * $syy - pp($i,$j)
                endif
            endif
        end loop
    end loop
end
;$Ko limits
;set dyn off
set mech on
set flow off

water bulk 0

set sratio 1e-3

;step 20000
solve
$extras

$Ko limits
solve
$extras

def $Kc calc
    loop $i (1,izones)
        loop $j (1,jzones)
            if model($i,$j) # 1

                $sxx = -sxx($i,$j) - pp($i,$j)
                $syy = -syy($i,$j) - pp($i,$j)
                $sxy = -sxy($i,$j)
                ;
                $Radius = ((($sxx-$syy)/2)^2 + $sxy^2)^0.5
                $smid   = ($sxx+$syy)/2
                $s3c    = $smid - $Radius
                $s1c    = $smid + $Radius
                $sfc    = $smid - $Radius*cos($ffang)
                $Kc     = $s1c/$s3c
                ;
                ex 19($i,$j) = $Kc

            endif
        endloop
    endloop
end
$Kc calc


```

A.6: Assign Plastic Properties and Equilibrium Solution

```
;**********************************************************************
;  Feijao Dam 1 embankment with creep
;  Tyler J. Oathes - May 2022
;    - Install PM4Scrp statically
;  Extra variables for plotting
;**********************************************************************
;
; Install PM4 constitutive models
;
model dll pm4scrp group 'Fine Tailings'
model dll pm4scrp group 'Slime'
model dll pm4scrp group 'Bedrock'
model dll pm4sand group 'Berm'
model dll pm4sand group 'Coarse Tailings'

; Set properties for Fine Tailings ;;;;;;;;;;;;;;;;;;;;;;;;;;;;;;;;;;;;

def $pm4 fine
    ;
    ;Primary Parameters
    ;
    $Go     = 994.0
    $SuRat  = 0.05
    $Su     = 0.0
    $hpo    = 100 ;;100
    ;
    ; Creep Parameters
    ;
    $Rate coeff p   = 0.0 ; 0.04 when implemented
    $Rate coeff M   = 0.0 ; 0.04 when implemented
    $Rate theta     = 0.0
    $Rate beta      = 0.0
    $ref rate       = 0.0
    $min rate ratio = 0.0 ; 0.01 when implemented
    ;
    ;  Secondary parameters
    ;
    $eo           = 0.97  ; Defaults to 0.9
    $Gexp         = 0.5  ; Defaults to 0.75 if equal to 0
    $ruMax        = 0.0  ; Defaults to 0.1 so it does not control pmin
    $nbwet        = 0.32 ; 0.34 ; Default is 0.8.  Must be <=1.0 and >0.0.
    $nbdry        = 0.32; 0.34 ; Defaults to 0.5
    $nd           = 0.0  ; Defaults to 0.3
    $Ado          = 0.0  ; Default is 0.8
    $ho           = 0.02  ; Default is 0.5
    $zmax         = 0.0  ; Default is 10 < 40SuRat < 20
    $cz           = 0.0  ; Default is 100
    $ce           = 0.0  ; Default varies from 0.5 to 1.1 for SuRat at 0.25 to 0.75
    $CGdegrad     = 0.0  ; Default is 3
    $phicv        = 34.0  ; Default is 32 degrees
    $lamda        = 0.039  ; Default is 0.06
    $Ckaf         = 0.0  ; Default is 4.0
    $Su factor 1  = 0.0  ; Default is 1.0 at initialization

end
$pm4 fine
;
; Set Fine tailings parameters
;
prop P atm = $Pa  &
     G o=$Go   h po=$hpo  &
     Su Rat =$SuRat S u=$Su  group = 'Fine Tailings'
prop Rate coeff p = $Rate coeff p  &
     Rate coeff M  = $Rate coeff M  &
     Rate theta   = $Rate theta    &
     Rate beta     = $Rate beta    &
     Ref rate     = $ref rate      &
     min rate ratio= $min rate ratio group = 'Fine Tailings'
prop e_o =$eo   G_exp=$Gexp  ru_max=$ruMax   &
```

```
     n bwet=$nbwet  n bdry=$nbdry  n d=$nd  &
     h o = $ho  z max =$zmax c e=$ce c z=$cz  &
     G degr = $CGdegrad  A do = $Ado &
     phi cv = $phicv  lamda = $lamda Ckaf = $Ckaf  &
     Su factor=$Su factor 1  group = 'Fine Tailings'

; Set properties for Bedrock ;;;;;;;;;;;;;;;;;;;;;;;;;;;;;;;;;;;;;;;;;;;;;;;;;;;;

def $pm4 Bedrock
    ;
    ;Primary Parameters
    ;
    $Go     = 645
    $SuRat  = 0.5 ;0.33
    $Su     = 0.0
    $hpo    = 100
    ;
    ; Creep Parameters
    ;
    $Rate coeff p   = 0.0 ; 0.05 when utilized
    $Rate coeff M   = 0.0 ; 0.05 when utilized
    $Rate theta     = 0.0
    $Rate beta      = 0.0
    $ref rate       = 0.0
    $min rate ratio = 0.0 ; 0.01 when utilized
    ;
    ;  Secondary parameters
    ;
    $eo           = 0.45  ; Defaults to 0.9
    $Gexp         = 0.68  ; Defaults to 0.75 if equal to 0
    $ruMax        = 0.0   ; Defaults to 0.1 so it does not control pmin
    $nbwet        = 0.0   ; Default is 0.8.  Must be <=1.0 and >0.0.
    $nbdry        = 0.0  ; Defaults to 0.5
    $nd           = 0.0  ; Defaults to 0.3
    $Ado          = 0.0  ; Default is 0.8
    $ho           = 0.05  ; Default is 0.5
    $zmax         = 0.0  ; Default is 10 < 40SuRat < 20
    $cz           = 0.0  ; Default is 100
    $ce           = 0.0  ; Default varies from 0.5 to 1.1 for SuRat at 0.25 to 0.75
    $CGdegrad     = 0.0  ; Default is 3
    $phicv        = 0.0  ; Default is 32 degrees
    $lamda        = 0.0  ; Default is 0.06
    $Ckaf         = 0.0  ; Default is 4.0
    $Su factor 1  = 0.0  ; Default is 1.0 at initialization

end
$pm4 Bedrock
;
; Set Bedrock parameters
;
prop P atm = $Pa  &
     G o=$Go   h po=$hpo  &
     Su Rat =$SuRat S u=$Su  group = 'Bedrock'
prop Rate coeff p = $Rate coeff p  &
     Rate coeff M  = $Rate coeff M  &
     Rate theta   = $Rate theta    &
     Rate beta     = $Rate beta    &
     Ref rate     = $ref rate      &
     min rate ratio= $min rate ratio group = 'Bedrock'
prop e o =$eo   G exp=$Gexp  ru max=$ruMax   &
     n bwet=$nbwet  n bdry=$nbdry  n d=$nd  &
     h o = $ho  z max =$zmax c e=$ce c z=$cz  &
     G degr = $CGdegrad  A do = $Ado &
     phi cv = $phicv  lamda = $lamda Ckaf = $Ckaf  &
     Su factor=$Su factor 1  group = 'Bedrock'

def $bedrock strength
    $su rat bedrock = $SuRat
    loop $i (1,izones)
```

```
        loop $j (1,jzones)
            if z group ($i,$j) = 'Bedrock'
                $Su bed = -1* $su rat bedrock * esyy($i,$j)
                $Su bed = max($Su bed,100000)
                command
                    prop S u = $Su bed i=$i j=$j
                end command
            end if
        end loop
    end loop

end
$bedrock strength

; Set properties for Slime ;;;;;;;;;;;;;;;;;;;;;;;;;;;;;;;;;;;;;;;;;;;;;;;;;;;;;;

def $pm4 Slime
    ;
    ;Primary Parameters
    ;
    $Go     = 800 ; 80% of fine tailings
    $SuRat  = 0.04
    $Su     = 0.0
    $hpo    = 100.0
    ;
    ; Creep Parameters
    ;
    $Rate coeff p   = 0.0
    $Rate coeff M   = 0.0
    $Rate theta     = 0.0
    $Rate beta      = 0.0
    $ref rate       = 0.0
    $min rate ratio = 0.0
    ;
    ;  Secondary parameters
    ;
    $eo           = 0.0  ; Defaults to 0.9
    $Gexp         = 0.0  ; Defaults to 0.75 if equal to 0
    $ruMax        = 0.0  ; Defaults to 0.1 so it does not control pmin
    $nbwet        = 0.28 ; Default is 0.8.  Must be <=1.0 and >0.0.
    $nbdry        = 0.28 ; Defaults to 0.5
    $nd           = 0.0  ; Defaults to 0.3
    $Ado          = 0.0  ; Default is 0.8
    $ho           = 0.05 ;assume to be ductile  ; Default is 0.5
    $zmax         = 0.0  ; Default is 10 < 40SuRat < 20
    $cz           = 0.0  ; Default is 100
    $ce           = 0.0  ; Default varies from 0.5 to 1.1 for SuRat at 0.25 to 0.75
    $CGdegrad     = 0.0  ; Default is 3
    $phicv        = 0.0  ; Default is 32 degrees
    $lamda        = 0.0  ; Default is 0.06
    $Ckaf         = 0.0  ; Default is 4.0
    $Su factor 1  = 0.0  ; Default is 1.0 at initialization

end
$pm4 Slime
;
; Set Slime parameters
;
prop P atm = $Pa  &
     G o=$Go   h po=$hpo  &
     Su Rat =$SuRat S u=$Su  group = 'Slime'
prop Rate coeff p = $Rate coeff p  &
     Rate coeff M  = $Rate coeff M  &
     Rate theta   = $Rate theta    &
     Rate beta     = $Rate beta    &
     Ref rate     = $ref rate      &
     min rate ratio= $min rate ratio group = 'Slime'
prop e o =$eo   G exp=$Gexp  ru max=$ruMax   &
     n_bwet=$nbwet  n_bdry=$nbdry  n_d=$nd  &
```

```
     h o = $ho  z max =$zmax c e=$ce c z=$cz  &
     G degr = $CGdegrad  A do = $Ado &
     phi cv = $phicv  lamda = $lamda Ckaf = $Ckaf  &
     Su factor=$Su factor 1  group = 'Slime'

; Set properties for Coarse Tailings ;;;;;;;;;;;;;;;;;;;;;;;;;;;;;;;;;;;;;;;;;;;;;;;;;

def $pm4 coarse
    ;
    ;  Primary parameters
    ;
    $Go           = 994
    $Dr           = 0.35
    $hpo          = 7.5   ; Currently working, change with nb and ho
    ;
    ; Secondary parameters
    ;
    $ho     =  0.1     ; (currently working, change with nb/ho)Defaults to value calculated as a function of Dr
    $emin   =  0.0     ; Defaults to 0.5
    $emax   =  0.0     ; Defaults to 0.8
    $nb     =  0.0     ; Defaults to 0.5
    $nd     =  0.0     ; Defaults to 0.1
    $Ado    =  0.0     ; Defaults to value calculated to honor Bolton's relationship
    $zmax   =  0.0     ; Defaults to value calculated as a function of the rel. state parameter
    $cz     =  0.0     ; Defaults to 250
    $ce     =  0.0     ; Defaults to value calculated as a function of Dr
    $phicv  =  0.0     ; Defaults to 33 degrees
    $pois   =  0.0     ; Defaults to 0.3
    $Gdegr  =  0.0     ; Defaults to 2.0
    $CDR    =  0.0     ; Defaults to value calculated as a function of Dr
    $Ckaf   =  0.0     ; Defaults to value calculated as a function of Dr
    $Q      =  0.0     ; Defaults to 10.0
    $R      =  0.0     ; (calculated again down below) Defaults to 1.5
    $m      =  0.0     ; Defaults to 0.01
    $Fsed   =  0.0     ; Defaults to 0.04
    $psedo  =  0.0     ; Defaults to -Patm/5

end
$pm4 coarse

; Set Coarse Tailings parameters

prop D r = $Dr G o = $Go h po = $hpo P atm = $Pa group = 'Coarse Tailings'

prop  h o    = $ho      e min = $emin    e max  = $emax     &
      n b    = $nb      n d   = $nd     A do   = $Ado      &
      z max  = $zmax    c e   = $ce     c z    = $cz       &
      phi cv = $phicv  pois  = $pois    G degr = $Gdegr    &
      C DR   = $CDR     C kaf = $Ckaf    Q bolt = $Q        &
      R bolt = $R       m par = $m      F sed  = $Fsed     &
      p sedo = $psedo  group = 'Coarse Tailings'

def $Coarse R
    $Sucs rat = 0.09
    $M coarse = 1.089

        loop $i (1,izones)
            loop $j (1,jzones)
                if z group ($i,$j) = 'Coarse Tailings'
                $R temp = 100 * 2* $Sucs rat * (-1)* esyy($i,$j)
                $R ij = $Dr * (10-ln( $R temp /$M coarse / $Pa ))
                    command
                        prop R bolt = $R ij i = $i j = $j
                    end command
                end if
            end loop
        end_loop
```

```
275
276  end
277  $Coarse R
278  ;
279  ;  Set berm properties ********************************************
280  ;
281  def $pm4 berm
282      ;
283      ;  Primary parameters
284      ;
285      $Go           = 667   ; Currently using default, could change if needed
286      $Dr           = 0.55 ; Assumed to relatively medium dense
287      $hpo          = 0.4   ; currently using default
288      ;
289  end
290  $pm4 berm
291  ;
292  ; Set dike parameters
293  ;
294  prop  P atm = $Pa   &
295        G o=$Go   h po=$hpo D r =$Dr  group = 'Berm'
296  ;
297
298
299
300  ;  ***************************************************************************************
301  ;
302  ;  Establish equilibrium again
303  ;
304
305  initial xdisp 0 ydisp 0
306  initial xvel  0 yvel  0
307
308   water bulk 0
309
310   set mech on
311   set flow off
312
313
314  solve
315
316   $extras
317   $Kc calc
318
```

A.7: Drained Consolidation with Creep

```
;*********************************************************************
;  Feijao Dam Section 3-3'
;
;  T.J. Oathes - May 2022
;
;   - Consolidation with creep (Drained)
;
;*********************************************************************
;
;  Install creep rate parameters for this analysis case
;

def $Creep_FineTailings

    $Rate_coeff_p   = 0.04
    $Rate_coeff_M   = 0.04
    $min_rate_ratio = 0.01
end
$Creep_FineTailings

prop Rate_coeff_p = $Rate_coeff_p   &
     Rate_coeff_M = $Rate_coeff_M   &
     min_rate_ratio = $min_rate_ratio group = 'Fine Tailings'

def $Creep_Bedrock

    $Rate_coeff_p   = 0.00
    $Rate_coeff_M   = 0.00
    $min_rate_ratio = 0.01
end
$Creep_Bedrock

prop Rate_coeff_p = $Rate_coeff_p   &
     Rate_coeff_M = $Rate_coeff_M   &
     min_rate_ratio = $min_rate_ratio group = 'Bedrock'

def $Creep_Slime

    $Rate_coeff_p   = 0.05
    $Rate_coeff_M   = 0.05
    $min_rate_ratio = 0.01
end
$Creep_Slime

prop Rate_coeff_p = $Rate_coeff_p   &
     Rate_coeff_M = $Rate_coeff_M   &
     min_rate_ratio = $min_rate_ratio group = 'Slime'

; Set up drained creep consol

def $case1

    ; Allow consol by setting WATER BULK = 0

    $xDispMax = 0         ; Initialize the control parameters
    $yDispMax = 0

    $xDispLimit = 5.0     ; Limit that stops solution
    $yDispLimit = 5.0     ; Limit that stops solution

    $maxCreepIndex = 0.00001

    $mindtFactor = 0.1     ; during rupture, dt is no smaller than $mindtFactor * dt_ref
    $maxdtFactor = 1000.0  ; as things slow/stabilize, dt is no larger than
    $maxdtFactor * dt_ref

    $time_creep = 100 * (24*60*60) ; 3 days was enough if FS is large, but need > 10
    days if marginally stable
```

```
68      $ileft = 50           ; Limit the range over which solver control is conditioned
69      $iright= 450
70
71
72  end
73  $case1
74
75  ;*********************************************************************
76  ;   Zero displacements and velocities
77  ;
78  initial xdisp 0 ydisp 0
79  initial xvel  0 yvel  0
80  ;
81  ;  History variables
82  ;
83   call 7_creep_histories.fis ;
84  ;
85  ;*********************************************************************
86  ;
87  ;  Creep solution
88  ;
89  water bulk 0  ; Set zero so no pwp (consols) during creep
90
91  set creeptime 0.0
92  set crdt=auto
93
94  set flow off
95
96
97
98
99  def $creep_solve
100
101     $xDispMax = 0.0
102     $yDispMax = 0.0
103     $maxBlocks= 1.0e8
104
105     $dtCreep = 1.0e12
106     loop $i ($ileft,$iright)
107         loop $j (1,jzones)
108             if model($i,$j) # 1
109                 if z_model($i,$j) = 'pm4scrp'
110                     $dtCreep = min($dtCreep, z_prop($i,$j,'dt_max'))
111                 end_if
112             end_if
113         end_loop
114     end_loop
115     $dtCreepRef = $dtCreep
116
117     $time = 0.0
118     loop $iBlocks (1,$maxBlocks)
119         $time = $time + 1000.0 * $dtCreep
120         command
121             set mindt=$dtCreep
122             set maxdt=$dtCreep
123             solve age $time auto
124         end_command
125         $maxdtAllow  = 1.0e12
126         $CreepIndex = 0.0
127         loop $i ($ileft,$iright)
128             loop $j (1,jzones)
129               if model($i,$j) # 1
130                 if z_model($i, $j) = 'pm4scrp'
131                     $maxdtAllow  = min($maxdtAllow, z_prop($i,$j,'dt_max'))
132                     $CreepIndex  = max($CreepIndex, z_prop($i,$j,'CreepIndex'))
133                 end_if
134               end_if
135             end_loop
136         end_loop
```

```
137           if $maxdtAllow < $dtCreepRef
138               $maxdtAllow = max($maxdtAllow,$mindtFactor*$dtCreepRef)
139           else
140               $maxdtAllow = min($maxdtAllow,$maxdtFactor*$dtCreepRef)
141           end if
142
143           if $dtCreep <  $maxdtAllow
144               $dtCreep = min($dtCreep * 1.2,$maxdtAllow)
145           else
146               $dtCreep = max($dtCreep * 0.8,$maxdtAllow)
147           end if
148
149           loop $i ($ileft,$iright)
150               loop $j (1,jgp)
151                   $xDispMax = max($xDispMax,abs(xdisp($i,$j)))
152                   $yDispMax = max($yDispMax,abs(ydisp($i,$j)))
153               endloop
154           endloop
155
156           if $xDispMax > $xDispLimit
157               $iBlocks = $maxBlocks + 1
158           endif
159           if $yDispMax > $yDispLimit
160               $iBlocks = $maxBlocks + 1
161           endif
162           if $CreepIndex < $maxCreepIndex
163               $iBlocks = $maxBlocks + 1
164           endif
165           if $time > $time creep
166               $iBlocks = $maxBlocks + 1
167           endif
168
169       end loop
170   end
171   $creep solve
172   ;
173   ;*************************************************************************
174   ;
175   def $extras after consol
176       loop $i (1,izones)
177           loop $j (1,jzones)
178               if model($i,$j) # 1
179                   ex 6($i,$j) = pp($i,$j)
180                   ex 7($i,$j) = syy($i,$j) + pp($i,$j)
181               endif
182           endloop
183       endloop
184   end
185   def $extras after creep
186       loop $i (1,izones)
187           loop $j (1,jzones)
188               if model($i,$j) # 1
189                   ex 10($i,$j) = 1.0-(syy($i,$j) + pp($i,$j))/ex 7($i,$j)
190                   ex 11($i,$j) = -(pp($i,$j)-ex 6($i,$j))/ex 7($i,$j)
191               endif
192           endloop
193       endloop
194
195   end
196
197   $extras
198   $Kc calc
199   $extras after consol
200   $extras after creep
201
202   ;*************************************************************************
203
204
```

A.8: Histories

```
;*********************************************************************
;  Tailing embankment with creep
;
;  T. J. Oathes - May 2022
;
;   - Histories for creep loading phase
;
;*********************************************************************
;
his nstep 500
his  10 unbalance
his  90 crtime

his 100 xdisp i= 86, j=68
his 101 xdisp i=110, j=79
his 102 xdisp i=148, j=102
his 103 xdisp i=185, j=123

his 200 ydisp i= 86, j=68
his 201 ydisp i=110, j=79
his 202 ydisp i=148, j=102
his 203 ydisp i=185, j=123

his 300 esyy i= 80, j=53
his 301 esxx i= 80, j=53
his 302 sxy  i= 80, j=53
his 303 pp   i= 80, j=53
his 304 ssi i= 80, j=53
his 305 st param i= 80, j=53
his 306 Mb   i= 80, j=53
his 307 Mcur   i= 80, j=53
his 308 eqrate i= 80, j=53
his 309 syy i= 80, j=53

his 310 esyy i= 110, j=78
his 311 esxx i= 110, j=78
his 312 sxy i= 110, j=78
his 313 pp   i= 110, j=78
his 314 ssi i= 110, j=78
;his 315 st param i= 110, j=78
his 316 Mb   i= 110, j=78
his 317 Mcur   i= 110, j=78
;his 318 eqrate i= 110, j=78
his 319 syy i= 110, j=78

his 320 esyy i= 148, j=101
his 321 esxx i= 148, j=101
his 322 sxy i= 148, j=101
his 323 pp   i= 148, j=101
his 324 ssi i= 148, j=101
;his 325 st param i= 148, j=101
his 326 Mb   i= 148, j=101
his 327 Mcur   i= 148, j=101
;his 328 eqrate i= 148, j=101
his 329 syy i= 148, j=101

his 330 esyy i= 185, j=122
his 331 esxx i= 185, j=122
his 332 sxy i= 185, j=122
his 333 pp   i= 185, j=122
his 334 ssi i= 185, j=122
;his 335 st param i= 185, j=124
his 336 Mb   i= 185, j=122
his 337 Mcur   i= 185, j=122
;his 338 eqrate i= 185, j=124
his 339 syy i= 185, j=122

his 340 esyy i= 176, j=80
his 341 esxx i= 176, j=80
```

```
his 342 sxy i= 176, j=80
his 343 pp  i= 176, j=80
his 344 ssi i= 176, j=80
;his 345 st param i= 176, j=80
his 346 Mb  i= 176, j=80
his 347 Mcur   i= 176, j=80
;his 348 eqrate i= 176, j=80
his 349 syy i= 176, j=80

```

A.9: Wetting Event Solution

```
;*********************************************************************
;  Tailing embankment with creep
;
;  T. J. Oathes - May 2022
;  Wetting event (undrained)
;
;  ********************************************************************************


initial xdisp 0 ydisp 0
initial xvel  0 yvel  0

;  ********************************************************************************
;*********************************************************************
;
;  Creep solution with wetting and loss of suction
;
;  Reset the bulk modulus for undrained creep, but keeping dike drained


water bulk $Kwater
initial fmod = 0 group 'Berm'

; Flags for incremental saving of model

def $incrementalsav
    $disp stop1 = -0.02
    $disp stop2 = -0.1
    $disp stop3 = -0.4
    $disp stop4 = -1.0

    $sav stop1  = 0
    $sav stop2  = 0
    $sav stop3  = 0
    $sav stop4  = 0
end
$incrementalsav



def $creep solve2

;   $xDispMax = 0.0
;   $yDispMax = 0.0
    $maxBlocks= 1.0e8

    $wetSat   = 0.05;      ; Increase in saturation above water table in Tailings (adds
    mass)
    $maxBlocksWet= 30   ; Block for wetting and suction reduction
                        ; Check: dt = 5.3e-3; 1000 steps/block; total wetting time =

    $time creep = $time creep + 100*24*60*60 ; 365*24*60*60 ; add one year


    $xDispLimit = 5.0     ; Limit that stops solution
    $yDispLimit = 5.0     ; Limit that stops solution
    $maxCreepIndex = 0.0

;

    loop $iBlocks (1,$maxBlocks)

        if $iBlocks < $maxBlocksWet
          loop $i (1,izones)
            loop $j (1,jzones)
                if z group($i,$j) # 'Bedrock'
                ;Allow wetting & suction loss at top grid pts
                    $ip1 = $i + 1
                    $jp1 = $j + 1
```

```
                    if sat($i,$jp1) < 1.0
                        sat($i,$jp1) = min(1.0, sat($i,$jp1) + ($wetSat/2)/$maxBlocksWet)
                    end if
                    if sat($ip1,$jp1) < 1.0
                        sat($ip1,$jp1) = min(1.0, sat($ip1,$jp1) +
                        ($wetSat/2)/$maxBlocksWet)
                    end if
                    if gpp($i,$jp1) < 0.0
                        gpp($i,$jp1)  = gpp($i,$jp1) * 0.8
                    end if
                    if gpp($ip1,$jp1) < 0.0
                        gpp($ip1,$jp1)  = gpp($ip1,$jp1) * 0.8
                    end if
                end if
            end loop
          end loop
        end if

        ; Assuming that dtCreep is retained from prior analysis stage
        $time = $time + 1000.0 * $dtCreep
        command
            set mindt=$dtCreep
            set maxdt=$dtCreep
            solve age $time auto
        end command
        $maxdtAllow  = 1.0e12
        $CreepIndex = 0.0
        loop $i (1,izones)
            loop $j (1,jzones)
              if model($i,$j) # 1
                if z model($i, $j) = 'pm4scrp'
                    $maxdtAllow  = min($maxdtAllow, z prop($i,$j,'dt max'))
                    $CreepIndex  = max($CreepIndex, z prop($i,$j,'CreepIndex'))
                end if
              end if
            end loop
        end loop
        if $maxdtAllow < $dtCreepRef
            $maxdtAllow = max($maxdtAllow,$mindtFactor*$dtCreepRef)
        else
            $maxdtAllow = min($maxdtAllow,$maxdtFactor*$dtCreepRef)
        end if

        if $dtCreep <  $maxdtAllow
            $dtCreep = min($dtCreep * 1.2,$maxdtAllow)
        else
            $dtCreep = max($dtCreep * 0.8,$maxdtAllow)
        end if

        loop $i (1,igp)
            loop $j (1,jgp)
                $xDispMax = max($xDispMax,abs(xdisp($i,$j)))
                $yDispMax = max($yDispMax,abs(ydisp($i,$j)))
            endloop
        endloop

        if xdisp(86,68) < $disp stop1
            if $sav stop1= 0
                $savefile = 'savstop1.sav'
                command
                    save @$savefile
                endcommand
            endif
            $sav stop1 = 1
        endif

        if xdisp(86,68) < $disp stop2
            if $sav stop2= 0
                $savefile = 'savstop2.sav'
```

```
                command
                    save @$savefile
                endcommand
            endif
            $sav stop2 = 1
        endif

        if xdisp(86,68) < $disp stop3
            if $sav stop3= 0
                $savefile = 'savstop3.sav'
                command
                    save @$savefile
                endcommand
            endif
            $sav stop3 = 1
        endif

        if xdisp(86,68) < $disp stop4
            if $sav stop4= 0
                $savefile = 'savstop4.sav'
                command
                    save @$savefile
                endcommand
            endif
            $sav stop4 = 1
        endif


        if $xDispMax > $xDispLimit
            $iBlocks = $maxBlocks + 1
        endif
        if $yDispMax > $yDispLimit
            $iBlocks = $maxBlocks + 1
        endif
        if $CreepIndex < $maxCreepIndex
            $iBlocks = $maxBlocks + 1
        endif
        if $time > $time creep
            $iBlocks = $maxBlocks + 1
        endif

    end loop
end
$creep solve2

;
;*************************************************************************
;
$extras
$Kc calc
$extras after creep

def $extra after wet

    loop $ii (2,izones)
        loop $jj (2,jzones)

            ex 18($ii,$jj)  = ssi($ii,$jj) * 100 * 2
            ex 18($ii,$jj)  =  min(ex 18($ii,$jj),15)

        end loop
    end loop
end
$extra after wet

set hisfile xdisp 400 94wet.txt

his write 90 vs 101 close

```